University of Natal

Gas Residence Time Testing and Model Fitting: A Study of Gas–Solids Contacting in Fluidised Beds

R.J. Dry

Gas Residence Time Testing and Model Fitting:

A Study of Gas-Solids Contacting in Fluidised Beds

by

Rodney James Dry

B.Sc. Eng. (UCT)
M.Sc. Eng. (Natal)

A thesis submitted in partial fulfilment of the requirements for the degree of Doctor of Philosophy in the Department of Chemical Engineering, University of Natal, Durban, South Africa.

DECLARATION

I hereby certify that, unless specific indication to the contrary is made in the text, everything contained in this thesis is my own original work. This work has not been accepted in substance, or submitted in candidature for a degree at any university other than the University of Natal, Durban, South Africa.

R. J. Dry
.....
R.J. DRY

29/11/84
.....
DATE

ACKNOWLEDGEMENTS

Special thanks to Professor M.R. Judd and Dr. T. Shingles who between them provided the main stimulation and guidance throughout this work.

Thanks to Mr. G. Vermeulen for setting up and helping run the equipment.

I am grateful to Sasol Limited for the use of facilities and general support of this research effort.

Thanks to Mrs. Elza van Rooyen and Mrs. Bev. White for typing this thesis.

Finally, thanks to my wife, Linda, for her continued encouragement and support.

ABSTRACT

This work is concerned with the effect of vessel geometry on the hydrodynamics of fluidisation of a bed of milled iron oxide. The effect of going from a cold model representative of a typical pilot plant reactor to one simulating a semi-commercial unit is quantified, and various reactor internal configurations on the latter are evaluated.

The experimental approach is one based on residence time testing and model fitting with parameter optimisation. A model screening aimed at identifying the most reasonable modelling approach is included, and altogether seven models in two categories are formulated and solved in the dynamic mode. Three of these models are considered novel at present, along with the dynamic solutions to two of the others.

The residence time technique involves methane as an inert tracer in air, and continuous analysis of gas withdrawn from the bed via sample probes by a pair of flame ionisation detectors. The process stimulus is governed by a pseudo-random binary sequence, and correlation analysis is employed for noise reduction. A Fourier transform routine, developed from first principles, converts a pair of correlation functions to a process frequency response, and model predictions are compared with the experimental data in this form. Two parameters per model are fitted, and the residual error at the optimum parameter combination provides a

means of identifying the best-fitting model. The optimised parameters of this model are regarded as estimates of those of the actual process.

Five models compete in the first screening category. Four of these have appeared in the literature in one form or another, and the fifth is novel in that it accounts for axial mixing in the bubble phase by employing multiple plug flow units. This model, referred to as the multiple bubble-track or MBT model, is shown to fit the experimental data better than any of the other models in both bubbling and slugging systems. This suggests that employing multiple plug flow units in parallel for the bubble phase is mechanistically more correct than employing a single plug flow unit.

The second screening category is related to the situation in which gas is sparged into an already fluidised bed at some height above the main distributor. The two models in this category are both considered novel, and describe opposite extremes of possible behaviour in one particular sense: one assumes rapid coalescence between grid and sparger bubbles, and the other none at all. The laterally segregated bubble phase or LSBP model emerges as the better process description. The formulation of this model suggests that physically, bubbles from the sparger tend to retain their identity as they pass through the bed.

Crossflow ratios estimated on the basis of the best-fitting model in each category point to the existence of a very strong scale-up

effect. From the shape of the crossflow profiles it appears that most of the interphase mass transfer occurs in the bottom meter or so of the bed, and it is suggested that grid design is the most significant controlling factor. The presence or otherwise of vertical coils in the bed is shown to have no significant effect on crossflow, and mass transfer between sparger bubbles and the dense phase is shown to be similar to that between grid bubbles and the dense phase.

Finally, it is demonstrated that the axial crossflow profile in the bubbling bed is consistent with the concept of an axially invariant mass transfer coefficient based on bubble to dense phase interfacial area.

NOTES TO THE EXAMINER

This work involves, in certain areas, information which may not be divulged for proprietary reasons. These areas are in particular -

(i) The exact nature of the powder, including its full particle size distribution.

(ii) The mechanical details of the multi-orifice distributor and the sparger in the 0.64 m cold model.

(iii) The mechanical details of the dummy coils and supports in the same unit.

TABLE OF CONTENTS

LIST OF FIGURES

LIST OF TABLES

LIST OF PRINCIPAL SYMBOLS

A_i	constants defined in model solution descriptions
A_t	tube or bed cross-sectional area
a_i	constants defined in model solution descriptions
a_b	interfacial area per unit bubble volume
$\bar{a}$	amplitude of PRBS signal
b_i	constants defined in model solution descriptions
C_b	bubble concentration
C_{bi}	concentration in bubble-track i
C_{bg}	grid bubble concentration
C_{bs}	sparger bubble concentration
C_c	cloud concentration
C_e	emulsion or dense phase concentration
C_o	inlet concentration
$\bar{C}$	average concentration
C_{bo}	bubble concentration at z = o
C_{co}	cloud concentration at z = o
C_{eo}	emulsion concentration at z = o
C_{in}	process stimulus concentration
C_{out}	process response concentration
d_b	bubble diameter
d_o	initial bubble diameter
d_p	particle diameter
D_b	bubble phase dispersion coefficient
D_d	dense phase dispersion coefficient
$\bar{D}$	delay operator

D_t	tube diameter
D	diffusion coefficient
D_f	effective film diffusion coefficient
f_i	bubble-track weighting fraction
f_s	sparger bubble phase weighting fraction
g	gravitational acceleration
G_e	experimental frequency response
G_m	model frequency response
G_p	process transfer function
G_{ls}	lower sampling system transfer function
G_{us}	upper sampling system transfer function
h	bed height
H_d	height of the dense phase
j	imaginary multiplier
$(K_{be})_s$	bubble-dense phase MTC, ref. interfacial area
$(K_{bc})_b$	bubble-cloud MTC, ref. bubble volume
$(K_{ce})_b$	cloud-emulsion MTC, ref. bubble volume
$(K_{be})_b$	bubble-dense phase MTC, ref. bubble volume
K_l	bubble-dense phase MTC in lower region, ref. bbl vol
K_u	bubble-dense phase MTC in upper region, ref. bbl vol
K_{gl}	grid bbl-dense phase MTC in lower region, ref. bbl vol
K_{gu}	grid bbl-dense phase MTC in upper region, ref. bbl vol
K_s	sparger bbl-dense phase MTC, ref. bbl vol
L_f	expanded bed height
L_t	vertical sampling probe separation, i.e. test section height
L_s	sparger height above the grid

N_b	bubble phase dispersion number
N_d	dense phase dispersion number
N	number of decisions in PRBS
ΔP	pressure differential
$r(\tau)$	true auto- or crosscorrelation
$R(\tau)$	estimate of auto- or crosscorrelation
S	spectral density function
s	Laplace-transformed time variable
t	time
t_f	time beyond which analytical decay tail is applied
Δt_p	PRBS decision time
Δt_s	sampling interval
Δt_{pp}	peak-to-peak transmission time
U_b	bubble velocity
U_{br}	rise velocity of an isolated bubble
U_d	velocity of gas relative to the solids in the dense phase
U_e	velocity of gas in the emulsion phase relative to the vessel wall
U_s	velocity of solids relative to the vessel wall
U_o	superficial gas velocity
U_{mf}	minimum fluidisation velocity
U_r	reduced dense phase velocity
U_{bl}	bbl velocity in lower region
U_{bu}	bbl velocity in upper region
U_{bs}	velocity of sparger bubbles
U_{bg}	velocity of grid bubbles
U_{pp}	peak-to-peak transmission velocity

U_{bi}	bubble velocity of track i
U^{*}_{bi}	reduced bubble velocity of track i
$\bar{U}_b$	average bubble velocity
V_b	volume of bubbles
W	weight of powder charge
X_b	bubble to dense phase crossflow ratio
X_{bc}	bubble to cloud crossflow ratio
X_{ce}	cloud to emulsion crossflow ratio
X_e	weighted X_b defined $\delta X_b / (1-\delta)\varepsilon_d$
X_s	sparger bubble to dense phase crossflow ratio
X_1	constant defined by eq. (4.73)
X_2	constant defined by eq. (4.74)
x	cloud thickness co-ordinate
X(s)	exciting function in the Laplace domain
$Y_1(s)$	lower sample station signal in the Laplace domain
$Y_2(s)$	upper sample station signal in the Laplace domain
z,Δz	bed height co-ordinate, height increment

GREEK SYMBOLS:

α	ratio of cloud plus wake to bubble volume
α_i	constants defined in model solution descriptions
β	constant defined by eq. (4.128)
β_i	constants defined in model solution descriptions
γ_i	constants defined in model solution descriptions
γ_c	cloud thickness
Δ	determinant
δ	fractional volumetric bubble holdup
$\mathcal{E}$	ensemble expectation value
ε_d	dense phase voidage
ε_{mf}	minimum fluidisation voidage
λ_i	complex polynomial roots
ζ	dimensionless cloud thickness co-ordinate
θ	dimensionless time
ν	Laplace transformed height co-ordinate
ξ	dimensionless height co-ordinate
ρ_k	constants defined in MBT model solution
ρ_p	particle density
ρ_f	fluid density
τ	correlation lag
τ_p	process time constant
ϕ	bubble rise coefficient
ϕ_i	constants defined in model solution descriptions
ψ	constant

SUBSCRIPTS

i, k, 1	counters
n	running counter specifying number of time increments

ABBREVIATIONS

A/D	analog to digital
BC	boundary condition
BPD	bubble-phase dispersion (model)
CCBM	countercurrent backmixing (model)
FCC	fluidised catalytic cracking
FID	flame ionisation detector
FT	Fourier transform
IC	initial condition
LMBP	laterally mixed bubble phase (model)
LSBP	laterally segregated bubble phase (model)
MBT	multiple bubble-track (model)
MVD	May-Van Deemter (model)
MTC	mass transfer coefficient
PRBS	pseudo random binary sequence
RTD	residence time distribution
WFD	Werther film diffusion (model)

CHAPTER 1

INTRODUCTION

The performance of a fluidised bed as a chemical reactor depends on the reaction kinetics and the quality of gas-solids contact. For a solid-catalysed, gas-phase reaction the idealised chemical conversion process may be described as a sequence of steps or resistances as set out in Figure 1.1. Gas enters the reactor mainly in the form of bubbles. These bubbles are essentially catalyst-free, and some of the gas is transported across the bubble-cloud boundary. This step represents the first resistance (R_1) to the overall process, and reaction in the catalyst-rich cloud phase represents the second (R_2). A portion of the gas which leaves the bubble and enters the cloud does not react in this phase, but is transported to the emulsion phase (R_3). In the latter phase reaction occurs as in the cloud phase (R_4).

In general, either the interphase mass transfer or the chemical reaction could be rate-limiting. In terms of the resistances in Figure 1.1, overall reactor performance is largely dependent on the balance between R_1 and R_3 as opposed to R_2 and R_4.

The chemical reaction resistances are functions of local process conditions and of the catalyst itself. Local reaction rates may be enhanced or retarded by changing, for example, the catalyst composition, porosity or temperature. Investigations of this

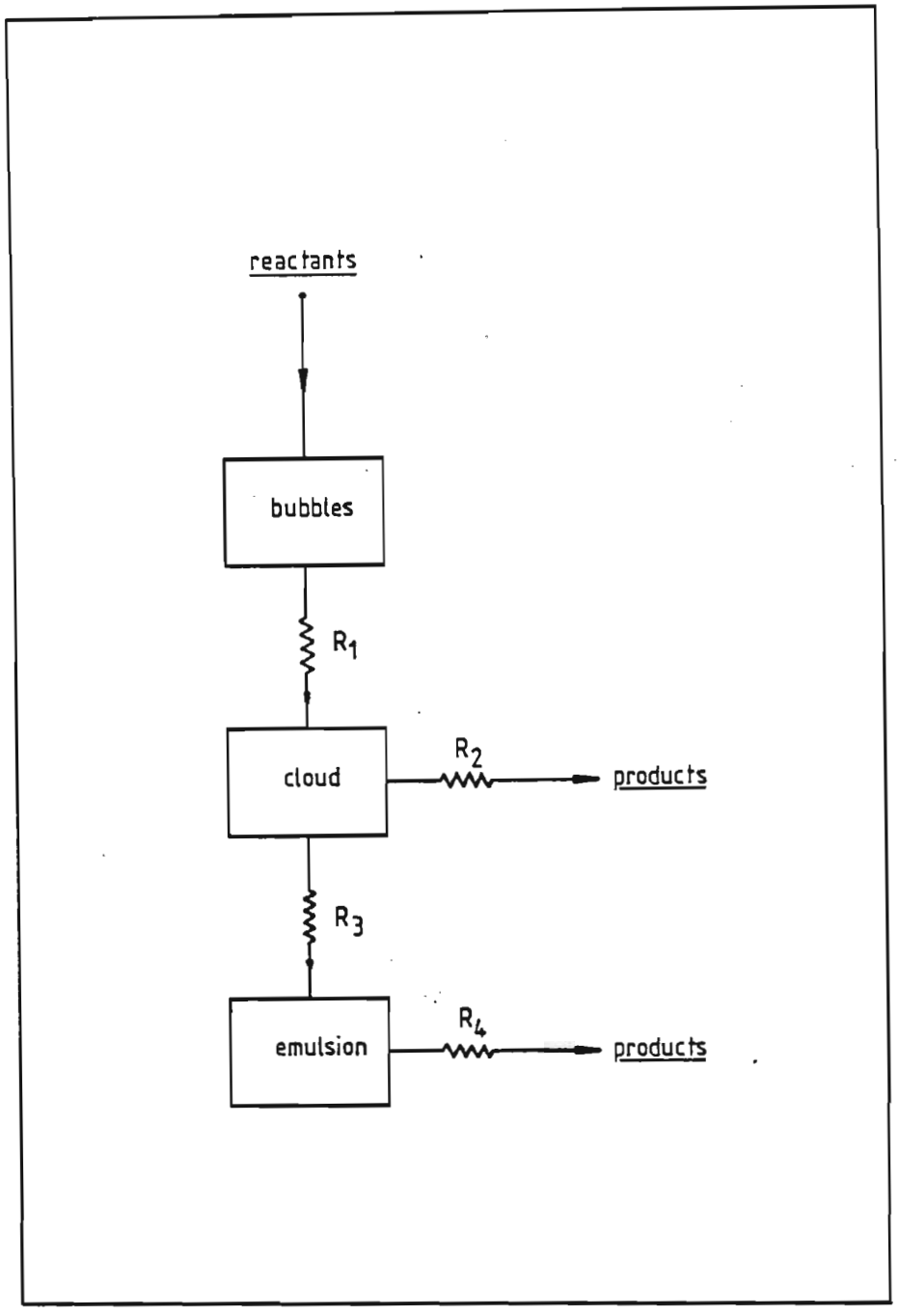

FIGURE 1.1 IDEALISED PROCESS RESISTANCES

nature are usually conducted in laboratory-scale units, and conditions are often carefully selected and controlled to eliminate or at least minimise hydrodynamic effects.

A different but related problem facing the practising engineer is that of scale-up. The chemical reaction resistances are generally considered fixed in this case, and some idea of how the hydrodynamic resistances are affected by vessel geometry is needed. Data from a pilot plant of some type is usually available, and as such provides the basis for a full-scale commercial design. The effect of exchanging the pilot reactor hydrodynamics for those of its larger counterpart need to be accounted for in some suitable manner - indeed the success or failure of the entire venture could depend on how well the hydrodynamics of scale are understood.

This study is concerned with the latter of these problems. The process involves Fischer-Tropsch synthesis in fluidised beds of fine iron-based catalysts of the type presently used in Sasol's Synthol process. Small-scale pilot reactors have been successfully operated for many years, and a research drive is currently under way to demonstrate the feasibility of this operation in full-scale units. The work reported here forms an integral part of the broader research initiative, and is aimed specifically at quantifying the effect of vessel geometry on the hydrodynamics of the system.

The concept of Fischer-Tropsch synthesis in a fluidised bed is by no means a new one. In order to place the current effort in context and to highlight the need for this study, it is necessary to sketch briefly the history of fluidisation and of this process in particular.

1.1 The Early Years

The world's first commercial catalytic fluidised bed reactor was commissioned at Exxon's Baton Rouge refinery in May 1942. This fluidised catalytic cracker was introduced as a competitor for the existing Houdry fixed-bed process, and its development was undoubtedly spurred on by the increased demand for high-grade gasoline associated with the war effort (1). Design data for this 13300 bbl/day plant was obtained from a 100 bbl/day pilot unit, i.e. a scale-up factor of about 130 (2). Numerous mechanical and materials problems required attention, but the actual process scale-up was relatively trouble-free. So successful was the fluid cat cracker that, two years later, its total capacity in the United States surpassed that of the Houdry units.

Other commercial applications for this form of gas-solids contacting device soon emerged. These included thermal coking, catalytic hydroforming of naptha, iron ore reduction, ore roasting and many more. Amongst these is the Fischer-Tropsch synthesis over iron-based catalysts.

1.2 Fischer-Tropsch Synthesis in a Fluidised Bed

During the war, Germany produced a significant portion of her gasoline and lubricating oil requirements by Fischer-Tropsch synthesis in fixed beds (3). This process was studied in the United States during and immediately after the war, and it was recognised that an enormous increase in space-time yield could be obtained if the fixed bed were replaced by a fluidised bed. This is a result of the strongly exothermic reaction and the higher heat transfer rates attainable in fluidised beds.

In the late 1940's construction began on a 7000 bbl/day plant for the conversion of reformed natural gas to liquid products by Fischer-Tropsch synthesis in fluidised beds. This plant was located at Brownsville, Texas, and design data were obtained mainly from a 0.122 m pilot reactor located at Trenton, New Jersey. The economics of the overall venture were based on conversions obtained in the pilot unit, and it was only once the 5 m commercial reactors were in place and nearly completed that disturbing data from larger pilot units became available. This data suggested that conversion dropped progressively as the reactor diameter was increased. This trend was confirmed when the commercial reactors were commissioned, and for an excellent account of the ensuing modifications and attempts to improve conversion the reader is referred to a paper by Squires (1). Finally, plagued by poor reactor performance and the rising cost of natural gas, the Brownsville plant was forced to close down in 1957.

While the Brownsville experience was in progress, a different form of fluidised bed reactor for Fischer-Tropsch synthesis was being developed by the M.W. Kellogg Company. This sytem was based on a dilute-phase transported or entrained bed, and a catalyst grind very much finer than that employed at Brownsville. The concept was demonstrated on a 0.102 m pilot reactor, and data from this unit provided the basis for the design of the commercial-scale synthesis reactors built at Sasolburg, South Africa in the early 1950's. The start-up in this case was also by no means trouble-free and many practical problems were initially encountered. The basic concept was sound, however, as has been borne out by many years of successful operation.

It is against this background that the present research drive is under way to re-evaluate the feasibility of Fischer-Tropsch synthesis in a conventional fluidised bed. The potential advantages of such a system over the existing entrained bed design are lower capital and operating costs and probably less maintenance. A demonstration-scale conventional fluidised bed reactor with diameter a little less than 1 m is presently being commissioned at Sasolburg. The pilot plant fluidised bed rectors which Sasol has been operating for 20 years or so have a diameter of ca 0.05 m, and an understanding of the hydrodynamic differences between these small units and their larger counterpart could provide the key to successful operation. Equally important is the effect of various internals and gas distribution strategies on the effective-- ness of gas-solids contact in the larger bed - hence the aim of the work described in this dissertation: to investigate the hydrodynamic

differences between a small and a large fluidised bed of fine iron oxide powder, and to examine the effects of various internal geometries on the larger of these.

CHAPTER 2

LITERATURE SURVEY AND AN OVERVIEW

The fluidisation literature has expanded enormously in the past three decades or so, and has now reached the stage where a complete review is all but impossible. Given the rather specific objectives of this study it is clear that certain literary areas are not directly relevant, so only that material which does have some direct bearing on the problem at hand will be considered.

By way of a general introduction into the literature on modelling fluidised bed reactors it is instructive to follow briefly the historical development of concepts which have led to the current state of understanding. Before proceeding, however, it would seem appropriate to give a brief qualitative description of the physics involved in the process under discussion.

The situation envisaged is essentially one in which gas is passed upwards through a bed of finely divided solids. If virtually the entire weight of the solid is borne by the gas rather than by the walls and base of the containing vessel, the solids are said to be fluidised. There are some very definite practical limitations to the range of particle sizes that may be fluidised in this way - if the particles are too large then the gas velocities required to support them become excessive. At the other end of the spectrum, once the particle size drops below a certain minimum, interparticle

forces predominate over body forces and a cohesive mass which cannot be fluidised in any normal way results. If a fluidised bed is to be employed as a catalytic reactor it is generally considered favourable to use a solid which is fine but not cohesive, since this allows a large catalyst surface area to be present in the system while proper fluidisation is maintained.

The appearance of a fluidised bed at a gas velocity significantly above that required to just fluidise it is generally similar to that of a boiling liquid. Gas voids which are usually referred to as bubbles are generated at the gas distribution points. They rise through the mass of closely-spaced solid particles, commonly referred to as the dense phase, in much the same way as they would in a liquid. They undergo coalescence and possibly splitting before bursting at the bed surface, and this overall bubbling action leads to rapid axial solids mixing. Excellent temperature uniformity is possible - a very important advantage over the packed bed for catalytic operations.

When a bubble bursts at the surface of the bed, some particles are thrust into the above-bed region, i.e. the freeboard. Some of these particles return to the bed, but others, in particular the finer ones, are carried out of the system with the gas stream and are said to have been elutriated. The freeboard region is very often a non-trivial part of the overall system, since additional gas-solids contact and chemical reaction is possible in this zone.

2.1 The Historical Development of Modelling

As with most new processes, the earliest modelling efforts were fairly crude by modern standards. Gilliland and co-workers at MIT were amongst the first to attempt fluidised bed modelling in the late 1940's, and Gilliland and Mason (4) reported the results of gas tracer tests on 1 and 3 inch cold models in the form of a quasi-Fickian dispersion process superimposed on plug flow. This approach was not very satisfactory, however, since it failed to account for the essential two-phase nature of the system. Until around the end of the 1950's a more general application of gas residence time distribution (RTD) concepts was also popular, the principal aim being to establish the degree of gas mixing in the bed between the extremes of plug flow and perfect mixing. Gilliland and Mason (5), Dankwerts et al. (6) and Huntley et al. (7) published studies along these lines, but because the two-phase nature of the bed was still not accounted for, these results were applicable to uncatalysed gas-phase reactions only.

In 1952 Toomey and Johnstone (8) made a very significant contribution: they formulated what is presently known as the two-phase theory of fluidisation. This theory states that all gas in excess of that required to bring a bed to minimum fluidisation conditions passes through in the form of bubbles. It is usually formulated thus:

$$\frac{Q_B}{A} = U_o - U_{mf} \qquad (2.1)$$

where Q_B is the volumetric gas flow as bubbles, A is the bed cross-section and U_o and U_{mf} the superficial and minimum fluidisation velocities respectively. A second assumption usually associated with this theory is that the voidage in the dense phase ε_d is maintained at its minimum fluidisation value ε_{mf}, though it is not clear whether the formulators implied this or not.

Application of the two-phase concept led to a very definite improvement in the interpretation of fluidised bed data. Thus, for example, in 1955 Shen and Johnstone (9) applied a two-phase model to the catalytic decomposition of nitrous oxide in a fluid bed, and a year later Mathis and Watson (10) used a similar approach to investigate fluidised catalytic cumene dealkylation. This approach rapidly gained popularity as attested to by the studies of Lewis et al. (11), May (12), Lanneau (13), Gomezplata and Shuster (14) and Van Deemter (15) amongst others. The models used generally described two phases with interphase mass transfer, and in all the studies quoted immediately above other than that of Lanneau (13), this mass transfer parameter essentially had the status of some kind of correlation parameter. Both reaction and gas tracer data were employed, and the general technique was to adjust the mass transfer coefficient for maximum closure between the model and these data.

The next major development in the field of fluidised bed modelling was the evolution of a link between the physical bubbling behaviour and the interphase mass transfer characteristics. In 1957 Zenz (16) put forward a theory describing the gas flow between a single bubble and the dense phase, though the main contribution in this area undoubtedly came from Davidson (17) in 1961. Davidson analysed the motion of a spherical bubble in terms of the velocity field of potential flow in an ideal fluid, and predicted gas flow patterns in and around single bubbles which were soon verified experimentally (18, 19). The theory was capable of predicting convective cross-flow between a bubble and the dense phase in terms of minimum fluidisation velocity and bubble diameter, and even though this model was subsequently extended by Jackson (20) and Murray (21) to conform more closely to physical reality, it is its essential correctness that makes it stand out clearly still today.

Orcutt, Davidson and Pigford (22) were probably first, in 1962, to interpret fluidised bed data on the basis of a bubble model. The same kind of two-phase model as that used by Shen and Johnstone (9) was assumed, but the essential difference lay in the interphase mass transfer coefficient no longer assuming the role of a correlating parameter. It was instead specified in terms of a convective component from Davidson's bubble model and a diffusive component based on Higbie's (23) penetration theory, and closure between this model and ozone decomposition data generated by Orcutt (24) was found to be remarkably good. The basis for testing the model was bubble diameter: this parameter was calculated from conversion data

(via the model) and also more directly from bed expansion data.

The significance of this development in fluid bed modelling is quite clear: it placed the description of the system on a more mechanistic footing by building into it a recognition of the fact that bubbles exist as individual entities rather than just a "phase" of some kind. It should be noted, though, that the approach is very definitely a two-stage one. In the first stage a two-phase model was assumed, and in the second the interphase mass transfer coefficient in this model was itself modelled in terms of bubble properties. (The reason for drawing the reader's attention to this will become clear in section 2.3.1).

A further refinement in the models used to describe fluidised beds was initiated by the work of Rowe and co-workers at Harwell, England in the early to mid 1960's. In a series of publications (25-27) these investigators showed, amongst other things, that solid particles rise in the wake of a bubble and are deposited on the upper surface of the bed as the bubble breaks through. This led several other groups of workers, of whom Kunii and Levenspiel (28) and Potter and co-investigators (29, 30) are probably best recognised, to postulate a model which describes the resultant solids circulation pattern. This model, unlike the two-phase models used earlier, describes the bed as being divided into three distinct phases: bubbles, a cloud-wake phase and the rest of the dense phase which is often referred to as the emulsion. A very

important feature of this model is the fact that, if the downward drift of solids in the emulsion (which must exist to compensate for the upflow in the cloud-wake phase) occurs at a velocity which exceeds the interstitial velocity, then emulsion gas will be drawn downwards in this phase.

Since the establishment of the basic building blocks described thus far, the number of models proposed has increased enormously. It would seem pointless to pursue the current discussion of development along historical lines any further, and rather more appropriate to switch attention to the current state of affairs.

2.2 Present State-of-the-Art

Any model describing a fluidised bed necessarily contains a number of assumptions. This section examines each individual class or subset of assumptions from which an element may, or in some cases must be drawn in order to allow the construction of a complete model. Synthesising these assumptions into a complete picture is deferred to Section 2.3.

2.2.1 Phase Division

The basis of any reactor model is the assumed phase division, and as with most other aspects of fluidised bed modelling,

several plausible suggestions have been put forward. The earlier models, as discussed in the previous section, relied mainly on the simple two-phase theory (8) and accordingly assumed the presence of a solids-rich dense phase and either a solids-free (e.g. refs. (9, 12, 14)) or a solids-lean (e.g. refs. (10, 11, 13)) bubble phase. The work of Rowe and others (25-27) and the subsequent introduction of the Kunii-Levenspiel (28) type of three-phase model opened up two more possibilities: a division of the bed into solids-rich cloud-wake and emulsion phases, with either solids-lean or empty bubble phases. Another possibility is to include a stationary or fixed phase as has been suggested by Kühne and Wippern (31) amongst others, though this only really applies to the situation in which gas is adsorbed onto the solids and effectively removed from any of the other phases. This variant will not be considered here since adsortption is not an important factor in the present investigation.

Four common possibilities are shown in Figure 2.1. All of these have been employed (9, 10, 28, 32), though it could be argued that they are not quite as independent of one another as they may appear. The two-phase direct contact model, for example, could be viewed as a limiting case of the simple three-phase model: a zero mass transfer resistance beteen the bubble and cloud phases. The three-phase direct contact model does not appear to have attracted nearly as much attention as any of the other models, possibly due to the fact that it offers little advantage over the basic three-phase model in exchange for a substantial increase in mathematical complexity.

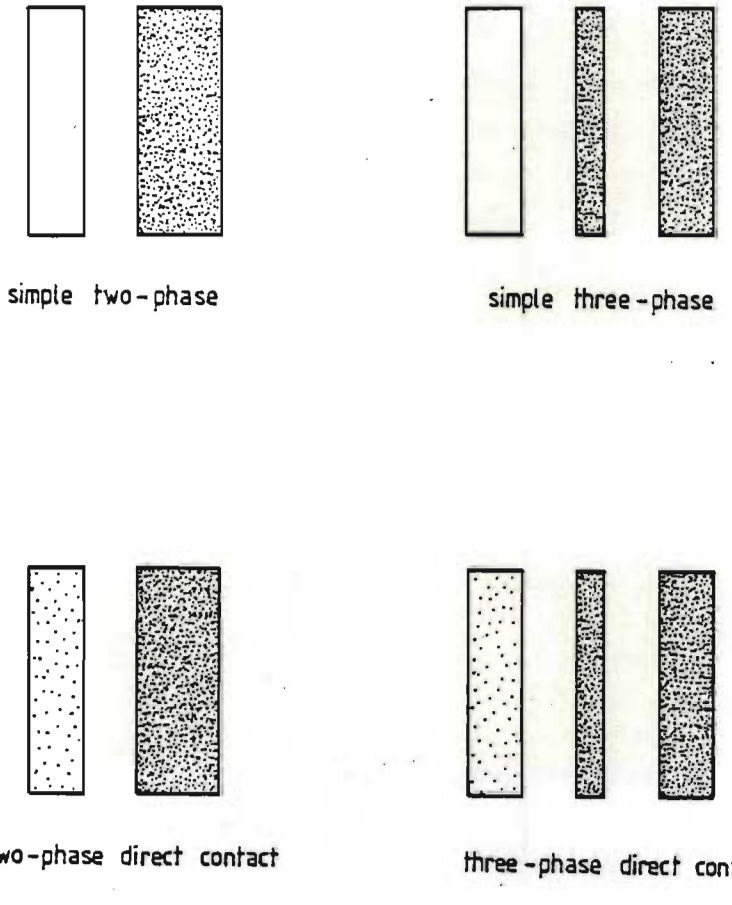

FIGURE 2.1 PHASE CONFIGURATIONS

Miyauchi (32) is one of the main proponents of such a phase division and Miyauchi, Furusaki, Morooka and Ikeda (33) argue that the presence of some catalyst in the bubble phase is essential if changes in conversion with changing reaction velocity constant are to be explained correctly. An important factor to consider when using such a model is how the solids loading within the bubbles is to be quantified. Direct measurements have been reported by Lanneau (13) and Kobayashi et al. (34) amonst others, but very little information on how this quantity changes in going from one system to another is available. This suggests the need for repeating such measurements in each case if an arbitrary assumption is to be avoided. Alternatively, if the solids loading within the bubbles is to be regarded as simply a correlating parameter, then the motivation for its introduction into the model in the first place would require very careful examination.

According to Grace (35) current modelling tendencies appear to favour the Kunii-Levenspiel (28) type of simple three-phase division. This division is perhaps most commonly associated with the so-called countercurrent backmixing model, and its popularity no doubt owes much to Fryer and Potter's (36) study of axial concentration profiles for a reacting tracer. These workers measured a minimum in the axial concentration profile at a point *within* the bed, and showed that such a profile could be generated by a three-phase model with solids circulation.

It is extremely unlikely, though, that a single phase division is most appropriate in every instance. Davidson's bubble model (17), for example, suggests a vanishingly thin cloud when the ratio of bubble to remote interstitial gas velocities exceeds about 20 or so (37). A high velocity ratio is characteristic of fine powder systems, and this suggests that for such systems the cloud-wake phase should be lumped with the emulsion phase, i.e. that a two-phase model is more appropriate than a three-phase one. Grace (38) has developed a similar argument based on Murray's (21) model, and concludes that "cloud models seem to offer no advantages over the simpler models when dealing with small particle systems".

2.2.2 Axial Gas Mixing in the Dense Phase

According to Grace (35), no other feature of fluidised bed modelling has been subjected to as many alternative assumptions. The earliest two-phase models such as those of Shen and Johnstone (9) assumed plug flow and perfect mixing alternatively, and this is also reflected in the earlier bubble models such as those of Orcutt et al. (22) and Davidson and Harrison (39). May (12) was probably first, in 1959, to suggest the use of an axial dispersion parameter, and this approach was also adopted some two years later by Van Deemter (15). Meanwhile, in 1960 Lanneau (13) put forward the idea of downflow in the dense phase, and five years later Mamuro and Muchi (40) proposed the use of ideal mixing stages in series. Shortly afterwards the introduction of the three-phase countercurrent backmixing (29) type

of model imparted some further momentum to the downflow concept, while Kunii and Levenspiel (28) assumed stagnant cloud and emulsion phases in the course of development of their mass transfer model. Since then a number of other suggestions including bubble-induced turbulent fluctuations (41) have also been put forward.

The relationship between solids movement and dense phase gas mixing is important in deciding which assumption is most appropriate for a given system. In particular, when the particles are small, gas-solids slip in the dense phase is likely to be small and the gas mixing is likely to be very similar to that of the solids. May (12) recognised and used this fact: he measured the solids mixing characteristics using a radio-active tracer technique and assumped the resulting dispersion coefficients to be applicable to the dense phase gas. The whole question becomes more complex, however, when one considers the interaction between solids movement and bubbles. Experiments carried out by Rowe and Partridge (27) and Gabor (42) suggest that particles on or near the vertical axis of a bubble suffer a vertical upward displacement as a result of the bubble passing through, and based on this observation Haines, King and Woodburn (43) developed a stochastic mixing model which accounts for such random upward migration.

Lateral variations in the nature of the bed and the establishment of gross circulation cells are further complicating factors. Valenzuela and Glicksman (44) found that lateral solids mixing was

considerably affected by the lateral component of motion of the bubbles, while Potter, Whitehead and Nguyen (45) have shown how gross circulation characteristics depend on bed geometry and gas velocity. When these factors are taken into account, it becomes clear that no simple model is ever likely to describe the dense phase mixing in a fluidised bed with any degree of precision. However, according to Grace (35), the assumption used in describing this mixing process is only really important when conversions in excess of 90% are being considered. This in turn suggests that, for most applications involving modelling the bed as a whole, the selection of a "reasonable" assumption from the list of those already put forward would suffice.

2.2.3 Axial Mixing in the Bubble Phase

The assumptions applied to axial mixing in the bubble phase contrast sharply in number to those applied to the dense phase. This perhaps not too surprising since the bubbles usually move only upwards and backmixing effects are not expected. This suggests that the bubble phase should be treated as a simple plug flow unit, and indeed this is by far the most common assumption.

Shen and Johnstone's (9) models incorporated this feature, and since then little has changed in this particular area - it is probably true to say that this description of the bubble phase is still the most popular one today.

A variation on this appeared in 1965 when Mamuro and Muchi (40) proposed the partitioned model referred to previously. This model assumed a number of ideal mixing stages in series for both phases, with the height of each stage given by the bubble diameter in that stage. Kato and Wen's (46) bubble assemblage model contains a similar description of the bubble phase, as do the more recent versions of this model due to Mori and Wen (47) and Peters et al. (48).

Another assumption which has been employed is that of dispersed plug flow. Wippern et al. (49), Lehmann and Schügerl (50) and Kühne and Wippern (31) are amongst those who have used this approach, and their reasoning appears to be based more on the form of the appropriate two-phase continuity expressions than on heuristic arguments. This approach does, however, carry with it a penalty: in solving such a model an extra boundary condition (BC) is called for at the top of the bubble phase, and there does not appear to be any obvious way in which it should be specified.

Certain investigators have reported the existence of bimodal bubble size distributions in fluidised beds (51, 52): none of the assumptions discussed thus far are capable of describing the bimodal velocity distribution which would presumably accompany such a size distribution. In larger units where the formation of gross circulation cells and preferred bubble paths is possible one might also expect these simple assumptions to become somewhat less appropriate than they might be in smaller units, and the same holds when bubble chains

of the type observed by Werther (53) are present. It would seem reasonable to suggest that in certain instances an assumption other than plug flow, dispersed plug flow or stages in series might be called for - this is taken up again in section 3.2.1.5.

2.2.4 Local Bubble Properties

Bubbles introduced at the distributor of a fluidised bed usually grow rapidly by coalescence as they rise. This is an important characteristic of such systems, and a great number of experimental investigations have been aimed at measuring local bubble properties and correlating these with the operating parameters of the system. Such experiments usually involve X-rays (54), photographing bubble eruptions at the bed surface (55) or small local bubble probes of some kind (56, 57). The information thus obtained is generally in the form of individual bubble sizes and velocities, and bubble growth correlations are most commonly presented as a variation in average bubble diameter with height and gas velocity. The nature of the distributor is usually incorporated into the correlation as either an equivalent height term or an initial bubble diameter - a few such correlations are given in Table 2.1.

The relationship between the rise velocity and the size of a single bubble is fairly well established. It is based on a theoretical expression due to Davies and Taylor (63) for spherical cap bubbles

AUTHOR	REFERENCE	EQUATION NO.	CORRELATION
Rowe	(58)	(2.2)	$d_b = (U_o - U_{mf})^{0.5} (h + h_o)^{0.75}/g^{0.25}$
Werther	(59)	(2.3)	$d_b = 0.00853 (1 + 27.2 (U_o - U_{mf}))^{0.33} (1 + 6.84h)^{1.21}$
Darton	(60)	(2.4)	$d_b = 0.54 (U_o - U_{mf})^{0.4} (h + 4\sqrt{A_o})^{0.8}/g^{0.2}$
Kobayashi	(61)	(2.5)	$d_b = d_o + 0.14 d_p \rho_p (U_o/U_{mf}) h$
Mori and Wen	(62)	(2.6)	$(d_m - d_b)/(d_m - d_o) = \exp(-0.3 h/D_t)$
			where $d_m = 0.652 (A_t(U_o - U_{mf}))^{0.4}$
			and $d_o = 0.347 (A_t(U_o - U_{mf})/N_D)^{0.4}$ for perforated plates
			and $d_o = 0.00376 (U_o - U_{mf})^2$ for porous plates

TABLE 2.1 BUBBLE GROWTH EXPRESSIONS (SI UNITS)

in a liquid, and is usually presented thus:

$$U_b \text{ (single bubble)} = \phi \sqrt{g\, d_b} \qquad (2.7)$$

The bubble rise coefficient ϕ is often taken to be 0.71 (39), though Rowe (64) argues that a value of around unity is more appropriate and that this quantity should vary with dense phase voidage. When many bubbles are present in the bed the rise velocity of each individual bubble is commonly assumed to be augmented by the excess gas velocity according to Davidson and Harrison's (39) expression:

$$U_b \text{ (many bubbles)} = (U_o - U_{mf}) + \phi \sqrt{g\, d_b} \qquad (2.8)$$

Rowe (64) has pointed out that little experimental support exists, but this expression has nevertheless been widely accepted. Several modifications have also been put forward. Werther (65), for example, noting that bubbles of the same size rise faster in a larger diameter vessel, has suggested that ϕ should increase with increasing vessel size. Weimer and Clough (66) have suggested the use of what is effectively a distribution coefficient premultiplying the excess gas velocity term to account for lateral variations in bubble concentration.

There is an important factor to bear in mind when considering the application of local bubble size and velocity expressions, and it relates to the existence (or otherwise) of a maxmimum stable bubble

size. If such a maximum does exist in the system under investigation, then bubbles might be expected to grow only to this limiting size and to remain more or less constant thereafter. The confidence with which this maximum may be predicted is perhaps not as great as that with which bubble growth characteristics may be forecast, and the theories that have been put forward are decidely at odds with one another under certain conditions. One of these is due to Harrison et al. (67), and states that bubbles will break up when their rise velocity reaches the terminal falling velocity of the particles. Squires (68) suggested that, for fine powders at least, saltation off the floor of the bubble is more likely to be responsible for bubble breakup. For 70 micron FCC catalyst fluidised in air at ambient conditions these criteria predict maximum stable sizes of about 0.009 and 1.5 m respectively, and neither embraces Rowe's (69) observations of splitting by stalactite formation from the bubble roof.

When bubble growth proceeds unhindered to the stage where the bubble diameter approaches about one half of the bed diameter, wall effects become very significant and slugging occurs. This kind of behaviour is characteristic of small, high aspect ratio beds such as those used in pilot plants: the conditions under which slugging is expected have been described by Stewart and Davidson (70). The gas voids or slugs (for type A behaviour (70)) are elongated and bullet-shaped, and the velocity of rise is significantly lower than it would be if the same gas void were present in a much larger bed. Under these conditions the slug velocity may be assumed to be controlled

more by the diameter of the tube than by any characteristic dimension of the slug itself, and the appropriate analogue of equation (2.8) is:

$$U_s = (U_o - U_{mf}) + 0.35 \sqrt{g\ D_t} \qquad (2.9)$$

Stewart and Davidson (70) adopted this expression from the results of Nicklin et al. (71) for an air-water system, and the slug rise coefficient of 0.35 and the square root dependence can be traced back to the earlier work of Dumitrescu (72).

Slugs need not necessarily rise along the centre of the column - they may also rise along the wall. Birkhoff and Carter (73) pointed out that assymetric slugs might move as if they were in a column twice the actual size, thus giving:

$$U_s = (U_o - U_{mf}) + 0.35 \sqrt{2g\ D_t} \qquad (2.10)$$

Hovmand and Davidson (74) presented an analysis of slug velocity data from various sources and concluded that equations (2.9) and (2.10) provide a satisfactory basis on which to model such systems. It should perhaps be noted, though, that in view of Rowe's (64) comments regarding the dependence of the bubble rise coefficient on dense phase voidage, one might expected the slug rise coefficient to display a similar dependence.

The type of information discussed here may be used to predict reactor performance in a number of ways. For the bubbling bed case an axial variation in bubble size and velocity could be built into an overall reactor model as in the cases of Mamuro and Muchi (40) and Kato and Wen (46). Alternatively, such information could be used to determine a suitable average for use in conjunction with models such as that of Kunii and Levenspiel (28) which do not account for axial variations. Care should be taken, however, to ensure that the particular expression proposed for use is indeed applicable to the system being studied. The empirical or semi-empirical nature of the bubble growth correlations should be borne in mind and any extrapolation should be treated with extreme caution.

2.2.5 Interphase Mass Transfer

An early estimate of the mass transfer coefficient describing gas exchange between an isolated bubble and the surrounding dense phase was given by Zenz (16) as:

$$(K_{be})_b = 3\left(\frac{U_{mf}}{d_b}\right) \qquad (2.11)$$

The mass transfer coefficient is presented here in the form referred to bubble volume, and in terms of the three-phase bed division it describes overall, i.e. bubble to emulsion mass transfer. (This

notation is essentially that suggested by Kunii and Levenspiel (28) and will be used throughout.)

Zenz's (16) expression for interphase transfer is based on the assumption that gas flows radially through the walls of a bubble at a velocity equal to U_{mf}. This flow pattern was entirely conjectured, however, and Davidson's (17) subsequent analysis of bubble motion led to the following expression for convective crossflow:

$$(K_{be})_b = 4.5 \left(\frac{U_{mf}}{d_b}\right) \tag{2.12}$$

while Murray's (21) analysis led to:

$$(K_{be})_b = 1.5 \left(\frac{U_{mf}}{d_b}\right) \tag{2.13}$$

For the slug flow case similar expressions have been put forward to describe convective crossflow, e.g.

$$(K_{be})_b = \left(\frac{U_{mf}}{\text{slug length}}\right) \tag{2.14}$$

as given by Hovmand and Davidson (74).

A second, diffusive component of mass transfer was derived from Higbie's (23) penetration theory, and for a bubbling bed Davidson

and Harrison (39) presented the following expression for combined crossflow:

$$(K_{be})_b = 4.5 \left(\frac{U_{mf}}{d_b}\right) + 5.85 \left(\frac{gD^2}{d_b^5}\right)^{\frac{1}{4}} \qquad (2.15)$$

This expression was adopted by Kunii and Levenspiel (28) to describe mass transfer between the bubble and the cloud, and a further expression was derived from penetration theory to model cloud-emulsion transfer:

$$(K_{ce})_b = 6.78 \left(\frac{\varepsilon_{mf} D U_b}{d_b^3}\right)^{\frac{1}{2}} \qquad (2.16)$$

Many other expressions have also been put forward to describe the phenomena under discussion. A broad study of this class of expression has been carried out by Sit and Grace (75), and they conclude that the soundest basis for modelling local mass transfer between isolated bubbles and the dense phase is provided by penetration theory combined with Murray's (21) expression for convection, equation (2.13).

These expressions, however, only account for convection and diffusion. Effects such as wake shedding and gas adsorption on catalyst moving past the bubble remain unaccounted for. Another possible effect is that of bubble coalescence - this is a controversial area of investigation, and the conclusions drawn are probably dependent on the exact nature of each system studied. Sit and Grace (76), for example, investigated mass transfer for pairs of interacting bubbles in a two-dimensional bed. They reported a mass transfer enhancement of 20-30% and presented a corrected crossflow expression:

$$(K_{be})_b = 2\left(\frac{U_{mf}}{d_b}\right) + 12\left(\frac{\varepsilon_{mf} D U_b}{d_b^3 \pi}\right)^{\frac{1}{2}} \qquad (2.17)$$

Pereira and Calderbank (77), on the other hand, reported the total destruction of all bubble to dense phase concentration profiles upon the coalescence of two equal-sized bubbles. This no doubt represents a limiting extreme of some kind, but nevertheless suggests that the conventional mass transfer expressions may not be applicable to systems in which vigorous splitting and coalescence effects are present.

2.2.6 Grid Region and Sparger Effects

For fast reactions, it is well known that most of the conversion can take place in the first half-meter or so of the bed. Ob= servations to this effect have been reported by Cooke et. al. (78) and Hovmand et. al. (79), and both groups of workers found that

conversion was sensitive to grid geometry.

The first step in modelling the grid region is to establish the phase division, i.e. to estimate jet volumes and in particular penetration depths. Several jet penetration correlations, similar in principle to the bubble growth correlations discussed in Section 2.2.4, have been published (80-84), though the question of what actually defines a jet has not yet been fully resolved (85-88).

Interphase mass transfer in the grid region was measured by Behie (89). These results were interpreted in terms of Kunii and Levenspiel's (28) crossflow expressions for a bubbling bed, and it was concluded that the mass transfer rate in the grid region is of the order of 50 times greater than that in the bubbling bed higher up.

Several reactor models which account for the grid region have appeared in the literature. These include models for FCC regenerators by Errazu et. al. (90) and De Lasa et. al. (91), and a fluidised bed gasifier model by Weimer and Clough (92). The type of configuration used is shown in Figure 2.2, along with the assumed mass transfer coefficient (MTC) profile. It is apparent that this type of model acknowledges the fact that the mass transfer coefficient is an axially distributed parameter, and accounts for this by employing a two-stage rather than a single-stage model.

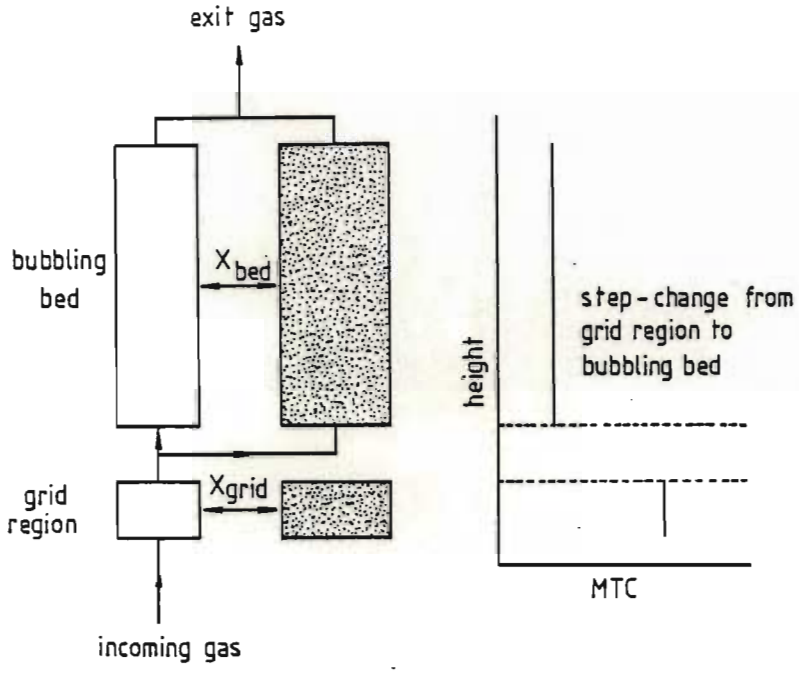

FIGURE 2.2 TYPICAL GRID REGION MODEL CONFIGURATION

A closely related problem which has received very little attention to date is that of mass transfer in the vicinity of a gas sparger. Split feed reactors are not uncommon in industry, since this type of configuration is often necessitated by the undesirability of pre-mixing reactant gases. One would expect, in principle at least, that the mass transfer situation would be similar to that near the grid. Several very important questions remain unanswered. For example, how does the nozzle orientation affect crossflow - is it better to direct the nozzles upward, sideways or downward? Another question is how do bubbles rising from below affect the (presumably) small bubbles generated at the sparger? Do they allow the small bubbles to exist in substantial numbers, or do they simply "gobble up" their smaller counterparts by coalescence?

In the context of this study, the question is how one would model a split feed system. A few guidelines are available from grid region studies, but it is clear that the literature is lacking in this particular area.

2.2.7 Disengaging and Freeboard Regions

As bubbles burst at the surface of a fluidised bed, particles are thrust into the freeboard region. The solids holdup decreases progressively from the bed surface to some constant value at and beyond transport disengaging height. Additional gas-solids contact and chemical reaction is possible here as stated previously,

though it is most commonly ignored in reactor models (35). This effect will not be considered in this study.

A slightly different, but nevertheless related phenomenon has been observed in the transition region between the bed and the freeboard. In a slugging bed, Miyauchi et al. (93) reported an *increase* in crossflow in the transition region. This is probably a result of increased turbulence associated with slugs breaking through the bed surface. The gas escapes rapidly once the slug has broken through, leaving the solids to fall back violently along the column walls. This effect is also generally ignored in the setting up of reactor models.

2.3 An Overview from a Model Classification Point of View

The concept of a general model classification does not appear to have taken root in the fluidisation literature. In recent reviews by Potter (94) and Miyauchi et al. (33) complete individual models only are considered. In the Grace (35) review individual model assumptions are discussed, but no attempt is made to identify groups or classes of model beyond descriptions such as two and three-phase and bubble models. In an older review Grace (95) refers to the models typical of those employed in the 1950's as Type I models, and those based on bubble properties appearing from 1962 onwards as Type II models. Rowe (96) refers to the same broad classes as "arbitrary two-phase" and "physical bubble" models respectively, but this is where the classification ends.

A slightly more comprehensive classification has been suggested by Horio and Wen (97). According to this scheme Level I models are the "arbitrary two-phase" models mentioned above, while the earlier models which do not account for axial variations in bubble properties are regarded as Level II models. Those which do account for axial changes in bubble properties are associated with Level III. Though this classification undoubtedly has its merits, it is incomplete in several ways. For instance, how would one classify a three-phase model, such as the countercurrent backmixing model, if no assumption relating crossflow to bubble parameters were employed? Also how would one classify a

mechanistic (computer) bubble growth simulation?

A suggestion for a somewhat more general classification is presented in the following section. It should be noted that the author in no way wishes to imply that this classification is complete in any absolute sense, and it is hoped that this classification will serve as a starting point for discussion and development.

2.3.1 A Suggested Model Classification

Before proceeding it is necessary to set out clearly the assumptions and restrictions associated with this classification. These are:

(i) The analysis applies to the hydrodynamic modelling of bubbling or slugging fluidised bed reactors only.

(ii) The reaction kinetics are known and do not dominate the overall process.

(iii) It is assumed that a prediction of gas conversion is required.

Having stated this, we may now proceed to define four general classes of model. An overall prediction of reactor performance involves calculations based on a component drawn from at least one of these classes, and in most cases several components from different classes constitute the complete description.

Class A:

A model in this class represents a macroscopic mass balance description of the system, with parameters lumped in time and space. This type of model typically results from writing a material balance over the reactor, making no assumption on the parameters other than their spacial and temporal independence. Class A models may describe any number of phases. The countercurrent back-mixing model, for example, may be considered class A if the crossflow parameters are left unspecified - the commonly employed link between crossflow and bubble properties is in fact a class C model.

Class B:

This class is essentially the distributed-parameter analogue of class A. Such models also result from an overall material balance, but in this instance the crossflow term(s) and other parameters such as the velocity in the bubble phase are allowed to vary in time and space.

Class C:

Class C models describe local interphase transfer processes: the most well-known is probably Davidson's (17) bubble model. Models describing the transfer from a grid jet to the surrounding dense phase fall into this class, as do models describing interphase transfer when bubbles split or coalesce.

Class D:

Models in class D are those which describe bubble and dense phase parameters as functions of solids and gas properties, operating conditions and vessel geometry. Models in this class do not attempt to describe the interaction between phases - they are confined to predicting properties such as jet penetration depths, bubble size variations with height and dense phase voidages. Class D models are generally empirical or semi-empirical in nature.

Figure 2.3 gives an overall description of how the four classes of model are related and how they can be used to predict chemical conversion in fluidised beds. The diagram also shows the sources of information required by the models, and it is interesting to note that this information can itself be classified into different levels of complexity:

Level 1:

Directly measurable quantities such as superficial gas velocity and particle size distribution.

Level 2:

Quantities describing the holdup and throughflow of gas in each phase. Probes and/or indirect measurement techniques are often called for to obtain information on this level.

Level 3:

Interphase mass transfer coefficients (MTC's). The measurement of these quantities is generally very difficult if not impossible in three-dimensional beds. The use of 2D beds facilitates the acquisition of data on this level, but the hydrodynamics are probably not representative of a 3D system.

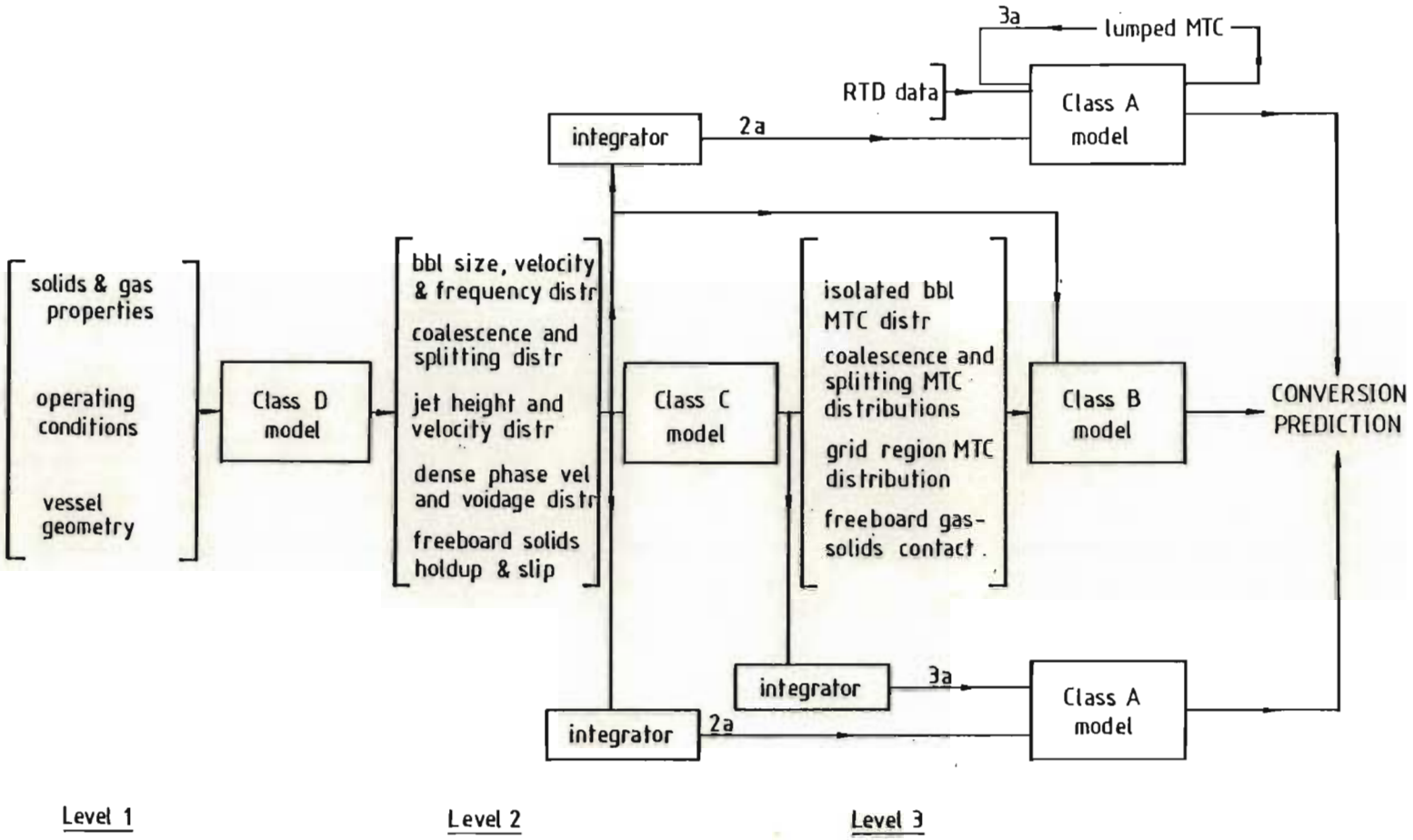

FIGURE 2.3 A PROPOSED MODEL CLASSIFICATION

If the information is averaged in time and space, it is designated level 1a, 2a or 3a. The "a" implies that some suitable averaging has been performed.

In terms of the model classes and information levels defined and the layout shown in Figure 2.3, one could formulate the following "rules":

1. Level 3 information may be measured directly, modelled on level 2 information by a class C model or modelled in two stages on level 1 information by class D and C models respectively.

2. Level 3a information may be extracted from RTD data on the basis of a class A model.

3. Level 3 information may be used to predict conversion by integration (averaging) and subsequent use in a class A model, or directly in a class B model.

These "rules" are essentially nothing new - they are merely statements of known facts in terms of the classification presented here.

As a final comment on Figure 2.3, it should be noted that a complete, unified fluidised bed theory would probably involve

level 1 input data processed by adequate class D, C and B models respectively. The present state-of-the-art is probably not sufficiently developed, however, to allow the general use of this approach with any confidence.

In order to demonstrate the usefulness of the proposed classification, the author has analysed a number of popular literature models in terms of component classes. This analysis may be found in Appendix A.

CHAPTER 3

CHOICE OF METHOD AND MODELS

From the discussion presented in Chapter 2 it is abundantly clear that several approaches to the problem should be considered. This chapter deals with a sifting of the various alternatives and the selection of a suitable technique. Also dealt with is the selection of a number of models from the literature.

3.1 Choice of Method

With reference to Figure 2.3, there are four possible modelling strategies. These are:

(i) Class D-C-B/A Route

Level 1 input data is supplied, and a suitable bubble growth expression (i.e. a class D model) is used to predict the variation in bubble size with height. A suitable class C model is then applied and the axially distributed MTC is used to predict conversion on the basis of a class B model. An alternative is to average the MTC in some appropriate manner and to employ a class A model to predict conversion.

(ii) Class C-B/A Route

Level 2 input data is obtained from some form of local bubble probe. (It should be noted that an X-ray technique is regarded as unsuitable due to the nature of the solids employed). A class C model is applied, and the resulting MTC is used in either a distributed (class B) or lumped (class A) form to predict conversion.

(iii) RTD Route

Residence time data and level 2a input are processed by a class A model to yield a lumped MTC. This MTC, which may be regarded as level 3a information, is subsequently used as input to a class A model for the prediction of conversion.

(iv) Reacting Tracer Route

Chemical conversion is measured under steady-state conditions for a tracer reacting according to a first-order rate law. (Kinetics which are non-linear introduce complicating effects which will not be considered here).

Route (i) involves amongst other things, relying on the applicability of previously established class D models to the system under investigation. Some of these models, in particular the bubble growth expressions such as those of Mori and Wen (62) or Werther (59), could be applied to this

system without much extrapolation being involved. This would result in a fairly complete picture of bubble size, velocity and (by inference) coalescence distribution throughout the bed, and a class C model could then be applied to these data.

This route was not selected for two main reasons. The first of these is the fact that the maximum stable bubble size, if one does in fact exist, could become very important in modifying the bubble size distribution. The techniques for assessing this maximum stable size, in fine powders in particular, are somewhat less well established than the bubble growth correlations themselves as discussed previously. In a relatively deep bed a small change in particle size distribution of an already fine powder could conceivably have a strong effect on bubble sizes in the upper reaches of the bed - if this change in particle size represented even a small extrapolation in terms of the bubble growth expression (as would be expected here), it is felt that the results would require direct validation before being relied upon.

The second reason is that the established bubble growth expressions do not readily lend themselves to predicting behavior in beds with spargers and vertical coils. Since establishing the effect of such internals was regarded as one of the aims of this investigation, it was decided that this route should be disregarded in favour of one of the alternatives.

Route (ii) may be considered more reliable for the purposes of this study, though the approach is still a somewhat indirect one. Bubble sizes and size distributions could conceivably be measured by one of any number of local bubble probes (54), and some hydrodynamic information on the grid region might be obtained by the same technique. Certainly, the effect of vessel internals on bubble size and velocity could be quantified. Bubble interaction effects such as coalescence and splitting could also yield to quantification by techniques of this nature, though data interpretation is likely to be difficult.

The use of local bubble probes would yield a fairly complete matrix of level 2 information, but an estimation of the interaction between phases would still be dependent on a class C model. As discussed in Chapter 2, bubble coalescence and splitting effects could seriously affect the applicability of existing crossflow models, and in view of these uncertainties, it was felt that this route should not form the primary basis for the experimental investigation.

Route (iii), based on RTD information, represents a more direct approach. It is limited to a lumped parameter or class A description of the process, but does have the advantage that the (level 3a) inferred MTC reflects real phase interaction phenomena such as coalescence, splitting and grid region effects. The lumped nature of this approach may be at

least partially overcome by experimentation at different bed heights - in particular, the grid region may be accounted for by simply allowing the model parameters to assume appropriate values for a shallow bed. This entire procedure is, however, strongly dependent on the assumptions on which the model is based. It should also be pointed out that this approach is insensitive to the assumption as to whether or not solids are present in the lean phase, and data interpretation on the basis of a simple solids-free bubble phase model is possible.

Route (iv), based on a reacting tracer, undoubtedly represents the most direct approach. A conversion is measured, and no modelling at all is called for. This is desirable *within* the range of experimentation, but when scale-up extrapolations are required such information is of little direct use. Scale-up extrapolations are generally performed on the basis of a hydrodynamic model. It is, however, possible to extract an MTC from conversion data by working backwards. An MTC arrived at in this way is subject to the same considerations as that inferred from RTD information, though it should be noted that the presence of solids within the bubbles could lead to biased MTC's if the model assumes catalyst-free bubbles. The RTD approach is essentially free of this complicating factor as mentioned above.

Given the aim of developing and screening hydrodynamic models for potential scale-up purposes, the RTD route (iii) is

potentially the most direct and trouble-free in the opinion of the author. An ideal strategy might involve a combination of routes, but in this investigation the use of the RTD route was accepted as most suitable within the constraints on time and capital.

3.2 Choice of Models

The sensitivity of the RTD model approach to the exact form of the class A model dictates that several models, representing a broad cross-section of possible assumptions, should be employed. A model screening should be performed to isolate the most realistic of these sets of assumptions, and the interpretation of fluidised bed data should be based on this model.

The model screening in this study has two main components. The first of these examines the situation in which all the gas is fed via the grid, and in this case five models are considered. Four of these are drawn from the literature, and the fifth is considered novel. This screening will be referred to as the

general screening, and the five associated models as general models.

The second screening component deals with split feed systems. Two models, both considered novel, constitute the screening basis. These will be referred to as sparger models, and the two-model screening as the sparger screening.

3.2.1 General Models

3.2.1.1 May-Van Deemter Model

The May-Van Deemter or MVD model is selected because it reasonably accounts for all the simple two-phase models appearing in the literature. This model is shown in Figure 3.1.

3.2.1.2 Countercurrent Backmixing Model

The countercurrent backmixing or CCBM model is selected because of its current popularity. As shown in Figure 3.2, it considers the bed to be divided into three plug flow phases with solids circulation and the possibility of gas downflow in the emulsion phase. It should be noted that only the class A component of this model is considered here.

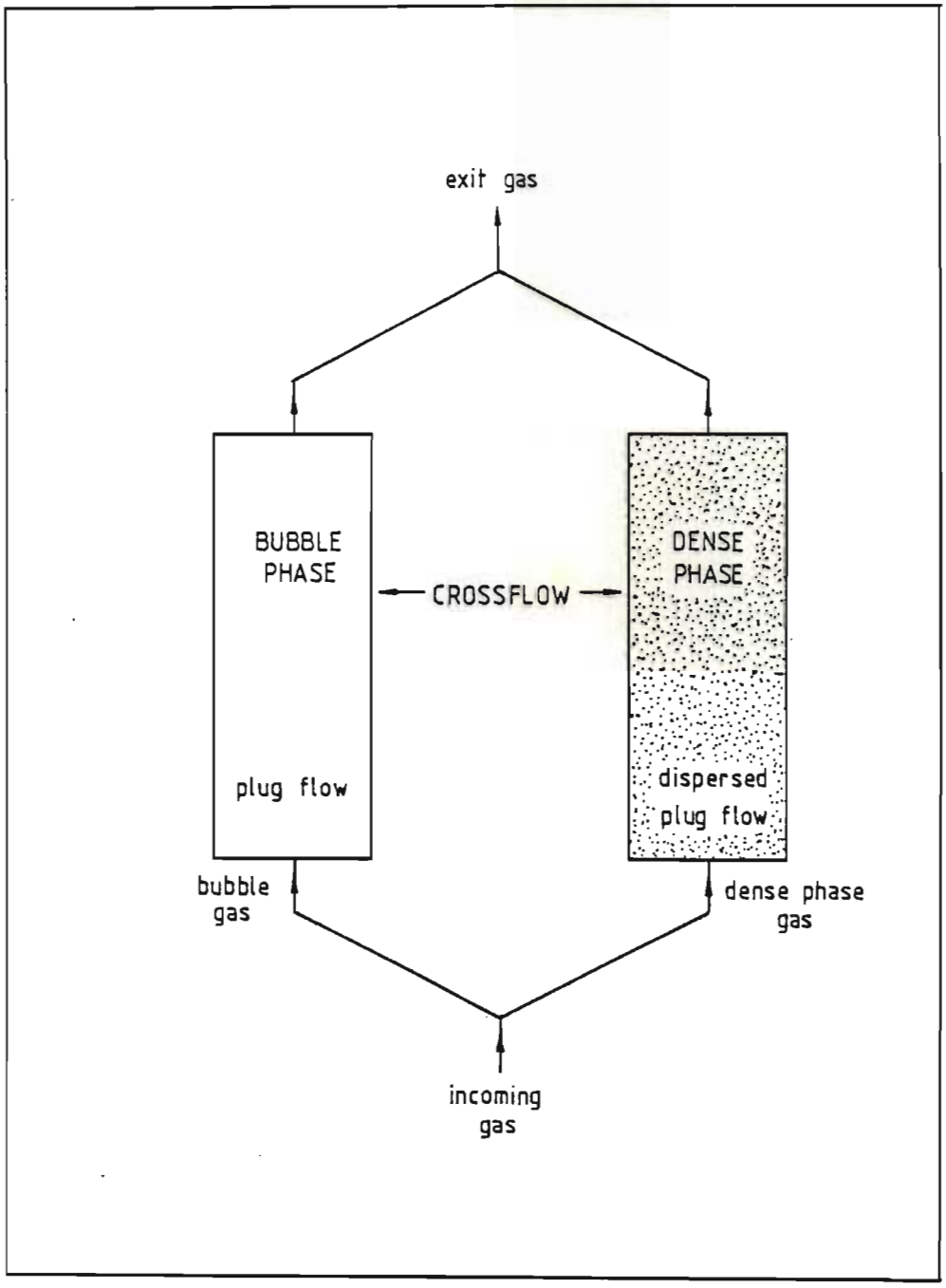

FIGURE 3.1 MVD MODEL

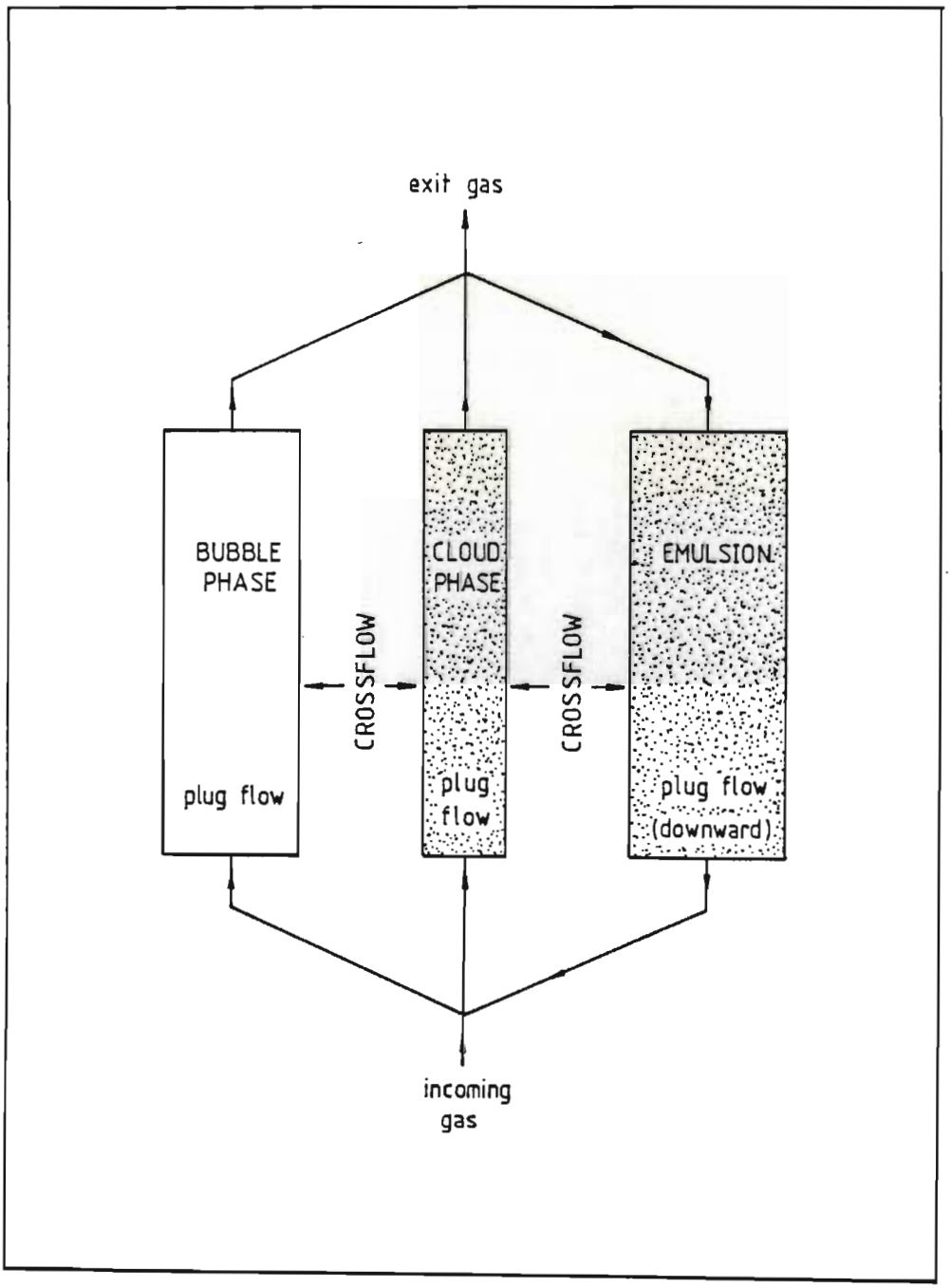

FIGURE 3.2 CCBM MODEL

3.2.1.3 Werther Film Diffusion Model

Werther's (98) film diffusion model, which will be referred to as the WFD model, represents a somewhat novel approach in that lateral diffusion in the cloud phase is presented as the main phase interaction feature. This model employes three phases as shown in Figure 3.3, with plug flow in the bubble phase and axially stagnant cloud and emulsion phases.

3.2.1.4 Bubble-Phase Dispersion Model

The three models considered so far all assume plug flow in the bubble phase. In the light of the discussion in section 2.2.3, it would seem worthwhile to include a model which employs dispersed plug flow in this phase. The bubble-phase dispersion or BPD model is essentially an analogue of the MVD model, and is shown in Figure 3.4.

3.2.1.5 Multiple Bubble-Track Model

In section 2.2.3 it is suggested that stages in series or dispersion models for the bubble phase may not be appropriate for a freely bubbling bed. Physically, the fact that large bubbles could overtake small ones or bubble chains could overtake individually rising bubbles suggests the formulation of a model with multiple plug flow units in parallel for the bubble phase. It might be suggested that such a formulation would represent a rather trivial variant of the MVD model, so it would seem appropriate at this stage to explore the

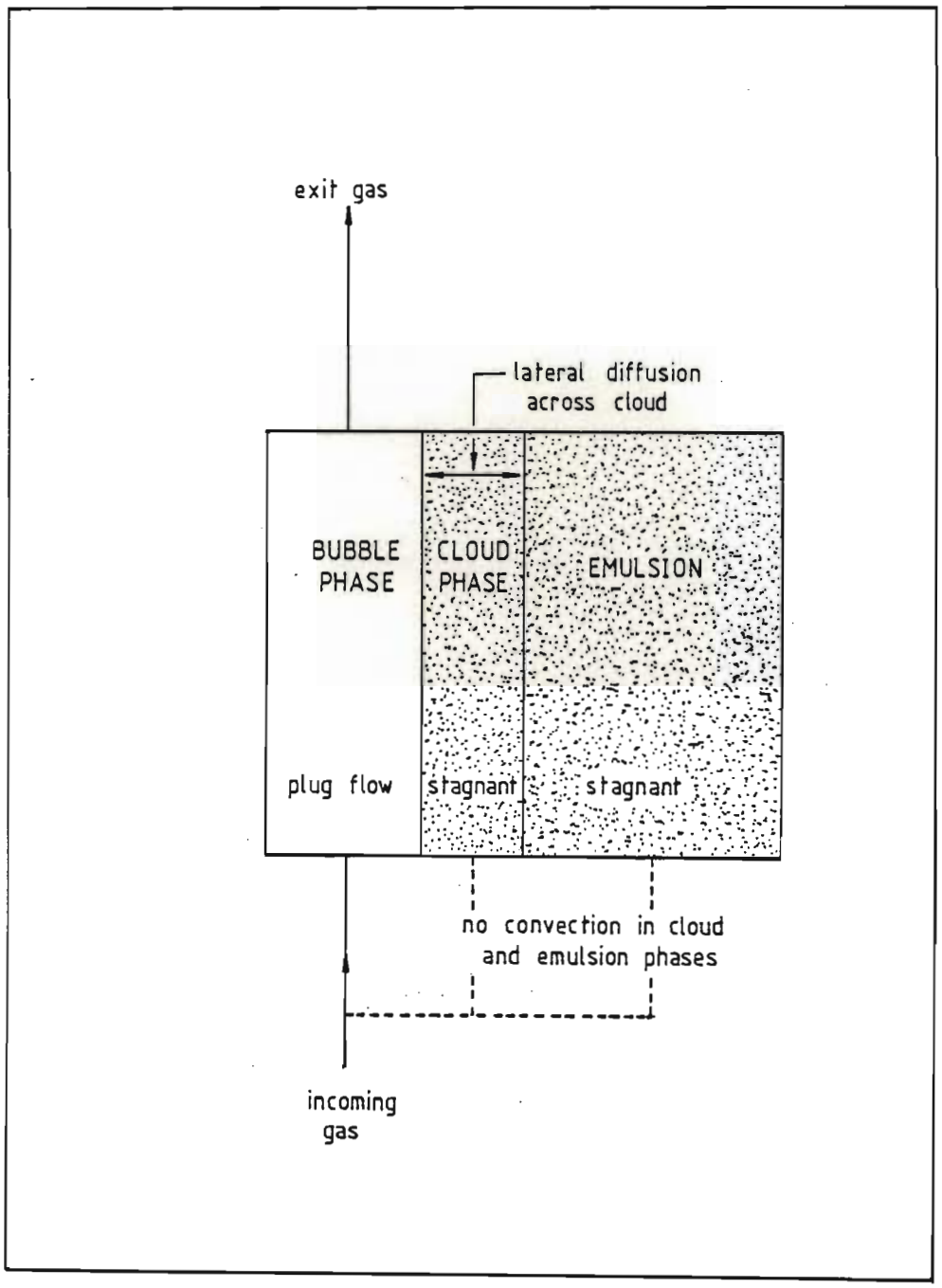

FIGURE 3.3 WFD MODEL

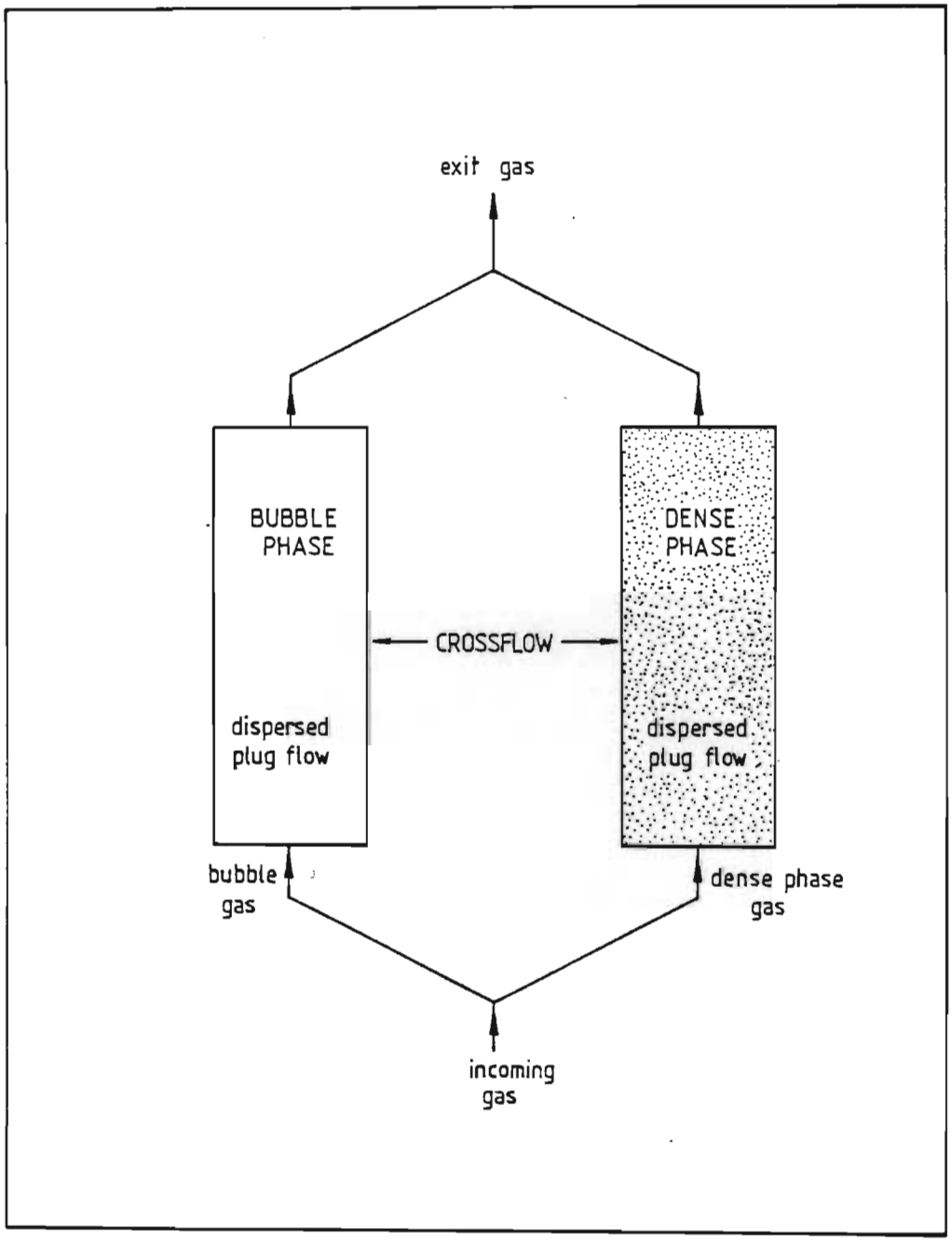

FIGURE 3.4 BPD MODEL

possible advantages of such a model over its simpler counterpart.

As stated earlier, gross circulation cells and preferred bubble tracks are known (45, 53) to exist in fluidised beds: this situation is potentially better described by a multiple plug flow approach, since each plug flow unit could conceivably account for one preferred bubble path. This would introduce some degree of lateral variation into the simulation - something the MVD model is not capable of. A further point is that this model is able to describe a bimodal type of bubble velocity distribution, something which has been observed (51, 52) but which neither the MVD nor any of the other three models are capable of simulating.

As regards the potential application of this model to a slugging bed or a bubbling bed where a single probe is used as in this study, it is noted that although the argument based on lateral variation of bubble properties is no longer valid, the model still has merit in accounting for stochastic time variations in bubble (or slug) properties. The advantage of this model over the BPD model becomes less clear under these conditions, however, though it is by no means obvious that the multiple bubble-track approach is any less appropriate than those based on dispersed plug flow or mixed stages in series for the bubble phase.

A further possible criticism of this model is that it is of little practical use since the assumption of N tracks introduces an additional (N-1) degrees of freedom into the problem. It will be

shown, however, that the additional degrees of freedom may be accounted for independently and do not detract from its usefulness.

The multiple bubble-track or MBT model is shown in Figure 3.5 with an arbitrary number of five tracks - a discussion on the number of tracks used is deferred to section 4.1.5.

3.2.2 Sparger Models

When gas is introduced at some horizontal plane into an already fluidised system, how much catalyst does this gas "see" on its way through the bed?

It is relatively easy, in principle at least, to run cold model simulations with a split feed system. Residence time tests may be carried out by introducing an inert tracer into the sparger, and sampling the bed higher up. What is less obvious, however, is how to interpret such information.

An overall lumped parameter model is obviously no good, since the bed properties change abruptly with bed height at the level

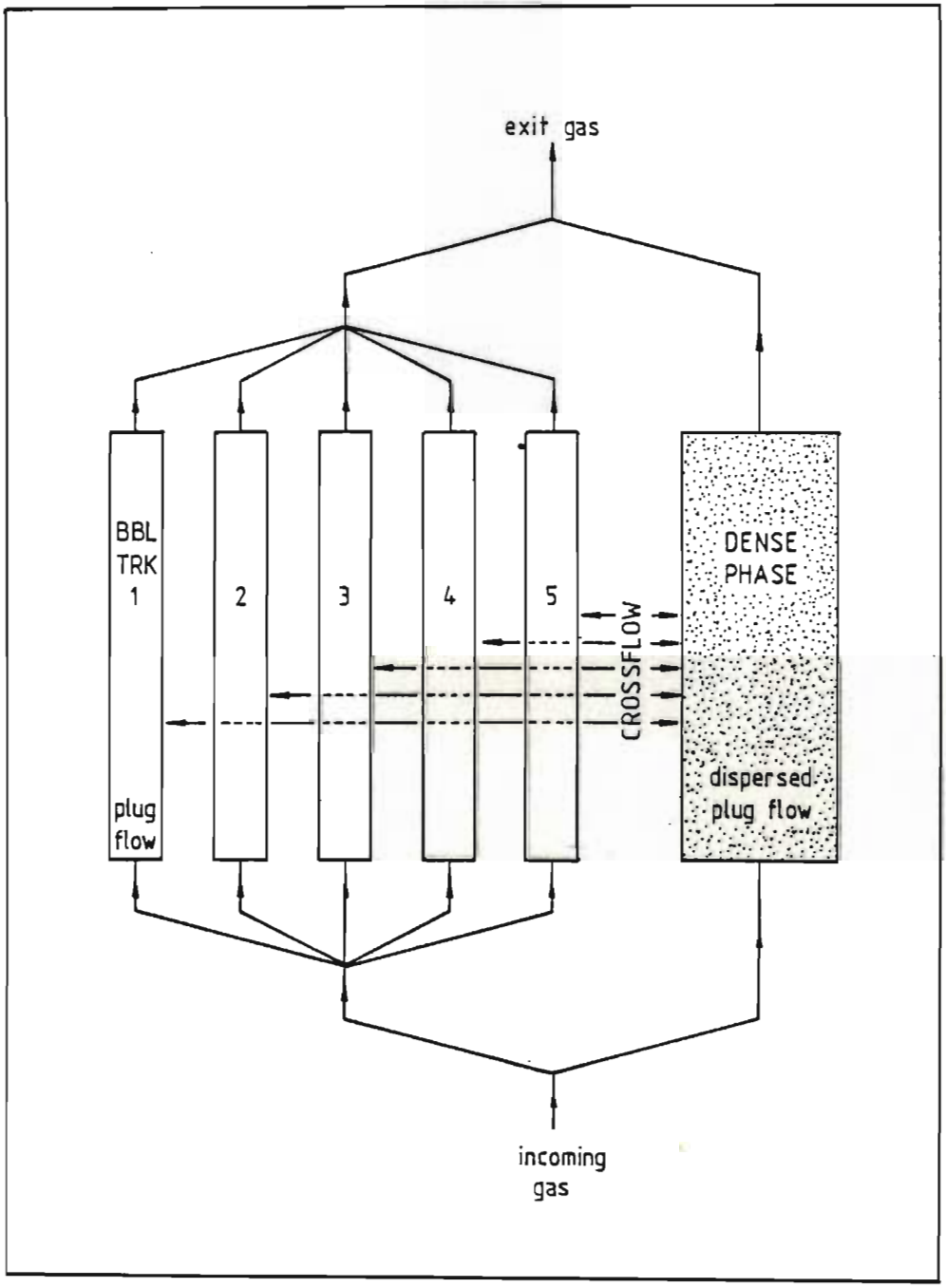

FIGURE 3.5 MBT MODEL

of the sparger. Furthermore, it is not clear whether the bubbles originating from the sparger should be regarded as a separate bubble phase or not. If coalescence effects are strong it is possible that most of these bubbles would join up with those originating from the grid to effectively form a single lean phase. If coalescence does not achieve significant lateral integration (of the grid and sparger bubbles) a segregated model might be more appropriate. For any real system the best description would probably be found somewhere between these extremes.

Two models are put foward for the interpretation of sparger RTD data. They correspond to the extreme cases of perfect lateral mixing and complete lateral segregation of the bubble phase. A model describing some intermediate case is not considered justified at this stage. The form of the models is that of a two-phase model with axial dispersion in the dense phase.

3.2.2.1 Laterally Mixed Bubble-Phase Model

The laterally mixed bubble-phase or LMBP model considers the bed to be divided into two phases as shown in Figure 3.6. Gas flow in the bubble phase is augmented by gas from the sparger at some height L_s, and the bubble velocity and holdup change accordingly from lumped values in the lower region to lumped values in the upper. The interphase mass transfer coefficient is also considered lumped in the lower and upper regions - RTD tests with tracer introduced via the sparger are in fact aimed at measuring the MTC in the upper region.

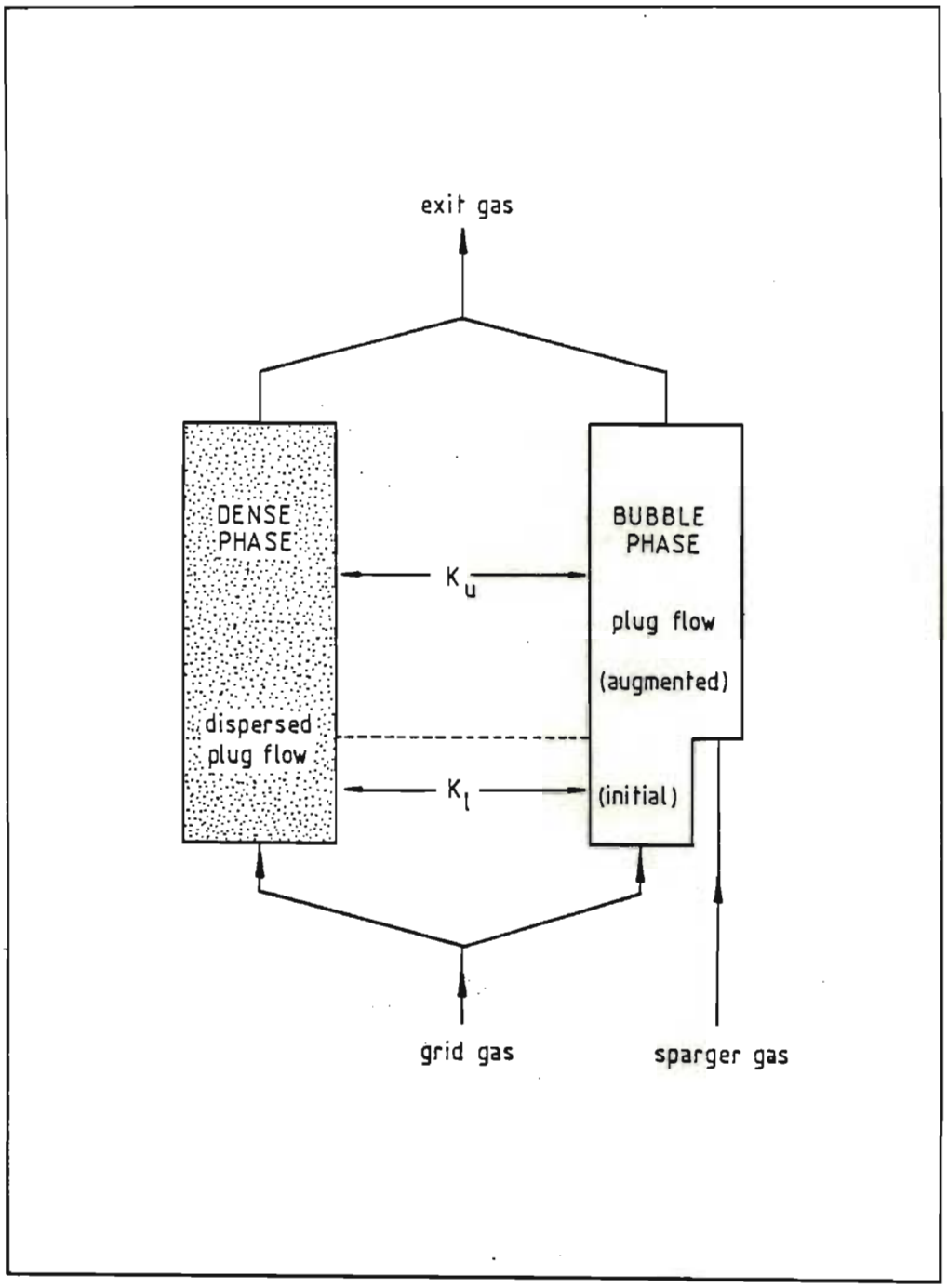

FIGURE 3.6 LMBP MODEL

3.2.2.2 Laterally Segregated Bubble-Phase Model

The laterally segregated bubble-phase or LSBP model is shown in Figure 3.7. Bubbles originating from the grid and from the sparger are considered to form separate bubble phases, and interaction between them is via the dense phase only. The MTC describing mass transfer between the grid bubbles and the dense phase is assumed to change abruptly from one constant value to another at the height of the sparger - this accounts for, in part at least, the axial dependence of the MTC.

It should be noted that the LMBP and LSBP models do not conform strictly to the definition of a class A model, since the parameters change at the height of the sparger. However, as far as the tests employed in this study are concerned, they are in fact class A : it is the lumped MTC in the region between the sparger and the bed surface that is inferred from RTD data.

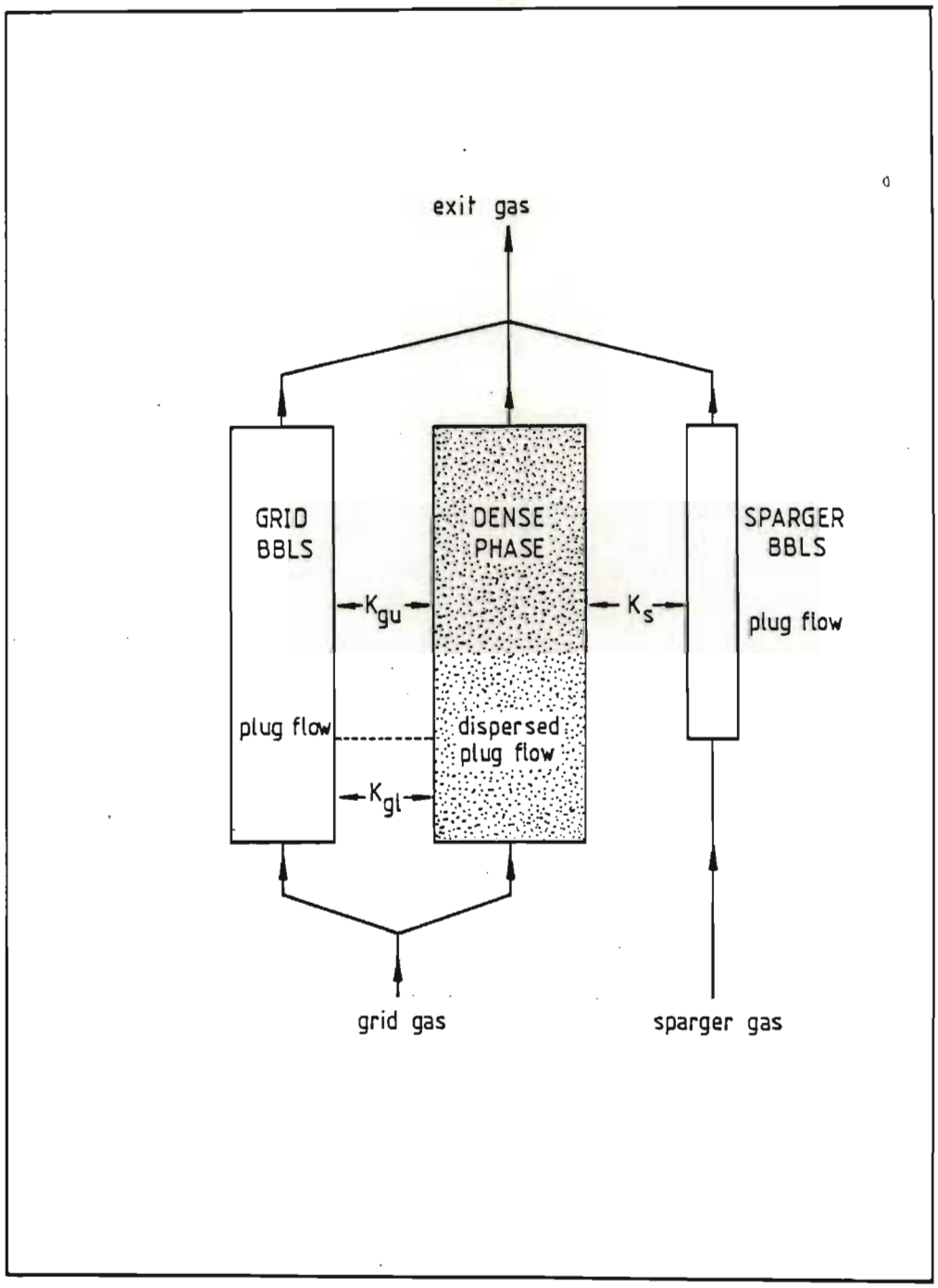

FIGURE 3.7 LSBP MODEL

CHAPTER 4

SOFTWARE DEVELOPMENT FOR RTD INTERPRETATION

The experimental data and the model predictions may be compared in either the time, Laplace or frequency domains. Each approach has its merits, and the most suitable domain for the problem at hand should be employed.

(i) Time Domain

The measured RTD data is used as is, and the model is solved to yield a response in the time domain. The comparison is direct, and a suitable measure of the degree of closure would be:

$$\Phi = \int_0^\infty [Y(t) - \hat{Y}(t)]^2 dt \qquad (4.1)$$

where Φ is an objective function to be minimised, $Y(t)$ the measured response and $\hat{Y}(t)$ the model response. This is a least squares criterion for the estimation of model parameters.

(ii) Laplace Domain

The measured stimulus-response data is transformed by the (one-sided) Laplace operator:

$$Y(s) = \int_0^\infty e^{-st} Y(t)\, dt \qquad (4.2)$$

where s is the Laplace variable. The model is solved in terms of s rather than the time variable t, and comparison is carried

out in the Laplace domain. However, if a least squares criterion is applied in the Laplace domain:

$$\Phi = \sum_{s}[Y(s) - \hat{Y}(s)]^2 \qquad (4.3)$$

it is not possible to estimate analytically the possible bias in the model parameters (99). It may be shown (99) that least squares in the time domain yields unbiased estimates - unfor= tunately it is not known what criterion in the Laplace domain is equivalent to least squares in the time domain.

(iii) Frequency Domain

The measured RTD data is re-cast to the form of a frequency response on the basis of the Fourier transform operator:

$$Y(jw) = \frac{1}{\sqrt{2\pi}} \int_{-\infty}^{\infty} e^{-jwt} Y(t)\, dt \qquad (4.4)$$

where j is the complex multiplier and w represents frequency. The model is solved for frequency response, and is compared to the measured data in this form.

In the case of RTD stimulus-response data the lower half of the transform integral (from $-\infty$ to 0) falls away, since Y(t) is zero for $t<0$. Ignoring the factor $\sqrt{2\pi}$, one may write:

$$Y(jw) = \int_{0}^{\infty} e^{-jwt} Y(t)\, dt \qquad (4.5)$$

It is immediately apparent that this represents a special case of the Laplace transform operator, where the complex variable s is replaced by an imaginary component jw. In this instance a criterion in the frequency domain equivalent to least squares in the time domain does exist. Parseval's equality

$$\int_0^\infty [f(t)]^2 \, dt = \frac{1}{\pi} \int_0^\infty |f(jw)|^2 \, dw \qquad (4.6)$$

applied to equation (4.1) leads to:

$$\Phi = \frac{1}{\pi} \int_0^\infty |Y(jw) - \hat{Y}(jw)|^2 \, dw \qquad (4.7)$$

which effectively calls for the minimisation of real and imaginary deviations squared (99).

A scan of the literature and a cursory examination of the mathematical form of the models considered in this study shows that analytical solutions in the time domain are not feasible. The models are, however, amenable to analytical solution in the Laplace or frequency domains, and the latter is preferred due to the existence of a suitable objective function for unbiased parameter estimation as discussed above. The alternative is to solve the models numerically in the time domain by some suitable finite difference technique. This approach generally requires a large amount of computing power - this does not appear to present any significant obstacle at first glance. However, when it is

noted that the overall procedure involves repeated model response evaluations for different parameter values, it becomes clear that the cost in terms of computer time could become excessive - this was indeed found to be the case in the early stages of this investigation. It was decided that analytical frequency response expressions should be employed wherever possible.

The rest of this chapter is divided into three sections. The first of these deals with the formulation and analytical solution (in the frequency domain) of the five general models discussed in Chapter 3. The second describes the formulation and solution of the two (specialised) sparger models, and in the third section the overall data processing and information flow strategy is set out.

4.1 General Model Formulation and Analytical Solution

4.1.1 MVD Model

The May-Van Deemter or MVD model has been solved in the open literature (15) for $U_d = 0$. The solution presented here follows a similar pattern, with the restriction on U_d removed.

The model formulation proceeds as follows: a dynamic material balance over an incremental height Δz of the bubble phase leads to

$$\begin{bmatrix}\text{accumulation}\end{bmatrix} = \begin{bmatrix}\text{flow in - flow out by convection}\end{bmatrix} + \begin{bmatrix}\text{net gain by interphase transfer}\end{bmatrix}$$

In mathematical symbols:

$$\delta A_t \Delta z \frac{\partial C_b}{\partial t} = \delta A_t U_b \left[C_{b|z} - C_{b|z+\Delta z}\right] - (K_{be})_b \delta A_t \Delta z \left[C_b - C_e\right] \qquad (4.8)$$

Dividing through by $\delta A_t \Delta z$ and taking the limit as $\Delta z \to 0$:

$$\frac{\partial C_b}{\partial t} + U_b \frac{\partial C_b}{\partial z} + (K_{be})_b \left[C_b - C_e\right] = 0 \qquad (4.7)$$

Define dimensionless time $\theta = t(U_b/L_f)$

and dimensionless distance $\xi = z/L_f$

and substitute:

$$\frac{\partial C_b}{\partial \theta} + \frac{\partial C_b}{\partial \xi} + X_b\left[C_b - C_e\right] = 0 \qquad (4.10)$$

where $X_b = (K_{be})_b L_f/U_b$ is defined as the crossflow ratio.

For the dense phase:

$$\left[\text{accumulation}\right] = \left[\begin{array}{l}\text{in-out by}\\ \text{convention}\end{array}\right] + \left[\begin{array}{l}\text{in-out by}\\ \text{interphase}\\ \text{transfer}\end{array}\right] + \left[\begin{array}{l}\text{in-out by}\\ \text{axial}\\ \text{dispersion}\end{array}\right]$$

or
$$(1-\delta)\varepsilon_d A_t \Delta z \frac{\partial C_e}{\partial t} = (1-\delta) U_d A_t \left[C_{e|z} - C_{e|z+\Delta z}\right] + (K_{be})_b \delta A_t \Delta z \left[C_b - C_e\right] - D_d (1-\delta) A_t \varepsilon_d \left[\frac{\partial C_e}{\partial z}\Big|_z - \frac{\partial C_e}{\partial z}\Big|_{z+\Delta z}\right] \qquad (4.11)$$

Dividing through by $(1-\delta)\ \varepsilon_d\ A_t\ \Delta z$ and taking the limit as $\Delta z \to 0$:

$$\frac{\partial C_e}{\partial t} + \left(\frac{U_d}{\varepsilon_d}\right) \frac{\partial C_e}{\partial z} - \frac{\delta (K_{be})_b}{(1-\delta)\varepsilon_d} \left[C_b - C_e\right] - D_d \frac{\partial^2 C_e}{\partial z^2} = 0 \qquad (4.12)$$

Introducing the dimensionless variables θ and ξ:

$$\frac{\partial C_e}{\partial \theta} + \left(\frac{U_d}{\varepsilon_d U_b}\right) \frac{\partial C_e}{\partial \xi} - \frac{\delta X_b}{(1-\delta)\varepsilon_d} \left[C_b - C_e\right] - N_d \frac{\partial^2 C_e}{\partial \xi^2} = 0 \qquad (4.13)$$

where $N_d = D_d/(U_b L_f)$ is the number of dense phase dispersion units.

The initial condition or I.C. is:

$$C_b(\xi,0) = C_e(\xi,0) = 0 \qquad (4.14)$$

and the boundary conditions or B.C.'s:

$$\text{(i)} \quad C_b(0,\theta) = C_0 \qquad (4.15)$$

$$\text{(ii)} \quad \left.\frac{\partial C_e}{\partial \xi}\right|_{\xi=0} = 0 \qquad (4.16)$$

$$\text{(iii)} \quad \left.\frac{\partial C_e}{\partial \xi}\right|_{\xi=1} = 0 \qquad (4.17)$$

These B.C.'s are in fact those used by Van Deemter (15), and the suitability or otherwise of the last two is a matter for debate. This question will not be ventured into at this stage, however, since it is the generally accepted form of the model that is required for the purpose of comparison with other models.

The reader's attention is drawn to the fact that, in the ensuing sections, the Laplace transform is used rather than the Fourier transform. It is understood that, for the conditions encountered in this study, the Laplace variable s may be replaced by the frequency variable jw at any stage.

The solution for frequency response proceeds as follows: equations (4.10) and (4.13) are transformed, with the I.C.'s zero in both phases, to yield

$$\frac{dC_b}{d\xi} + (X_b+s)\, C_b = X_b C_e \tag{4.18}$$

and $$N_d \frac{d^2C_e}{d\xi^2} - \left(\frac{U_d}{\varepsilon_d U_b}\right) \frac{dC_e}{d\xi} - \left(\frac{\delta X_b}{(1-\delta)\varepsilon_d} + s\right) C_e = \left(\frac{\delta X_b}{(1-\delta)\varepsilon_d}\right) C_b \tag{4.19}$$

Now C_e is written in terms of C_b from equation (4.18) and the resulting expression is substituted into (4.19). The result is:

$$\frac{d^3C_b}{d\xi^3} + \left[X_b+s - \frac{U_d}{\varepsilon_d U_b}\,\frac{1}{N_d}\right] \frac{d^2C_b}{d\xi^2} - \left[\frac{U_d(X_b+s)}{\varepsilon_d U_b N_d} + \left(\frac{\delta X_b}{(1-\delta)\varepsilon_d} + s\right)\frac{1}{N_d}\right] \frac{dC_b}{d\xi}$$
$$+ \left[\frac{\delta X_b^{\,2}}{(1-\delta)\varepsilon_d N_d} - \left(\frac{\delta X_b}{(1-\delta)\varepsilon_d} + s\right)\frac{X_b+s}{N_d}\right] C_b = 0 \tag{4.20}$$

The transformed boundary conditions are:

$$C_b(\xi = 0, s) = 1 \tag{4.21}$$

(since C_0 is taken to be a Dirac delta function)

$$\left.\frac{dC_e}{d\xi}\right|_{\xi=0} = 0 \tag{4.22}$$

$$\left.\frac{dC_e}{d\xi}\right|_{\xi=1} = 0 \tag{4.23}$$

Now assume that equation (4.20) has a solution of the form:

$$C_b(\xi,s) = A_1 e^{\lambda_1 \xi} + A_2 e^{\lambda_2 \xi} + A_3 e^{\lambda_3 \xi} \tag{4.24}$$

where the A_i are constants to be determined, and λ_i the roots of:

$$\lambda^3 + \left[X_b + s + \frac{U_d}{\varepsilon_d U_b N_d}\right] \lambda^2 + \left[\frac{U_d (X_b+s)}{\varepsilon_d U_b N_d} + \left(\frac{\delta X_b}{(1-\delta)\varepsilon_d} + s\right) \frac{1}{N_D}\right] \lambda$$

$$+ \left[\frac{\delta X_b^{\,2}}{(1-\delta)\varepsilon_d N_d} - \left(\frac{\delta X_b}{(1-\delta)\varepsilon_d} + s\right) \frac{X_b+s}{N_d}\right] = 0 \tag{4.25}$$

B.C. (4.21) gives:

$$C_b(0,s) = A_1 + A_2 + A_3 = 1 \tag{4.26}$$

or $$A_3 = 1 - A_1 - A_2 \tag{4.27}$$

Now, from (4.18):

$$\frac{dC_e}{d\xi} = \frac{1}{X_b} \frac{d^2 C_b}{d\xi^2} + \frac{X_b+s}{X_b} \frac{dC_b}{d\xi} \tag{4.28}$$

In terms of (4.24) this becomes:

$$\frac{dC_e}{d\xi} = \frac{1}{X_b} \left[A_1(\lambda_1^2 e^{\lambda_1 \xi} - \lambda_3^2 e^{\lambda_3 \xi}) + A_2(\lambda_2^2 e^{\lambda_2 \xi} - \lambda_3^2 e^{\lambda_3 \xi}) + \lambda_3^2 e^{\lambda_3 \xi}\right] + \frac{X_b+s}{X_b} \left[A_1(\lambda_1 e^{\lambda_1 \xi} - \lambda_3 e^{\lambda_3 \xi}) + A_2(\lambda_2 e^{\lambda_2 \xi} - \lambda_3 e^{\lambda_3 \xi}) - \lambda_3 e^{\lambda_3 \xi}\right] \tag{4.29}$$

Setting this expression equal to zero at $\xi = 0$ and $\xi = 1$ and eliminating A_1 leads to:

$$A_2 = \frac{(e^{\lambda_3}-e^{\lambda_1})/\gamma_2}{(e^{\lambda_1}-e^{\lambda_2})/\gamma_3 + (e^{\lambda_3}-e^{\lambda_1})/\gamma_2 + (e^{\lambda_2}-e^{\lambda_3})/\gamma_1} \qquad (4.30)$$

where $\gamma_i = \lambda_i^2 + (X_b+s)\,\lambda_i$. (4.31)

For ease of manipulation define

$$\beta_i = (e^{\lambda l}-e^{\lambda k})/\gamma_i \qquad (4.32)$$

where $l = 3$, $k = 1$ for $i = 2$

$l = 2$ $k = 3$ for $i = 1$

$l = 1$ $k = 2$ for $i = 3$

In terms of β_i's, A_2 becomes

$$A_2 = \frac{\beta_2}{\beta_1+\beta_2+\beta_3} \qquad (4.33)$$

Solving for A_1 and A_3 leads to:

$$A_1 = \frac{\beta_1}{\beta_1+\beta_2+\beta_3} \qquad (4.34)$$

and $$A_3 = \frac{\beta_3}{\beta_1+\beta_2+\beta_3} \qquad (4.35)$$

The Laplace domain solution for C_b is therefore

$$C_b(\xi,s) = \frac{\beta_1 e^{\lambda_1\xi}+\beta_2 e^{\lambda_2\xi}+\beta_3 e^{\lambda_3\xi}}{\beta_1+\beta_2+\beta_3} \qquad (4.36)$$

with:

$$\beta_1 = \frac{1}{\lambda_1} \frac{e^{\lambda_2} - e^{\lambda_3}}{\lambda_1 + X_b + s} \tag{4.37}$$

$$\beta_2 = \frac{1}{\lambda_2} \frac{e^{\lambda_3} - e^{\lambda_1}}{\lambda_2 + X_b + s} \tag{4.38}$$

$$\beta_3 = \frac{1}{\lambda_3} \frac{e^{\lambda_1} - e^{\lambda_2}}{\lambda_3 + X_b + s} \tag{4.39}$$

The solution for C_e is obtained by substituting (4.36) into (4.18). The result is:

$$C_e(\xi,s) = \frac{1}{X_b(\beta_1+\beta_2+\beta_3)} \left[\beta_1 e^{\lambda_1 \xi}(\lambda_1 + X_b + s) + \right.$$

$$\left. \beta_2 e^{\lambda_2 \xi} (\lambda_2 + X_b + s) + \beta_3 e^{\lambda_3 \xi}(\lambda_3 + X_b + s)\right] \tag{4.40}$$

Now the concentration measured by an aspirating probe in the bed is given by:

$$\bar{C} = (\delta C_b + (1-\delta)\varepsilon_d C_e)/(\delta + (1-\delta)\varepsilon_d) \tag{4.41}$$

and equations (4.36) and (4.40) are combined accordingly.

This solution, programmed in FORTRAN V, is evaluated on a Univac 1160 computer. A listing is given in Appendix B. The roots of the complex third-order polynomial (equation 4.25) are determined numerically by the Univac library routine ROOTCP.

4.1.2 CCBM Model

To the best of the author's knowledge, no dynamic solution for this model has been published previously. The solution presented here is for a boundary condition at the top of the bed which is somewhat different to that normally employed; the nature of the model in the dynamic mode necessitates this modification.

A dynamic material balance on the bubble phase yields:

$$\begin{bmatrix}\text{accm}\end{bmatrix} = \begin{bmatrix}\text{in-out}\\ \text{convection}\end{bmatrix} + \begin{bmatrix}\text{net gain by}\\ \text{interphase}\\ \text{transfer}\end{bmatrix}$$

$$\text{or} \quad \delta A_t \Delta z \frac{\partial C_b}{\partial t} = \delta A_t U_b \left[C_b|_z - C_b|_{z+\Delta z}\right] - (K_{bc})_b \, \delta A_t \Delta z \left[C_b - C_c\right] \quad (4.42)$$

Dividing by $\delta A_t \Delta z$ and taking the limit on Δz:

$$\frac{\partial C_b}{\partial t} + U_b \frac{\partial C_b}{\partial z} + (K_{bc})_b \left[C_b - C_c\right] = 0 \quad (4.43)$$

and introducing dimensionless time and distance variables:

$$\frac{\partial C_b}{\partial \theta} + \frac{\partial C_b}{\partial \xi} + X_{bc}\left[C_b - C_c\right] = 0 \quad (4.44)$$

A similar treatment on the cloud phase leads to:

$$\begin{bmatrix}\text{accm}\end{bmatrix} = \begin{bmatrix}\text{in-out}\\ \text{convention}\end{bmatrix} + \begin{bmatrix}\text{net gain by}\\ \text{bbl-cloud}\\ \text{transfer}\end{bmatrix} + \begin{bmatrix}\text{net gain by}\\ \text{cloud-emulsion}\\ \text{transfer}\end{bmatrix}$$

If α is the volume ratio of this phase to the bubble phase, then:

$$\alpha\,\delta\,\varepsilon_d\,A_t\Delta z\,\frac{\partial C_c}{\partial t} = A_t\,\alpha\,\delta\,\varepsilon_d\,U_b\left[C_c\Big|_z - C_c\Big|_{z+\Delta z}\right]$$

$$+ (K_{bc})_b\,\delta\,A_t\,\Delta z\,[C_b - C_c] - (K_{ce})_b\,\delta\,A_t\,\Delta z\,[C_c - C_e] \quad (4.45)$$

Dividing by $\alpha\,\delta\,\varepsilon_d\,A_t\,\Delta z$ and letting $\Delta z \to 0$:

$$\frac{\partial C_c}{\partial t} + U_b\frac{\partial C_c}{\partial z} + \frac{(K_{bc})_b + (K_{ce})_b}{\alpha\varepsilon_d}C_c = \frac{(K_{bc})_b}{\alpha\varepsilon_d}C_b + \frac{(K_{ce})_b}{\alpha\varepsilon_d}C_e \quad (4.46)$$

or, in terms of θ and ξ:

$$\frac{\partial C_c}{\partial\theta} + \frac{\partial C_c}{\partial\xi} + \frac{(X_{bc} + X_{ce})}{\alpha\varepsilon_d}C_c = \left(\frac{X_{bc}}{\alpha\varepsilon_d}\right)C_b + \left(\frac{X_{ce}}{\alpha\varepsilon_d}\right)C_e \quad (4.47)$$

A mass balance on the emulsion gives:

$$\begin{bmatrix}\text{accm}\end{bmatrix} = \begin{bmatrix}\text{in-out}\\ \text{convection}\end{bmatrix} + \begin{bmatrix}\text{net gain by}\\ \text{interphase}\\ \text{transfer}\end{bmatrix}$$

$$\text{i.e.}\quad (1-\delta-\alpha\delta)\varepsilon_d\,A_t\,\Delta z\,\frac{\partial C_e}{\partial t} = (1-\delta-\alpha\delta)\,\varepsilon_d\,U_e\,A_t\left[C_e\Big|_z - C_e\Big|_{z+\Delta z}\right]$$

$$+ (K_{ce})_b\,\delta\,A_t\,\Delta z\,[C_c - C_e] \quad (4.48)$$

Dividing by $(1-\delta-\alpha\delta)\,\varepsilon_d\,A_t\,\Delta z$ and taking the limit:

$$\frac{\partial C_e}{\partial t} + U_e\frac{\partial C_e}{\partial z} - \frac{(K_{ce})_b}{(1-\delta-\alpha\delta)\varepsilon_d}[C_c - C_e] = 0 \quad (4.49)$$

and in terms of the dimensionless variables:

$$\frac{\partial C_e}{\delta\theta} + \left(\frac{U_e}{U_b}\right)\frac{\partial C_e}{\partial\xi} - \frac{\delta X_{ce}}{(1-\delta-\alpha\delta)\varepsilon_d}[C_c - C_e] = 0 \quad (4.50)$$

The associated I.C.'s are:

$$C_b(\xi,0) = C_c(\xi,0) = C_e(\xi,0) = 0 \tag{4.51}$$

and two of the B.C.'s

$$C_b(0,\theta) = C_0 \tag{4.52}$$

$$C_c(0,\theta) = \frac{(U_0-\delta U_b)\ C_0 - (1-\delta-\alpha\delta)\varepsilon_d\ U_e\ C_e(0,\theta)}{\alpha\ \delta\ \varepsilon_d\ U_b} \tag{4.53}$$

The third boundary condition is usually specified as:

$$C_c(L_f,\theta) = C_e(L_f,\theta) \tag{4.54}$$

Several attempts at a solution for this model with B.C. (4.54) were made. Bivariate Laplace transform and transition matrix techniques were employed, and in both cases solutions which appeared perfectly normal on paper were obtained. However, when these solutions were programmed and run on the computer, nonsensical results were obtained for negative (i.e. downflowing) emulsion velocities. The cause was traced to the emergence of a complex root with a positive real component. The magnitude of this component was such that numbers of the order of 10^{26} were added to numbers of the order of unity, the result being a complete loss of numerical significance. In order to suppress this pole in the right-hand half-plane, it was deemed necessary to replace the boundary condition given by equation (4.54) by the condition that all concentrations remain finite as bed height tends to infinity, i.e.

$$\lim_{\xi\to\infty} C_b(\xi,\theta),\ C_c(\xi,\theta),\ C_e(\xi,\theta) \ < \ \infty \qquad (4.55)$$

Applying the Laplace transform with respect to time, using the I.C. given by (4.51) gives, for equation (4.44):

$$\frac{dC_b}{d\xi} + (X_{bc} + s)\, C_b = X_{bc}\, C_c \qquad (4.56)$$

For equation (4.47)

$$\frac{dC_c}{d\xi} + \left[\frac{X_{bc} + X_{ce}}{\alpha\varepsilon_d} + s\right] C_c = \left[\frac{X_{bc}}{\alpha\varepsilon_d}\right] C_b + \left[\frac{X_{ce}}{\alpha\varepsilon_d}\right] C_e \qquad (4.57)$$

and for (4.50)

$$\frac{dC_e}{d\xi} + \left(\frac{U_b}{U_e}\right)\left[\frac{\delta X_{ce}}{(1-\delta-\alpha\delta)\varepsilon_d} + s\right] C_e = \left(\frac{U_b}{U_e}\right)\left[\frac{\delta X_{ce}}{(1-\delta-\alpha\delta)\varepsilon_d}\right] C_c \qquad (4.58)$$

For ease of manipulation define

$$a_1 = X_{bc} + s \qquad (4.59)$$

$$a_2 = (X_{bc} + X_{ce})/\alpha\varepsilon_d + s \qquad (4.60)$$

$$a_3 = (U_b/U_e)\left[\delta X_{ce}/((1-\delta-\alpha\delta)\varepsilon_d) + s\right] \qquad (4.61)$$

$$a_4 = X_{bc}/(\alpha\varepsilon_d) \qquad (4.62)$$

$$a_5 = X_{ce}/(\alpha\varepsilon_d) \qquad (4.63)$$

$$a_6 = (U_b/U_e)\left[\delta X_{ce}/((1-\delta-\alpha\delta)\varepsilon_d)\right] \qquad (4.64)$$

Equations (4.56) to (4.58) then become:

$$\frac{dC_b}{d\xi} + a_1 C_b = X_{bc}\, C_c \qquad (4.65)$$

$$\frac{dC_c}{d\xi} + a_2 C_c = a_4 C_b + a_5 C_e \tag{4.66}$$

$$\frac{dC_e}{d\xi} + a_3 C_e = a_6 C_c \tag{4.67}$$

Transforming these equations for a second time, this time with respect to ξ,and letting the transformed distance variable be ν:

$$C_b \nu - C_b(\xi=0,s) + a_1 C_b = X_{bc} C_c \tag{4.68}$$

$$C_c \nu - C_c(\xi=0,s) + a_2 C_c = a_4 C_b + a_s C_e \tag{4.69}$$

$$C_e \nu - C_e(\xi=0,s) + a_3 C_e = a_6 C_c \tag{4.70}$$

The boundary condition given by (4.52), in its tranformed state and for C_0 a delta function, gives

$$C_b(\xi=0,s) = 1 \tag{4.71}$$

The B.C. given by (4.53) then gives

$$C_c(\xi=0,s) = X_1 - X_2 C_e(\xi=0,s) \tag{4.72}$$

where $X_1 = (U_0 - \delta U_b)/(\alpha \delta \varepsilon_d U_b)$ (4.73)

and $X_2 = (1-\delta-\alpha\delta) U_e \varepsilon_d/(\alpha \delta \varepsilon_d U_b)$ (4.74)

Substituting from (4.71) and (4.72) and writing equations (4.68) to (4.70) in matrix form:

$$\begin{bmatrix} \nu+a_1 & -X_{bc} & 0 \\ -a_4 & \nu+a_2 & -a_5 \\ 0 & -a_6 & \nu+a_3 \end{bmatrix} \begin{bmatrix} C_b \\ C_c \\ C_e \end{bmatrix} = \begin{bmatrix} 1 \\ X_1-X_2C_{eo} \\ C_{eo} \end{bmatrix} \qquad (4.75)$$

where $C_e(\xi=0,s)$ is abbreviated C_{eo}. Now the exponential factors in ξ are specified by the roots of the 3x3 determinant:

$$\Delta = \nu^3 + (a_1+a_2+a_3)\nu^2 + (a_2a_3-a_5a_6+a_1a_2+a_1a_3-a_4X_{bc})\nu + a_1(a_2a_3-a_5a_6) - a_3a_4X_{bc} \qquad (4.76)$$

Define a_7, a_8 and a_9 such that

$$\Delta = \nu^3+a_7\nu^2+a_8\nu+a_9 \qquad (4.77)$$

For negative or downward emulsion velocities this expression has two roots with negative real components and one with a positive real component. To satisfy B.C. (4.55) this pole must be constrained to coincide with a zero on the complex plane.

From equation (4.75):

$$C_b = \frac{1}{\Delta}\{[(\nu+a_2)(\nu+a_3) - a_5a_6]+ (X_1-X_2C_{eo})\ [X_{bc}(\nu+a_3)] + C_{eo}\ [a_5X_{bc}]\} \qquad (4.78)$$

by Cramer's Rule, and this may be re-written as:

$$C_b = \frac{1}{\Delta}\left[\nu^2 + (a_2+a_3+X_{bc}X_1-X_{bc}X_2C_{eo})\nu \right.$$
$$\left. + (a_2a_3-a_5a_6+X_{bc}a_3X_1+a_5X_{bc}C_{eo}-X_2X_{bc}a_3C_{eo})\right] \qquad (4.79)$$

If the roots of (4.77) are given by λ_i, where λ_3 has a positive real component, then the numerator of (4.79) must equal $(\nu-\lambda_3)(\nu-\gamma_1)$ where γ_1 is some constant. Equating the numerators:

$$\nu^2-(\lambda_3+\gamma_1)\nu+\lambda_3\gamma_1 = \nu^2 + (a_2+a_3+X_{bc}X_1-X_{bc}X_2C_{eo})\nu$$
$$+ a_2a_3 - a_5a_6 + X_{bc}\,a_3\,X_1 - (a_5X_{bc}-X_2X_{bc}a_3)C_{eo} \qquad (4.80)$$

Comparing coefficients:

$$(a_2+a_3+X_{bc}X_1) - (X_{bc}X_2)C_{eo} = -(\lambda_3+\gamma_1) \qquad (4.81)$$

$$(a_2a_3-a_5a_6+X_{bc}a_3X_1) + (a_5X_{bc}-X_2X_{bc}a_3)C_{eo} = \lambda_3\gamma_1 \qquad (4.82)$$

Define a_{10} through a_{13} such that

$$a_{10} + a_{11}C_{eo} = -(\lambda_3+\gamma_1) \qquad (4.83)$$

$$a_{12} + a_{13}C_{eo} = \lambda_3\gamma_1$$

and solving this sytem for C_{eo} yields:

$$C_{eo} = -\frac{\lambda_3^2+\lambda_3a_{10}+a_{12}}{\lambda_3a_{11}+a_{13}} \qquad (4.85)$$

and $\gamma_1 = (a_{12}+a_{13}C_{eo})/\lambda_3$ (4.86)

Now $C_b(\nu,s) = \dfrac{\nu-\gamma_1}{(\nu-\lambda_1)(\nu-\lambda_2)}$ (4.87)

Splitting into partial fractions and inverse transforming with respect to ν:

$$C_b(\xi,s) = \left(\frac{\lambda_1-\gamma_1}{\lambda_1-\lambda_2}\right)e^{\lambda_1\xi} + \left(\frac{\lambda_2-\gamma_1}{\lambda_2-\lambda_1}\right)e^{\lambda_2\xi} \quad (4.88)$$

For the cloud phase, Cramer's Rule applied to (4.75) gives:

$$C_c = \frac{C_{co}}{\Delta}\left\{\nu^2 + \left[a_1+a_3 + \frac{a_5C_{eo}+a_4}{C_{co}}\right]\nu + \left[a_1a_3 + \frac{a_1a_5C_{eo}+a_3a_4}{C_{co}}\right]\right\} \quad (4.89)$$

where $C_{co} = X_1-X_2C_{eo}$. As before, the numerator must equal $C_{co}(\nu-\lambda_3)(\nu-\gamma_2)$, so

$$a_1 + a_3 + \frac{a_5C_{eo}+a_4}{C_{co}} = -(\lambda_3+\gamma_2) \quad (4.90)$$

and $$a_1a_3 + \frac{a_1a_5C_{eo}+a_3a_4}{C_{co}} = \lambda_3\gamma_2 \quad (4.91)$$

Therefore $$\gamma_2 = \frac{1}{\lambda_3}\left[a_1a_3 + \frac{a_1a_5C_{eo}+a_3a_4}{C_{co}}\right] \quad (4.92)$$

or $$\gamma_2 = -\lambda_3 - \left[a_1+a_3 + \frac{a_5C_{eo}+a_4}{C_{co}}\right] \quad (4.93)$$

Equations (4.92) and (4.93) in fact yield identical values for γ_2, and $C_c(\xi,s)$ becomes

$$C_c(\xi,s) = C_{co}\left[\left(\frac{\lambda_1-\gamma_2}{\lambda_1-\lambda_2}\right)e^{\lambda_1\xi} + \left(\frac{\lambda_2-\gamma_2}{\lambda_2-\lambda_1}\right)e^{\lambda_2\xi}\right] \tag{4.94}$$

Cramer's Rule applied to (4.75) for the emulsion phase leads to:

$$C_e = \frac{C_{eo}}{\Delta}\left\{\nu^2 \left[a_1+a_2+a_6\frac{C_{co}}{C_{eo}}\right]\nu + \left[a_1a_2-a_4X_{bc} + \frac{a_1a_6C_{co}+a_4a_6}{C_{eo}}\right]\right\} \tag{4.95}$$

The numerator must contain a $(\nu-\lambda_3)$ term, so setting it equal to $C_{eo}(\nu-\lambda_3)(\nu-\gamma_3)$ and equating coefficients:

$$a_1 + a_2 + a_6\frac{C_{co}}{C_{eo}} = -(\lambda_3+\gamma_3) \tag{4.96}$$

$$a_1a_2 - a_4X_{bc} + \frac{a_1a_6C_{eo}+a_4a_6}{C_{eo}} = \lambda_3\Phi_3 \tag{4.97}$$

and $$\gamma_3 = \frac{1}{\lambda_3}\left[a_1a_2-a_4X_{bc} + \frac{a_1a_6C_{co}+a_4a_6}{C_{eo}}\right] \tag{4.98}$$

or $$\gamma_3 = -\lambda_3 - \left[a_1+a_2+a_6\frac{C_{co}}{C_{eo}}\right] \tag{4.99}$$

Once again, these expressions yield identical values for γ_3 and $C_e(\xi,s)$ may be obtained by inverse transformation:

$$C_e = C_{eo}\left[\left(\frac{\lambda_1-\gamma_3}{\lambda_1-\lambda_2}\right)e^{\lambda_1\xi} + \left(\frac{\lambda_2-\gamma_3}{\lambda_2-\lambda_1}\right)e^{\lambda_2\xi}\right] \tag{4.100}$$

For an aspirating probe in the bed:

$$\bar{C} = \frac{\delta C_b + \alpha\delta\varepsilon_d C_c + (1-\delta-\alpha\delta)\varepsilon_d C_e}{\delta + \alpha\delta\,\varepsilon_d + (1-\delta-\alpha\delta)\varepsilon_d} \tag{4.101}$$

and the solutions for C_b, C_c and C_e are combined accordingly to yield an overall frequency response. A FORTRAN V listing of the solution is given in Appendix B.

4.1.3 WFD Model

As far as the author is aware, no dynamic-mode solution to the Werther film diffusion or WFD model has been published. Werther (98) has solved this model for a reacting tracer under steady-state conditions, but does not appear to have considered an unsteady-state application as yet.

The WFD model employs axially stagnant cloud and emulsion phases. The bubble and emulsion phases are laterally well mixed, and the cloud phase offers (lateral) diffusional resistance to tracer migration. The diffusion law is defined as:

$$\frac{dN}{dt} = -D_f \, a_b \, V_b \, \frac{\partial C_c}{\partial x} \qquad (4.102)$$

where $\frac{dN}{dt}$ is the rate of transfer of the species under consideration, D_f the diffusion coefficient and $\frac{\partial C_c}{\partial x}$ the lateral concentration gradient in the cloud. The volume of the bubble phase is represented by V_b, and a_b is the bubble-cloud interfacial area per unit bubble volume. If the overall cloud thickness is γ_c and the cloud is reasonably thin, one can reasonably assume

$$(K_{be})_b = \left(\frac{D_f \, a_b}{\gamma_c}\right) \qquad (4.103)$$

In addition, the ratio of cloud to bubble volume α may be written:

$$\alpha = a_b \gamma_c \tag{4.104}$$

This model may thus be formulated in terms of a conventional mass transfer coefficient, even though a different transfer mechanism is put forward.

A mass balance on the bubble phase yields:

$$\begin{bmatrix}\text{accm}\end{bmatrix} = \begin{bmatrix}\text{in-out}\\ \text{convection}\end{bmatrix} + \begin{bmatrix}\text{gain by}\\ \text{interphase}\\ \text{transfer}\end{bmatrix}$$

$$\delta A_t \Delta z \frac{\partial C_b}{\partial t} = \delta A_t U_b \left[C_b\Big|_z - C_b\Big|_{z+\Delta z}\right] + D_f a_b \delta A_t \Delta z \frac{\partial C_c}{\partial x}\Big|_{x=0} \tag{4.105}$$

Dividing by $\delta A_t \Delta z$ and letting $\Delta z \to 0$:

$$\frac{\partial C_b}{\partial t} + U_b \frac{\partial C_b}{\partial z} - D_f a_b \frac{\partial C_c}{\partial x}\Big|_{x=0} = 0 \tag{4.106}$$

Introducing θ, ξ and $\zeta = x/\gamma_c$:

$$\frac{\partial C_b}{\partial \theta} + \frac{\partial C_b}{\partial \xi} - \left(\frac{D_f a_b L_f}{U_b \gamma_c}\right) \frac{\partial C_c}{\partial \zeta}\Big|_{\zeta=0} \tag{4.107}$$

or, in terms of a mass transfer coefficient

$$\frac{\partial C_b}{\partial \theta} + \frac{\partial C_b}{\partial \xi} - X_b \frac{\partial C_c}{\partial \zeta}\Big|_{\zeta=0} = 0 \tag{4.108}$$

A mass balance on the cloud phase:

$$\left[\begin{array}{c}\text{accm}\end{array}\right] = \left[\begin{array}{c}\text{in-out by}\\ \text{lateral diffusion}\end{array}\right]$$

$$\text{so} \quad \delta A_t \Delta z\, a_b \Delta x\, \varepsilon_d \frac{\partial C_c}{\partial t} = D_f a_b A_t \Delta z\, \delta\left[\left.\frac{\partial C_c}{\partial x}\right|_x \left.\frac{\partial C_c}{\partial x}\right|_{x+\Delta x}\right] \qquad (4.109)$$

dividing through by $\delta A_t \Delta z\, a_b \Delta x\, \varepsilon_d$ and letting Δx tend to zero:

$$\frac{\partial C_c}{\partial t} - \frac{D_f}{\varepsilon_d} \frac{\partial^2 C_c}{\partial x^2} = 0 \qquad (4.110)$$

Introducing dimensionless variables and substituting from (4.103) and (4.104):

$$\frac{\partial C_c}{\partial \theta} - \frac{X_b}{\alpha \varepsilon_d} \frac{\partial^2 C_c}{\partial \zeta^2} = 0 \qquad (4.111)$$

A material balance on the emulsion gives:

$$\left[\begin{array}{c}\text{accm}\end{array}\right] = \left[\begin{array}{c}\text{in-out by}\\ \text{lateral diffusion}\end{array}\right]$$

$$\text{or} \quad A_t \Delta z\, (1-\delta-\alpha\delta)\varepsilon_d \frac{\partial C_e}{\partial t} = D_f a_b A_t \Delta z\, \delta \left.\frac{\partial C_c}{\partial x}\right|_{x=\gamma_c} \qquad (4.112)$$

Dividing by $A_t \Delta z\, (1-\delta-\alpha\delta)\varepsilon_d$ and introducing θ and ζ:

$$\frac{\partial C_e}{\partial \theta} + \frac{\delta X_b}{(1-\delta-\alpha\delta)\varepsilon_d} \left.\frac{\partial C_c}{\partial \zeta}\right|_{\zeta=1} \qquad (4.113)$$

The initial conditions are:

$$C_b(\zeta,0) = C_c(\xi,\zeta,0) = C_e(\xi,0) = 0 \qquad (4.114)$$

and the boundary conditions:

$$C_b(0,\theta) = C_0 \qquad (4.115)$$

$$C_c(\xi,0,\theta) = C_b(\xi,\theta) \qquad (4.116)$$

$$C_c(\xi,1,\theta) = C_e(\xi,\theta) \qquad (4.117)$$

The solution of this model for frequency response proceeds as follows: firstly, transform equations (4.108), (4.111) and (4.113) with respect to θ employing (4.114). This leads to:

$$\frac{dC_b}{d\xi} + sC_b - X_b \left.\frac{dC_c}{d\zeta}\right|_{\zeta=0} = 0 \qquad (4.118)$$

$$\frac{d^2C_c}{d\zeta^2} - \left(\frac{\alpha\varepsilon_d s}{X_b}\right) C_c = 0 \qquad (4.119)$$

and $$sC_e + \frac{\delta X_b}{(a-\delta-\alpha\delta)\varepsilon_d} \left.\frac{dC_c}{d\zeta}\right|_{\zeta=1} = 0 \qquad (4.120)$$

Define $\psi = (\alpha \varepsilon_d s/X_b)^{0.5}$ and solve (4.119):

$$C_c = A_1 \cosh(\psi\zeta) + A_2 \sinh(\psi\zeta) \qquad (4.121)$$

where A_1 and A_2 are constants to be determined. Boundary condition (4.116) gives

$$A_1 = C_b(\xi,s) \qquad (4.122)$$

and B.C. (4.117)

$$A_2 = \frac{C_e - C_b \cosh(\psi)}{\sinh(\psi)} \tag{4.123}$$

These expressions for A_1 and A_2 may be substituted into (4.121) and the latter differentiated with respect to ζ. At $\zeta = 0$ this yields:

$$\left.\frac{\partial C_c}{\partial \zeta}\right|_{\zeta=0} = [C_e - C_b \cosh(\psi)]\ \psi/\sinh(\psi) \tag{4.124}$$

and at $\zeta = 1$

$$\left.\frac{\partial C_c}{\partial \zeta}\right|_{\zeta=1} = C_b\ \psi \sinh(\psi) + \left[\frac{C_e - C_b \cosh(\psi)}{\sinh(\psi)}\right] \psi \cosh(\psi) \tag{4.125}$$

Substitution of (4.125) into (4.120) leads to

$$C_e = C_b \frac{\delta X_b\ \psi\ [\cosh^2(\psi) - \sinh^2(\psi)]}{(1-\delta-\alpha\delta)\varepsilon_d\ s \sinh(\psi) + \delta X_b\ \psi \cosh(\psi)} \tag{4.126}$$

and substitution of this expression and (4.124) into (4.118) yields

$$\frac{dC_b}{d\zeta} + \beta C_b = 0 \tag{4.127}$$

$$\text{where } \beta = \frac{(1-\delta-\alpha\delta)\varepsilon_d\ s\ [s \tanh(\psi) + \psi X_b] + \delta X_b \psi [s + X_b \psi \tanh \psi]}{(1-\delta-\alpha\delta)\varepsilon_d\ s \tanh(\psi) + \delta X_b\ \psi} \tag{4.128}$$

Equation (4.127) may be solved directly, and applying the transformed B.C. given by (4.115) leads to:

$$C_b(\xi, s) = e^{-\beta\xi} \qquad (4.129)$$

Now C_e is given in terms of C_b by equation (4.126), and for a thin cloud (i.e. small γ_c and α) the concentration at the tip of an aspirating probe is reasonably approximated by:

$$\bar{C} = \delta C_b + (1-\delta)\varepsilon_d C_e / [\delta + (1-\delta)\varepsilon_d] \qquad (4.130)$$

A FORTRAN V listing of the model solution is given in Appendix B.

4.1.4 BPD Model

The bubble-phase dispersion or BPD model has been employed in the dynamic mode by other investigators (50), and the solution presented here is not new. It follows essentially the same pattern as that established by Kühne and Wippern (31), and is included mainly for completeness.

Formulation proceeds as follows: a material balance on a height increment Δz of the bubble phase leads to

$$\begin{bmatrix}\text{accm}\end{bmatrix} = \begin{bmatrix}\text{in-out}\\ \text{convection}\end{bmatrix} + \begin{bmatrix}\text{gain by}\\ \text{interphase}\\ \text{transfer}\end{bmatrix} + \begin{bmatrix}\text{in-out}\\ \text{axial}\\ \text{dispersion}\end{bmatrix}$$

$$\text{i.e. } \delta A_t \Delta z \frac{\partial C_b}{\partial t} = \delta A_t U_b \left[C_b|_z - C_b|_{z+\Delta z}\right] - (K_{be})_b \delta A_t \Delta z \left[C_b - C_e\right] - D_b \delta A_t \left[\frac{\partial C_b}{\partial z}\Big|_z - \frac{\partial C_b}{\partial z}\Big|_{z+\Delta z}\right] \qquad (4.131)$$

Dividing by $\delta A_t \Delta z$ and letting Δz tend to zero:

$$\frac{\partial C_b}{\partial t} + U_b \frac{\partial C_b}{\partial z} - D_b \frac{\partial^2 C_b}{\partial z^2} + (K_{be})_b [C_b - C_e] = 0 \qquad (4.132)$$

and introducing θ and ξ:

$$\frac{\partial C_b}{\partial \theta} + \frac{\partial C_b}{\partial \xi} - N_b \frac{\partial^2 C_b}{\partial \xi^2} + X_b [C_b - C_e] = 0 \qquad (4.133)$$

where N_b is the number of bubble-phase dispersion units defined as $D_b/(U_b L_f)$. A material balance on the dense phase gives:

$$\begin{bmatrix}\text{accm}\end{bmatrix} = \begin{bmatrix}\text{in-out}\\ \text{convection}\end{bmatrix} + \begin{bmatrix}\text{gain by}\\ \text{interphase}\\ \text{transfer}\end{bmatrix} + \begin{bmatrix}\text{in-out}\\ \text{by axial}\\ \text{dispersion}\end{bmatrix}$$

$$\text{or } (1-\delta)\varepsilon_d A_t \Delta z \frac{\partial C_e}{\partial t} = (1-\delta)A_t U_d [C_e|_z - C_e|_{z+\Delta z}]$$

$$+ (K_{be})_b \delta A_t \Delta z [C_b - C_e] - D_d(1-\delta)\varepsilon_d A_t \left[\frac{\partial C_e}{\partial z}\Big|_z - \frac{\partial C_e}{\partial z}\Big|_{z+\Delta z}\right] \qquad (4.134)$$

Dividing by $(1-\delta)\varepsilon_d A_t \Delta z$ and taking the limit:

$$\frac{\partial C_e}{\partial t} + \left(\frac{U_d}{\varepsilon_d}\right) \frac{\partial C_e}{\partial z} - D_d \frac{\partial^2 C_e}{\partial z^2} - \frac{\delta (K_{be})_b}{(1-\delta)\varepsilon_d} [C_b - C_e] = 0 \qquad (4.135)$$

or in terms of θ and ξ:

$$\frac{\partial C_e}{\partial \theta} + \left(\frac{U_d}{\varepsilon_d U_b}\right) \frac{\partial C_e}{\partial \xi} - N_d \frac{\partial^2 C_e}{\partial \xi^2} - \frac{\delta X_b}{(1-\delta)\varepsilon_d} [C_b - C_e] = 0 \qquad (4.136)$$

The initial condition is:

$$C_b(\xi,0) = C_e(\xi,0) = 0 \qquad (4.137)$$

And the B.C.'s

$$C_b - N_b \frac{\partial C_b}{\partial \xi} = C_0 \text{ at } \xi = 0, \text{ all } \theta \tag{4.138}$$

$$\left(\frac{U_d}{\varepsilon_d U_b}\right) C_e - N_d \frac{\partial C_e}{\partial \xi} = 0 \text{ at } \xi = 0, \text{ all } \theta \tag{4.139}$$

and C_b, C_e finite as $\xi \to \infty$ (4.140)

The solution to this model proceeds thus: equations (4.133) and (4.136) are transformed with respect to time, and with zero initial concentration in both phases this leads to:

$$-N_b \frac{d^2 C_b}{d\xi^2} + \frac{dC_b}{d\xi} + (X_b + s) C_b = X_b C_e \tag{4.141}$$

and $$-N_d \frac{d^2 C_e}{d\xi^2} + U_r \frac{dC_e}{d\xi} + (X_e + s) C_e = X_e C_e \tag{4.142}$$

where U_r is defined as $U_d/(\varepsilon_d U_b)$ and X_e as $\delta X_b/((1-\delta)\varepsilon_d)$.

A transformation with respect to ξ is performed, using boundary conditions (4.138) and (4.139) and assuming C_0 to be an ideal impulse or Dirac delta function. The result, in matrix notation, is

$$\begin{bmatrix} (-N_b\nu^2 + \nu + X_b + s) & -X_b \\ -X_e & (-N_d\nu^2 + U_r\nu + X_e + s) \end{bmatrix} \begin{bmatrix} C_b \\ C_e \end{bmatrix} = \begin{bmatrix} 1 - N_b\nu\, C_{bo} \\ -N_d\nu\, C_{eo} \end{bmatrix} \tag{4.143}$$

where the transformed distance variable is ν, and where $C_b(\xi=0,s)$ and $C_e(\xi=0,s)$ are abbreviated C_{bo} and C_{eo} respectively. The unknowns at this stage are C_{bo} and C_{eo}, and B.C. (4.140) must be applied to determine them.

The exponential factors of the response are given by the roots of the 2x2 determinant. This determinant may be written:

$$\Delta = N_b N_d \left[\nu^4 - \left(\frac{N_d + U_r N_b}{N_b N_d}\right)\nu^3 - \left(\frac{N_d (X_b+s) + N_b(X_e+s) - U_r}{N_b N_d}\right)\nu^2 + \left(\frac{(X_e+s) + U_r(X_b+s)}{N_b N_d}\right)\nu + \frac{(X_b+s)(X_e+s) - X_b X_e}{N_b N_d}\right] \quad (4.144)$$

Let the roots of this expression be λ_i. For the conditions of interest, two of these roots have positive real components. These poles in the right-hand half-plane must coincide with zeros if B.C. (4.140) is to be satisfied. Solving equation (4.143) for C_b by Cramer's Rule gives:

$$C_b = \frac{1}{\Delta}\left[(N_d\nu^2 + U_r\nu + X_e + s)(1 - N_b\,\nu\,C_{bo}) - X_b\,N_d\,\nu\,C_{eo}\right] \quad (4.145)$$

If the roots in the right-hand half-plane are λ_3 and λ_4, then this expression must take the form:

$$C_b = \frac{1}{\Delta}\left[C_{bo}\,N_b\,N_d\,(\nu-\lambda_3)(\nu-\lambda_4)(\nu-\gamma_1)\right] \quad (4.146)$$

where γ_1 is a constant to be determined.

Comparing coefficients of the numerator terms of (4.145) and (4.146) yields:

$$\lambda_3 + \lambda_4 + \gamma_1 = \frac{N_d + N_b U_r C_{bo}}{N_b N_d C_{bo}} \tag{4.147}$$

$$-(\lambda_3\lambda_4 + \lambda_3\gamma_1 + \lambda_4\gamma_1) = \frac{N_b C_{bo}(X_e+s) + X_b N_d C_{eo} - U_r}{N_b N_d C_{bo}} \tag{4.148}$$

$$-\lambda_3\lambda_4\gamma_1 = \frac{X_e + s}{N_b N_d C_{bo}} \tag{4.149}$$

Similarly, solving (4.143) for C_e yields

$$C_e = \frac{1}{\Delta}\left[(1-N_b\nu C_{bo})X_e + (N_b\nu^2 - \nu - X_b - s)(N_d\nu C_{eo})\right] \tag{4.150}$$

and to satisfy (4.140):

$$C_e = \frac{1}{\Delta}\left[C_{eo} N_b N_d (\nu-\lambda_3)(\nu-\lambda_4)(\nu-\gamma_2)\right] \tag{4.151}$$

Comparing coefficients as before leads to:

$$\lambda_3 + \lambda_4 + \gamma_2 = \frac{N_d C_{eo}}{N_b N_d C_{eo}} \tag{4.152}$$

$$-(\lambda_3\lambda_4 + \lambda_3\gamma_2 + \lambda_4\gamma_2) = \frac{N_d C_{eo}(X_b+s) + N_b X_e C_{bo}}{N_b N_d C_{eo}} \tag{4.153}$$

$$-\lambda_3\lambda_4\gamma_2 = \frac{X_e}{N_b N_d C_{eo}} \tag{4.154}$$

Now equations (4.147) to (4.149) and (4.152) to (4.154) represent a system of six equations and four unknowns (C_{bo}, C_{eo}, γ_1 and γ_2). Any four equations may be used, however, since any combination of

four yields the same numerical values for the unknowns (this assertion was tested by using different equations in the computer model). A representative set of solutions for the four unknowns is:

$$C_{bo} = \frac{X_b + s + \lambda_3\lambda_4 N_D}{N_4\lambda_3\lambda_4 [N_d(\lambda_3+\lambda_4) - U_r]} \tag{4.155}$$

$$C_{eo} = \frac{X_e}{N_d\lambda_3\lambda_4 [N_b(\lambda_3+\lambda_4)-1]} \tag{4.156}$$

$$\gamma_1 = \frac{X_b + s}{N_b N_d \lambda_3\lambda_4 C_{bo}} \tag{4.157}$$

$$\gamma_2 = \frac{1}{N_b} - \lambda_3 - \lambda_4 \tag{4.158}$$

with all the unknowns accounted for, C_b may be written as

$$C_b(\nu,s) = \frac{C_{bo} N_b N_d (\nu-\lambda_3)(\nu-\lambda_4)(\nu-\gamma_1)}{N_b N_d (\nu-\lambda_1)(\nu-\lambda_2)(\nu-\lambda_3)(\nu-\lambda_4)}$$

Cancelling the factors containing λ_3 and λ_4 and inverse transforming with respect to ν:

$$C_b(\xi,s) = C_{bo}\left[\left(\frac{\lambda_1-\gamma_1}{\lambda_1-\lambda_2}\right)e^{\lambda_1\xi} + \left(\frac{\lambda_2-\gamma_1}{\lambda_2-\lambda_1}\right)e^{\lambda_2\xi}\right] \tag{4.159}$$

Similarly:

$$C_e(\xi,s) = C_{eo}\left[\left(\frac{\lambda_1-\gamma_2}{\lambda_1-\lambda_2}\right)e^{\lambda_1\xi} + \left(\frac{\lambda_2-\gamma_2}{\lambda_2-\lambda_1}\right)e^{\lambda_2\xi}\right] \tag{4.160}$$

Finally,

$$\bar{C} = \frac{\delta\, C_b + (1-\delta)\varepsilon_d\, C_e}{\delta + (1-\delta)\varepsilon_d} \tag{4.161}$$

A FORTRAN V listing of this solution is given in Appendix B. A warning is printed if the roots λ_3 and λ_4 do not both display positive real components.

4.1.5 MBT Model

As stated previously, the multiple bubble-track or MBT model is considered original to this study.

The model is shown in Figure 3.5 with five tracks or plug flow units in parallel for the bubble phase. In principle any number of plug flow units could be used, and one would usually employ the maximum number considered practical for any particular application. In this investigation the number of plug flow bubble tracks is fixed at five. The reason for this is that the

Univac library routine ROOTCP, which is used to find the roots of the (complex) polynomial which emerges in the model solution algorithm, has a practical limit on the order of the polynomial it is able to handle. If the order of the polynomial is too high, the range of numbers generated in this routine becomes too large and an error condition results. Five tracks in the MBT model generates a seventh-order polynomial: this was found to be close to the ROOTCP practical limit.

A material balance on an incremental height Δz of bubble track i leads to:

$$\begin{bmatrix}\text{accm}\end{bmatrix} = \begin{bmatrix}\text{in-out}\\ \text{convection}\end{bmatrix} + \begin{bmatrix}\text{in-out}\\ \text{interphase}\\ \text{transfer}\end{bmatrix}$$

$$\text{or} \quad f_i \delta A_t \Delta z \frac{\partial C_{bi}}{\partial t} = f_i \delta A_t U_{bi} \left[C_{bi|z} - C_{bi|z+\Delta z}\right] - (K_{be})_b f_i \delta A_t \Delta z \left[C_{bi} - C_e\right] \qquad (4.162)$$

where $f_i \delta$ is the fractional bubble hold-up of track i, or equivalently, f_i is the fraction of δ assigned to track i. Dividing by $f_i \delta A_t \Delta z$ and letting Δz tend to zero:

$$\frac{\partial C_{bi}}{\partial t} + U_{bi} \frac{\partial C_{bi}}{\partial z} + (K_{be})_b \left[C_{bi} - C_e\right] = 0 \qquad (4.163)$$

Letting $\xi = z/L_f$ and $\theta = t(\bar{U}_b/L_f)$ where $\bar{U}_b$ is the average bubble velocity for all the tracks given by $\sum_i f_i U_{bi}$:

$$\frac{\partial C_{bi}}{\partial \theta} + U_{bi}^{+} \frac{\partial C_{bi}}{\partial \xi} + X_b [C_{bi} - C_e] = 0 \qquad (4.164)$$

where U_{bi}^{+} is a dimensionless relative velocity defined as $U_{bi}/\bar{U}_b$.

A material balance on the dense phase yields:

$$\begin{bmatrix}\text{accm}\end{bmatrix} = \begin{bmatrix}\text{in-out}\\ \text{convection}\end{bmatrix} + \begin{bmatrix}\text{in-out}\\ \text{axial}\\ \text{dispersion}\end{bmatrix} + \begin{bmatrix}\text{in-out}\\ \text{interphase}\\ \text{transfer}\end{bmatrix}$$

$$\text{i.e. } (1-\delta)\varepsilon_d A_t \Delta z \frac{\partial C_e}{\partial t} = (1-\delta) A_t U_d [C_e|_z - C_e|_{z+\Delta z}]$$

$$- D_d (1-\delta)\varepsilon_d A_t \left[\frac{\partial C_e}{\partial z}\Big|_z - \frac{\partial C_e}{\partial z}\Big|_{z+\Delta z}\right] + \sum_{i=1}^{5} (K_{be})_b f_i \delta A_t \Delta z [C_{bi} - C_e] \qquad (4.165)$$

Dividing by $(1-\delta)\varepsilon_d A_t \Delta z$ and taking the limit:

$$\frac{\partial C_e}{\partial t} + \left(\frac{U_d}{\varepsilon_d}\right)\frac{\partial C_e}{\partial z} - D_d \frac{\partial^2 C_e}{\partial z^2} - \left[\frac{\delta (K_{be})_b}{(1-\delta)\varepsilon_d}\right] (\Sigma f_i C_{bi} - C_e) = 0 \qquad (4.166)$$

and introducing θ and ξ:

$$\frac{\partial C_e}{\partial \theta} + \left(\frac{U_d}{\varepsilon_d \bar{U}_b}\right) \frac{\partial C_e}{\partial \xi} - N_d \frac{\partial^2 C_e}{\partial \xi^2} - \left[\frac{\delta X_b}{(1-\delta)\varepsilon_d}\right] (\Sigma f_i C_{bi} - C_e) = 0 \qquad (4.167)$$

where N_d is the number of dense phase dispersion units defined $D_d/(\bar{U}_b L_f)$. The initial conditions are, as before,

$$C_{bi}(\xi,0) = C_e(\xi,0) = 0 \quad \text{for all } i \qquad (4.168)$$

and the B.C.'s

$$C_{bi}(0,\theta) = C_o \quad \text{for all } i \tag{4.169}$$

$$\left(\frac{U_d}{\varepsilon_d U_b}\right) C_e - N_d \frac{\partial C_e}{\partial \xi} = 0 \quad \text{at } \xi = 0, \text{ all } \theta \tag{4.170}$$

and

$$\frac{\partial C_e}{\partial \xi} = 0 \text{ at } \xi = 1, \text{ all } \theta \tag{4.71}$$

The last two boundary conditions appear to be at odds with each other, since the bottom is treated as an open system and the top as a closed one (from a dispersion point of view). There is no particular physical reason for this choice - in fact the velocity in the dense phase is so small relative to that in the bubble phase (for the system studied here) that the choice either way is of little consequence.

The solution of this model is straightforward in principle, but involves some fairly complicated algebraic manipulations. The first step is to transform the time variable, employing the initial condition given by (4.168). Equation (4.164) gives:

$$U_{bi}^{+} \frac{dC_{bi}}{d\xi} + (X_b + s) C_{bi} = X_b C_e \tag{4.172}$$

and (4.167) leads to:

$$- N_d \frac{d^2 C_e}{d\xi^2} + U_r \frac{dC_e}{d\xi} + (X_e + s) C_e = X_e \Sigma f_i C_{bi} \tag{4.173}$$

where U_r and X_e are defined as $U_d/(\varepsilon_d \bar{U}_b)$ and $\delta X_b/((1-\delta)\varepsilon_d)$ respectively.

The second step involves transforming with respect to ξ, using B.C.'s (4.169) and (4.170). Equation (4.172), in its transformed state, may be written

$$C_{bi}(\nu,s) = \frac{1 + b_i\, C_e\,(\nu,s)}{\nu + a_i} \tag{4.174}$$

where $a_i = (X_b + s)/U_{bi}^{+}$ (4.175)

and $b_i = X_b/U_{bi}^{+}$ (4.176)

Equation (4.173) leads to

$$(-N_d\nu^2 + U_r\nu + X_e + s)\, C_e - X_e \,\Sigma\, f_i\, C_{bi} = -N_d\, \nu\, C_{eo} \tag{4.177}$$

where C_{eo} is an abbreviation for $C_e(\xi = 0,s)$ and represents an unknown to be determined by applying the third B.C.

Equation (4.174) may be substituted into (4.177) to yield

$$C_e = \frac{-N_d\nu\, C_{eo} + X_e\, \Sigma\, f_i/(\nu+a_i)}{-N_d\nu^2 + U_r\nu + X_e + s - X_e\, \Sigma\, f_i\, b_i/(\nu+a_i)} \tag{4.178}$$

Several steps are omitted at this stage for brevity. It is clear, however, that (4.178) may be multiplied out to the form of a ratio of two polynomials in ν, and that C_e may be written in the form:

$$C_e = \frac{C_{eo}\nu^6 + \alpha_5 C_{eo}\nu^5 + (\alpha_4\, C_{eo} - \frac{\alpha_6\, X_e}{N_d})\nu^4 + (\alpha_3\, C_{eo} - \frac{\alpha_7\, X_e}{N_d})\nu^3}{(\nu-\lambda_1)(\nu-\lambda_2)(\nu-\lambda_3)(\nu-\lambda_4)} \cdots$$

$$\cdots \frac{+ (\alpha_2\, C_{eo} - \frac{\alpha_8\, X_e}{N_d})\nu^2 + (\alpha_1\, C_{eo} - \frac{\alpha_9\, X_e}{N_d})\nu - (\frac{\alpha_{10}\, X_e}{N_d})}{(\nu-\lambda_5)(\nu-\lambda_6)(\nu-\lambda_7)} \tag{4.179}$$

where λ_i are the roots of

$$\alpha_{16}\nu^7 + \alpha_{17}\nu^6 + \alpha_{18}\nu^5 + \alpha_{19}\nu^4 + \alpha_{20}\nu^3 + \alpha_{21}\nu^2 + \alpha_{22}\nu + \alpha_{23} = 0 \quad (4.180)$$

and the α_i terms are defined in Table 4.1. Equation (4.179) may be split into partial fractions and inverse transformed with respect to ν to give:

$$C_e(\xi,s) = C_{eo} \sum_{k=1}^{7} \left(\frac{\beta_k}{\rho_k}\right) e^{\lambda_k \xi} - \sum_{k=1}^{7} \left(\frac{\gamma_k}{\rho_k}\right) e^{\lambda_k \xi} \quad (4.181)$$

where the β_k, γ_k and ρ_k terms are also defined in Table 4.1. Differentiating (4.181) with respect to ξ and applying boundary condition (4.171) leads to:

$$C_{eo} = \sum_{k=1}^{7} \left(\frac{\gamma_k}{\rho_k}\right) \lambda_k e^{\lambda_k} \Big/ \sum_{k=1}^{7} \left(\frac{\beta_k}{\rho_k}\right) \lambda_k e^{\lambda_k} \quad (4.182)$$

With C_{eo} specified by (4.182), equation (4.181) represents a solution for $C_e(\xi,s)$. To solve for $C_{bi}(\xi,s)$, integrate (4.172) to give:

$$C_{bi} = e^{-a_i \xi} + b_i\, e^{-a_i \xi} \int_0^{\xi} C_e(\xi^1,s)\, e^{a_i \xi^1}\, d\xi^1 \quad (4.183)$$

where ξ^1 represents a dummy variable. Substitute (4.181) into (4.183) and integrate to obtain

$$C_{bi} = e^{-a_i \xi} + b_i\, e^{-a_i \xi} \left[\sum_{k=1}^{7} \frac{C_{eo}\, \beta_k - \gamma_k}{\rho_k (a_i + \gamma_k)} \left(e^{(a_i+\gamma_k)\xi} - 1\right) \right] \quad (4.184)$$

TABLE 4.1

MBT MODEL CONSTANT DEFINITIONS

$$\alpha_1 = a_1\, a_2\, a_3\, a_4\, a_5$$

$$\alpha_2 = a_1\, a_2\, a_3\, a_4 + a_1\, a_2\, a_3\, a_5 + a_1\, a_2\, a_4\, a_5 + a_1\, a_3\, a_4\, a_5 + a_2\, a_3\, a_4\, a_5$$

$$\alpha_3 = a_1\, a_2\, a_3 + a_1\, a_2\, a_4 + a_1\, a_2\, a_5 + a_1\, a_3\, a_4 + a_1\, a_3\, a_5 + a_1\, a_4\, a_5 + a_2\, a_3\, a_4 + a_2\, a_3\, a_5 + a_3\, a_4\, a_5 + a_2\, a_4\, a_5$$

$$\alpha_4 = a_1\, a_2 + a_1\, a_3 + a_1\, a_4 + a_1\, a_5 + a_2\, a_3 + a_2\, a_4 + a_2\, a_5 + a_3\, a_4 + a_3\, a_5 + a_4\, a_5$$

$$\alpha_5 = a_1 + a_2 + a_3 + a_4 + a_5$$

$$\alpha_6 = f_1 + f_2 + f_3 + f_4 + f_5 \; (= 1)$$

$$\alpha_7 = f_1\,(a_2 + a_3 + a_4 + a_5) + f_2\,(a_1 + a_3 + a_4 + a_5) + f_3\,(a_1 + a_2 + a_4 + a_5) + f_4\,(a_1 + a_2 + a_3 + a_5) + f_5\,(a_1 + a_2 + a_3 + a_4)$$

$$\begin{aligned}\alpha_8 = {} & f_1\,(a_2\, a_3 + a_2\, a_4 + a_2\, a_5 + a_3\, a_4 + a_3\, a_5 + a_4\, a_5) \\ & + f_2\,(a_1\, a_3 + a_1\, a_4 + a_1\, a_5 + a_3\, a_4 + a_3\, a_5 + a_4\, a_5) \\ & + f_3\,(a_1\, a_2 + a_1\, a_4 + a_1\, a_5 + a_2\, a_4 + a_2\, a_5 + a_4\, a_5) \\ & + f_4\,(a_1\, a_2 + a_1\, a_3 + a_1\, a_5 + a_2\, a_3 + a_2\, a_5 + a_3\, a_5) \\ & + f_5\,(a_1\, a_2 + a_1\, a_3 + a_1\, a_4 + a_2\, a_3 + a_2\, a_4 + a_3\, a_4)\end{aligned}$$

$$\begin{aligned}\alpha_9 = {} & f_1\,(a_2\, a_3\, a_4 + a_2\, a_3\, a_5 + a_2\, a_4\, a_5 + a_3\, a_4\, a_5) \\ & + f_2\,(a_1\, a_3\, a_4 + a_1\, a_3\, a_5 + a_1\, a_4\, a_5 + a_3\, a_4\, a_5) \\ & + f_3\,(a_1\, a_2\, a_4 + a_1\, a_2\, a_5 + a_1\, a_4\, a_5 + a_2\, a_4\, a_5) \\ & + f_4\,(a_1\, a_2\, a_3 + a_1\, a_2\, a_5 + a_1\, a_3\, a_5 + a_2\, a_3\, a_5) \\ & + f_5\,(a_1\, a_2\, a_3 + a_1\, a_2\, a_4 + a_1\, a_3\, a_4 + a_2\, a_3\, a_4)\end{aligned}$$

TABLE 4.1 (continued)

$$\alpha_{10} = f_1 (a_2\, a_3\, a_4\, a_5) + f_2 (a_1\, a_3\, a_4\, a_5) + f_3 (a_1\, a_2\, a_4\, a_5) + f_4 (a_1\, a_2\, a_3\, a_5) + f_5 (a_1\, a_2\, a_3\, a_4)$$

$\alpha_{11} - \alpha_{15}$ = $\alpha_6 - \alpha_{10}$ with f_i replaced by $f_i b_i$

$$\alpha_{16} = - N_D$$

$$\alpha_{17} = - \alpha_5 N_D + U_r$$

$$\alpha_{18} = - \alpha_4 N_D + \alpha_5 U_r + (X_e + s)$$

$$\alpha_{19} = - \alpha_3 N_D + \alpha_4 U_r + \alpha_5 (X_e + s) - \alpha_{11} X_e$$

$$\alpha_{20} = - \alpha_2 N_D + \alpha_3 U_r + \alpha_4 (X_e + s) - \alpha_{12} X_e$$

$$\alpha_{21} = - \alpha_1 N_D + \alpha_2 U_r + \alpha_3 (X_e + s) - \alpha_{13} X_e$$

$$\alpha_{22} = \alpha_1 U_r + \alpha_2 (X_e + s) - \alpha_{14} X_e$$

$$\alpha_{23} = \alpha_1 (X_e + s) - \alpha_{15} X_e$$

$$\beta_i = \lambda_i^6 + \alpha_5 \lambda_i^5 + \alpha_4 \lambda_i^4 + \alpha_3 \lambda_i^3 + \alpha_2 \lambda_i^2 + \alpha_1 \lambda_i \qquad (i = 1 \text{ to } 7)$$

$$\gamma_i = (\alpha_6 \lambda_i^4 + \alpha_7 \lambda_i^3 + \alpha_8 \lambda_i^2 + \alpha_9 \lambda_i + \alpha_{10}) \left(\frac{X_e}{N_D}\right) \qquad (i = 1 \text{ to } 7)$$

$$\rho_i = (\lambda_i - \lambda_1)(\lambda_i - \lambda_2)(\lambda_i - \lambda_3)(\lambda_i - \lambda_4)(\lambda_i - \lambda_5)(\lambda_i - \lambda_6)(\lambda_i - \lambda_7)$$

$(i = 1 \text{ to } 7;\ i \neq k)$

The average concentration at the probe tip is then given by:

$$\bar{C}_o = \frac{\delta \Sigma f_i C_{bi} + (1-\delta)\varepsilon_d C_e}{\delta + (1-\delta)\varepsilon_d} \qquad (4.185)$$

A FORTRAN V listing of this solution is given in Appendix B.

4.2 Sparger Model Formulation and Numerical Solution

To the best of the author's knowledge, no models describing a split feed fluidised bed system have appeared in the open literature. Both the models put forward here are considered original.

The sparger models are formulated in much the same way as the general models. The solution, however, is by finite differences in the time domain. The sparger models are not amenable to any reasonable analytical solution in the Laplace or frequency domains because of the discontinuity in model parameters at some elevation in the bed.

4.2.1 LMBP Model

The mathematical formulation of the LMBP model, shown in Figure 3.6, is identical to that for the MVD model for the upper and lower regions in isolation. The differential equation resulting from a material balance on an incremental height of the bubble phase is:

$$\frac{\partial C_b}{\partial t} + U_b \frac{\partial C_b}{\partial z} + (K_{be})_b \left[C_b - C_e\right] = 0 \qquad (4.186)$$

Now U_b and $(K_{be})_b$ change abruptly at a height L_s. If the bubble velocity in the lower region is written U_{bl} and its counterpart in the upper U_{bu}, and similarly $(K_{be})_b$ in each region is abbreviated K_l and K_u, then:

$$\frac{\partial C_b}{\partial t} + U_{bl} \frac{\partial C_b}{\partial z} + K_l \left[C_b - C_e\right] = 0 \qquad (4.187)$$

for $0 \leq z < L_s$, and

$$\frac{\partial C_b}{\partial t} + U_{bu} \frac{\partial C_b}{\partial z} + K_u \left[C_b - C_e\right] = 0 \qquad (4.188)$$

for $L_s \leq z \leq L_f$. For the dense phase:

$$\frac{\partial C_e}{\partial t} + \left(\frac{U_d}{\varepsilon_d}\right) \frac{\partial C_e}{\partial z} - \frac{\delta K_s}{(1-\delta)\varepsilon_d} \left[C_b - C_e\right] - D_d \frac{\partial^2 C_e}{\partial z^2} = 0 \qquad (4.189)$$

for $0 \leq z < L_s$ and

$$\frac{\partial C_e}{\partial t} + \left(\frac{U_d}{\varepsilon_d}\right) \frac{\partial C_e}{\partial z} - \frac{\delta K_u}{(1-\delta)\varepsilon_d} \left[C_b - C_e\right] - D_d \frac{\partial^2 C_e}{\partial z^2} = 0 \qquad (4.190)$$

for $L_s \leq z \leq L_f$. The initial condition is:

$$C_b(z,0) = C_e(z,0) = 0 \qquad (4.191)$$

and the boundary conditions:

$$C_b(0,t) = 0 \tag{4.192}$$

$$C_b(L_s,t) = C_0 \tag{4.193}$$

$$\left.\frac{\partial C_e}{\partial z}\right|_{z=0} = 0 \quad \text{for all } t \tag{4.194}$$

and $$\left.\frac{\partial C_e}{\partial z}\right|_{z=L_f} = 0 \text{ for all } t \tag{4.195}$$

These equations are solved directly by a Crank-Nicholson finite difference technique as described by Carnahan, Luther and Wilkes (100). In essence, this method involves describing the partial derivatives of a function f(x,y) on a grid with spacings Δx and Δy at a point $(x, y + \frac{1}{2}\Delta y)$ by:

$$\frac{\partial f}{\partial x} \doteq \frac{f(x+\Delta x,y) - f(x-\Delta x,y)}{4\ \Delta x} + \frac{f(x+\Delta x,y+\Delta y) - f(x-\Delta x,y+\Delta y)}{4\ \Delta x} \tag{4.196}$$

and $$\frac{\partial f}{\partial y} \doteq \frac{f(x,y+\Delta y) - f(x,y)}{\Delta y} \tag{4.197}$$

This method is correct to second order differences in both independent variables, and the implicit computational procedure thus defined displays stability characteristics far superior to those of the related explicit procedures (101). The implicit procedure requires the solution of an MxM matrix in x for each

Δy increment, where M is the number of x-nodes. This matrix appears in tridiagonal form, however, and may be efficiently solved by the application of a suitable recursion formula (100).

Equation (4.187), in finite difference form, becomes:

$$\frac{C_{b\ i,n+1} - C_{b\ i,n}}{\Delta t} + U_b \frac{C_{b\ i+1,n+1} - C_{b\ i-1,n+1} + C_{b\ i+1,n} - C_{b\ i-1,n}}{4\ \Delta z}$$

$$+ K_1 \left[\frac{C_{b\ i,n+1} + C_{b\ i,n}}{2} - C_{e\ i,n}\right] = 0 \qquad (4.198)$$

and on rearrangement:

$$\left(\frac{U_{b1}\ \Delta t}{4\ \Delta z}\right) C_{b\ i+1,n+1} + \left(1 + \frac{\Delta t\ K_1}{2}\right) C_{b\ i,n+1} - \left(\frac{U_{b1}\ \Delta t}{4\ \Delta z}\right) C_{b\ i-1,n+1}$$

$$= -\left(\frac{U_{b1}\ \Delta t}{4\ \Delta z}\right) C_{b\ i+1,n} + \left(1 - \frac{\Delta t\ K_1}{2}\right) C_{b\ i,n} + \left(\frac{U_{b1}\ \Delta t}{4\ \Delta z}\right) C_{b\ i-1,n} \qquad (4.199)$$

where the subscript i refers to the number of Δz increments and n to Δt increments. Equation (4.188) may be written:

$$\left(\frac{U_{bu}\ \Delta t}{4\ \Delta z}\right) C_{b\ i+1,n+1} + \left(1 + \frac{\Delta t\ K_u}{2}\right) C_{b\ i,n+1} - \left(\frac{U_{bu}\ \Delta t}{4\ \Delta z}\right) C_{b\ i-1,n+1}$$

$$= -\left(\frac{U_{bu}\ \Delta t}{4\ \Delta z}\right) C_{b\ i+1,n} + \left(1 - \frac{\Delta t\ K_u}{2}\right) C_{b\ i,n} + \left(\frac{U_{bu}\ \Delta t}{4\ \Delta z}\right) C_{b\ i-1,n} \qquad (4.200)$$

Equation (4.189) becomes:

$$\frac{C_{e\ i,n+1} - C_{e\ i,n}}{\Delta t} + \left(\frac{U_d}{\varepsilon_d}\right) \frac{C_{e\ i+1,n+1} - C_{e\ i-1,n+1} + C_{e\ i+1,n} - C_{e\ i-1,n}}{4\ \Delta z}$$

$$- \frac{\delta K_1}{(1-\delta)\varepsilon_d} \left[C_{b\ i,n} - \frac{C_{e\ i,n+1} - C_{e\ i,n}}{2}\right]$$

$$- D_d \frac{C_{e\ i+1,n+1} - 2\ C_{e\ i,n+1} + C_{e\ i-1,n+1} + C_{e\ i+1,n} - 2\ C_{e\ i,n} + C_{e\ i-1,}}{2(\Delta z)^2}$$

(4.201)

and may be rearranged to:

$$\left(\frac{U_d\ \Delta t}{\varepsilon_d\ 4\Delta z} - \frac{D_d\ \Delta t}{2\ \Delta z^2}\right) C_{e\ i+1,n+1} + \left(1 + \frac{\delta K_1\ \Delta t}{(1-\delta)\varepsilon_d 2} + \frac{D_d\ \Delta t}{\Delta z^2}\right) C_{e\ i,n+1}$$

$$+ \left(-\frac{U_d\ \Delta t}{\varepsilon_d\ 4\Delta z} - \frac{D_d\ \Delta t}{2\Delta z^2}\right) C_{e\ i-1,n+1}$$

$$= \left(-\frac{U_d\ \Delta t}{\varepsilon_d\ 4\Delta z} + \frac{D_d\ \Delta t}{2\Delta z^2}\right) C_{e\ i+1,n} + \left(1 - \frac{\delta K_1\ \Delta t}{(1-\delta)\varepsilon_d 2} - \frac{D_d\ \Delta t}{\Delta z^2}\right) C_{e\ i,n}$$

$$+ \left(\frac{U_d\ \Delta t}{\varepsilon_d\ 4\Delta z} + \frac{D_d\ \Delta t}{2\ \Delta z^2}\right) C_{e\ i-1,n} + \frac{\delta K_1\ \Delta t}{(1-\delta)\varepsilon_d} C_{b\ i,n} \qquad (4.202)$$

Equation (4.190) may be written in the same form, with K_u replacing K_1. The node boundaries are accounted for as follows:

(i) At the node corresponding to z=0, C_b is constrained to be zero at all times. C_e is accounted for by creating an artificial node at $(-\Delta z)$, and letting $C_{e\ -1,n} = C_{e\ 1,n}$. This is effectively an application of B.C. (4.194).

(ii) At the top of the bed, i.e. $M\Delta z = L_f$, a backward difference on the interval (M-1,M) is used for C_b. An artificial node is created at (M+1), and $C_{e\ M+1,n} = C_{e\ M-1,n}$ as required by (4.195).

At the node corresponding to L_s, C_b is constrained to:

$$C_b(L_s,t) = C_0(t) \tag{4.203}$$

A FORTRAN V listing of the solution is given in Appendix B.

4.2.1.1 Numerical Solution Details

In the early stages of the development of numerical solutions such as the one presented here, the models were excited (numerically) by a very sharp stimulus function $C_0(t)$. The response to such an input displayed damped oscillations, which according to Bettencourt et. al. (102), are typical of most finite difference procedures. Decreasing the sharpness of the exciting function was found to stabilise the numerical response, though excessive flattening of this function would clearly lead to a loss of resolution in the parameter estimation procedure. A suitable compromise for $C_0(t)$ was found to be:

$$C_0(t) = t^4 \exp(-20\ t/\tau_p)$$

where t is time in seconds and τ_p represents the lumped process time constant. This represents an ideal impulse convolved with

four perfectly mixed stages in series, each with a time constant of 1/20 th of that of the process. With this input, a reasonable number of time and distance increments (200 x 100 respectively) was found to produce a smooth frequency response to frequencies significantly higher than those obtainable from the experimental apparatus. An investigation into the influence of the magnitudes of Δt and Δz showed that the model response is relatively insensitive to increases in the number of nodes beyond about 100 Δt's by 50 Δz's.

A problem associated with the truncation of the (time-domain) response at some finite time and the actual numerical trans= formation into the frequency domain will not be described in this section. The experimental data and the time-domain model response are equivalent from a transformation point of view, and the procedures developed for this manipulation are described in the context of experimental data processing in section 4.3.

4.2.2 Laterally Segregated Bubble-Phase Model

A material balance over a height increment of either bubble phase yields results similar to that for the MVD model. For the grid bubbles:

$$\frac{\partial C_{bg}}{\partial t} + U_{bg} \frac{\partial C_{bg}}{\partial z} + K_{gl} \left[C_{bg} - C_e\right] = 0 \qquad (4.205)$$

for $0 \leq z < L_s$, and

$$\frac{\partial C_{bg}}{\partial t} + U_{bg} \frac{\partial C_{bg}}{\partial z} + K_{gu} [C_{bg} - C_e] = 0 \qquad (4.206)$$

for $L_s \leq z \leq L_f$. The subscript g refers to bubbles originating from the grid. For bubbles from the sparger:

$$\frac{\partial C_{bs}}{\partial t} + U_{bs} \frac{\partial C_{bs}}{\partial z} + K_s [C_{bs} - C_e] = 0 \qquad (4.207)$$

The dense phase material balance is formulated thus:

$$\begin{bmatrix} \text{accm} \end{bmatrix} = \begin{bmatrix} \text{in-out} \\ \text{convection} \end{bmatrix} + \begin{bmatrix} \text{net gain} \\ \text{from grid} \\ \text{bubbles} \end{bmatrix} + \begin{bmatrix} \text{net gain} \\ \text{from sparger} \\ \text{bubbles} \end{bmatrix}$$

$$+ \begin{bmatrix} \text{in-out} \\ \text{by axial} \\ \text{dispersion} \end{bmatrix}$$

$$\text{i.e. } (1-\delta)\varepsilon_d A_t \frac{\partial C_e}{\partial t} = (1-\delta) A_t U_d [C_{e|z} - C_{e|z+\Delta z}]$$

$$+ K_{gk} f_{gk} \delta A_t \Delta z [C_{bg} - C_e] + K_s f_s \delta A_t \Delta z [C_{bs} - C_e]$$

$$- D_d (1-\delta)\varepsilon_d A_t \left[\frac{\partial C_e}{\partial z}\bigg|_z - \frac{\partial C_e}{\partial z}\bigg|_{z+\Delta z}\right] \qquad (4.208)$$

where f_s and f_g are fractions of the total bubble holup assigned to the sparger and grid bubbles respectively, and the subscrip k represents l below the sparger and u above. Below the sparger f_s is zero. Dividing by $(1-\delta)\varepsilon_d \Delta z$ and letting Δz tend to zero:

$$\frac{\partial C_e}{\partial t} + \left(\frac{U_d}{\varepsilon_d}\right) \frac{\partial C_e}{\partial z} - D_d \frac{\partial^2 C_e}{\partial z^2} + \frac{\delta \left(f_s K_s + f_{gk} K_{gk}\right)}{(1-\delta)\varepsilon_d} C_e$$

$$= \frac{\delta}{(1-\delta)\varepsilon_d} \left[f_s K_s C_{bs} + f_{gk} K_{gk} C_{bg}\right] \qquad (4.209)$$

The finite difference form of (4.205) is:

$$\left(\frac{U_{bg}\,\Delta t}{4\Delta z}\right) C_{bg\ i+1,n+1} + \left(1 + \frac{K_{gl}\,\Delta t}{2}\right) C_{bg\ i,n+1} - \left(\frac{U_{bg}\,\Delta t}{4\Delta z}\right) C_{bg\ i-1,n+1}$$

$$= -\left(\frac{U_{bg}\,\Delta t}{4\Delta z}\right) C_{bg\ i+1,n} + \left(1 - \frac{K_{gl}\,\Delta t}{2}\right) C_{bg\ i,n} + \left(\frac{U_{bg}\,\Delta t}{4\Delta z}\right) C_{bg\ i-1,n}$$

$$+ K_{gl}\,\Delta t\, C_{e\ i,n} \qquad (4.210)$$

Equation (4.206) and (4.207) may be written in the same form, with the appropriate subscripts. The finite difference version of (4.209) is:

$$\left(\frac{U_d\,\Delta t}{\varepsilon_d\,4\Delta z} - \frac{D_d\,\Delta t}{2\Delta z^2}\right) C_{e\ i+1,n+1} + \left(1 + \frac{D_d\,\Delta t}{\Delta z^2} + \frac{\delta \Delta t \left(f_s K_s + f_{gk} K_{gk}\right)}{2(1-\delta)\varepsilon_d}\right) C_{e\ i,n+1}$$

$$+ \left(-\frac{U_d\,\Delta t}{\varepsilon_d\,4\Delta z} - \frac{D_d\,\Delta t}{2\Delta z^2}\right) C_{e\ i-1,n+1}$$

$$= \left(-\frac{U_d\,\Delta t}{\varepsilon_d\,4\Delta z} + \frac{D_d\,\Delta t}{2\Delta z^2}\right) C_{e\ i+1,n} + \left(1 - \frac{D_d\,\Delta t}{\Delta z^2} - \frac{\delta \Delta t (f_s K_s + f_{gk} K_{gk})}{2(1-\delta)\varepsilon_d}\right) C_{e\ i,n}$$

$$+ \left(\frac{U_d\,\Delta t}{\varepsilon_d\,4\Delta z} + \frac{D_d\,\Delta t}{2\Delta z^2}\right) C_{e\ i-1,n} + \frac{\delta\,\Delta t}{(1-\delta)\varepsilon_d} \left(f_{gk} K_{gk} C_{bg\ i,n} + f_s K_s C_{bs\ i,n}\right) \qquad (4.211)$$

The initial condition is:

$$C_{bg}(z,0) = C_{bs}(z,0) = C_e(z,0) = 0 \tag{4.212}$$

and the boundary conditions:

$$C_{bg}(0,t) = 0 \tag{4.213}$$

$$C_{bs}(L_s,t) = C_0(t) \tag{4.214}$$

$$\left.\frac{\partial C_e}{\partial z}\right|_{z=0} = 0 \text{ for all } t \tag{4.215}$$

$$\left.\frac{\partial C_e}{\partial z}\right|_{z=L_f} = 0 \text{ for all } t \tag{4.216}$$

The node boundaries are accounted for as follows:

(i) At $z = 0$, C_b is constrained to be zero at all times. Boundary condition (4.215) is accounted for by letting $C_{e\ -1,n} = C_{e\ 1,n}$.

(ii) At $z = L_f$, backward differences are used on (M-1,M) for C_{bg} and C_{bs}. B.C. (4.216) is accounted for by letting $C_{e\ M-1,n} = C_{e\ M+1,n}$.

(iii) At $z = L_s$, C_{bs} is constrained to be equal to $C_0(t)$.

The discussion on the shape of the exciting function and numerical stability of the response in the preceeding section applies equally well to this model, and a FORTRAN V listing of the solution is given in Appendix B.

4.3 Data Processing and Information Flow

In this section the processing of experimental data to frequency response form is described, and the method of comparison and parameter optimisation is discussed.

An overall information flow diagram is given as Figure 4.1. A dynamic stimulus is applied to the actual fluidised bed, and this stimulus, together with the system response, is processed by a Fourier transform (FT) routine to yield the experimental transfer function $G_e(jw)$. (It is understood that both the stimulus and the response are such that the form of the FT given by equation (4.5) is valid). The model frequency response is generated either directly (as in section 4.1) or indirectly as shown in Figure 4.1, depending on whether the model has been solved in the frequency or time domains. The model transfer function $G_m(jw)$ is subsequently compared to $G_e(jw)$, and the model parameters are changed and $G_m(jw)$ re-evaluated until the greatest possible degree of closure has been obtained.

The rest of this section is taken up with a discussion of the Fourier transform routine and a brief description of the parameter

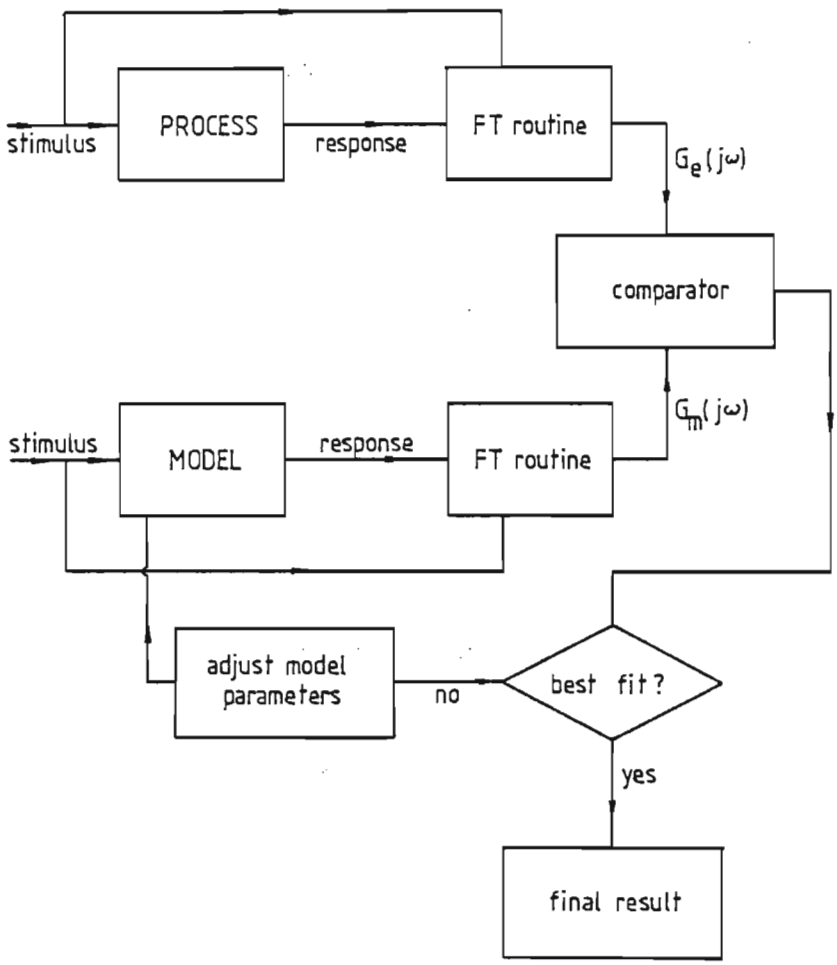

FIGURE 4.1 INFORMATION FLOW STRATEGY

adjustment strategy. This pair of data processing steps essentially completes the software development matrix.

4.3.1 Fourier Transform Routine

It is well known that highly efficient numerical Fourier Transform routines are available commercially. None was immediately accessible to the author at the time of this investigation, however, and it was decided to develop an FT routine as applied to this problem from first principles.

The development details and a listing of the routine are given in Appendix C. The main features incorporated to minimise information loss in the face of numerical integration (to infinity) are:

(i) Integration is performed by an overlapping double application of Simpson's rule.

(ii) An analytical decay tail is fitted to the last 20% of the data. The integration is extended to infinity on this basis.

Appendix C also includes the results of a test against a simple tanks-in-series model, and this routine is shown to perform well even at frequencies significantly higher than those obtainable from the experimental apparatus.

4.3.2 Parameter Optimisation Routine

The parameter adjustment strategy is based on the Nelder and Mead (103) sequencial search algorithm. The procedure involves the minimisation a function of n variables by comparison of function values at the (n+1) vertices of a general simplex. This simplex adapts to local landscape and contracts on the final minimum. The overall procedure has been shown (103) to be effective and computationally compact.

The objective function to be minimised is set up as follows:

$$\phi = \sum_{w} (\text{Re}\,[G_e(jw)] - \text{Re}\,[G_m(jw)])^2 + \sum_{w} (\text{Im}[G_e(jw)] - \text{Im}[G_m(jw)])^2 \qquad (4.217)$$

where Re and Im specify real and imaginary components respectively. This formulation is consistent with least squares in the time domain, as required by equation (4.7).

Listings of the sequencial search routine and the objective function subroutine are given in Appendix D. A listing of the main driving program is included for completeness.

CHAPTER 5

EXPERIMENTAL APPARATUS, PROCEDURE AND STRATEGY

5.1 Description of the Fluidised Beds

Two transparent cylindrical cold models were used, with internal diameters 0.05 m and 0.64 m. The small column was studied essentially as a reference point, since the pilot plant reactors at Sasol on which abundant synthesis information was available were of a similar dimension. An additional column with diameter 0.14 m was also available, though this was used only for various validation procedures and will not be described in any detail. The fluidising medium in all cases was air and the powder finely divided iron oxide.

5.1.1 0.05 m Cold Model

The small unit consisted of a 6.70 m high glass tube with an internal diameter of 0.05 m (2") as shown in Figure 5.1. The gas distributor was a porous metal plate with linear pressure drop vs gas velocity characteristics, and the plenum chamber was filled with 6 mm glass beads to reduce dead volume. Pressure taps were distributed along the side of the rig as shown in Figure 5.1, and these were connected to a bank of Hg-manometers. Pipe-cleaners were inserted into the pressure points to keep the pressure lines free of solids. Exhaust gas passed through an absolute filter to atmosphere, and this filter was periodically blown back to return any accumulated fines to the bed. Ports for the introduction of gas sampling probes were included at five levels in the glass column and in the plenum chamber as shown.

5.1.2 0.64 m Cold Model

The larger of the cold models was 6.14 m in height and had an internal diameter of 0.64 m. It was built up of six perspex sections

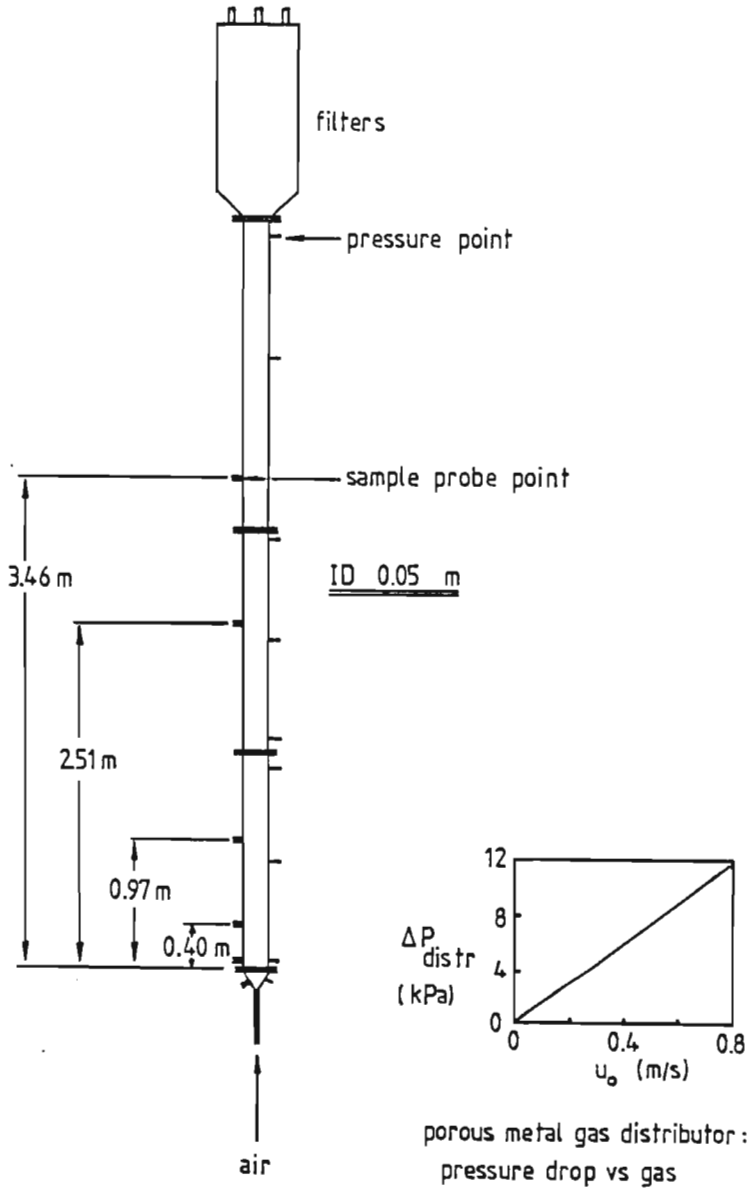

FIGURE 5.1 0.05 m COLD MODEL

as shown in Figure 5.2. The gas distributor consisted of a multi-orifice plate, the exact details of which are withheld for proprietary reasons. The plenum chamber was filled, as far as possible, with plastic bottles to decrease dead volume. Pairs of dummy vertical coils could be inserted to reduce the hydraulic diameter of the system, and a gas sparger could be introduced between the bottom of the coil bank and the main gas distributor. The exact details of the coils and the sparger are withheld for proprietary reasons.

Exhaust gas passed through a single-stage cyclone and the overhead gas was filtered and exhausted to atmosphere. Fines from the filter were periodically returned to the bed. The cyclone underflow was discharged near the bottom of the bed from a 0.05 m dipleg terminating in a flapper valve arrangement. Pressure taps were distributed as shown in Figure 5.2, and pressures were measured by Hg manometers as before. The pressure points extended about 0.1 m into the bed to avoid any anomolous wall backflow effects. Ports for gas sampling probes were included at five locations on the column and in the plenum chamber.

5.1.3 Air Supply and Metering System

Supply air was received at about 550 kPa (abs) and entered the fluidised beds at between 100 and 150 kPa (abs), depending on the powder charge. (Note that atmospheric pressure in Sasolburg is

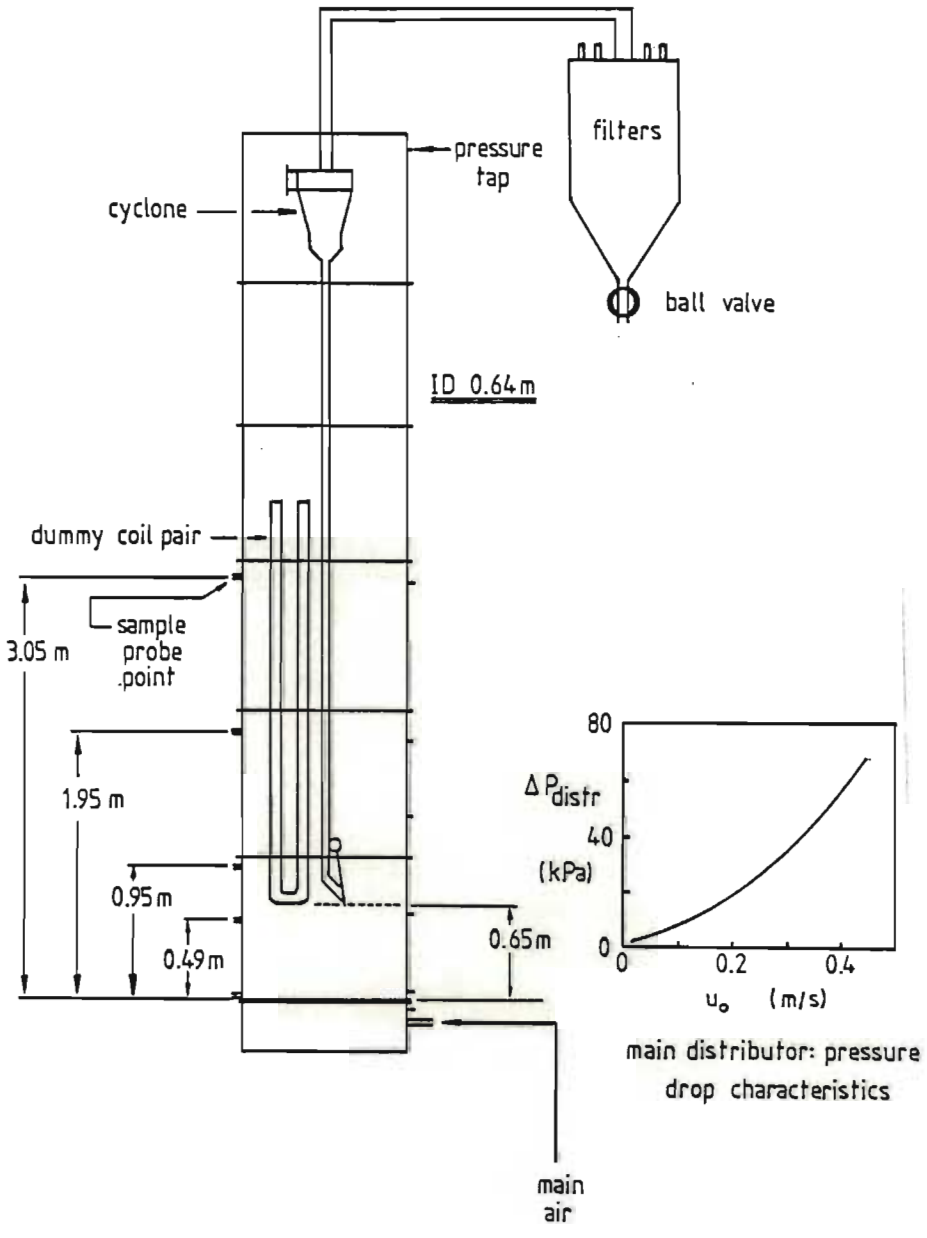

FIGURE 5.2 0.64m COLD MODEL

only about 86 kPa (abs)). Air received at 550 kPa was water-saturated at this pressure - the humidity level of the air in the fluidised beds was correspondingly lower and approximately constant.

The gas metering system consisted of a standard orifice and differential pressure (DP) cell arrangement. Frequent calibrations were carried out to guard against zero and range errors in the latter, and several different orifice sizes were employed to cover the wide range of flows required. For the smaller of the cold models orifice metering was found to be unsatisfactory at low velocities - a bellows-type gas meter measuring the exhaust from the filters was used instead.

The pressure drop across the bed means that the superficial gas velocity actually varies from the bottom to the top. In all cases an average superficial velocity was calculated on the basis of pressure at half the bed height, and it is this average U_o that is quoted throughout the text.

5.1.4 Powder Characterisation

The powder was finely ground iron oxide. This material had a negligible porosity and a particle density of 5190 kg/m^3 as determined by xylene displacement. The volume mean particle size, as measured by a technique involving low-angle forward scattering of light from a laser source (104), came to 40 μ.

Minimum fluidisation velocity for this material was determined by plotting bed pressure drop against gas velocity on logarithmic co-ordinates. This plot is shown in Figure 5.3 (for decreasing velocity), and U_{mf} was found to be about 0.0025 m/s.

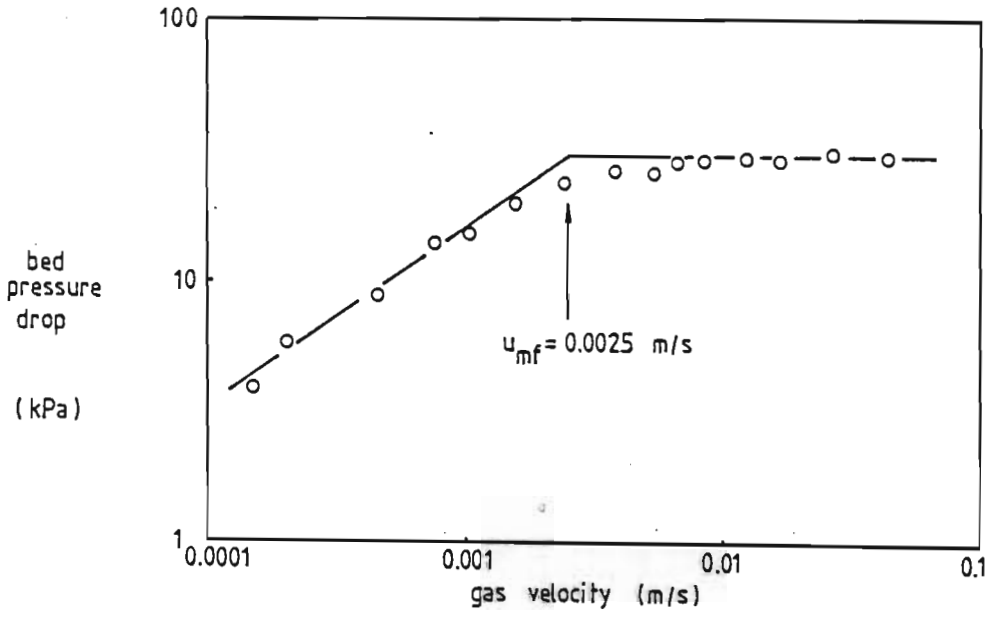

FIGURE 5.3 MINIMUM FLUIDISATION PLOT

5.2 The Development of RTD Hardware

5.2.1 Tracer Gas Type and Detection

A rapid, continuous tracer detection system was deemed necessary for this study. A flame ionisation detector (FID) was selected - this technique involves the combustion of sample and carrier gas streams in a hydrogen flame. The electrical conductivity of this flame gives an indication of the amount of combustible material present, and this system is accordingly limited to the use of combustible tracers such as hydrocarbons. The possibility of tracer adsorption on the solid particles exists, and the detection system is an atmospheric one. A pressure somewhat above ambient in the column is therefore required to provide a driving force for sampling, and pressure fluctuations associated with bubble movement are expected to show up as noise in the FID signal.

It was decided that both the process input and output signals should be measured to avoid any assumption on the exact form of the input. A pair of Varian 1400 gas chromatographs were obtained and adapted for direct use of the flame ionisation detectors.

The tracer gas selected was methane. This hydrocarbon was considered least likely to adsorb, and tests were carried out to establish the suitability or otherwise of this gas as a tracer. Adsorption tests over two grades of powder were conducted with

helium as a reference gas. The powders were neat iron oxide and iron oxide mixed with finely ground carbon (to simulate catalyst ageing), and the adsorption results are shown in Figures 5.4 and 5.5 respectively. It is clear that methane adsorbs strongly in the presence of carbon, but does not adsorb on the neat iron oxide powder.

5.2.2 Sampling System

The physical setup of the process and the two continuous gas sampling systems is shown in Figure 5.6. Also shown is an interpretation of the steps involved in terms of transfer functions. The output signals $Y_1(s)$ and $Y_2(s)$ are observable, while the overall aim is to measure the process transfer function $G_p(s)$. According to the rules of block diagram algebra:

$$Y_1(s) = G_{1s}(s)\ X\ (s) \qquad (5.1)$$

and

$$Y_2(s) = G_p(s)\ G_{us}(s)\ X\ (s) \qquad (5.2)$$

Solving for $G_p(s)$ in terms of $Y_1(s)$ and $Y_2(s)$ leads to:

$$G_p(s) = \frac{Y_2(s)\ .\ G_{1s}(s)}{Y_1(s)\ .\ G_{us}(s)} \qquad (5.3)$$

In other words, $G_p(s)$ can only be extracted from $Y_1(s)$ and $Y_2(s)$ if the upper and lower system transfer functions $G_{us}(s)$ and $G_{1s}(s)$ are known or equal. The dynamics of the sampling systems should be as fast and well balanced as possible to maximise

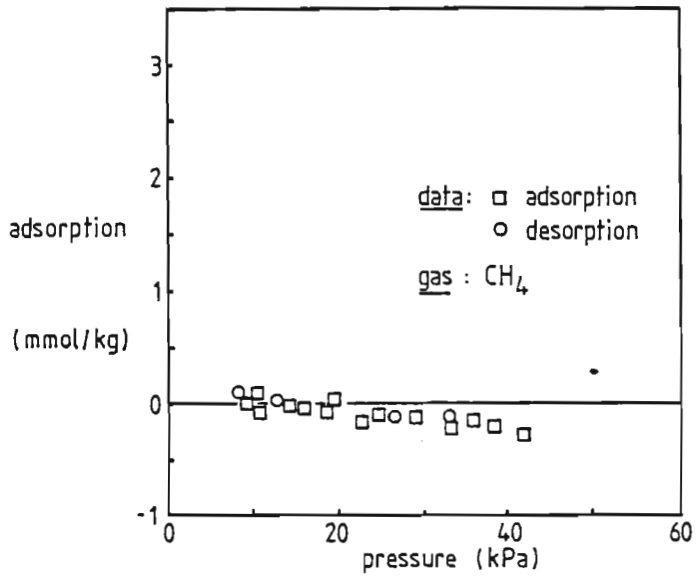

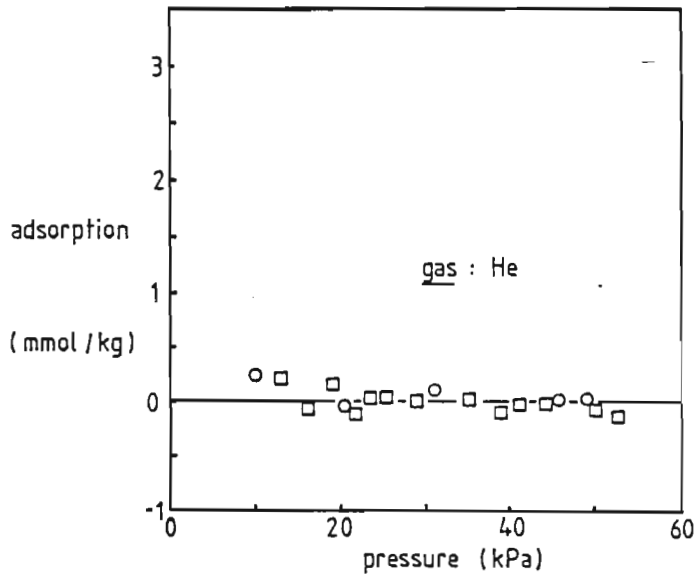

FIGURE 5.4 ADSORPTION ON NEAT IRON OXIDE

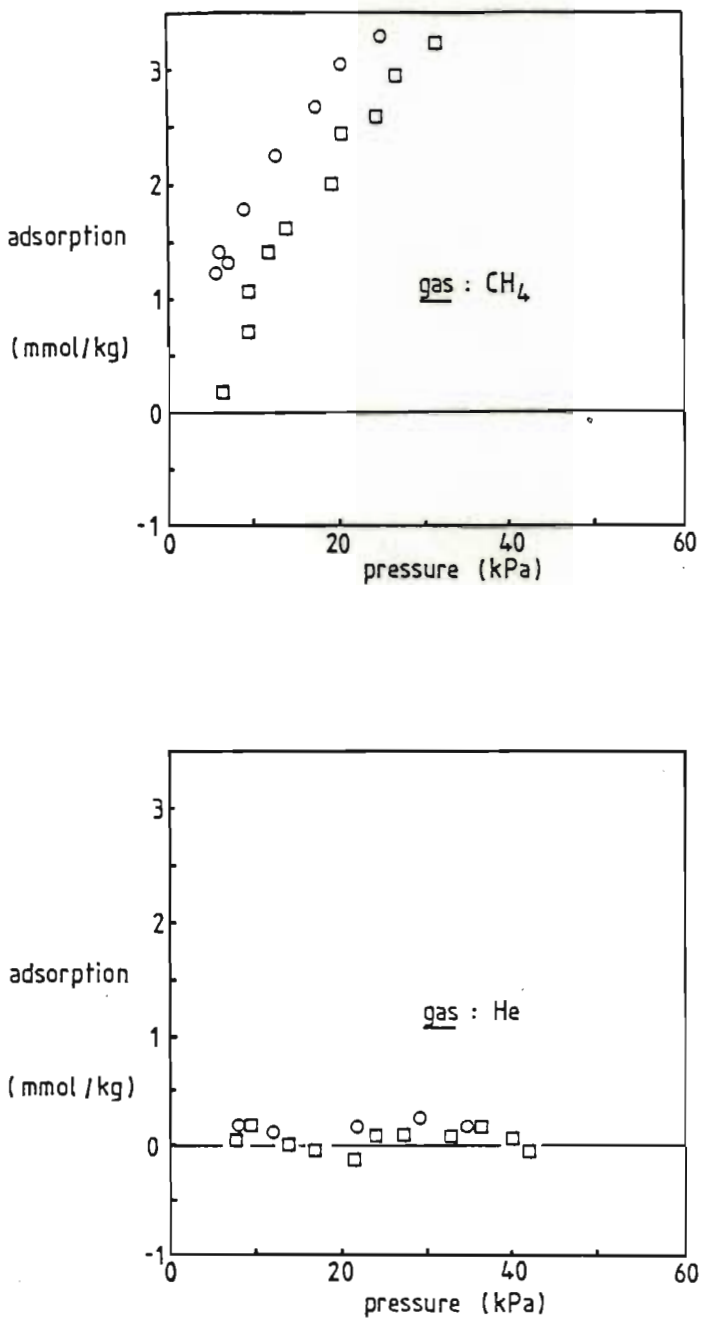

FIGURE 5.5 ADSORPTION ON IRON OXIDE MIXED WITH CARBON

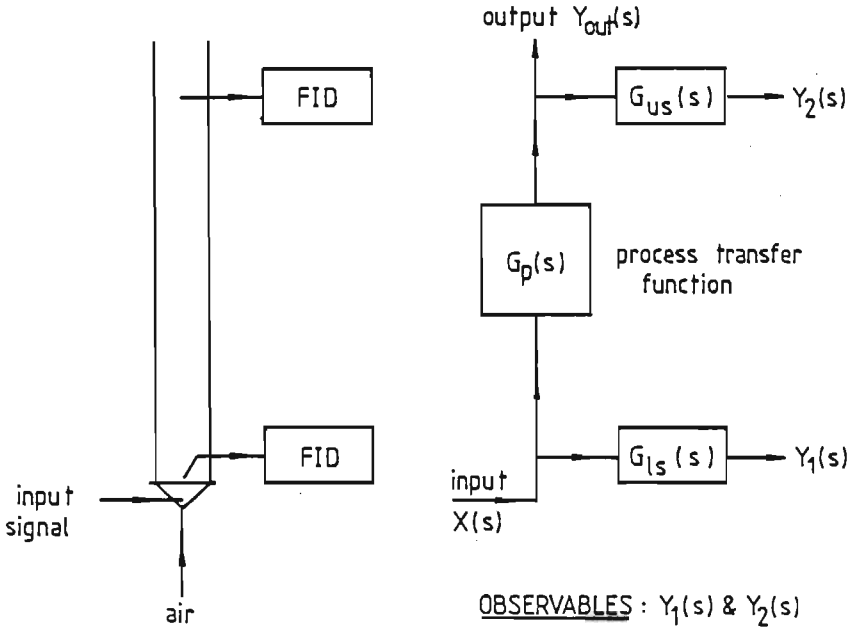

FIGURE 5.6 SAMPLING CONFIGURATION

the resolution of $G_p(s)$. In order to achieve this, the gas sampling lines were designed to minimise time-lag and signal dispersion. These lines were made as short and obstruction-free as possible, containing one-eighth inch valves for flow control only. A minimum length of about 0.4 m was dictated by the geometry of the beds and the FID units themselves, and one-sixteenth inch tubing with an ID of 0.51 mm was used.

The sample lines were flared at the sample points, and short pipe-cleaners were inserted to keep the lines and FID units free of solids. Suction velocities were dependent on the pressure in the bed, and were generally in the range 1.5-2.0 m/s.

The dynamics of the sampling system in both cases was accounted for by on-line calibration. A methane pulse point was introduced immediately adjacent to the sample suction point as shown in Figure 5.7. A differential pressure of about 60 kPa was allowed to build up across the solenoid valve, and the solenoid switch then opened and closed in rapid succession. The FID signal was recorded on a strip chart, and the dead and rise times read off. Repeated tests showed that the dead and rise times of the recorded signal were essentially independent of the solenoid pressure differential beyond about 5 kPa - it was concluded that the tracer signal appears at the sample point virtually the instant the solenoid is energised, and that the observed dead and rise time characteristics are essentially those of the sampling system alone.

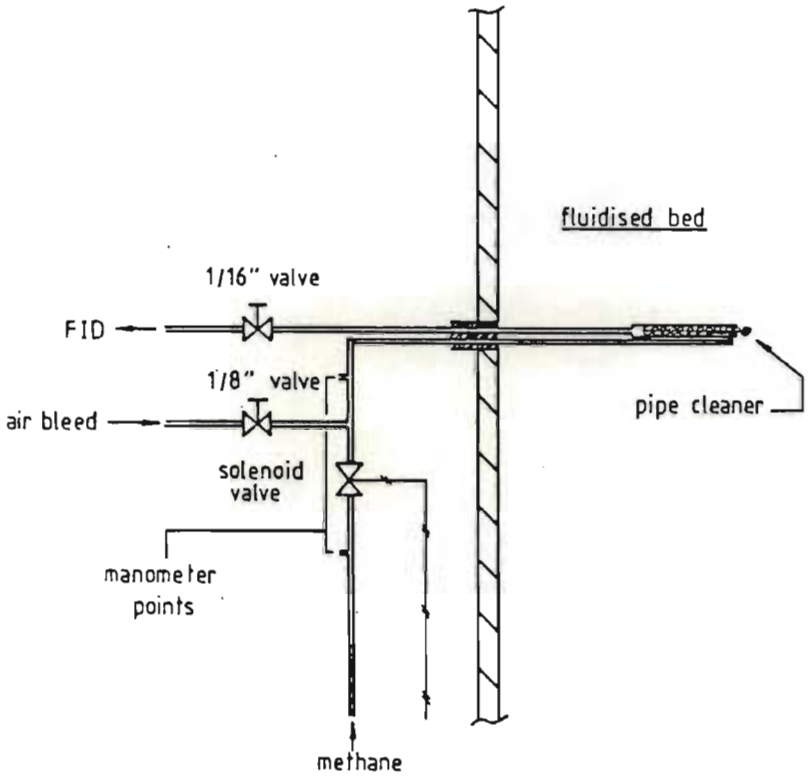

FIGURE 5.7 METHANE PULSE POINT

5.2.3 Calibration and System Validation

The FID output voltage vs methane concentration characteris= tics were tested by blending a constant, measured bleed of methane into the air supply below the grid. Linear responses were obtained for methane concentrations below about 1% (by volume) over a fairly wide range of sample flows - this type of test was repeated periodically to ensure that the operating point remained in the linear response region.

Linearity in the tracer detection system greatly simplifies the data capture sequence. The absolute magnitude of the response of a linear system is of no consequence as far as RTD studies are concerned, and in this case the electronic signals could be arbitrarily amplified or attenuated to acceptable levels for recording.

The tracer detection system and the sample line calibration procedure was tested by measuring impulse transmission velocities in an empty tube. The hardware configuration is shown in Figure 5.8, and the procedure involved first calibrating both sample lines in terms of dead and rise times as discussed previously. The lower solenoid was then opened and closed rapidly, and the relay configured to switch the chart recorder on the instant the solenoid was energised. The peak-to-peak transmission time t_{pp} was read off the chart trace as shown, and a transmission velocity computed by dividing the vertical separation by the

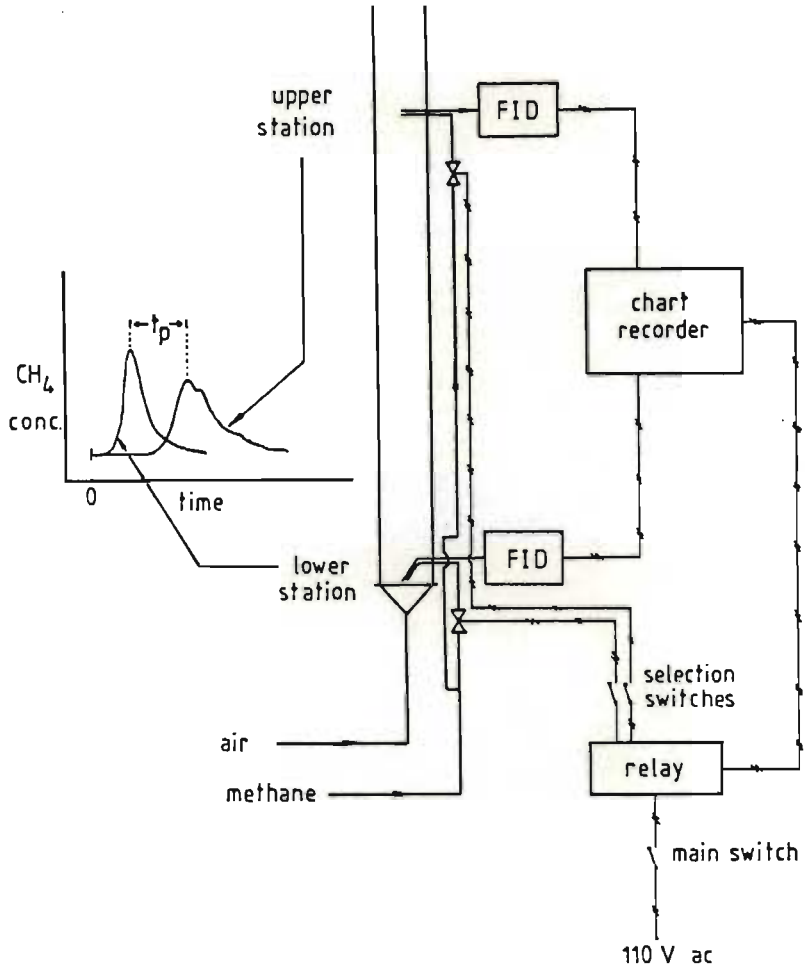

FIGURE 5.8 IMPULSE TRANSMISSION-TIME CONFIGURATION

corrected transmission time. This corrected transmission time was calculated as follows:

$$\Delta t_{pp}(corr) = \Delta t_{pp}(uncorr) + \left[(t_d + t_r)_{\substack{lower \\ station}} - (t_d + t_r)_{\substack{upper \\ station}} \right] \quad (5.4)$$

where the subscripts d and r refer to dead and rise times respectively. The results of a series of such transmission velocity tests are shown in Figure 5.9. A radial profile effect in the empty 0.14 m tube is evident - this is not surprising, since the flow regime is transitional between laminar and turbulent over the range of superficial velocities covered. In any event, it is clear that the calibration and data interpretation procedures are essentially correct in that no significant time-lags remain unaccounted for.

5.2.4 Choice of a Tracer Testing Technique

Preliminary experiments in beds containing the iron oxide powder revealed the presence of significant process noise: a typical response to an impulse supplied below the grid is shown in Figure 5.10. The RTD function as measured here is clearly stochastic in nature; the noise is probably a result of bubble motion and associated pressure fluctuations as reflected in gas flow to the FID units. Single impulse and step-change tests would probably be of little direct use, and the alternative is to employ a statistical technique for RTD estimation. An averaged

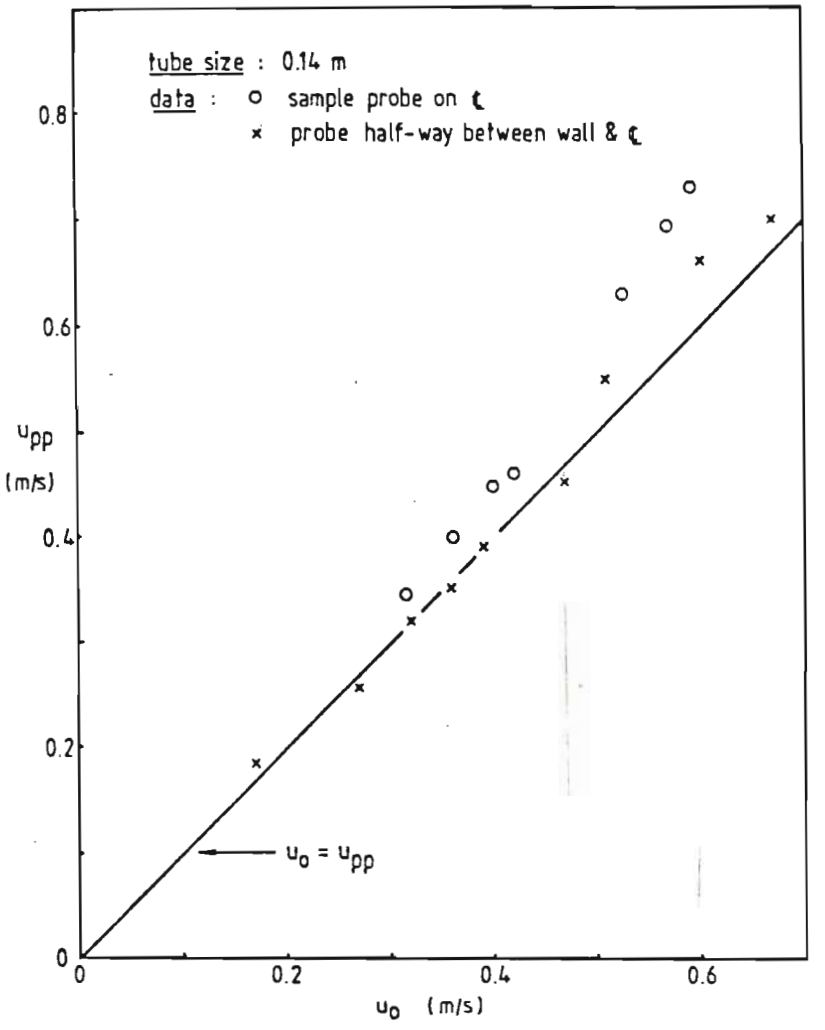

FIGURE 5.9 PULSE TRANSMISSION VELOCITY

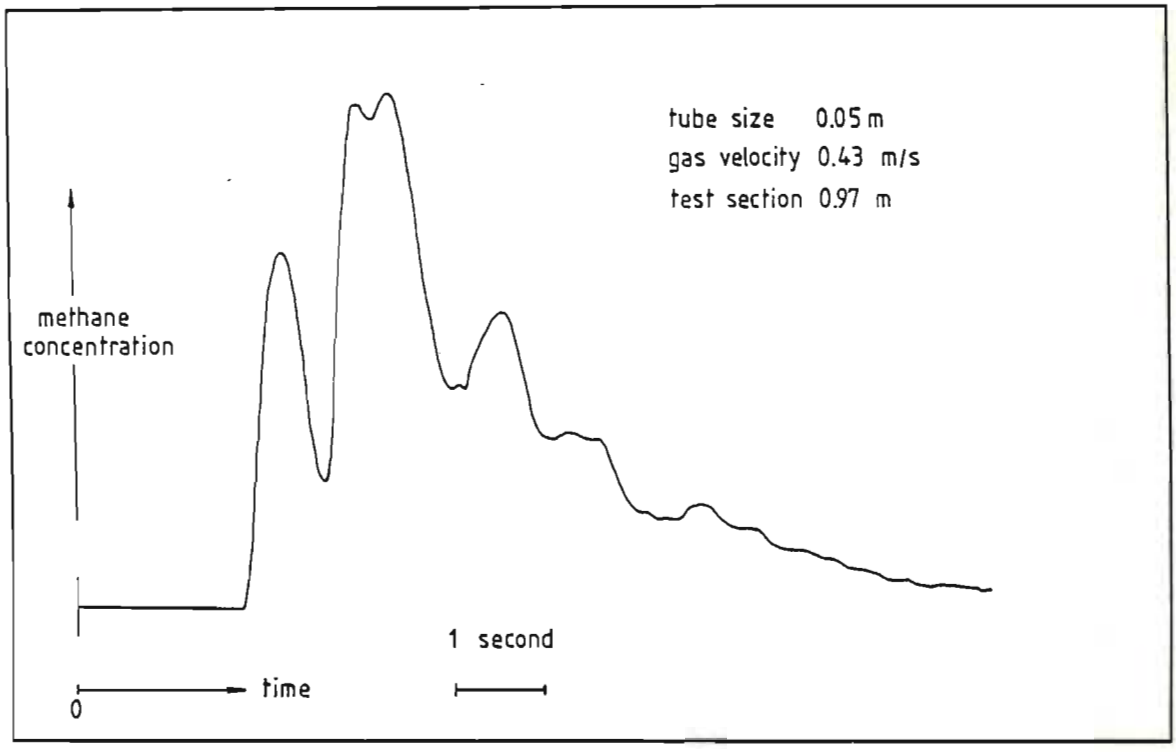

FIGURE 5.10 A TYPICAL NOISE-CORRUPTED IMPULSE RESPONSE

residence time function is required for comparison with model predictions, and noise removal should be inherent in whatever technique is applied.

A correlation technique was selected. This method consists of exciting the system with a random test signal, and forming the crosscorrelation function between the two observed signals. The autocorrelation of the lower sample station signal is also formed, and the two correlation functions are processed to the form of a system frequency response.

Consider a stationary random variable $Y_1(t)$. The autocorrelation function $r_{Y_1Y_1}(\tau)$ characterises the dependence of $Y_1(t)$ on $Y_1(t+\tau)$, and may be written:

$$r_{Y_1Y_1}(\tau) = \mathcal{E}\{Y_1(t)\ Y_1(t+\tau)\} \tag{5.5}$$

where $\mathcal{E}$ denotes ensemble expectation. The autocorrelation may be estimated from a sampled data time record as follows:

$$R_{Y_1Y_1}(\tau) = \frac{1}{n} \sum_{k=1}^{n} \{Y_1(t_k)\ Y_1(t_k + \tau)\} \tag{5.6}$$

Similarly, the dependence of $Y_1(t)$ on $Y_2(t+\tau)$ may be estimated from:

$$R_{Y_1Y_2}(\tau) = \frac{1}{n} \sum_{k=1}^{n} \{Y_1(t_k)\ Y_2(t_k + \tau)\} \tag{5.7}$$

A sufficient condition for equations (5.6) and (5.7) to yield unbiased estimates of their ensemble expectation values is that both Y_1 and Y_2 must be ergodic (99). Fourier transformation of the time-averaged estimates of the correlation functions gives estimates of the ensemble spectral densities:

$$S_{Y_1Y_1}(jw) = \int_{-\infty}^{\infty} e^{-jw\tau} R_{Y_1Y_1}(\tau)\, d\tau \qquad (5.8)$$

$$S_{Y_1Y_2}(jw) = \int_{-\infty}^{\infty} e^{-jw\tau} R_{Y_1Y_2}(\tau)\, d\tau \qquad (5.9)$$

Division of equation (5.9) by (5.8) yields an estimate of the process transfer function. The effect of time-lags in the sampling systems may be accounted for by shifting τ in equation (5.7) by an appropriate amount prior to the application of equation (5.9). The tacit assumption here is that rise time differences may be accounted for by small additional time shifts in equation (5.7) - a reasonable assumption in view of the fact that rise time differences are typically less than 10% of the corresponding dead time differences for the system employed here.

The exciting function for the generation of noise-corrupted time records (from which the correlation functions may be estimated) may take several forms. These include white noise, bandwidth limited white noise, random telegraph signals, random binary sequences and sinusoidal inputs. The last of these excites a single frequency only, and is considered impractical since

repeated experiments are called for. The other signal forms excite frequency ranges, but involve random processes which are extremely difficult to realise physically. From a practical point of view it is desirable to employ sequences which are only pseudorandom, but which have analytical autocorrelation functions. One such function is the pseudo random binary sequence or PRBS.

This function assumes one of two values with equal probability, and switchings take place at integral multiples of the decision time Δt_p. The signal is periodic, and the period is an integral number of decision times. A typical PRBS is shown in Figure 5.11. The autocorrelation function of such a PRBS is given by (105):

$$r(\tau) = \bar{a}^2\left(1 - \frac{N+1}{N}\frac{\tau}{\Delta t_p}\right) \text{ for } 0<|\tau|<\Delta t_p$$

$$\text{and } r(\tau) = -a^2/N \qquad \text{elsewhere} \qquad (5.10)$$

Where N is the number of decisions in the sequence. For large N, this reduces to:

$$r(\tau) = \bar{a}^2\left(1 - \frac{\tau}{\Delta t_p}\right) \qquad 0<|\tau|<\Delta t_p$$

$$r(\tau) = 0 \qquad \text{elsewhere} \qquad (5.11)$$

The analytical form of the PRBS autocorrelation is not used directly in this study, since a signal introduced below the grid

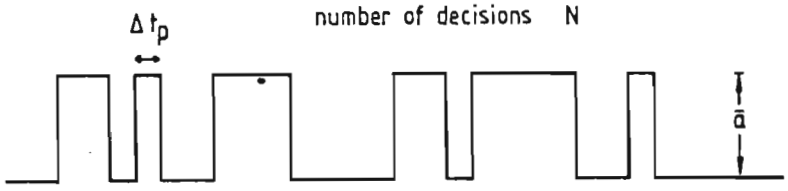

PRBS signal

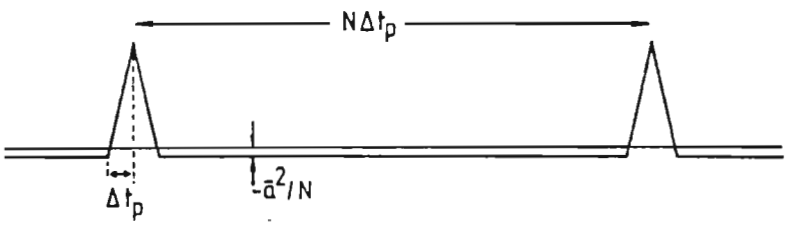

PRBS autocorrelation

FIGURE 5.11 PRBS CHARACTERISTICS

will necessarily be dispersed to some extent by the time it emerges at the lower sample station. Nevertheless, the autocorrelation observed at this point could be compared to equations (5.10) or (5.11), and any gross errors in the processing sequence should show up. The analytical auto= correlation thus provides a useful cross-check on the data capture and processing sequences.

5.2.5 Realisation of the Auto- and Crosscorrelations

In order to realise the correlation functions via equations (5.6) and (5.7), one needs to specify the sampling interval and the total number of data points per channel. The principal constraint on the former is that of folding or aliasing. If process frequencies greater than half the sampling frequency are in evidence, the danger exists that information at these frequencies may be folded back into and confused with information at lower frequencies. The maximum frequency at which information may be obtained, termed the folding of Nyquist frequency, is given by:

$$\omega_{max} = \pi/\Delta t_s \qquad (5.12)$$

where Δt_s is the sampling interval. Common practice is to set the sampling interval as small as possible (within practical limits). In this study, the highest process frequencies of interest were expected to be of the order of 4 radians per second. A sampling interval of 0.1 seconds was selected, giving a Nyquist frequency of about 31.4 radians per second.

The precision of the correlation function estimates is strongly dependent on the number of data points per channel employed. This is borne out by the results of Gallier et. al. (106), in which it is demonstrated that increasing the number of points from 930 to 5180 leads to a substantial improvement in the transfer function estimate. Woodburn, King and Everson (107) in fact showed that the standard deviation of errors associated with autocorrelation functions bears an inverse relationship to the number of readings (for their system at least). The improvement was found to be dramatic in the region 0-2000 points, and somewhat less so beyond 2000.

In this study it was decided to fix the number of points per channel at 5000. With a sampling interval of 0.1 seconds this gives a real-time record length of about 8.33 minutes, and any particular run therefore represents an RTD function averaged over this period.

Physical realisation was achieved by recording a time sequence on magnetic tape and processing the data off-line. The recording machine was a Philips ANA-LOG 7 unit operating in a frequency modulation mode, and during playback the tape speed was slowed by a factor of four. The computations were performed on an Apple II microcomputer based on an MCS 6502 microprocessor. The interface between the microcomputer and the tape recorder was an Interactive Structures AI 13 (12-bit)

A/D converter, sampling at 0.4 second intervals while playback was in progress.

The program for the evaluation of the correlation functions was written in the Apple version of BASIC, and a listing is given in Appendix E. The functional forms of equations (5.6) and (5.7) are also included.

5.2.6 Realisation of the PRBS Signal

There are at least two known ways of generating a PRBS signal. One is based on Gaussian number theory and makes use of quadratic residues (108,109). The other is based on the properties of digital filters and their maximum length null sequences (105), and makes use of a shift register circuit. The latter is employed here.

Consider a bit shift register circuit configured as shown in Figure 5.12. The $\oplus$ denotes modulo-2 addition so that the system variables only assume values of 0 or 1. The symbol $\bar{D}$ denotes a delay operator. The circuit is driven by a constant frequency clock, and with each shift the contents of one register is passed on to the next. The truth table for modulo-2 addition is:

$\oplus$	0	1
0	0	1
1	1	0

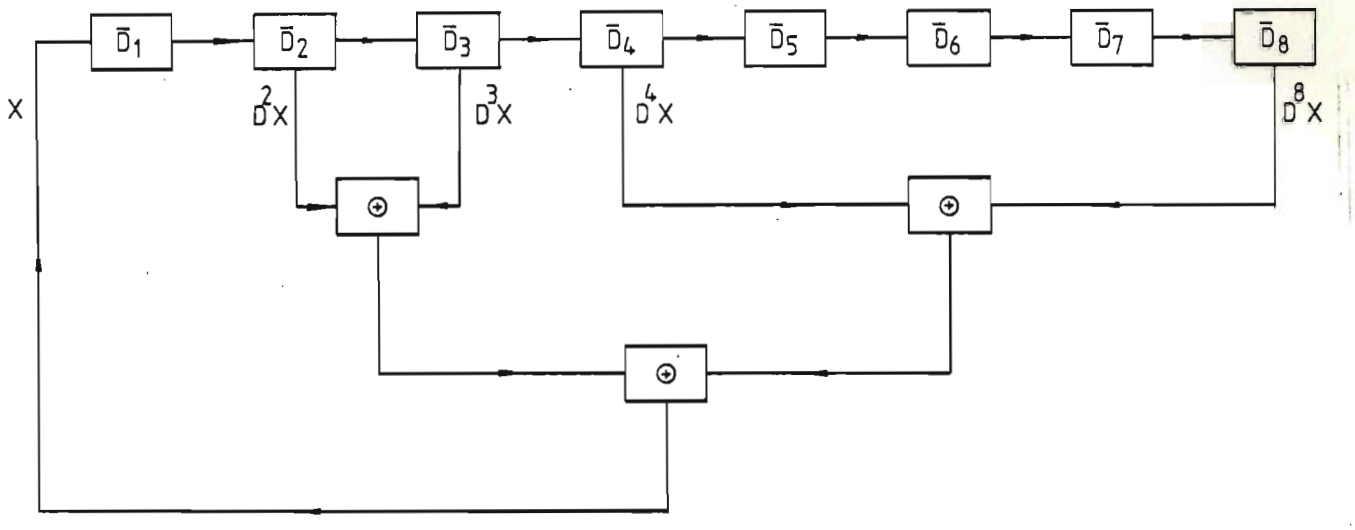

FIGURE 5.12 PRBS GENERATOR CIRCUIT

The characteristic polynomial governing the operation of this circuit is:

$$(1 \oplus \bar{D}^2 \oplus \bar{D}^3 \oplus \bar{D}^4 \oplus \bar{D}^8)X = 0 \qquad (5.13)$$

This polynomial has no factors and is itself not a factor of $(D^k \oplus 1)$ for $k < 2^8 - 1$. In other words, the characteristic polynomial is primitive, modulo 2 and will generate its maximum length null sequence if the starting condition is non-zero. The period of the sequence is given by $2^{np} - 1$ in general, where np is the order of the polynomial. In this instance a 255-decision PRBS is generated.

The circuit was constructed as shown in Figure 5.12, with an adjustable speed clock. A solid-state relay was operated off shift register number 8, and this relay in turn governed the operation of a solenoid valve feeding methane into the plenum chamber of whichever column was in operation. A pressure reservoir was included on the high pressure side of the solenoid, and bottled methane was fed to this reservoir via a hand-controlled needle valve. During a PRBS run the pressure in the reservoir was kept as constant as possible.

Three quantities related to the generation of a PRBS test signal need to be specified. These are the signal amplitude, the decision time and the number of decisions in the sequence. All

of these quantities should be chosen to maximise the resolution of the system transfer function.

5.2.6.1 Amplitude

The theoretical optimum for the amplitude of the PRBS signal is the maximum within the constraints imposed by linearity considerations. In this study it was evident that the amplitude of the test signal had very little effect on the results over a fairly wide range. This is mainly due to the fact that the FID units were extremely sensitive to low concentrations of methane. These detectors could be operated with different potentials across the electrodes, and the result was excellent resolution over a wide range of tracer concentrations (below about 1% by volume). In practice the PRBS amplitude was fixed at levels dictated by the geometry of the feed lines and the available pressure drop across the solenoid. The detector sensitivity rather than the PRBS amplitude was varied to achieve suitable signal strengths.

5.2.6.2 Decision Interval

Different criteria exist for selecting the PRBS decision time. Himmelblau (99) suggests that the decision time should be specified in such a way as to ensure that the first zero in the power spectral density function occurs at a frequency well above those of interest. The power spectral density function of a

PRBS signal is given by:

$$S_{PRBS}(j\omega) = \bar{a}^2 \Delta t \left[\frac{N+1}{N}\right] \left[\frac{\sin \omega\Delta t/2}{\omega\Delta t/2}\right] \qquad (5.14)$$

This function has a recurring zero at $\omega\Delta t/2 = k\pi$, k an integer. By this criterion the decision time should be smaller than about 1.57 seconds if the maximum frequency of interest is 4 radians per second.

A somewhat different criterion is suggested by King and Woodburn (81), based on experimental design from an information theory approach. They suggest that, for first order linear systems, the optimum decision time should be 1.2 times the process time constant. However, for diffusive mixing in a packed tower Everson (110) found that the decision interval becomes an insensitive variable in an optimum testing strategy.

Neither of the above criteria is strictly applicable to the system employed here. The signal observed at the lower sample station is dispersed to some extent as mentioned previously, and there is no reason why its spectral density function should conform closely to equation (5.14). King and Woodburn's (111) criterion is also probably not applicable, since the process under investigation is not first order. It could be argued that the exact form of the exciting signal is of little consequence, since the crosscorrelation function is formed between two observed signals. This line of

reasoning suggests that the decision time should be chosen in such a way that the PRBS frequency spectrum covers that of the process, but that the exact choice of decision interval is not critical.

A practical approach was used to resolve this question. For a fixed set of conditions, three experiments were carried out with decision time to lumped process time constant ratios of 0.74, 0.37 and 0.11. The data from these runs was processed to the form of a system frequency response, and the magnitude ratio components are shown in Figure 5.13. It is immediately apparent that the transfer function estimation procedure is insensitive to the choice of PRBS decision time in the range covered.

For the sake of uniformity, the PRBS decision interval was taken to be half the lumped process time constant.

5.1.6.3 Number of Decisions in the Sequence

Accepted practice appears to be to choose a PRBS period length to give a small deviation of the autocorrelation below the abscissa, i.e. to maximise the number of decisions in the sequence. However, if experimental and theoretical crosscorrelations are to be compared, it may be advantageous to employ a shorter decision sequence. King and Woodburn (111) suggested this, and Haines (112) deliberately used a short PRBS sequence.

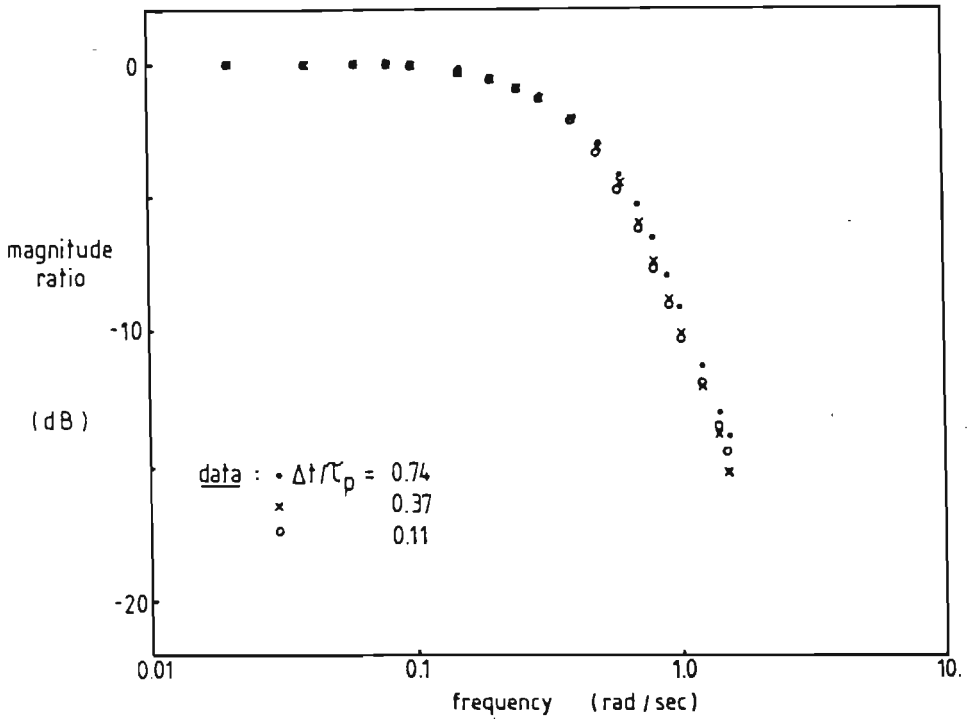

FIGURE 5.13 SENSITIVITY OF $G(j\omega)$ TO PRBS DECISION TIME

In this study there is no clear incentive to reduce the PRBS period length, since the experimental data is compared to the model predictions in the frequency domain. It is not clear how correlation function deviations below the abscissa will show up in the process transfer function, and it was decided to maximise the PRBS period length. A 255 decision sequence was used as discussed previously.

5.2.7 Overall Data Capture and Processing Sequence

The preceeding sections discuss the selection and realisation of the various components of a data capture and processing system. This section describes the overall system and sequence of events in the recording and processing of a single run.

The entire operation is executed in three stages. The first of these is the actual recording of data, and this is followed by off-line correlation analysis. The third stage involves time shifting and Fourier transformation to frequency response form.

Figure 5.14 illustrates the data recording process. Gas velocity in the bed is set to the desired value, and the pressure drop across the filters is controlled in such a way as to provide a suitable pressure driving force for sampling. The valves in the FID sample lines are then adjusted if necessary, and the methane pulse-points are engaged to determine dead and rise times associated with the sampling systems. Pressure in the methane

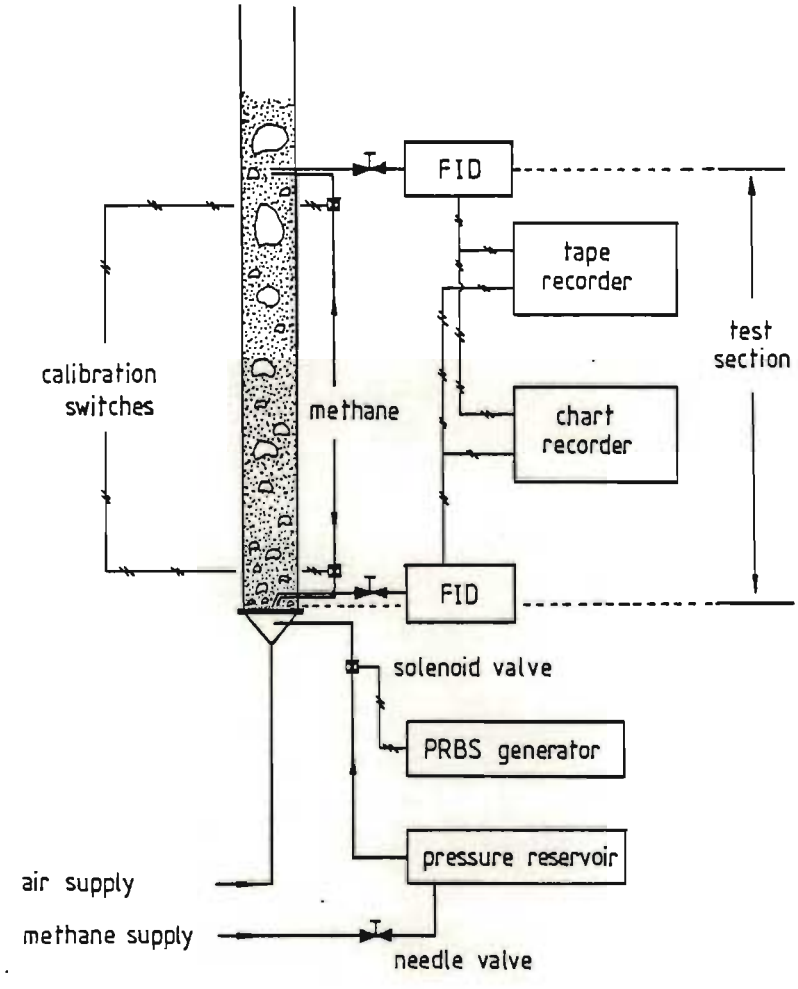

FIGURE 5.14 DATA RECORDING SETUP

reservoir is then set to provide a suitable pressure drop across the tracer injection solenoid, and the PRBS generator is switched on. Tracer flows into the plenum chamber as dictated by the PRBS signal, and the methane reservoir pressure is maintained at its initial level by hand control. The lower and upper station signals are monitored on the chart recorder, and are amplified or attenuated to suitable levels for recording. The tape recorder is then engaged, and a 10-minute time record of each of the signals is captured in analogue form. On completion of recording the PRBS generator is switched off, and the pulse-points employed once again to check sampling system dynamics. Average (before and after) dead and rise times are used in the data processing.

The correlation analysis layout is shown in Figure 5.15. The tape is played back at a reduced speed (a factor of four) into a 12-bit A/D converter via a 15Hz low-pass filter. This filter is included to eliminate high-frequency noise picked up during recording, and the filtered signal is monitored on an oscilloscope. The A/D converter samples at 0.4 second intervals as dictated by the microcomputer, and 5000 readings from each channel are stored in the memory of the latter. Once the digitisation and collection of data has been completed the tape recorder is switched off and correlation analysis commences. The microcomputer engages the printer, and correlation function values for successive time shift increments are printed as they are computed.

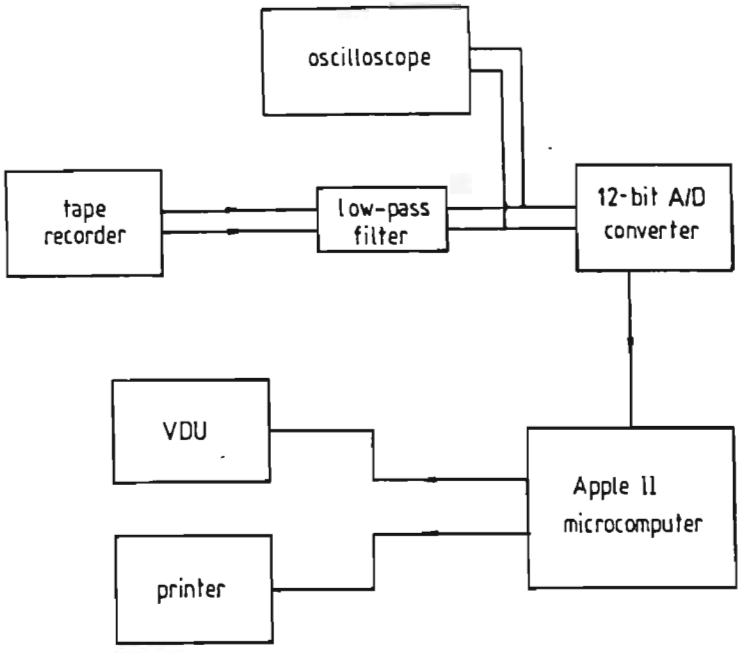

FIGURE 5.15 CORRELATION ANALYSIS CONFIGURATION

The time-lag shift and Fourier transform processes are carried out in the main model fitting program. The auto- and crosscorrelation functions are plotted by hand, and any obvious bumps or discontinuities are removed by drawing a smooth curve through the data. (This was in fact seldom necessary - the correlation functions generally described smooth curves as plotted). The correlation functions are then fed into the main program as though they represent a conventional impulse-response type of test. A time shift quantity calculated from the differences in sampling system dead and rise times is included, and the crosscorrelation is shifted relative to the input auto= correlation by this amount before the Fourier transform routine is called. Fourier transformation is then carried out as described in Chapter 4, and the overall result is an experimental transfer function against which model predictions may be optimised.

5.3 Parameter Reduction by Independent Measurement

The fluidised bed models described in Chapter 4 generate frequency responses as functions of model parameters. In principle any number of these parameters may be optimised by comparison with experimental RTD data. However, the greater the number of optimised parameters, the less the significance of any particular parameter value returned. The number of parameters to be determined by model fitting should clearly be held to a minimum to ensure maximum significance in those that are in fact estimated in this manner.

5.3.1 Parameter Identification

The input quantities required by the seven models employed in this study are listed in Table 5.1, and Table 5.2 identifies the parameters to be optimised by simplex sequencial search in each case. The parameters in Table 5.2 will henceforth be referred to as optimised parameters, and those appearing in Table 5.1 but not in Table 5.2 as auxiliary parameters.

As regards the auxiliary parameters, the geometric parameters in Table 5.1 and the superficial velocities are measured directly and need be considered no further. Bubble velocities, the bubble phase dispersion coefficient, dense phase voidage and velocity, bubble holdup and the ratio of cloud to bubble volume need to be estimated independently in some suitable manner.

5.3.2 Auxiliary Parameter Estimation

5.3.2.1 Bubble Velocity and Axial Dispersion Coefficient

Bubble velocity U_b was measured by injecting a pulse of methane into the bed at the lower sample station and measuring the time lag preceeding the emergence of the first local tracer peak at the upper station. After correction for sampling system dead and rise times (as for the set-up shown in Figure 5.8), a "bubble" transmission velocity was computed (104).

The technique described actually determines the transmission time of a tracer-rich packet of gas through the bed, and from a modelling

	PARAMETER	MODEL(S)
mass transfer coefficients :	$(K_{be})_b$	MVD, BPD, MBT, WFD
	$(K_{bc})_b$	CCBM
	$(K_{ce})_b$	CCBM
	K_u	LMBP
	K_1^*	LMBP
	K_{g1}^*	LSBP
	K_{g2}^*	LSBP
	K_s	LSBP
dispersion parameters :	D_d	MVD, BPD, MBT, LMBP, LSBP
	D_b	BPD
geometric parameters :	L_f	all
	L_t	all
	L_s	LMBP, LSBP
velocities :	U_o	all
	U_{og}, U_{os}	LMBP, LSBP
	U_{bi}, f_i	MBT
	U_{bl}	LMBP
	U_{bu}	LMBP
	U_{bg}	LSBP
	U_{bs}	LSBP
	U_d	all
	U_e	CCBM
other parameters :	ε_d	all
	δ	all
	α	CCBM

TABLE 5.1 PARAMETER IDENTIFICATION

MODEL	OPTIMISED PARAMETERS
MVD	$(K_{be})_b$
	D_d
CCBM	$(K_{bc})_b$
	$(K_{ce})_b$
WFD	$(K_{be})_b$
	α
BPD	$(K_{be})_b$
	D_d
MBT	$(K_{be})_b$
	D_d
LMBP	K_u
	D_d
LSBP	K_s
	D_d

TABLE 5.2 IDENTIFICATION OF PARAMETERS TO BE OPTIMISED

point of view it may be argued that this represents an appropriate bubble velocity. This technique does not distinguish between single bubbles and groups of bubbles undergoing coalescence and/or splitting, and this is certainly consistent with the type of model employed which recognises only a bubble phase and not individual bubbles.

Bubble velocity is inherently a stochastic quantity, and this calls for replicate experiments - some 40 to 60 individual bubble velocities were measured for each set of conditions. An average based on arithmatic mean transmission time was computed for use in conjunction with all but the MBT model, while for the latter, these data were drawn up in the form of a histogram describing five velocities (u_i's) and associated relative abundances (f_i's). The axial dispersion coefficient in the bubble phase D_b was inferred from the standard deviation of transmission times as follows:

$$\left(\frac{D_b}{U_b L_t}\right) = \frac{1}{2}\left(\frac{\text{standard deviation}}{\text{mean transmission time}}\right)^2 \qquad (5.15)$$

This expression is consistent with a one-phase axial dispersion model (for small amounts of dispersion) as assumed by the BPD model for the bubble phase.

The estimation of other auxiliary parameters and indeed the entire modelling procedure, depends heavily on bubble velocities thus determined, and in the light of this it was considered necessary to validate the procedure before proceeding. This validation consisted of measuring slug velocities in the small tube with 71 micron FCC

catalyst and ensuring that only fully established slug flow was present in the test section. The lower sample station was shifted to a point about 1 m above the distributor and the upper station located at a distance of 1.5 m above this. "Slug" velocities were then measured by the technique described, and compared with the appropriate literature expressions which are known to describe this system satisfactorily (74). The results of this comparison are shown in Figure 5.16, and from these data it appears that the technique gives results which are consistent with those obtained by other methods.

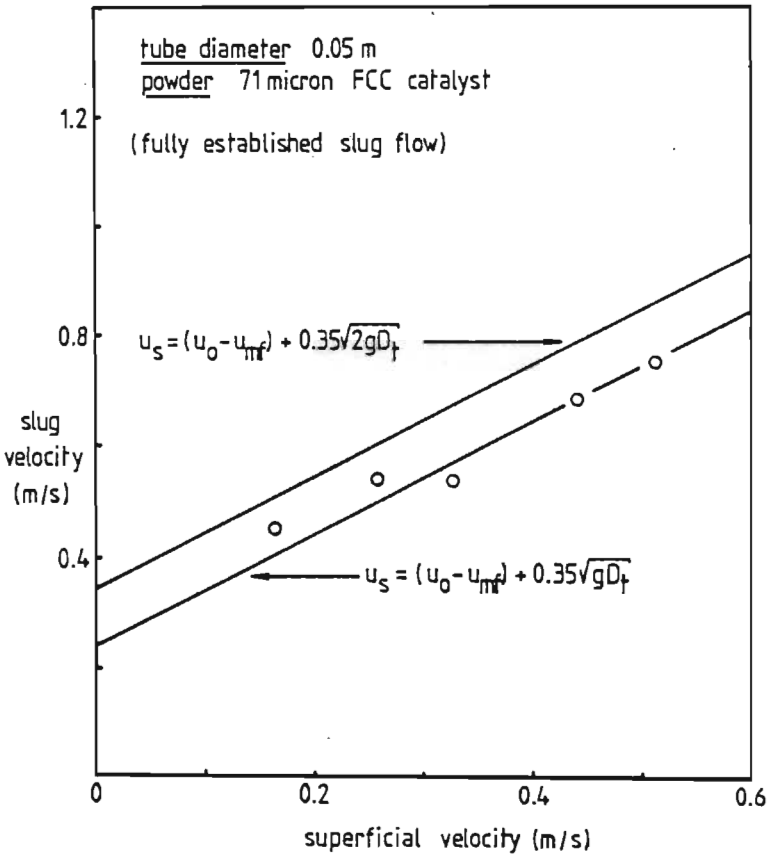

FIGURE 5.16 SLUG VELOCITIES IN AN FCC POWDER

The technique used here for measuring bubble velocities is not a conventional one, and its interpretation is likely to be a subject for debate. The success of the validation procedure under slug flow conditions allows some degree of confidence, though it might be suggested that what the probe sees in the larger bed is not representative of the bed as a whole: this applies to both the bubble velocity and RTD measurements, and is discussed in some detail in section 5.4. In defence of this procedure, it should be pointed out that the transmission velocity of gas in the lean phase is a fundamental parameter of the models employed, and this procedure aims at a direct measurement. There is no reason to suppose that an alternative measurement based on individual bubble observations (e.g. X-rays or local bubble probes) would yield a result any more appropriate, since as stated previously, the models employed here do not recognise individual bubbles.

It should be clearly stated that the assumption that this technique yields an appropriate bubble velocity for modelling purposes is fundamental to all the results quoted in this investigation. If this facet of the work is to be questioned, then the overall results are to be regarded as being subject to this limitation. However, it should also be noted that since all the models and both fluidised beds are treated in the same way the comparative aspect of the work, which is where its main strength lies in any event, is not in question.

5.3.2.2 Dense Phase Voidage and Velocity

The flow interruption or bed collapse technique as originally suggested by Rietema (113) was employed. The method involves rapidly cutting off the air supply, and plotting the bed height as it settles. Bubbles leave the bed in the first few seconds or so after the gas supply has been closed off, and thereafter the dense phase collapses slowly as interstitial gas escapes. This (steady) collapse may be extrapolated back to the time of flow interruption to yield the height of the dense phase alone in the bubbling bed, and the voidage in this phase may be computed directly from the material balance expression:

$$\varepsilon_d = 1 - \frac{W}{A_t H_d \rho_p} \qquad (5.16)$$

The dense phase velocity U_d may be inferred from the slope of the steady collapse portion of the height vs time curve. This quantity is dependent on the geometry of the system as demonstrated by Abrahamsen and Geldart (114), and the correction applied is described in detail in the author's Master's thesis (104).

It is recognised that the dense phase velocity as measured by this technique is essentially equivalent to the gas-solids slip velocity in the dense phase. Solids circulation is recognised by the CCBM model, i.e. solids ascend at more or less bubble rise velocity in the cloud-wake phase and descend (more slowly) in the emulsion phase. For the very fine powder used here and the low associated dense phase slip velocity (around 0.008 m/s), it is possible that down-

flowing solids could entrain gas and cause it to move downwards relative to the vessel wall (in the emulsion phase).

In order to meet the input requirements of the CCBM model it was considered necessary to measure the effective downflow velocity of gas in the emulsion. The technique employed is essentially the same as that used to determine bubble velocities: a pulse of methane was once again introduced into the bed, but this time the gas sampling was performed *below* rather than above the injection point. The downflowing emulsion solids entrained some of this tracer gas and generated a series of local peaks at the lower probe, the first of these appearing after a delay corresponding to some characteristic transmission time. This was interpreted as a mean gas velocity in the emulsion phase, and is subject to the same constraints as the measured bubble velocities. Validation was somewhat less satisfactory in this case but was nevertheless performed by timing the solids movement between two marks on the wall of the 0.05 m column with a stopwatch. After correction for the dense phase velocity according to the expression:

$$U_e = \frac{U_d}{\varepsilon_d} - U_s \qquad (5.17)$$

where U_s is the solids velocity and U_e the gas velocity in the emulsion relative to the vessel wall, it was found that the two measurements agreed to within ca 20%. The error was found not to show any consistency in terms of sign and therefore did not suggest

any systematic deviation, and was considered to be generated more by the stopwatch timing procedure than the tracer gas technique. The tracer technique for measuring emulsion velocities was accepted on this basis.

5.3.2.3 Bubble Holdup

The bubble holdup could be determined in two ways. The first of these is the bed collapse technique (104) - the difference between the height of the dense phase and that of the bubbling bed corresponds to the volume of gas in the bubble phase. The main problem with this approach is the fact that the height of a bubbling bed is poorly defined. The procedure is strongly sensitive to the exact choice of bed height, particularly at low superficial velocities.

The second technique employs a gas division model. Continuity considerations demand that, for a fine powder system:

$$U_b\delta = U_o - (1-\delta)\, U_d \qquad (5.18)$$

for a two-phase model, and

$$U_b\delta = U_o - (1-\delta-\alpha\delta)\, U_d \qquad (5.19)$$

for a three-phase one (such as the CCBM model). Equation (5.18)

may be solved for δ in terms of U_o, U_d and U_b and the former calculated directly, since the latter quantities are known. The stochastic quality inherent in δ is carried in U_b, and a suitably averaged bubble velocity is expected to yield an appropriately averaged bubble holdup. Equation (5.19) may be solved for δ in the same way, the only difference being the presence of the α term. The estimation of this quantity is described in the next section, and δ may once again be computed directly.

Of the two methods available for estimating δ, the second is preferable in the opinion of the author. It is this technique that is employed in this study.

5.3.2.4 Ratio of Cloud to Bubble Volume

The CCBM model is based on a solids circulation pattern: solids travel upwards in the clouds and wakes and downwards in the emulsion phase. The cloud and wake phases are usually lumped together, and according to this model solids continuity requires that (28):

$$\alpha\delta\ U_b = (1-\delta-\alpha\delta)\ U_s \qquad (5.20)$$

where U_s is the solids velocity relative to the vessel wall in the emulsion phase. This expression may be solved for α to yield:

$$\alpha = \left[\frac{1-\delta}{\delta}\right] \frac{U_s}{U_b + U_s} \qquad (5.21)$$

Now U_b is measured directly, and U_s may be obtained from U_e and U_d measurements (equation (5.17)). To evaluate α using equation (5.21) therefore requires one additional quantity: an independent estimate of δ. An examination of the magnitudes of the numbers involved in this study, however, suggested that to a first approximation at least, δ could be replaced by U_o/U_b. This effectively involved neglecting $(1-\delta)U_d$ or $(1-\delta-\alpha\delta)U_d$ in favour of U_o in equations (5.18) and (5.19) respectively, an assumption which does not appear to be too disturbing in this situation since U_d was constant at around 0.008 m/s and U_o varied from about 0.15 to 0.7 m/s. The maximum error expected in δ from this simplification is therefore around 4% - this was considered to be well within experimental error, and α was evaluated from

$$\alpha = \left[\frac{U_b - U_o}{U_o}\right] \frac{U_s}{U_b + U_s} \qquad (5.22)$$

No explicit validation of this procedure was attempted, mainly due to the fact that no direct measurement was possible within the constraints imposed on this investigation. Values of α thus computed were, however, checked against published values for reasonableness and found to be acceptable on this basis.

5.4 Overall Experimental Strategy

As stated previously, one of the aims of this investigation is to quantify the effects of vessel diameter and internal geometry on interphase mass transfer. The question of scale-up is implicit in the study of the diameter effect, while the investigation into the effect of coils and the presence or otherwise of the sparger is aimed at providing guidelines for the solution of problems on the demonstration reactor.

It is clear that tube size and internal configuration are not the only independent variables to be considered. The effect of bed height may be very significant, and some idea of the dependence on gas velocity could prove extremely useful. The cold model experimental programme accordingly considers the following independent variables:

(i) Gas velocity

(ii) Bed height

(iii) Tube size

(iv) Coils/no coils in the 0.64 m unit

(v) Sparger/no sparger in the 0.64 m unit.

The following strategy was decided on: at any particular combination of bed height and vessel geometry, a number of runs at different superficial velocities would be carried out. For

any particular vessel geometry, runs at different bed heights would be executed. Four geometric configurations are considered, and these are identified in Table 5.3.

Varying system geometry and gas velocity (within the limits of the supply and metering system) presents no problem. However, the same is not true for varying the bed height. There are two ways in which this may be performed: the first is to establish a deep bed, and to operate the gas tracer system over different heights within this bed. The second is to vary the powder charge, and to operate the tracer system over the whole bed in each case. An additional question associated with the latter is where to locate the upper sample station - average bed height, below minimum bed height or in the freeboard?

TUBE DIAMETER	INTERNAL GEOMETRY	EFFECTS COVERED
0.05 m	porous plate	U_o, L_f
0.64 m	coils	U_o, L_f
	no coils	U_o, L_f
	coils, sparger	U_o, L_f

TABLE 5.3 COLD MODEL GEOMETRIC CONFIGURATIONS

It is clear that the two strategies for varying L_f should yield different results. Lateral gradients are expected in the larger bed, and the results from gas sampling with a single probe at some intermediate axial position would probably depend on radial probe location. If a single probe is to be employed, it is imperative that sampling be carried out where the radial gradients are at a minimum. At first glance the appropriate location for the upper probe would appear to be the disengaging region, since appreciable lateral mixing is observed in this area. However, this would necessarily mean that a crossflow enhancement effect of the type reported by Miyauchi et al. (93), if present, would be reflected in the results. This in turn implies that any axial profile determined by operating with different powder charges would be distorted, since a shallow bed would contain a (disengaging) crossflow enhancement not present at the same axial location in a deeper bed. A further objection to locating the sample probe in the disengaging region is the fact that the gas holdup in this zone is poorly defined, and the assumption that the probe draws gas from bubbles and the dense phase in proportion to the presence of these phases in the system no longer holds.

In the light of this it was decided that the upper sample probe would be located immediately below minimum expanded bed height. This allows maximum advantage to be taken of the lateral mixing process in the disengaging region whilst avoiding the deleterious effects discussed above. The time-averaged nature of both the RTD and the bubble velocity measurements would ensure that maximum

radial averaging would be implicit in the results. It was also decided that the upper sample probe would be located radially at a point midway between the wall and the centreline of the vessel.

CHAPTER 6

RESULTS AND DISCUSSION

This chapter is presented in five sections. The first deals with auxiliary system parameters, and the second describes general features of the RTD data and the model fitting. The third section is devoted to the actual model screening, and the fourth covers crossflows and the effects of vessel geometry. In the fifth section the axial crossflow profile is examined in terms of bubble to dense phase interfacial areas.

6.1 Auxiliary System Parameters

6.1.1 Bubble Velocity and Axial Dispersion

6.1.1.1 0.05 m Unit

Slug velocities measured at three different bed heights are shown in Figure 6.1. There is no apparent dependence of U_s on axial probe location, and the results are adequately described by:

$$U_s = 1.15\ (U_o - U_d) + 0.63\ \sqrt{g\ D_t} \qquad (6.1)$$

The excess velocity coefficient (1.15) is probably a velocity profile effect, and is close to the 1.2 reported by Nicklin et. al. (71) for an air-water system. The slug rise coefficient (0.63), however, exceeds the commonly accepted values of 0.35 and $0.35\ \sqrt{2}$ (73, 74) by factors of about 1.8 and 1.3 respectively. This

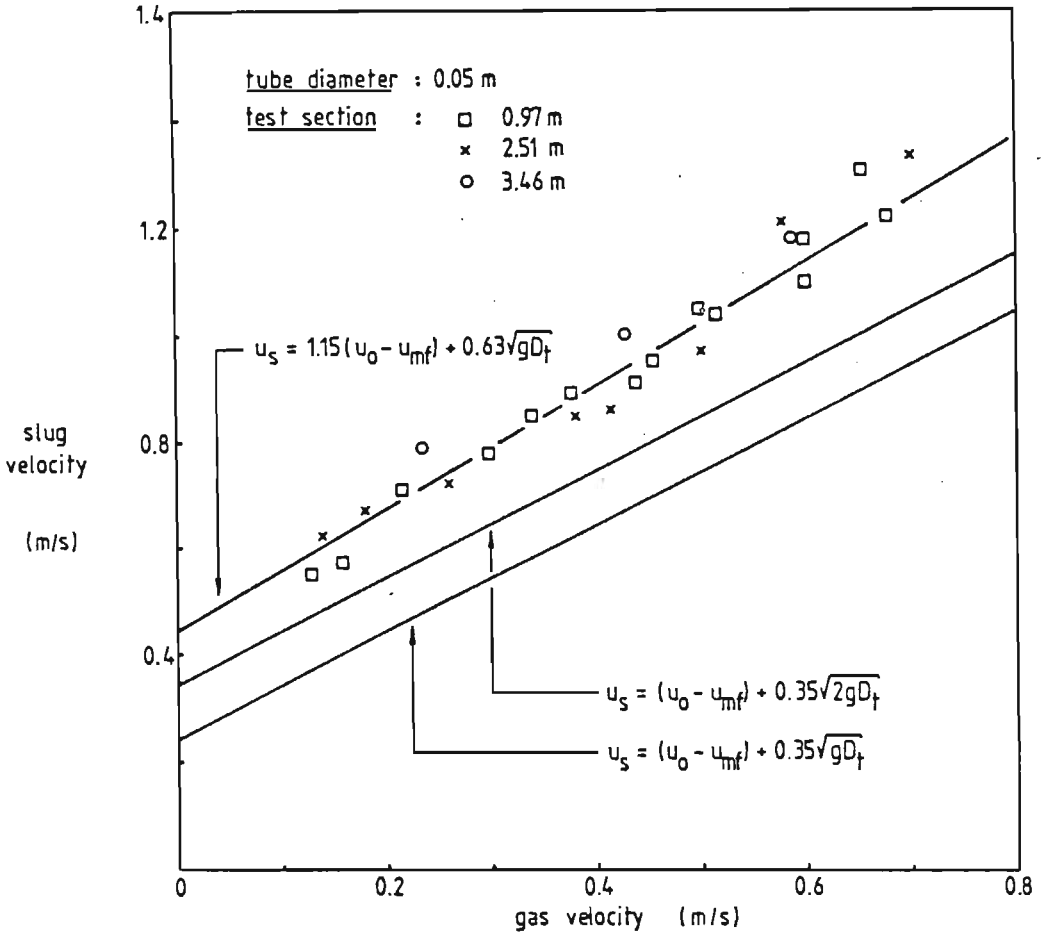

FIGURE 6.1 SLUG VELOCITIES ON THE 0.05 m UNIT

suggests that slugs in this system experience a smaller retarding force than those in systems involving coarser particles. The high dense phase voidages observed for this type of system (104) are probably consistent with low dense phase viscosities, and this could in turn be responsible for the high slug rise coefficient. It should also be noted that slug rise coefficients of the magnitude reported here are by no means unique to this study- data reported by Tsutsui and Miyauchi (115) for example, suggests a coefficient as high as 0.86 for a fine FCC powder.

Axial dispersion coefficient data for the bubble phase, as inferred from the spread in velocities (by applying equation 5.15), is given in Figure 6.2. Despite the large amount of scatter, it is clear that a deeper bed is associated with a larger dispersion coefficient. The scatter is probably a result of the rather small sample size - 40 to 60 observations per set of conditions is, in all likelihood, too small a number for obtaining a good estimate of the ensemble standard deviation. A few hundred observations might well be required for a significantly better estimate: the general techniques employed by Rowe (64), for example, involve very large numbers of individual bubble observations.

The small sample size was employed in this study for practical reasons. Experiments with larger numbers of observations were considered unjustified, since errors possibly introduced into the modelling routines from this source were considered small relative to those inherent in the overall procedure.

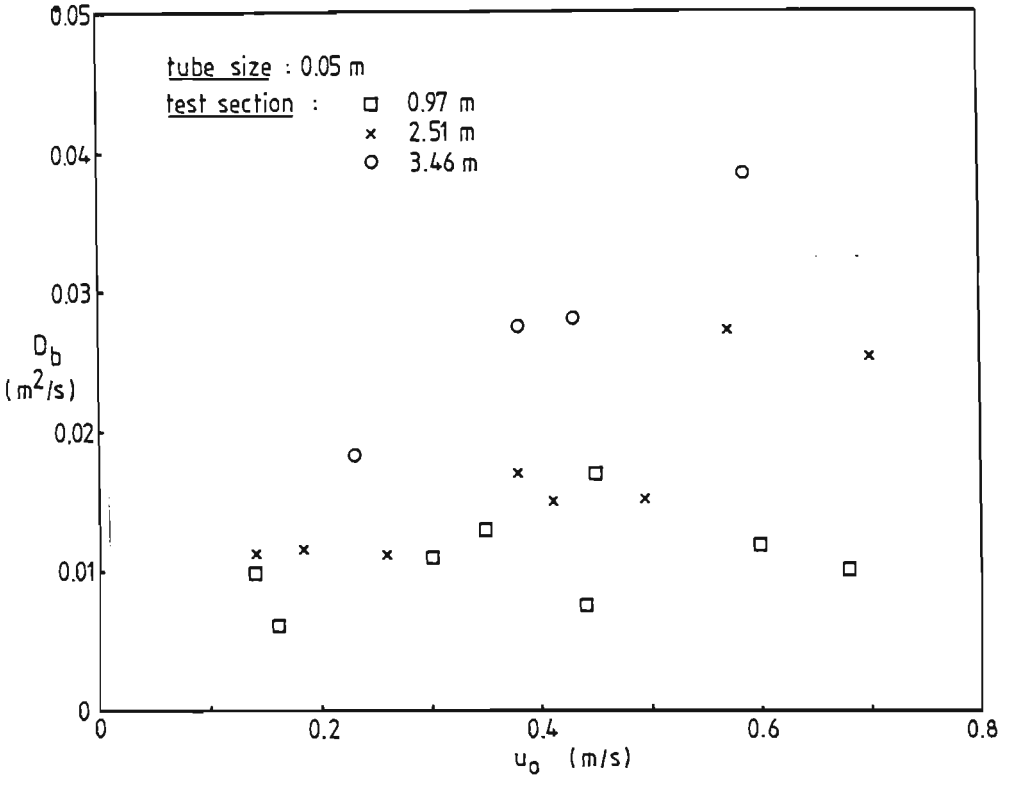

FIGURE 6.2 BUBBLE PHASE DISPERSION COEFFICIENTS IN THE 0.05m UNIT

6.1.1.2 0.64 m Unit : No Sparger

Bubble velocities measured at four different axial positions in the 0.64 m unit (with coils - hydraulic diameter 0.19 m) are given in Figure 6.3. The most striking feature is the strong axial velocity profile : it appears that bubbles rise at a moderate rate in the lower regions of the bed and accelerate progressively higher up. The data as presented represents average velocity in the test section. However, a local velocity profile at fixed superficial velocity may be inferred if a particular form of height dependence is assumed. One possibility is:

$$U_b = a + b.\exp(cz) \qquad (6.2)$$

where a, b and c are constants and z is axial position. The integrated or height-averaged form of equation (6.2) may be compared with data from Figure 6.3, and the constants adjusted for minimum error by the simplex technique. At a superficial velocity of 0.3 m/s, this procedure leads to:

$$U_b = 3.24 - 2.38 \exp(-0.32z) \qquad (6.3)$$

where U_b and z are in m/s and m respectively. This expression is plotted in Figure 6.4, and suggests that bubbles rise at velocities exceeding 2 m/s beyond about 2 m above the grid. It also suggests that these velocities approach a limit of about 3.2 m/s, though this could simply be a result of the form of the equation.

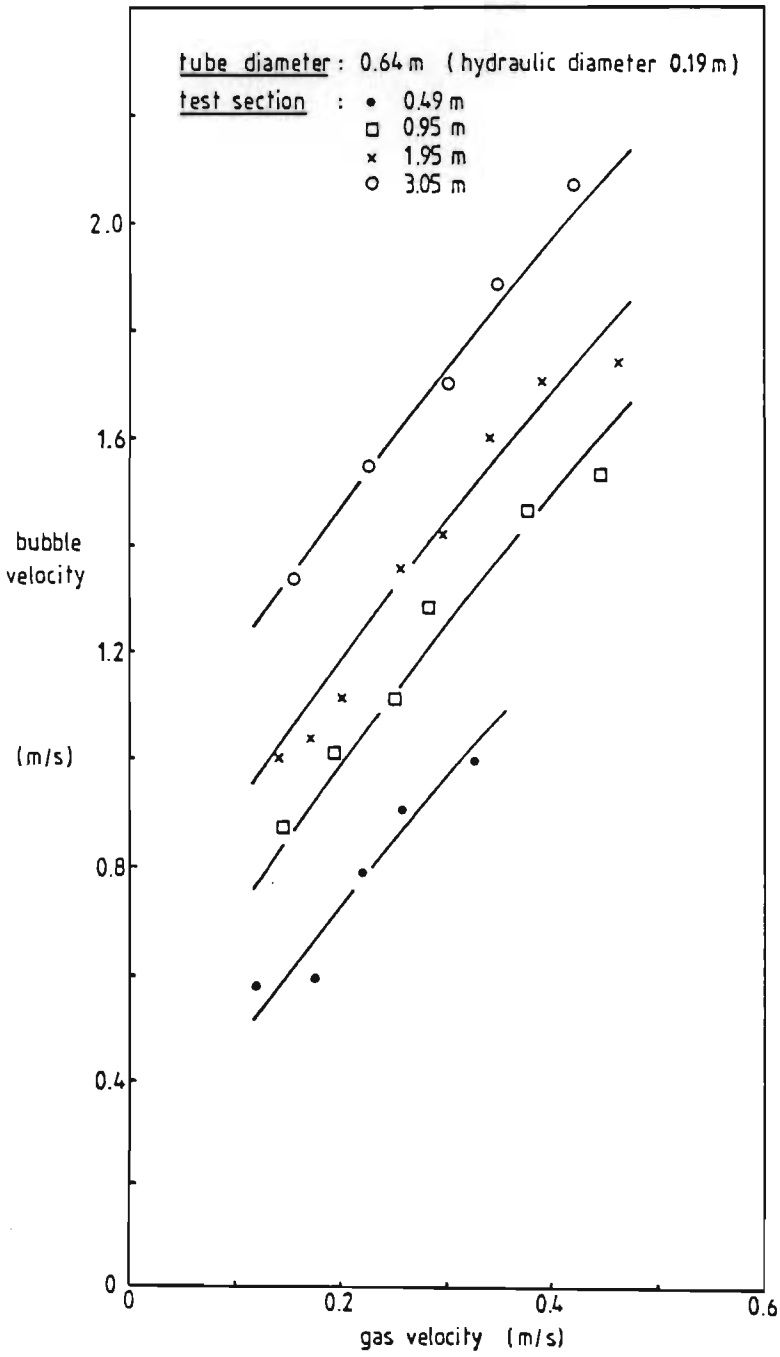

FIGURE 6.3 BUBBLE VELOCITIES IN THE 0.64m UNIT

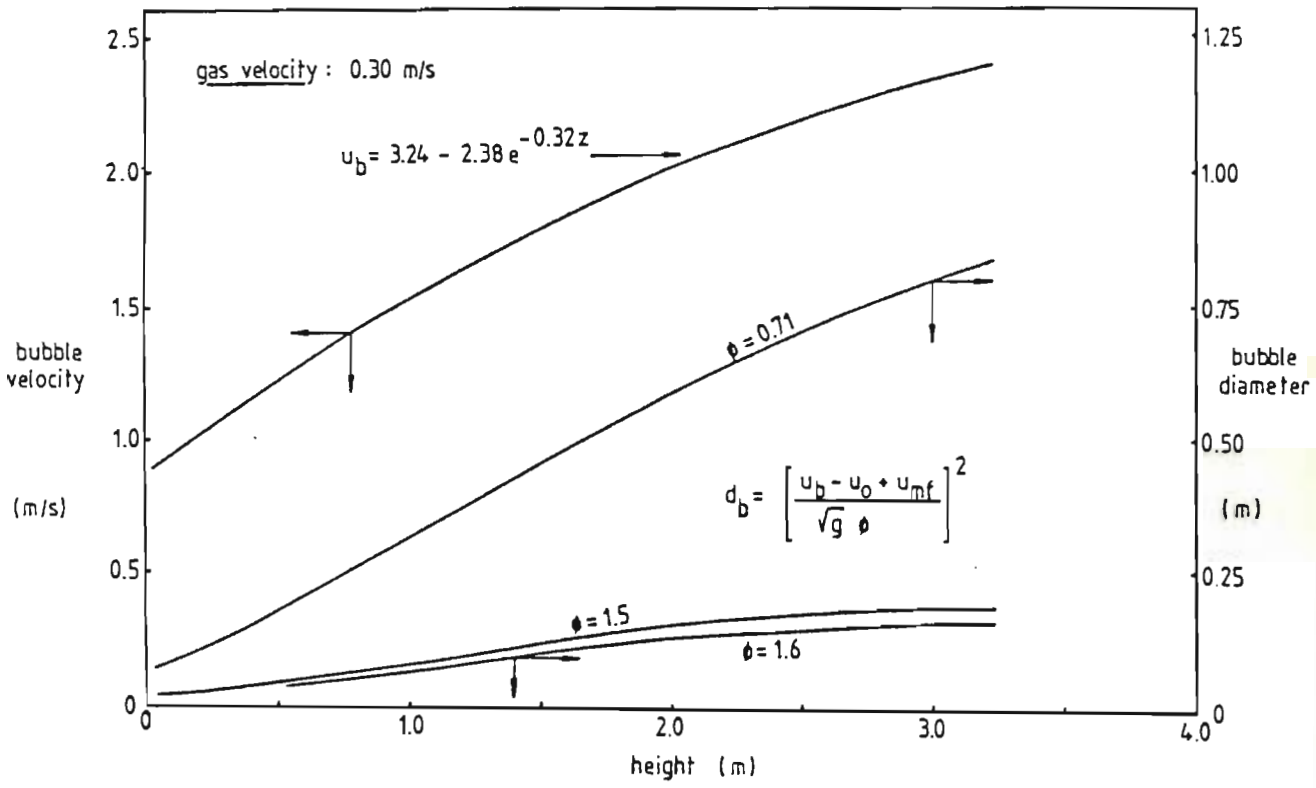

FIGURE 6.4 LOCAL BUBBLE VELOCITY PROFILE

Application of the well-known Davidson and Harrison (39) bubble rise expression (solved for d_b) to the local velocity profile yields the bubble diameter profile shown in Figure 6.4. It is clear that these diameters are not physically plausible, particularly when it is noted that the bed contained immersed coils giving a maximum free span of about 0.15 m only. These diameters only appear reasonable when the bubble rise coefficient is increased from 0.71 to about 1.5-1.6: this suggests a strong, inherent increase in this parameter over accepted literature values, possibly associated with a high dense phase voidage and a low dense phase viscosity. An equally plausible explanation is the existance of bubble chains and preferred bubble tracks of the type observed by Werther (53). He in fact modelled the chain phenomenon by allowing the bubble rise coefficient to increase with tube size, and suggested an upper limit of 1.6 for beds of 1 m or more in diameter. It is not possible, on the basis of the information given, to establish which of these effects more correctly explains the high velocities. It should be noted, however, that the difference is irrelevant as far as the overall modelling procedures are concerned since, as stated previously, the models do not recognise individual bubbles.

In the case where the coils were removed from the bed the bubble velocity profile changed somewhat relative to that in the coil-containing system. Bubble velocity data for the coil-free bed is shown in Figure 6.5, along with the trajectory for the same test section height from Figure 6.3. The coil-free system allows higher bubble transmission velocities in the

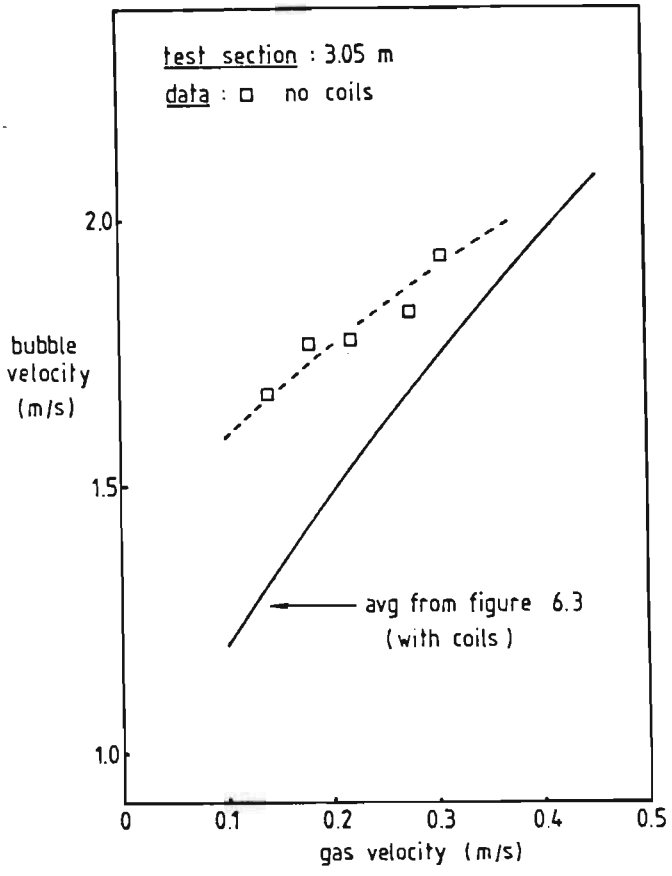

FIGURE 6.5 BUBBLE VELOCITIES IN THE 0.64 m UNIT (NO COILS)

superficial velocity region 0.1-0.3 m/s, and the profiles appear to converge at velocities in excess of 0.4 m/s. This behaviour could possibly be explained in terms of the inhibiting effect of coils on bubble growth: horizontal baffles are thought (116) to limit bubble size, and a similar but weaker effect could be operating here. It is also possible that coils somehow promote the formation of a relatively larger number of preferred bubble tracks, thus acting as a kind of distributor in the bed. Bubble chains might be expected to rise faster if they consist of relatively more bubbles and rise in relatively fewer tracks. In any event, it appears from this data that the presence of coils enhances bubble to dense phase contact times.

Bubble phase axial dispersion coefficients are given in Figure 6.6. The absolute magnitude of this parameter is significantly greater than was the case in the slugging bed, and in the 0.64 m coil-free system, dispersion coefficients are high relative to those in the coil-containing bed. In the latter the bed height dependence appears similar to that observed in the 0.05 m tube, though the large amount of scatter obscures any clear trends.

A large axial dispersion parameter in the coil-free bed relative to that in the coil-containing one could be explained as follows: at any instant in the coil-free system, the bubbles could conceivably exist in the form of a few high-speed bubble chains

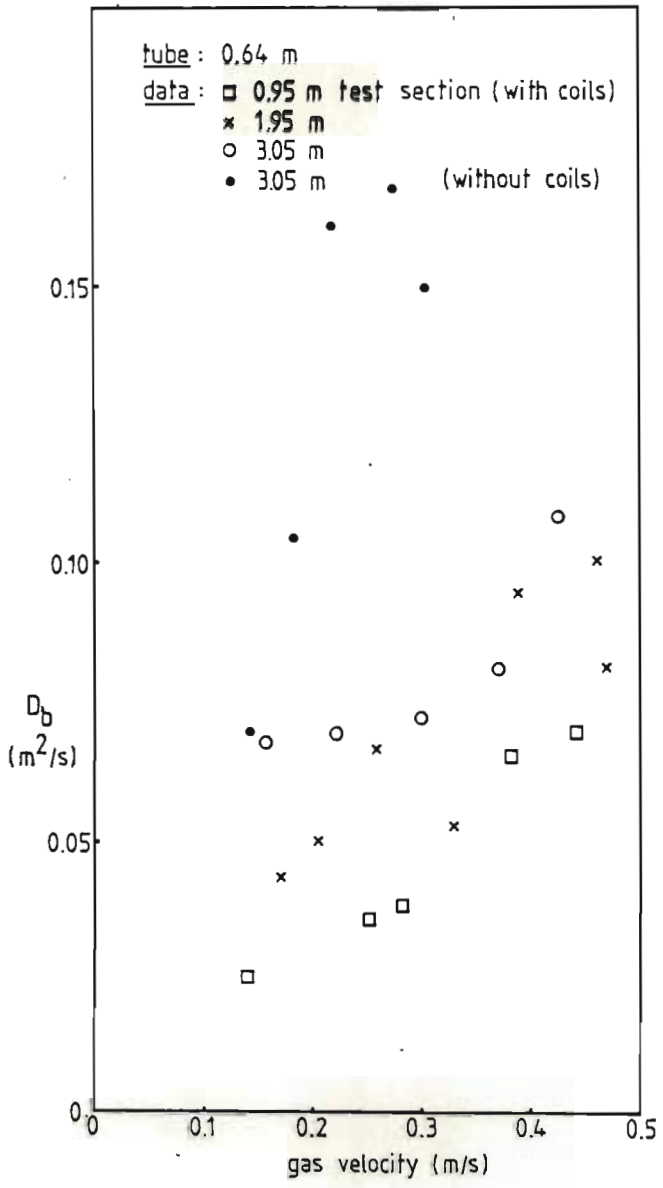

FIGURE 6.6 BUBBLE PHASE DISPERSION COEFFIENTS IN THE 0.64 m UNIT

superimposed on an otherwise randomly distributed population. The velocity difference between the chains and the randomly distributed component could be fairly high, and so too dispersion on a global scale. The introduction of coils into the bed could have the effect of distributing the bubble tracks more evenly as mentioned previously, and this could in turn shorten the length or period of existence of individual chains. The velocity difference between chains and randomly distributed bubbles would accordingly be reduced, and lower dispersion coefficients would be obeserved.

6.1.1.3 0.64 m Unit : Sparger Case

Bubbles sparged into the bed some distance above the main gas distributor might be expected to rise in a manner somehow related to that of bubbles originating at the grid. The bed above the sparger sees the some total volumetric gas flow in the form of bubbles as would have been the case if all the fluidising gas had been introduced via the grid. However, in this instance bubbles enter the region above the sparger as a mixture of presumably large (grid) and small (sparger) bubbles. Only the sparger bubbles are "tagged" with tracer, since it is the history of these that could dominate performance in the situation where some limiting reactant is sparged into a fluidised bed.

Measured rise velocities of bubbles introduced via the sparger are shown in Figure 6.7. The system was operated as follows:

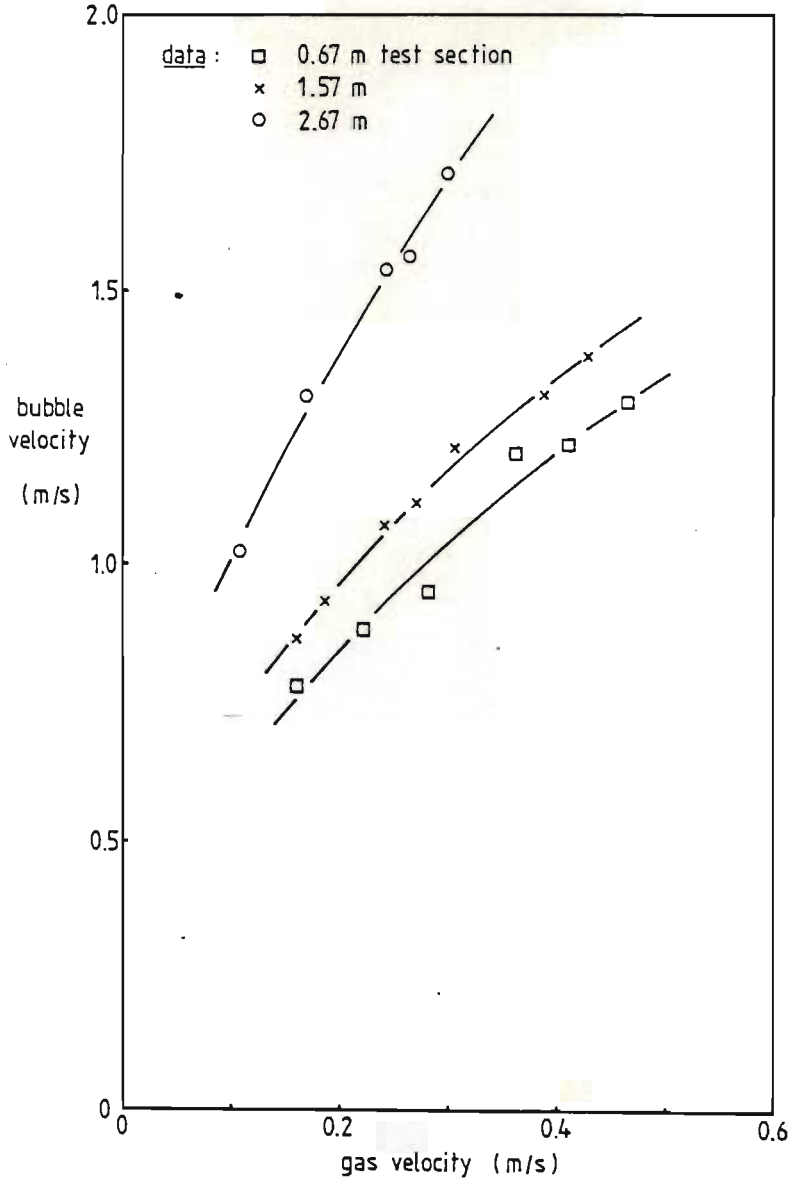

FIGURE 6.7 SPARGER CASE BUBBLE VELOCITIES

one third of the fluidising air was fed to the sparger, and the rest to the grid. Tracer was injected at one of the sparger nozzles, and bubble transmission velocities measured in the region between the sparger and the upper sample station.

From the data in Figure 6.7 it is clear that, relative to the bubble velocity trajectory shown in Figure 6.3 for the sparger-free system, the local axial velocity profile (at U_o = 0.3 m/s) is flat in the lower regions of the bed and increases sharply higher up. It appears, in fact, that bubbles from the sparger retain their smaller size and lower rise velocity to a distance of about 1.5 m above the level of their introduction into the bed. By about 2.7 m above the sparger, however, it would seem that these bubbles have either grown to a size and velocity similar to that of the grid bubbles, or participated in the formation of chains of bubbles of mixed origin. A clearer explanation of the axial velocity profile of sparger bubbles would do much to aid general understanding of this type of system, but it must be conceded that the data in Figure 6.7 is insufficient to support further speculation.

6.1.2 Dense Phase Parameters

6.1.2.1 Dense Phase Voidage and Velocity

In a previous study (104) it is shown that dense phase voidage is insensitive to gas velocity in 0.05 and 0.14 m tubes, and that measurements in these tubes agree. In the 0.64 m tube, on the

other hand, it is demonstrated that ε_d as measured by the bed collapse technique is apparently lower and increases (toward the smaller tube value) with increasing gas velocity. This type of behaviour could be a result of the presence of partially defluidised material in the bed, but could equally well be a result of the application of the bed collapse technique to too large a unit. Uniform slumping is more difficult to achieve in a large vessel, and preferential slumping of certain sections of the bed could conceivably give rise to misleading results.

Dense phase voidage was measured in the 0.05 m unit and confirmed on a 0.14 m tube. A value of $\varepsilon_d = 0.622$ was obtained. Anomalous behaviour was observed in the 0.64 m unit, and it was decided that the value obtained in the smaller units should be assumed applicable to the large cold model. This assumption is consistent with results obtained during the Shell Chlorine [117,118] scale-up study, and is defensible in the light of uncertainties associated with the application of the bed collapse technique. This assumption may also be supported as follows: if regions of partially defluidised material are in fact present and faithfully reflected by the bed collapse technique, it seems unlikely that bubbles would be exposed to this relatively low-voidage dense phase material to any significant extent. Partially defluidised powder would, in all probability, be found at the vessel walls and in the immediate vicinity of the coils. Bubbles would tend to avoid such regions by their very nature, and effectively be exposed to fully expanded

dense phase material only. The low dense phase voidage measured by bed collapse experimentation in the large unit would accordingly represent a poorer estimate of ε_d as seen by the bubbles than that measured in the small unit.

The same overall reasoning applies to the dense phase velocity U_d. A value of 0.0079 m/s was measured in the 0.05 m tube and assumed applicable to the 0.64 m unit.

6.1.2.2 Downward Gas Drift Velocity

Downward gas drift velocities as measured by the tracer technique in the 0.05 m tube are shown in Figure 6.8. The tracer method worked reasonably well on this unit, and also performed satis= factorily when tested on a 0.14 m tube. However, application to the 0.64 m unit yielded no significant results: gross circulation patterns and a general lack of radial uniformity confounded both the measurement and the definition of a simple average downward drift velocity. Velocities of the order of 0.5 m/s were in fact measured, but these were probably not consistent with the definition as required by the Kunii-Levenspiel (28) gas division model. In order to satisfy the modelling requirements, the data in Figure 6.8 was assumed to apply throughout. A similar assumption was applied to the ratio of cloud to bubble volume α, and the impact of both of these assumptions on the modelling procedures is discussed in section 6.1.3.

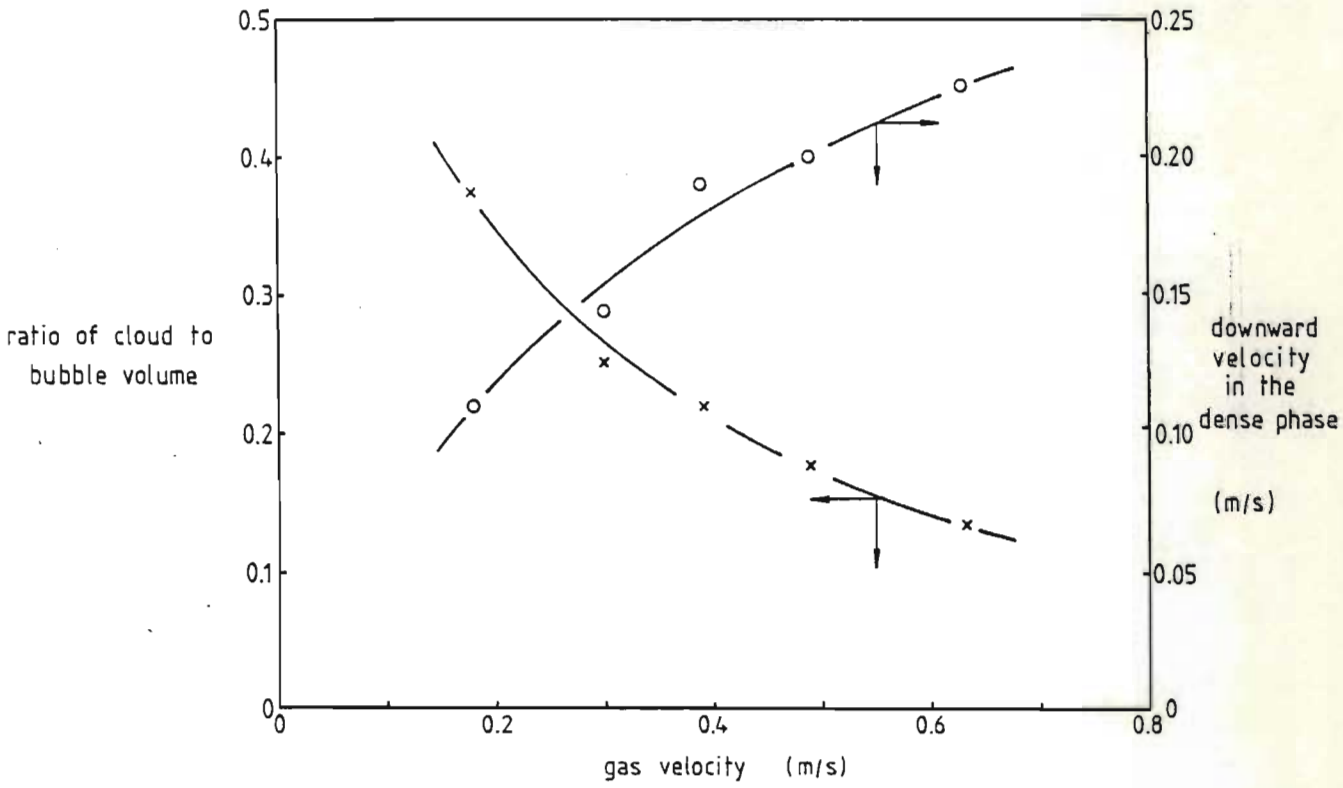

FIGURE 6.8 DOWNWARD DRIFT VELOCITY AND RATIO OF CLOUD (PLUS WAKE) TO BUBBLE VOLUME

6.1.3 Ratio of Cloud to Bubble Volume

The ratio of cloud to bubble volume α as calculated on the basis of equation (5.22) is shown in Figure 6.8 for the 0.05 m unit. Since no downward gas drift velocities were successfully recorded on the larger unit, an assumption was called for in order to satisfy the CCBM modelling requirements. It was reasoned that due to the low dense phase velocity relative to the bubble rise velocity, the bulk of the cloud-wake phase would most likely be centred in the wakes of the bubbles. If this be true, then the bubble wake data of Rowe and Partridge (27) would form a reasonable basis for estimating α in the large unit. However, it was also noted that the values in Figure 6.8 are in fair agreement with the range of possible values quoted by Rowe (64), and that a trend of decreasing α with increasing gas velocity might indeed be expected as coalescence and possible wake shedding effects come into play. It was therefore decided that, since the values obtained on the small unit were consistent with published data and the trend with gas velocity was not unreasonable, these values should be assumed applicable to the larger unit.

The impact of this assumption as well as its counterpart related to the downward gas drift velocity on the overall modelling scheme is not great. The inherent danger is that the CCBM model may be unfairly discriminated against if these parameter values are inappropriate, though it is easy to check this by testing the sensitivity of the model. In the early stages of this investigation the CCBM model was in fact run with α as an additional parameter to

be optimised against the experimental RTD data, and it was found that in the region of the optimum the sensitivity to changes in α was very weak indeed. This is not at all surprising, though, in view of the results quaoted in section 6.3.1 which suggest that the cloud and emulsion phases should be considered lumped to form a single dense phase. Though the model sensitivity to changes in downward gas drift velocity was not explicitly tested in the same way, the same remarks are assumed to apply.

6.2 General Characteristics of the RTD Data and Model Fitting

6.2.1 Experimental RTD Data

A time record of the kind of data that was obtained from the 0.64 m bed is shown in Figure 6.9. PRBS excitation is discernable in the signal from the lower sample station, though it is clear that some tracer dispersion has occurred. This is a result of the fluidised bed itself, as well as lags and dispersion processes in mainly the sample lines and FID units. It should be pointed out, however, that some sluggishness in the sampling system is not altogether undesirable.

Increasing the sample gas flow to the detectors has the effect of "sharpening up" the signal, but besides presenting possible linearity problems, makes system more sensitive to pressure fluctuations associated with bubble motion. The net result is a reduction in the signal-to-noise ratio. It should also be noted that dispersion in the sampling system is expected to impose a high-frequency limit on

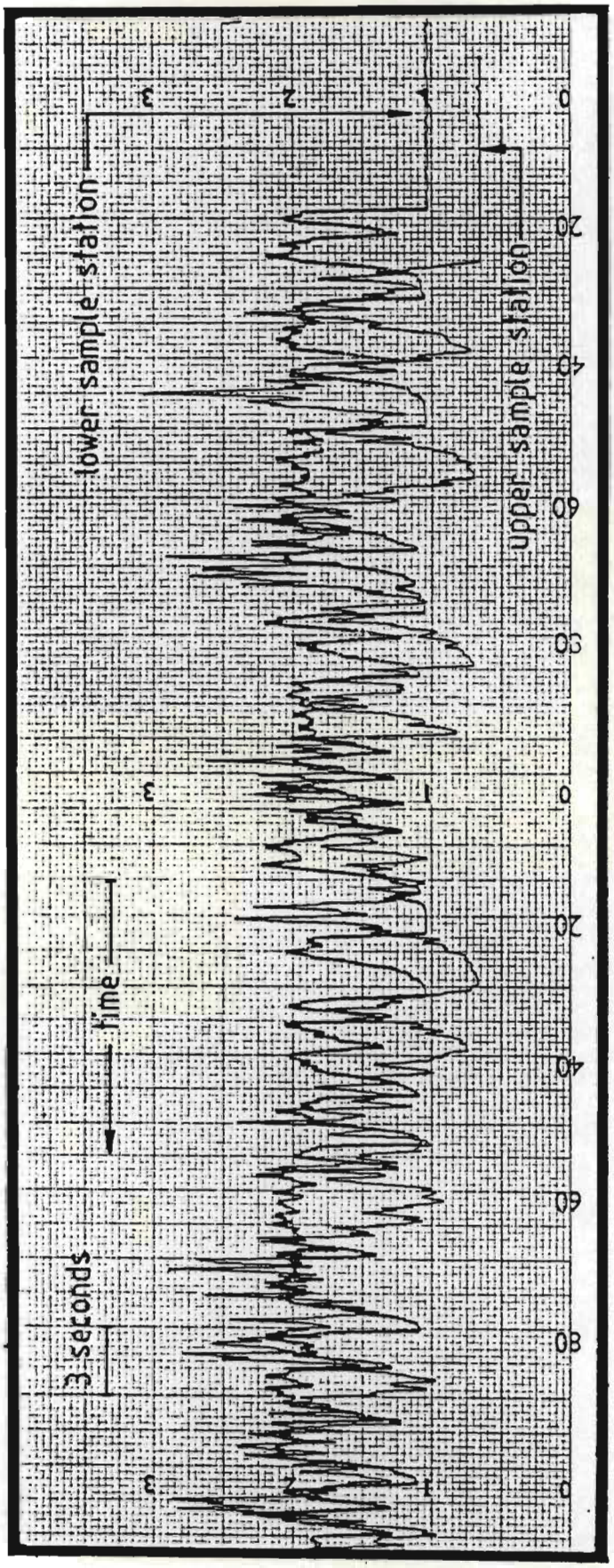

FIGURE 6.9 TYPICAL NOISE-CORRUPTED TIME-RECORD

the range at which useful information may be extracted.

The auto- and crosscorrelation functions are shown in Figure 6.10, and it appears that the noise elimination process is virtually complete. The lower sample station autocorrelation deviates somewhat from that of the PRBS signal as expected, the difference being ascribed to dispersion effects in the bed and sampling system as discussed above. Information in the tail of the crosscorrelation is clearly lost - this is regarded as an inherent system limitation.

It is interesting to compare the mean residence time of gas in the bed as computed from the bed volume and volumetric flow with the difference in first moments of the two curves in Figure 6.10. Theoretically they should give the same result, viz.:

$$\frac{L_t \varepsilon_f}{U_o} = \bar{t}_{auto} - \bar{t}_{cross} \qquad (6.4)$$

The RHS of equation (6.4) as applied to the data in Figure 6.10 comes to 8.02 s, and after correction for differences in sampling system dead and rise times this becomes 7.33 s. The corresponding LHS value comes to 6.64 s, i.e. the two (independent) calculations agree to within 11%. This is probably as good as might be expected under the circumstances: similar data published in context of the Shell Chlorine study (118) contains deviations of up to 21%. In any event, closure to within a reasonable limit certainly

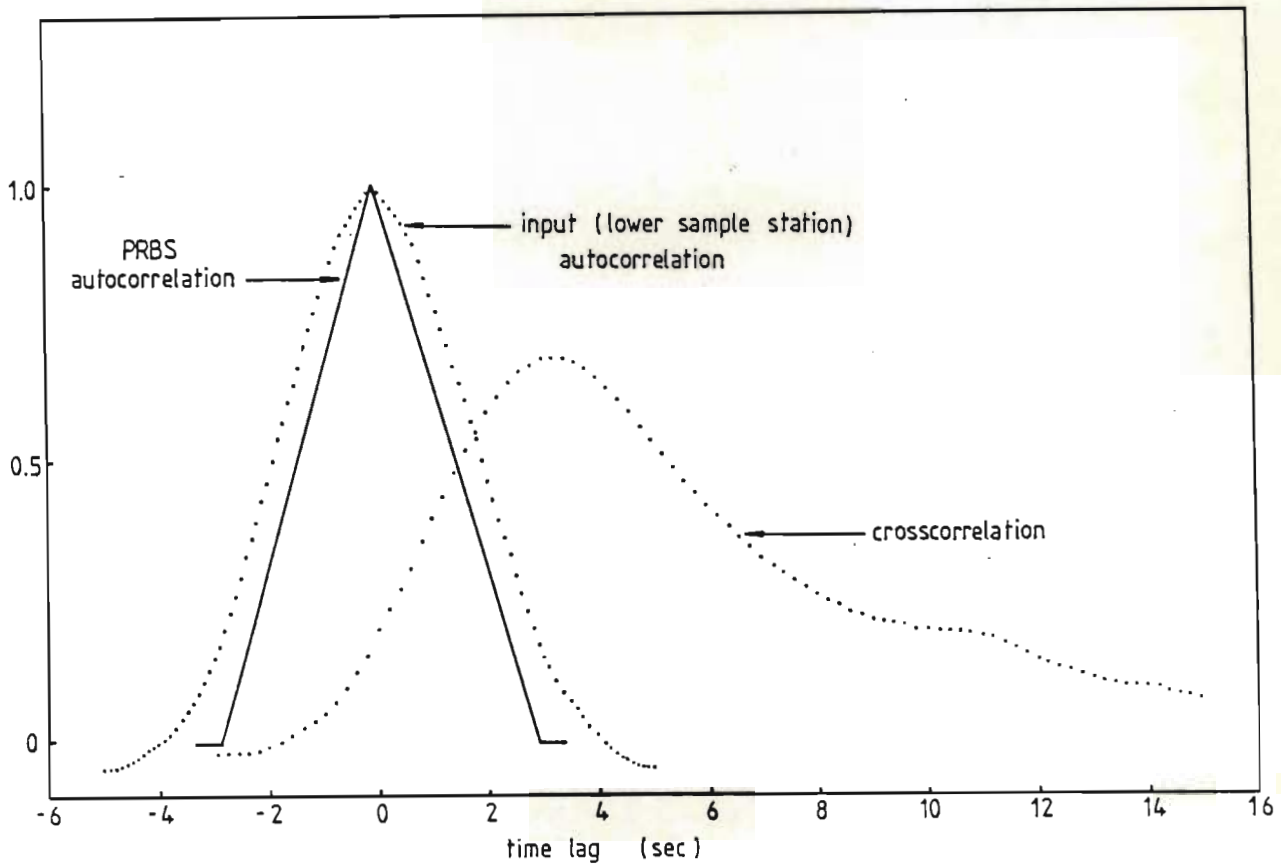

FIGURE 6.10 TYPICAL AUTO- AND CROSSCORRELATIONS

emphasises the fact that the data is consistent and reflects true system information.

The frequency response derived from this data is shown in Figure 6.11 as magnitude ratio and phase angle versus frequency. At frequencies beyond about 0.9 radians per second the response is seen to deviate from the trajectory established at lower fre= quencies - this type of deviation was interpreted as the upper frequency limit of useful information. A magnitude ratio of -12 dB or attenuation by a factor of about 4 is regarded as typical, and failure to obtain higher frequency information probably reflects once again an inherent system limitation in the form of dispersion in the sample lines and FID units.

Attenuation by a factor of about 4 appears to be typical for this type of experimentation. Everson (110) in fact produced very similar magnitude ratio plots for a system involving an absorption column and a radio-active tracer.

The reproducibility of the frequency response is effectively demonstrated in Figure 5.13. Despite differences in PRBS decision time, the three responses shown are remarkably close.

6.2.2 Model Fitting

Possibly the most critical step in the entire procedure is the actual fitting of a model to the experimental frequency data.

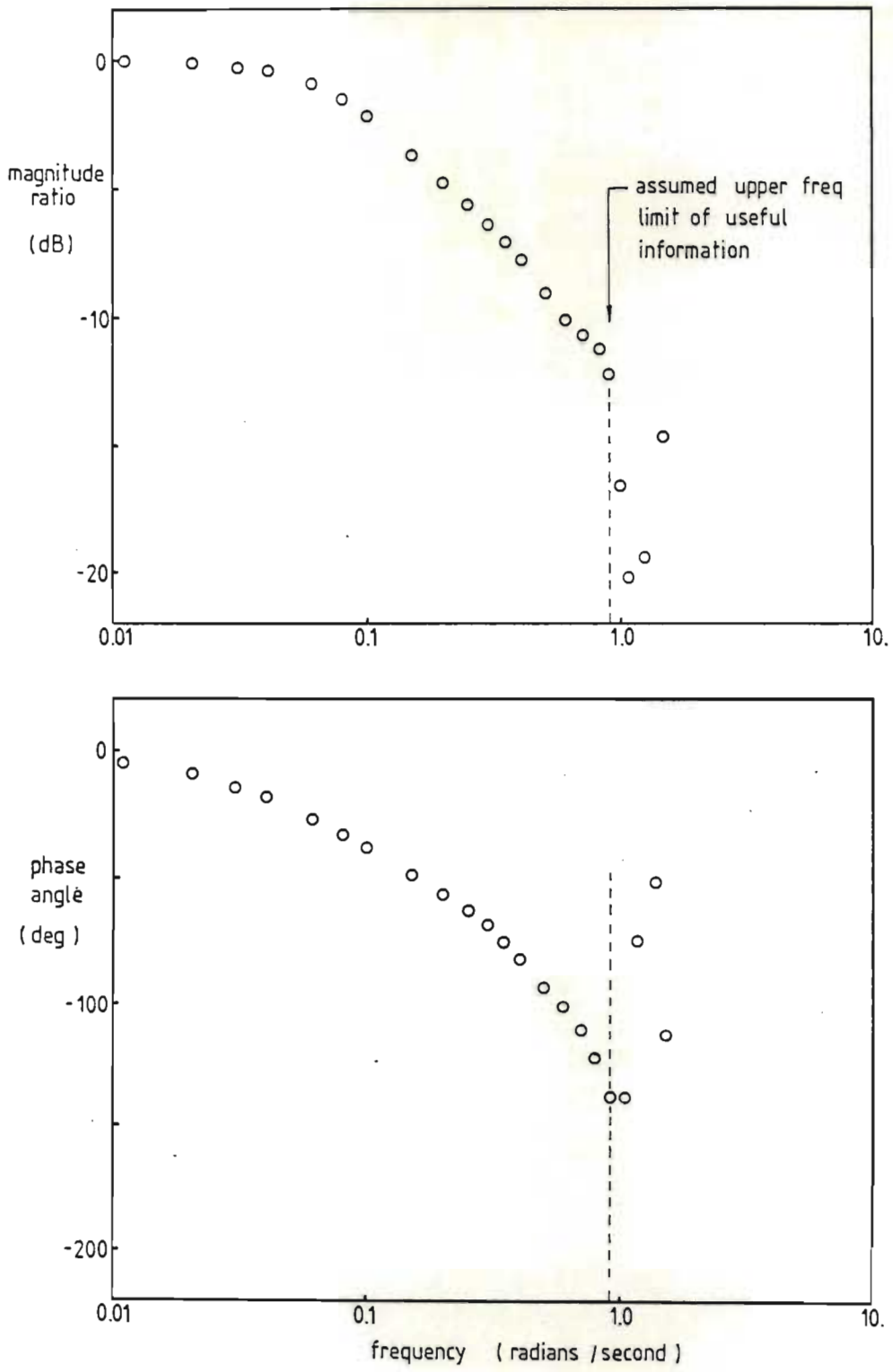

FIGURE 6.11 EXPERIMENTAL FREQUENCY RESPONSE

Each of the models considered contains two independent parameters, and the simplex routine sets out to vary these in such a way as to locate a minimum in the objective function. This process may be viewed as searching for the lowest point on a landscape defined by the difference between the model and the experimental frequency response, with the two model parameters as horizontal or ground co-ordinates and the objective function describing vertical elevation. This landscape may be conveniently depicted as a contour plot.

Certain requirements as regards the nature of this contour plot must be satisfied in order to ensure full significance in the result. Firstly, the parameter values at the optimum must be physically plausible - for example, a negative crossflow ratio would have no meaning. Secondly, the model parameters must be uncorrelated. If the contours display an elongated furrow or valley which does not run parallel to one or the other of the model parameter axes, the chances are that the optimum will not be unique. In other words, a range of pairs of parameter values will satisfy the model fitting criteria equally well, and it will not be possible in general to specify an exact value for either.

Contour plots for the five general models as applied to the experimental data in Figure 6.11 are shown in Figure 6.12. The contours for the MBT and MVD models are very similar as might be expected from their formulation - both are more specific in

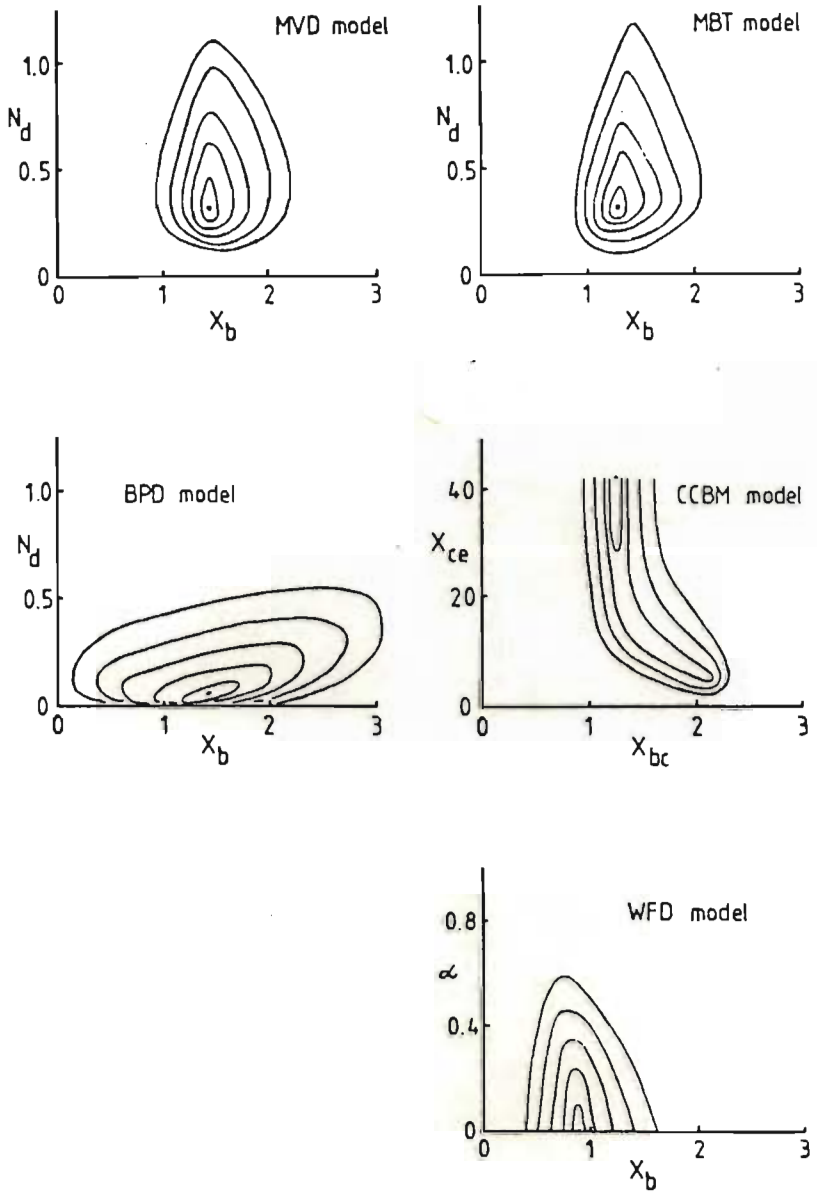

FIGURE 6.12 CONTOUR PLOTS FOR THE FIVE GENERAL MODELS

crossflow ratio than in dense phase dispersion number, and the two parameters appear to be uncorrelated.

The BPD model contour plot reveals a very poor crossflow sensitivity and a definite degree of correlation between cross= flow and dense phase dispersion number. This may seem surprising, but must be accepted in view of the model formulation and particu= larly the boundary condition at a theoretically infinite bed height.

The CCBM model contour diagram shows some correlation in the region of low X_{ce} values, but this disappears at higher values of this parameter and the system becomes very specific indeed to X_{bc}. Beyond a certain value X_{ce} in fact ceases to influence the optimisation, and an "optimum" is returned at whatever practical upper limit imposed on this quantity.

The contour plot for the WFD model shows that the optimisation is sensitive in X_b and converges on a zero α or cloud thickness.

Closure between the five models considered and the experimental data is shown in Figure 6.13. On the co-ordinate system used there is no clear distinction between the MBT and MVD model frequency response profiles, and it is clear that these models constitute a better process description than to the BPD, CCBM or WFD models.

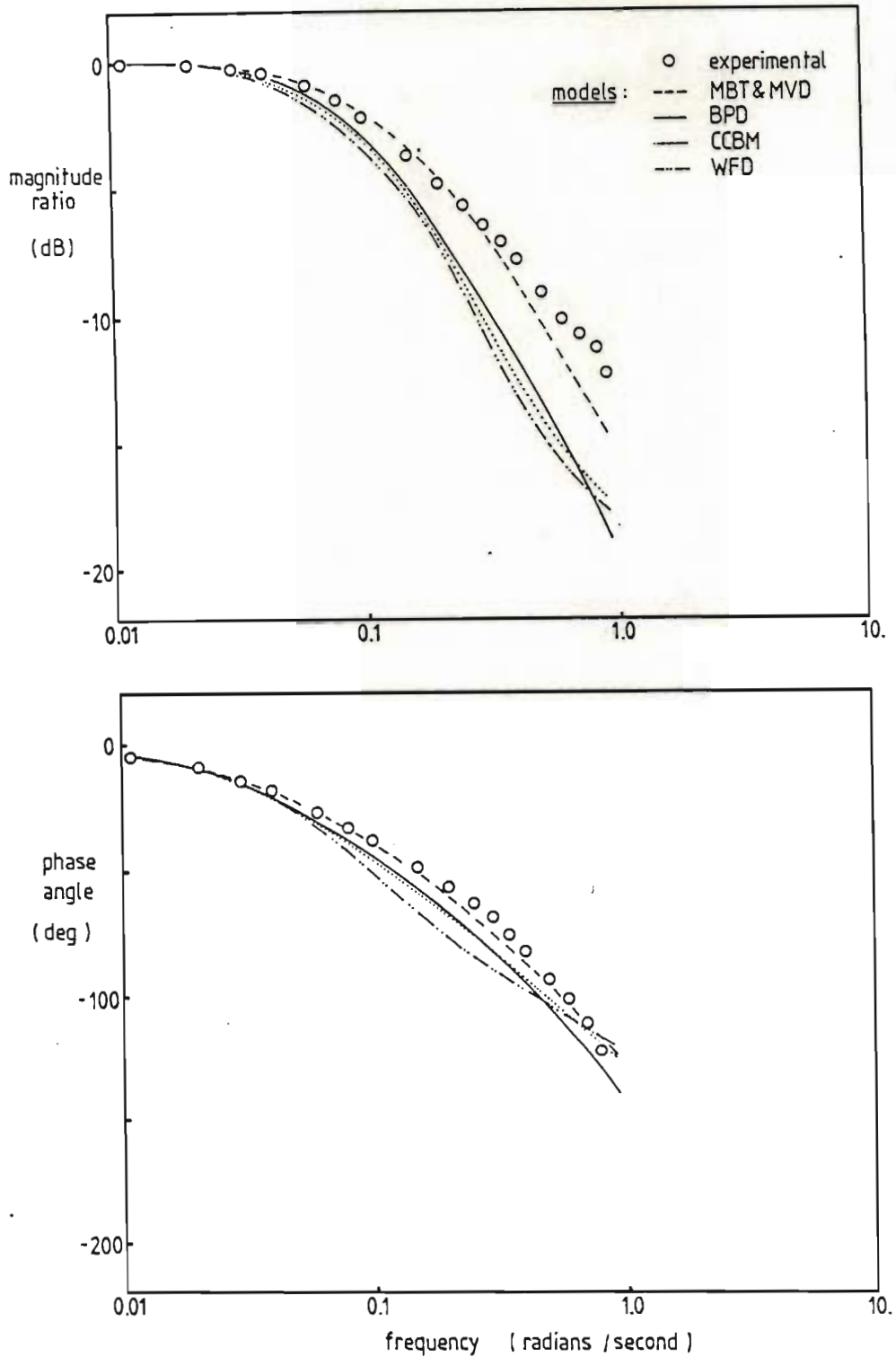

FIGURE 6.13 CLOSURE BETWEEN EXPERIMENTAL AND MODEL FREQUENCY RESPONSES

In order to test the robustness of the parameters optimised by the model fitting, it is necessary to examine the effect of possible errors in the auxiliary parameters. If, for example, average bubble velocity was out by 10%, how strongly would this affect the estimated crossflow ratio?

The effect of a 10% variation in superficial velocity, average bubble velocity and minimum expanded bed height is shown in Table 6.1. The MBT model is employed for this sensitivity analysis - the reason for this choice of model will become clear later. The dense phase parameters ε_d and U_d are not included in Table 6.1, since these auxiliary parameters were held constant throughout the entire investigation.

An examination of Table 6.1 shows that errors in L_f are weakly reflected in X_b, and that errors in U_b lead to similar errors in X_b on a percentage basis. Errors in superficial gas velocity, on the other hand, have a dramatic effect on the crossflow estimate. This is not particularly disturbing, though, since U_o is measured directly and large errors are not expected.

The dense phase dispersion number is far more sensitive to auxiliary parameter errors than is the crossflow ratio. This is very much in line with the MBT model contour plot in Figure 6.12 - the optimisation procedure is more specific in X_b than in N_d. This

MODEL: MBT

PARAMETER VARIED	VALUE INCREASED BY	CORRESPONDING CHANGE IN X_b	CORRESPONDING CHANGE IN N_d
U_o	+10%	-29%	-46%
	-10%	-70%	+193%
U_b	+10%	+7%	-24%
	-10%	-14%	-37%
L_f	+10%	-1%	-29%
	-10%	+1%	+37%

TABLE 6.1 SENSITIVITY ANALYSIS

is perhaps not too disturbing as far as this investigation is concerned, since the aim is to measure X_b rather than N_d. The statistical significance of values returned for N_d is clearly less than that of values returned for X_b, so it would seem inappropriate to attempt any meaningful analysis of this dense phase mixing parameter.

6.2.3 Definition of an Error Index

Closure between a particular model and a set of experimental data is reflected in the objective function value at the optimum parameter combination. For one particular experimental frequency response, objective function values for different models provide a measure of which model best describes the system. However, absolute objective function values do not consitute a good basis for comparing closure on different experimental frequency responses. The objective function value (at the optimum model parameter combination) depends on the number of frequency points involved, as well as on the spread. At very low frequencies none of the models deviate significantly from the experimental data; the greatest deviation occurs at some higher frequency. There does not appear to be any obvious way of ensuring that the objective function value for one set of data is directly related to that of another.

A slightly different measure of the residual error between the model and the experimental frequency response is called for. One possibility is to define an index based on closure between the best-fitting model and the experimental frequency response, and to measure all the other models relative to this. This approach was adopted in the present study, and an error index (abbreviated EI) was defined as follows: the best-fitting model for a particular experimental response is assigned an EI of unity. The other models are then assigned indices given by the ratio

of the objective function minimum to that of the best-fitting model. An EI of one is thus always present and associated with the best model, and all the other model EI's are greater than unity. This definition allows a meaningful average error index to be computed for a single model over a number of experimental frequency responses, since all runs are assigned an equal weight.

6.3 Model Screening

6.3.1 General Screening

The results of the general model screening are given in Table 6.2 in the form of average error indices, and a full breakdown of the parameters and EI's is given in Appendix F. It should be noted that

MODEL	TUBE DIAMETER			OVERALL AVERAGE EI
	0.05 m	0.64 m		
		Coils	No coils	
MBT	1.12	1.02	1.02	1.06
MVD	1.25	1.05	1.03	1.13
BPD	3.55	6.23	10.28	5.55
CCBM	4.67	6.97	7.81	6.09
WFD	5.01	7.59	10.08	6.78
No. of runs	19	21	5	45

TABLE 6.2 GENERAL SCREENING ERROR INDICES

an average error index of unity implies that the particular model fitted better than any other tried in every instance.

The results show that on average, the MBT model fits the experimental data better than any other in both slugging and bubbling units. The MVD model is clearly not far behind, and the residual error obtained in fitting the other three models is significantly greater.

The fact that a single model describes both bubbling and slugging systems with the greatest degree of precision is particularly gratifying. This result implies that the MBT model reflects physical reality more faithfully than any other model tested, and that the assumption of multiple plug flow units for the bubble phase is sound.

The MBT model accounts for two phases only. This suggests that the bubble cloud is indeed vanishingly thin as predicted by Davidson's (17) bubble model, and this is supported by the fact that the WFD model almost always returned a zero cloud thickness. The other three-phase model, i.e. the CCBM model, commonly returned an effectively zero cloud-emulsion mass transfer resistance, particularly in the 0.64 m unit. This suggests that there is no distinction between the cloud and emulsion phases, and further supports the conclusion that only two phases are effectively present.

The behaviour of the BPD model is somewhat surprising. Poor closure was obtained with data from the 0.64 m unit, and from beds of about a meter of less in depth in the 0.05 m tube. For a ca. 2.4 m bed in the 0.05 m tube, however, closure was in fact better than that achieved by applying the MBT model. At a bed height of about 3.5 m the situation was reversed once again, but the BPD maintained a degree of closure similar to that of the MVD model.

This behaviour could be interpreted as implying that the BPD model adequately describes fully established slug flow. It is not immediately clear why the formulation of this model should be consistent with a slug flow situation, though rapid nose-to-tail mixing of gas within the rather long slugs observed (0.3-0.4 m) could conceivably be consistent with axial dispersion in the bubble phase.

The performance of the WFD model is particularly disappointing. This model is more tractable than any of the others, and even a moderately better degree of closure with the experimental data might have promoted its use in design and control. It could be argued that, on the basis of Werther's (98) presentation of the model, it should reduce to something similar to the MVD model for a zero cloud thickness. This is not the case, however, since the mathematical formulations of and solutions to these models are quite different. In particular, it should be noted that the MVD

model solution is third order in z, whereas that of the WFD is only first order.

6.3.2 Sparger Screening

Average error indices for the sparger screening are given in Table 6.3, and a full breakdown is included in Appendix F as before.

The laterally segregated bubble phase model describes the results better than its mixed bubble phase counterpart in every instance. This suggests that sparger bubbles tend to retain their identity as they pass through the bed, i.e. that coalescence effects between grid and sparger bubbles are not very strong.

Conclusions of this nature should be regarded with caution, since the argument is very indirect. However, the suggestion that sparger bubbles retain their identity is consistent with the bubble velocity axial dependence shown in Figure 6.7 - average rise velocity of the sparger bubbles (below about 1.5 m above the sparger) does not appear to be dominated by that of bubbles rising from the grid.

6.4 Crossflow Ratio: The Effect of Vessel Geometry

In a fluidised bed containing a fine powder and operating at a gas velocity of some tens of centimeters per second, the gas which enters the dense phase from the grid directly is very small compared to that

MODEL	AVERAGE ERROR INDEX
LSBP	1.00
LMBP	6.69
No. of runs	18

TABLE 6.3 SPARGER SCREENING ERROR INDICES

which enters in the form of bubbles. Under these conditions the hydrodynamic resistances may be considered to function in series, and in a reactor operating under conditions of interphase mass transfer control conversion would be related mainly to crossflow ratio. In a situation of this type reactant material which finds its way into the dense phase is rapidly consumed, and overall conversion is effectively dictated by the percentage of gas originally present in the bubble which is swept across the bubble-dense phase interface. Dense phase mixing is of secondary importance in situations of this nature, provided the reaction velocity constant is high enough to ensure rapid reaction despite possible dilution effects in the dense phase.

Mass transfer-limited conversion represents a kind of performance ceiling for a fluidised bed reactor. If, for example, a reactor is operated under conditions of kinetic control, overall conversion will be related mainly to the intrinsic reaction rate. The partial pressure or concentration term(s) in the kinetic expression will be affected by mixing in the dense phase, and crossflow will probably be of relatively minor importance. If the situation were now altered by decreasing the reaction resistance by (say) increasing the temperature, overall conversion would initially increase. However, a point would eventually be reached where the mass transfer limitation took effect, and further temperature increases would do very little to increase overall conversion. The performance ceiling would have been reached, and to improve performance further one would need to change the crossflow ratio, i.e. the hydrodynamics of the system.

Crossflow ratio is a very important parameter in scale-up. If the pilot unit which serves as the basis for a demonstration or full-scale design is mass transfer limited, it is vitally important to ensure that the crossflow ratio in the large unit is at least as high as it is in the small one if conversion is to be maintained. If the pilot unit is not mass transfer limited, it is still advisable to ensure that the crossflow ratio will be high enough in the scaled-up reactor. It is quite conceivable that, as vessel diameter increases, an interphase mass transfer limitation not evident in the small unit could intrude and seriously depress conversion.

The importance attached to X_b in scale-up also applies to the evaluation of reactors with different internal geometries. For example, what is the effect of introducing baffles or cooling coils into the bed? If the system is mass transfer limited, the resulting change in crossflow ratio will also reflect the change in overall conversion. If the reactor is not mass transfer controlled, the change in X_b will probably reflect a change in performance ceiling rather than actual performance.

Overall, it is clear that crossflow ratio is probably the most important parameter describing the hydrodynamics of a fluidised bed. In this section the effect of scale-up and internal geometry on crossflow is examined on the basis of the results from the best-fitting model in each model category. The MBT model crossflow ratios are employed in all cases barring those in which the

sparger was present, and those returned by the LSBP model are used otherwise.

6.4.1 The Effect of Tube Diameter

Crossflow ratios obtained on the 0.05 and 0.64 m units are shown in Figures 6.14 and 6.15 respectively. The general trends are similar, and the strong dependence on superficial gas velocity is understandable in terms of bubble residence time effects. The superficial velocity effect appears strongest in a deep bed in the 0.64 m unit - this is consistent with the bubble velocity data given in Figure 6.3.

Crossflows are higher in the 0.05 m tube than in the 0.64 m unit. A cross-plot of the data in Figures 6.14 and 6.15 (at constant superficial velocity) is given as Figure 6.16, and this effectively illustrates the extremely powerful scale-up effect inherent in the system studied. According to the trajectories in Figure 6.16, a 4 m bed in the 0.64 m unit is equivalent to about a 0.2 m bed in the 0.05 m unit (from a crossflow point of view).

Figure 6.16 also illustrates some general characteristics of the system hydrodynamics. Firstly, most of the interphase transfer occurs in the bottom meter or so of the bed. The design of the gas distributor probably has a strong influence on the amount of crossflow activity in this region, and the enormous difference between the two units is probably typical of a porous plate versus a multi-orifice device.

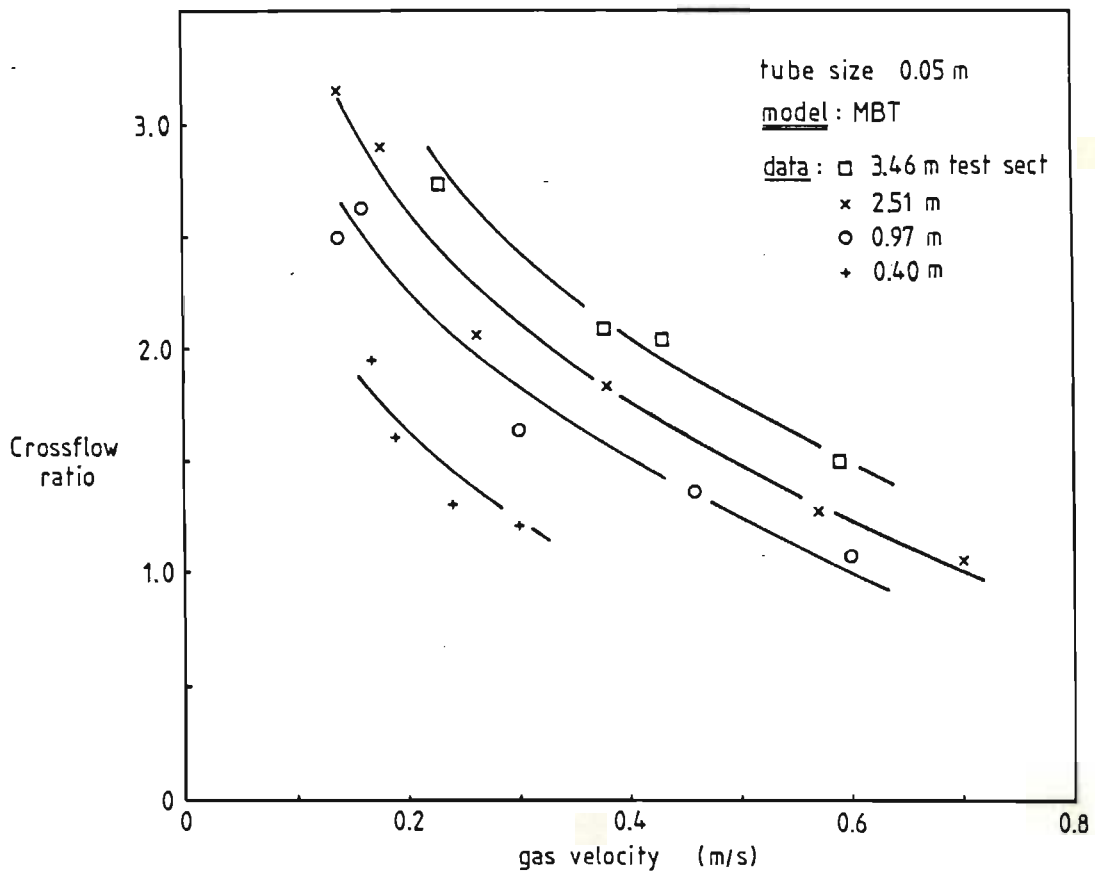

FIGURE 6.14 CROSSFLOW RATIO ON THE 0.05 m UNIT

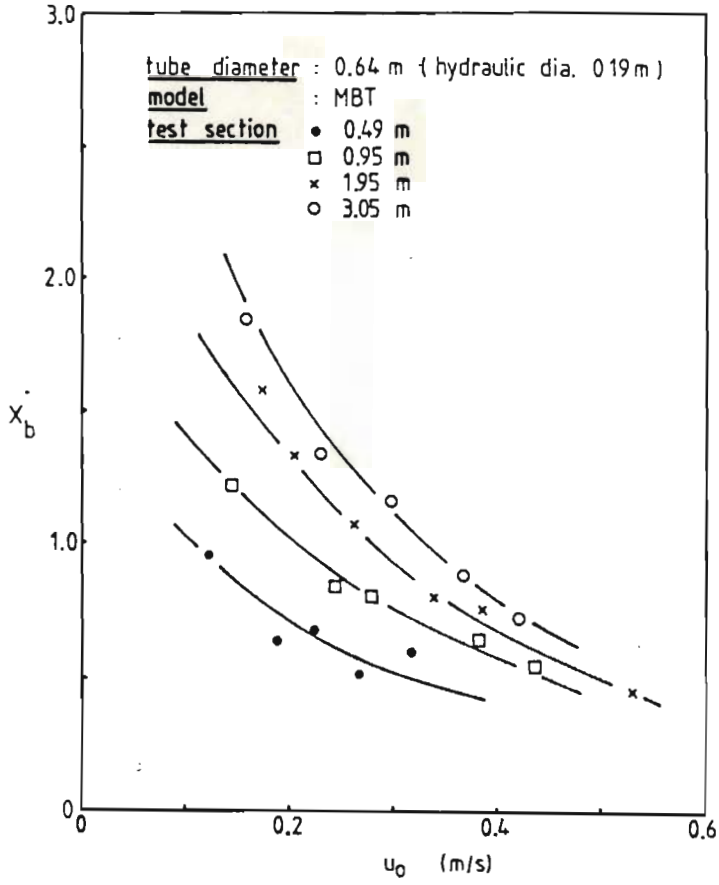

FIGURE 6.15 CROSSFLOW RATIO ON THE 0.64 m UNIT

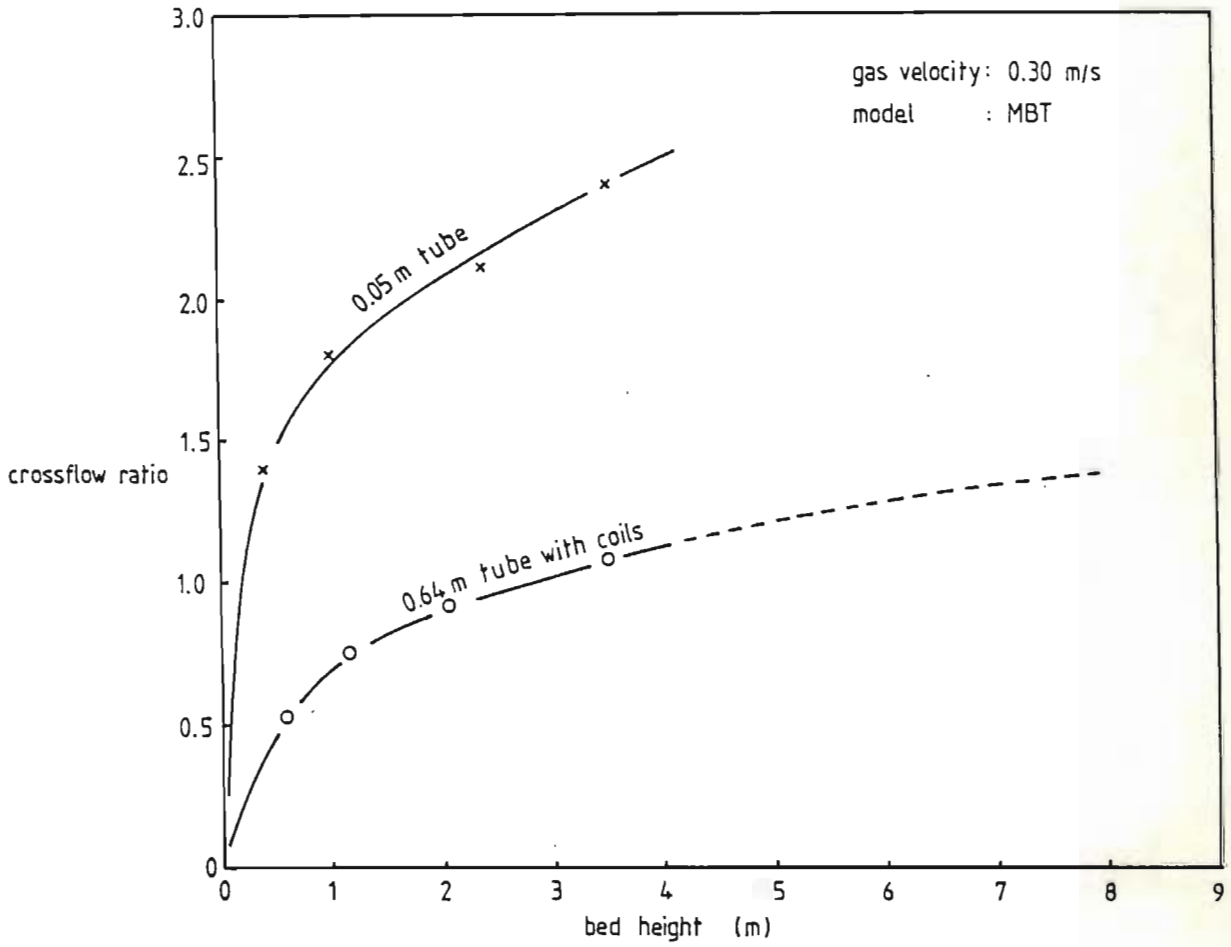

FIGURE 6.16 CROSSFLOW RATIO vs BED HEIGHT: THE SCALE-UP EFFECT

Crossflow activity in the upper regions of the bed appears to be fairly low in both cases. The 0.05 m tube remains more active, though this is probably a simple bubble/slug residence time effect. The rather flat profile in the upper regions of the large unit suggests that increasing the bed height would be of little benefit, since a large increase would probably lead to a marginal increase only in X_b.

6.4.2 The Effect of Vessel Internals

One of the first modifications attempted on the Brownsville units was the introduction of baffles (1). The results do not appear to have been very encouraging, and later dummy coils were installed to reduce the hydraulic diameter of the reactors. This change also appears to have failed to improve reactor performance to any significant extent (1).

In this study, the effect of hydraulic diameter was tested by running the 0.64 m unit with and without the (dummy) vertical cooling coils. With coils in place the hydraulic diameter came to 0.19 m, and with no coils essentially 0.64 m. To make the test as sensitive as possible, it was necessary to run at the maximum bed height the cold model would safely allow (i.e. a 3.05 m test section and about a 3.5 m bed height).

The crossflow results are shown in Figure 6.17. It appears that the presence or otherwise of coils has very little effect on

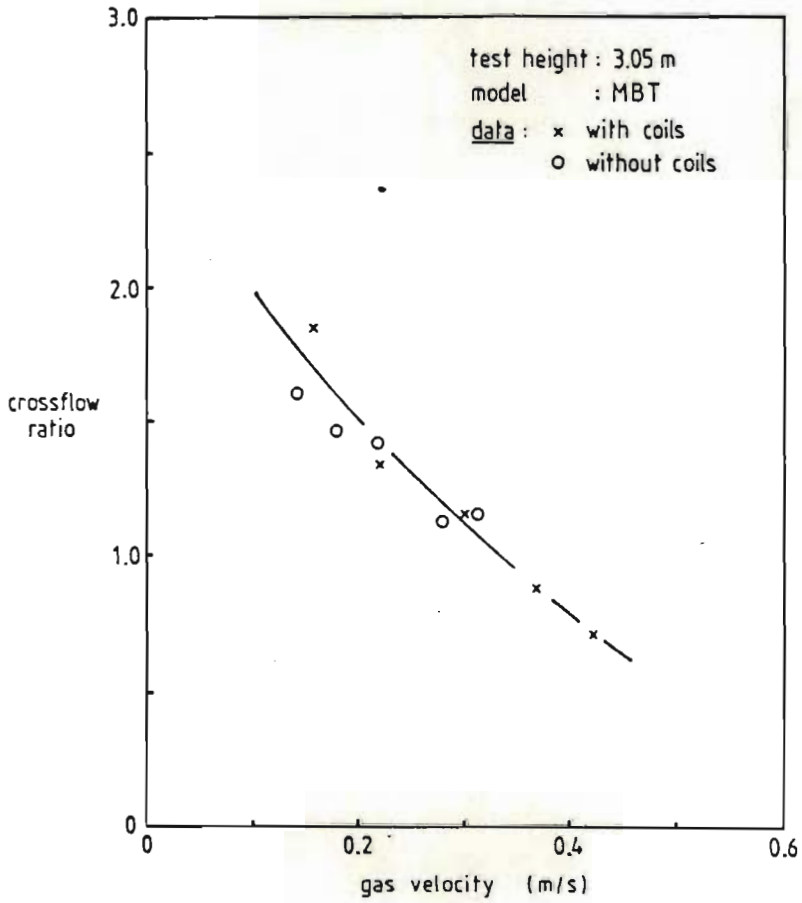

FIGURE 6.17 EFFECT OF VERTICAL COILS IN THE 0.64 m UNIT

interphase mass transfer, and this is certainly consistent with the performance of the Brownsville reactors. Physically, this result suggests that, even though a bubble velocity effect is evident as discussed previously, vertical coils do little to limit bubble size - this has in fact been observed by Botton (119) amongst others.

Figure 6.17, taken in conjunction with Figure 6.16, suggests that the upper regions of a large bed are inactive and insensitive to (all but radical) design changes. Furthermore, the presence of a strong axial gradient in crossflow activity possibly explains the failure of the hydraulic diameter concept as applied to fluidised beds. In this system at least, interphase transfer appears to be influenced largely by distributor design, and the geometry of the containing vessel in the upper regions is apparently of relatively minor importance.

6.4.3 The Effect of the Sparger

Crossflow between sparger bubbles and the dense phase as optimised on the basis of the LSBP model is illustrated in Figure 6.18. The general characteristics of this data are similar to those of the data shown in Figure 6.15, and a cross-plot at constant gas velocity is shown in Figure 6.19.

In Figure 6.19 crossflow ratios from two different model types are compared. The main difference, besides the presence or otherwise

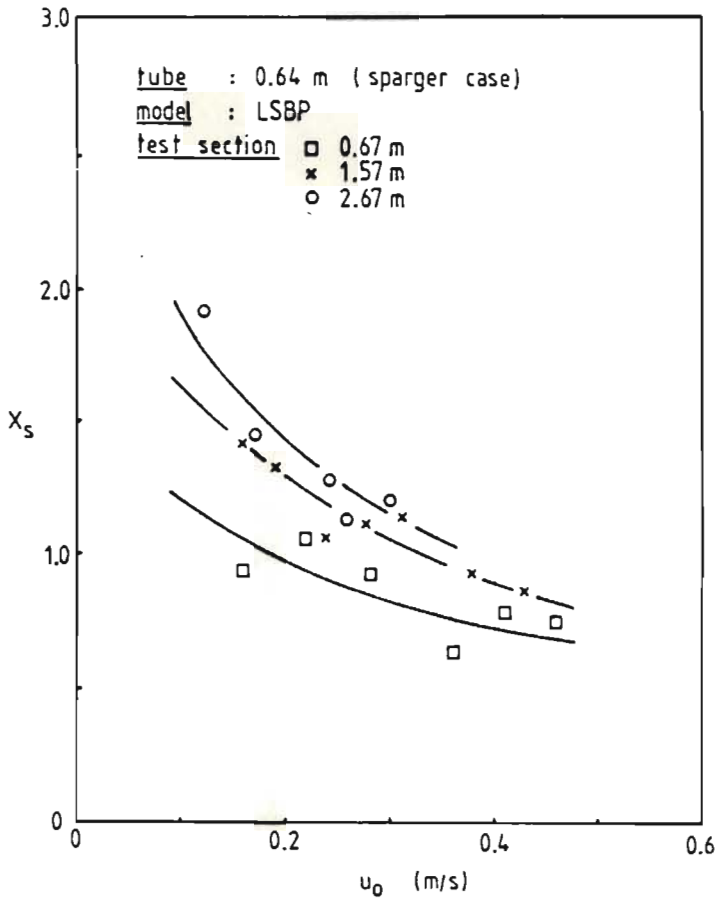

FIGURE 6.18 SPARGER CASE CROSSFLOW RATIOS

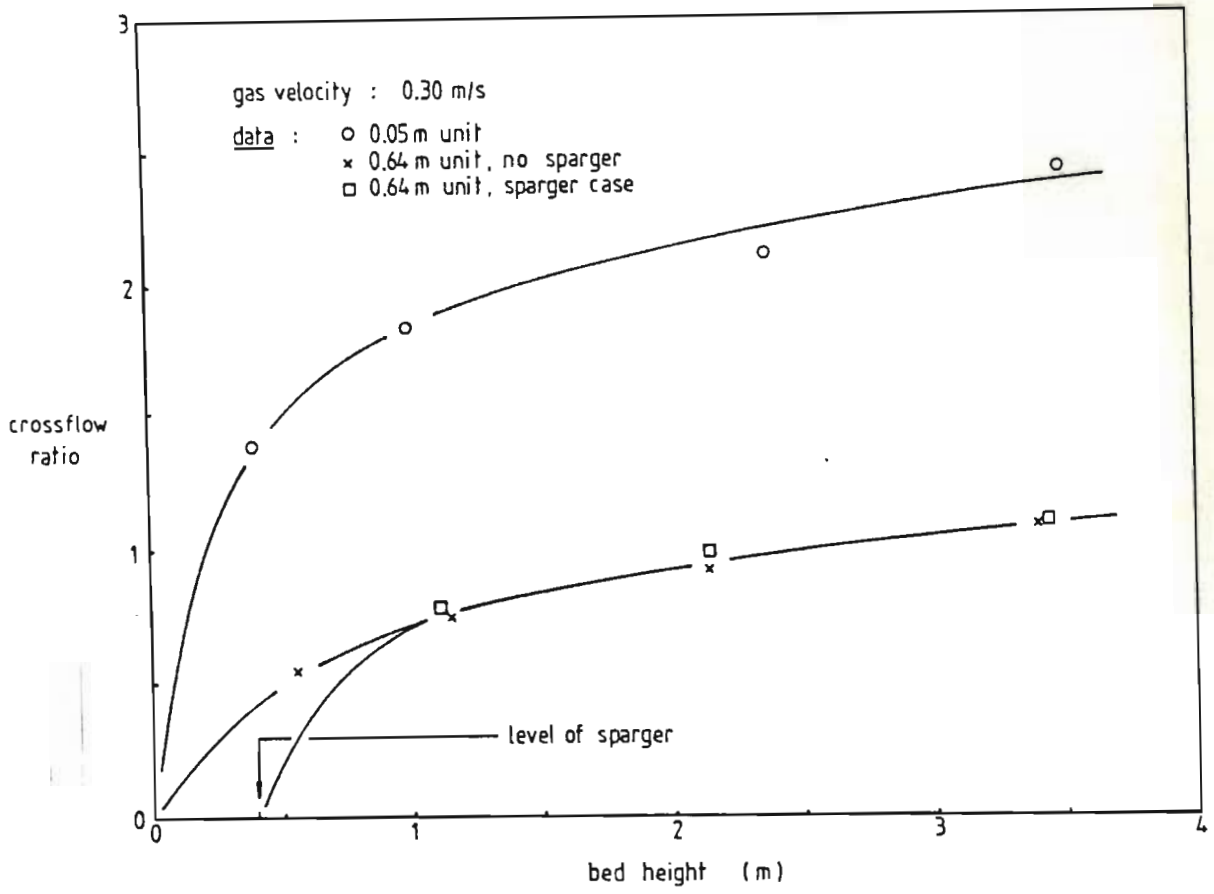

FIGURE 6.19 CROSSFLOW PROFILES IN SPARGER-CONTAINING AND SPARGER-FREE BEDS

of a split feed system, is that axial mixing in the bubble phase is accounted for in one model and not in the other. The nature of the model affects the crossflow estimate, and it would seem fair to compare LSBP model crossflows with MVD rather than MBT model ones. However, since the MBT model is accepted as the basis for crossflow comparison (in all cases where the sparger is not present), a slightly different approach is called for.

The difference between crossflows determined by applying the MBT and MVD models may be regarded as a measure of the effect of accounting for axial bubble mixing. From the data in Appendix F an average difference of 6% in X_b is evident, i.e. the MVD model returns crossflows which are, on average, 6% higher than those returned by the MBT model. It would seem reasonable, therefore, to decrease the LSBP model crossflow estimates by this amount prior to comparing them to MBT data - this has in fact been done in the preparation of Figure 6.19.

The data in Figure 6.19 suggests that the sparger does not significantly affect the crossflow progression. A region of vigorous mass transfer activity immediately above the sparger is evident, and this is probably analogous to the grid region in the sense that the design of the nozzles is likely to have a strong influence on crossflow. The fact that a similar amount of mass transfer activity occurred near the grid and just above the sparger is not surprising, since the nozzle outlets on the two gas distribution systems were essentially the same.

In practical terms, the results in Figure 6.19 suggest that the sparger may be employed to move the principal reaction zone closer to the cooling coils without any anticipated change in the quality of gas-solids contacting.

6.5 Axial Dependence of the Mass Transfer Coefficient

The axial crossflow profiles shown in Figure 6.16 are characterised by rapid activity in the grid region and a slower rate of inter= phase transfer higher up. It has been suggested that the design of the gas distributor is important in determining crossflow in the grid region, but no explanation of how interphase transfer and grid design are related is put forward.

Intuitively, one might expect some hydrodynamic property (describing mass transfer) to remain constant with bed height. Small bubbles are generated at the gas distributor, and these grow as they rise. A strong axial profile in bubble to dense phase interfacial area must exist as a result, and a question which arises is: does this axial dependence explain the shape of observed crossflow profile? If it does, one would expect to find an inter= phase mass transfer coefficient based on bubble to dense phase interfacial area to remain constant with bed height.

The data generated in this study does not allow a direct examination of bubble to dense phase interfacial areas, and certain assumptions are called for if an MTC based on interfacial area is to

be computed. Calculations of this nature do not prove anything, since they are not based directly on experimental observations. However, it is the intention of the author to show that the crossflow profiles generated in this study are at least consistent with the concept of an axially invariant MTC based on interfacial area.

6.5.1 MTC Based on Bubble Volume

By definition, crossflow ratio X_b is related to a mass transfer coefficient based on bubble volume:

$$(K_{be})_b = \frac{X_b \, U_b}{L_f} \tag{6.5}$$

This expression is inherent in the model formulations, and is understood to represent averaged or lumped quantities. More correctly, one could write:

$$\int_0^{L_f} (K_{be})_b \, (z) \, dz = \left(\frac{X_b}{L_f}\right) \int_0^{L_f} U_b(z) \, dz \tag{6.6}$$

The bubble velocity measurement technique employed in this study returns averaged or integrated quantities, and the RHS of equation (6.6) may be computed directly. Experimentation at different bed heights (with the application of a lumped parameter model at each stage) may therefore be regarded as measuring an integrated MTC for various upper limits of integration.

One way of extracting a local MTC profile from height-averaged data is to assume a form of z-dependence. The integrated form of

the assumed expression may be compared with the experimental height-averaged data, and the former adjusted for maximum closure. The local profile arrived at in this manner is not unique - a different assumed form of dependence would clearly yield a different result.

For practical purposes, however, it is probably sufficient to employ an expression with good flexibility and reasonable boundary conditions. At zero bed height, for example, one would expect $(K_{be})_b$ to assume moderate to large values, but to tend to neither zero nor infinity. At very large values of z, on the other hand, $(K_{be})_b$ might be expected to tend to some constant value. An expression which meets these requirements is:

$$(K_{be})_b\ (z) \quad = \quad a + b.\exp\ (c.z) \qquad (6.7)$$

where a, b and c are constants. This expression is in fact the same as that employed for extracting a local bubble velocity profile from height-averaged measurements (see Section 6.1.1.2). The main difference is that in this case the constant a is expected to be smaller than b.

Application of equation (6.7) to the data in Figure 6.16 with constant optimisation by the simplex technique leads to:

$$(K_{be})_b\ (z) \quad = \quad 3.7\ \exp\ (-2.8\ z) + 0.15 \qquad (6.8)$$

for the 0.05 m tube, and

$$(K_{be})_b\ (z) = 1.37 \exp(-1.8\ z) + 0.28 \qquad (6.9)$$

for the 0.64 m unit. $(K_{be})_b$ and z are in reciprocal seconds and m/s respectively, and equations (6.8) and (6.9) are plotted in Figure 6.20. The difference in grid region activity shows up strongly, and beyond about 0.7 m above the distributor the bubbling bed appears to be more active on a unit bubble volume basis. This may seem surprising at first, but is shown in Section 6.5.3 to be consistent with published literature results.

6.5.2 Bubble to Dense Phase Interfacial Area

The local bubble velocity profile inferred from height-averaged measurements on the 0.64 m unit, as described in Section 6.1.1.2, is given by:

$$U_b(z) = 3.24 - 2.38 \exp(-0.32\ z) \qquad (6.3)$$

No direct measurement of bubble size is carried out in this study. However, as discussed in Section 6.1.1.2, plausible bubble diameters emerge if Davidson and Harrison's (19) bubble rise expression is solved for d_b with ϕ = 1.5-1.6. The selection of a value for ϕ is rather arbitrary, and before proceeding it would seem worthwhile to apply some kind of cross-check.

Davidson and Harrison's (39) expression for $(K_{be})_b$, in conjunction with the proposed bubble size profile, should generate an MTC

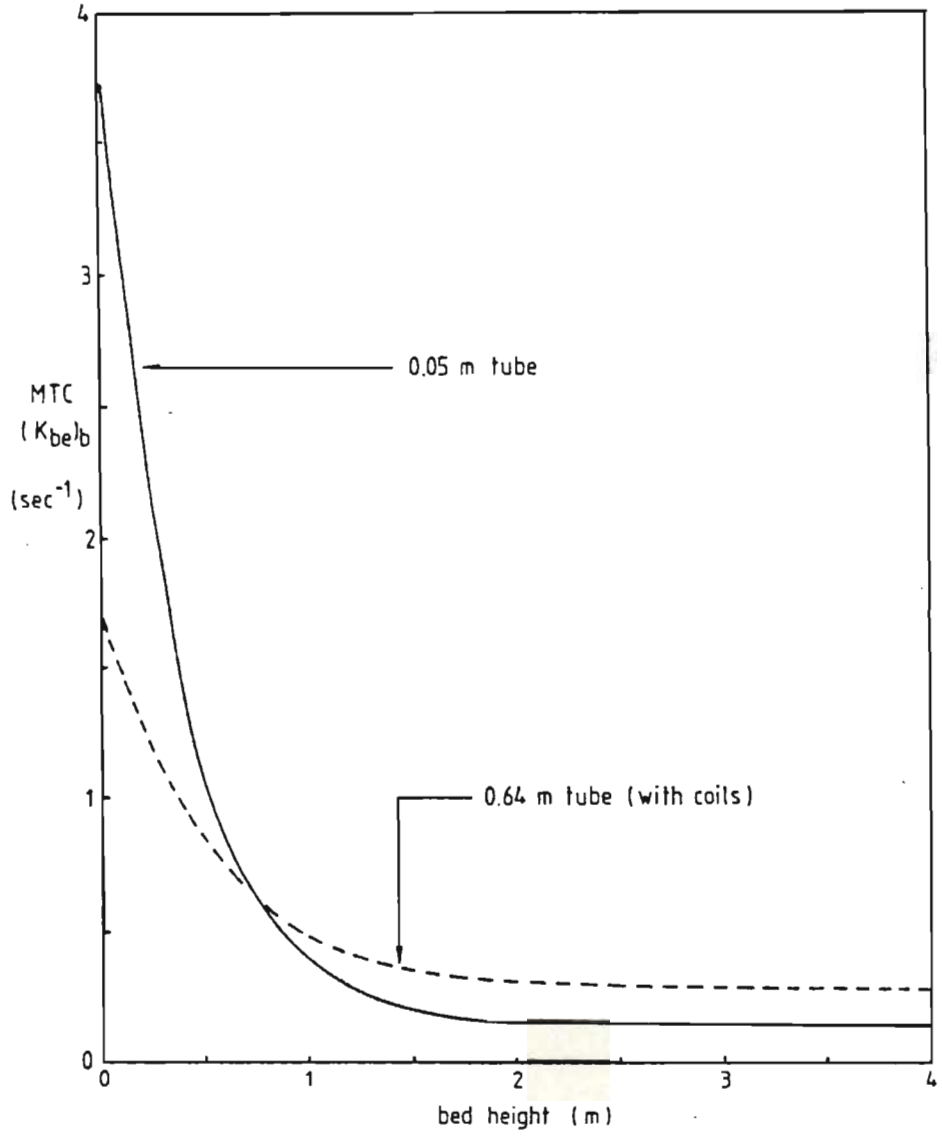

FIGURE 6.20 AXIAL MTC PROFILES

profile at least roughly in accord with that in Figure 6.20. Davidson and Harrison's expression:

$$(K_{be})_b = 4.5 \left(\frac{U_{mf}}{d_b}\right) + 5.85 \left(\frac{D^{0.5} g^{0.25}}{d_b^{1.25}}\right) \qquad (2.16)$$

for the conditions employed here ($\phi = 1.55$) becomes:

$$(K_{be})_b = 0.0003\ d_b^{-1} + 0.033\ d_b^{-1.25} \qquad (6.10)$$

where $(K_{be})_b$ and d_b are in reciprocal seconds and m respectively. This expression, applied to the bubble diameter profile shown in Figure 6.4 for $\phi = 1.55$, yields the MTC profile shown in Figure 6.21. The general shape is consistent with that obtained from crossflow data in the previous section, and the assumed bubble diameter profile may be considered reasonable on this basis.

Now if the bubbles are considered to be spherical, the ratio of surface to volume is given by:

$$S_b/V_b = 6/d_b \qquad (6.11)$$

In other words, interfacial area per unit bubble volume may be computed directly from a bubble diameter profile such as that shown in Figure 6.4.

A similar treatment for the 0.05 m unit is not possible since no axial dependence in bubble/slug velocity was observed. However, in the fully established bed, slugs of 0.3 m in length were typical. If a hemi-spherical cap and a flat base are assumed, the surface to volume ratio is of the order of 11 m^{-1}. This allows one to make a

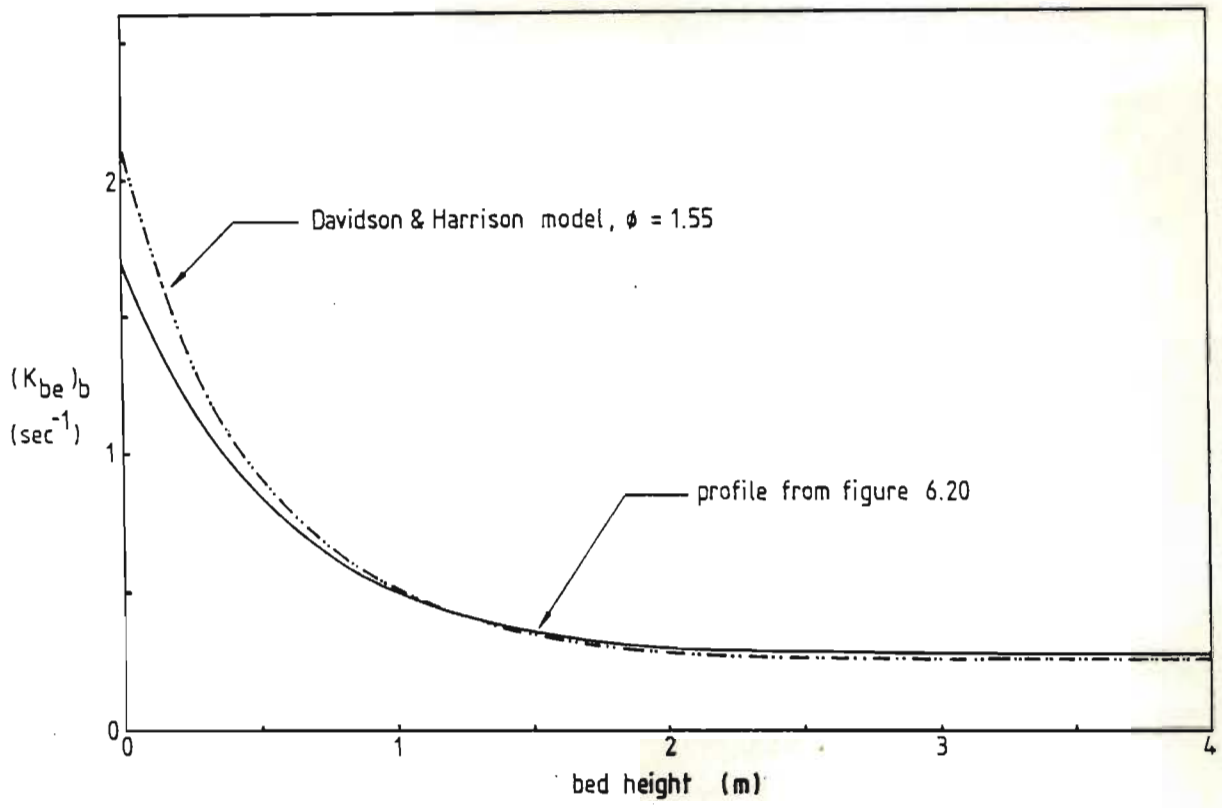

FIGURE 6.21 CROSS-CHECK ON THE BUBBLE DIAMETER PROFILE

rough estimate of an MTC based on interfacial area in the upper regions of the slugging bed.

6.5.3 MTC Based on Interfacial Area

For the case of spherical bubbles:

$$(K_{be})_s = (K_{be})_b \, (d_b/6) \qquad (6.12)$$

For the 0.64 m unit $(K_{be})_b$ and d_b may be taken from Figures 6.20 and 6.4 respectively. Values for $(K_{be})_s$ at 0.05 m bed height increments are shown in Figure 6.22, and it is immediately apparent that this quantity (as computed here) does not vary with bed height.

For the case of fully established slug flow in the 0.05 m unit, $(K_{be})_s$ may be estimated from:

$$(K_{be})_s = (K_{be})_b \, (1/11) \qquad (6.13)$$

For $(K_{be})_b = 0.15$ sec^{-1} as per equation (6.8) for z greater than about 2 m, $(K_{be})_s$ comes to 0.0014 m/s as shown in Figure 6.22.

It is interesting to compare the above results with published data. Bauer et. al. (120) recently measured $(K_{be})_s$ in a 1 m bed of 108 μ quartz sand by a residence time technique, and arrived at a constant value of 0.0089 m/s. This quantity was shown to be insensitive to the exact nature of the gas distributor, and its numerical value agrees almost perfectly with the 0.64 m bed data in Figure 6.22.

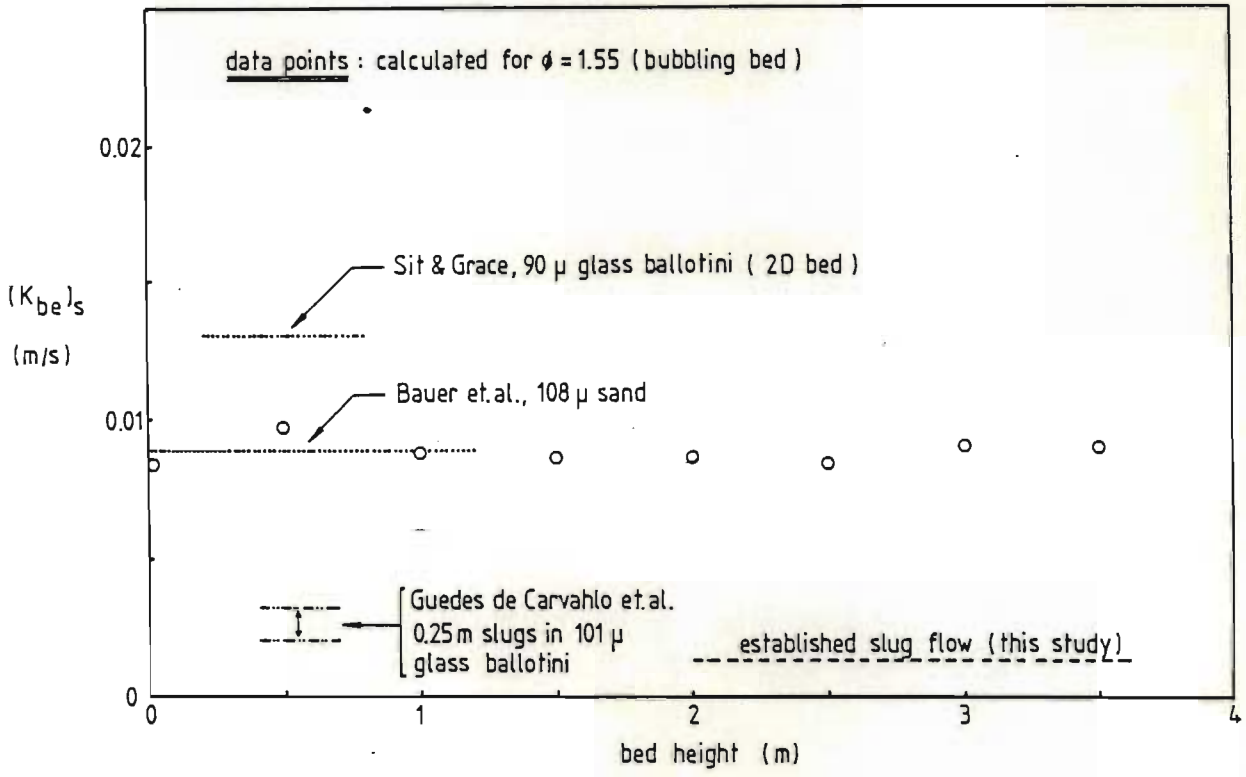

FIGURE 6.22 MTC BASED ON INTERFACIAL AREA

Sit and Grace (75) studied mass transfer in a 2-D bed of glass ballotini, and for the finest powder (90 μ) tested, obtained a value of $(K_{be})_s$ of 0.013 m/s. The coarser powders generally displayed larger MTC's as predicted by Davidson's (39) bubble model.

For slugging beds of 64 μ glass ballotini, Guedes de Carvahlo, King and Harrison (121) recently published data which suggests $(K_{be})_s$ = 0.0018 - 0.0032 m/s for 0.25 m slugs. For 101 μ particles and slugs of the same type their data may be interpreted as $(K_{be})_s$ = 0.0015 - 0.0019 m/s, and for both systems the MTC increased as slug length decreased.

The data in Figure 6.22 suggests that $(K_{be})_s$ is significantly smaller in established slug flow than in a freely bubbling system. This trend is evident in the data generated here, as well as in a comparison between the 101 μ ballotini data of Guedes de Carvahlo et. al.121) and the 90 μ ballotini data of Sit and Grace (75).

A tentative explanation for this is to be found in the flow field associated with a long slug. Streamlines are expected to run parallel to the side walls, and more perpendicular to the slug-dense phase interface in the regions of the nose and base only. In other words, the side walls of a slug could be fairly inert from a mass transfer point of view, and longer slugs consistent with a lower MTC (based on interfacial area).

The results in Figure 6.22 suggest that, in a bubbling bed, bubble to dense phase interfacial area or simply bubble size provides a sound basis for estimating crossflow. If a reasonable value for $(K_{be})_s$ is assumed, a bubble size/velocity growth expression which is known to apply to the system in question is effectively all that is required to compute crossflow ratios. The difficulty with this approach, however, is the fact that it relies on a class D model. The empirical or semi-empirical nature of these models make them unsuitable for general application, and in a situation of the type encountered in this study it would be necessary to actually measure bubble sizes. The time and effort involved would probably be similar to that required for obtaining RTD data, so there is no clear-cut advantage in this alternative approach.

The fact that bubble to dense phase interfacial area accounts for the observed axial profile suggests that coalescence plays a relatively minor role in the overall process. The frequency of coalescence is probably high in the lower regions of the bed, and a significant coalescence effect on mass transfer might be expected to confound attempts to explain the axial MTC profile on the basis of interfacial area.

The results in this study alone may not be regarded as firm evidence of the lack of a strong coalescence crossflow enhancement effect. However, when they are seen in conjunction with those of Bauer et. al. (120) and the observation by Sit and Grace (76) that coalescence enhances

mass transfer by a moderate 20-30% only, it seems reasonable to suggest that an overpowering coalescence effect of the type suggested by Pireira and Calderbank (77) is not in fact present in systems of this type.

CHAPTER 7

SUMMARY AND CONCLUSIONS

Five general fluidised bed models have been formulated in the dynamic mode and solved analytically for frequency response. Four of these have appeared in the literature in one form or another, and the fifth is novel in that it employs multiple plug flow units in parallel for the bubble phase. Two special models, also considered novel, are formulated and solved numerically to describe a fluidised bed containing a sparger.

An experimental technique based on correlation analysis is employed to measure gas residence time distributions in cold, atmospheric fluidised beds. The data are processed to the form of a frequency response, and the latter is compared with that of each model in turn. A simplex technique is employed to adjust two parameters per model for maximum closure with the experimental data and the residual error for each (at the optimum parameter combination) provides a means of isolating the best-fitting model. The optimised parameters of this model are regarded as estimates of those of the actual process.

Broadly speaking, the conclusions drawn from the results in this study may be regarded as falling into two categories. Firstly, the (model) fitting and screening is significant in

that it highlights some general characteristics of fine powder systems and how they should be modelled. The second category involves estimated crossflow ratios and implications for this particular system type. Conclusions in this category are rather specific in nature, and may be expected to apply only within a narrow range of particle types and vessel geometries.

7.1 General Conclusions on Modelling

1. For fine powders a two-phase model is more appropriate than a three-phase one. This is in accord with Davidson's (39) bubble model, and holds true for both bubbling and slugging systems. If a three-phase model is applied to a fine powder fluidised bed and parameter optimisation is carried out, either the cloud thickness or the cloud-emulsion mass transfer resistance will generally tend to zero.

2. For both bubbling and slugging beds the multiple bubble-track or MBT model provides the greatest degree of closure. This suggests that accounting for axial mixing in the bubble phase by employing multiple plug flow units in parallel is mechanistically more correct than employing a single plug flow unit.

3. In the case where gas is sparged into an already fluidised system, the laterally segregated bubble phase or LSBP model provides a better description of the process than does the laterally mixed bubble phase or LMBP model.

4. The axial crossflow profile in the larger of the cold models is consistent with the concept of an axially invariant mass transfer coefficient based on interfacial area.

7.2 Specific Conclusions on Crossflow

1. A very strong scale-up effect is evident in the system studied. Crossflow drops sharply in going from a cold model simulating a typical pilot plant unit to one simulating a semi-works reactor.

2. As expected (79, 81), most of the crossflow activity occurs in the bottom meter or so in both units.

3. The presence or otherwise of vertical coils in the bed has little effect on interphase mass transfer. The conventional concept of hydraulic diameter in single-

phase flow is probably not applicable to this system, since most of the activity is controlled by the nature of the grid rather than that of the containing vessel higher up.

4. The crossflow profile is very flat in the region beyond about 1 m above the grid. This suggests that a deep bed would have little advantage over a relatively shallow one from a mass transfer point of view.

5. The introduction of gas into the bed via the sparger does not significantly alter the pattern of gas-to-catalyst contacting.

APPENDIX A

AN ANALYSIS OF PUBLISHED MODELS IN TERMS OF THE PROPOSED MODEL CLASSIFICATION

(i) May's two-phase model (12) is a straightforward class A model. Level 2a and RTD input is used to obtain a lumped (level 3a) MTC, and the latter may be used to predict conversion.

(ii) Davidson and Harrison's (39) bubble models, with plug flow and well mixed dense phases respectively, represent a two-stage approach. A constant bubble size is assumed at level 2, and a class C model (based on Davidson's (17) bubble model and Highbie's (23) penetration theory) is employed to compute an MTC for non-interacting bubbles. Bubble interaction and end effects are ignored, and a class A model is used with level 2a input and this MTC to predict conversion.

(iii) Kunii and Levenspiel's (28) bubble model follows almost the same pattern as Davison and Harrison's (39) models. A constant bubble size is assumed at level 2, and class C models are used to predict a pair of MTC's. End effects and bubble interactions are once again ignored, and a three-phase class A model which calls for bubble-cloud and cloud-emulsion MTC's is employed to predict conversion.

(iv) The countercurrent backmixing model (29) follows a pattern identical to that of the Kunii and Levenspiel (28) model. The only difference is that the class A model includes convection in the cloud and emulsion phases.

(v) Werther's (98) model employes an empirical bubble growth expression, i.e. a class D model, and assumes a constant MTC per unit area of bubble-cloud interface as a class C model. The integration with respect to bed height to yield a lumped MTC is performed analytically, and a class A model is then applied. Bubble interactions and end effects are ignored.

(vi) Kato and Wen's (46) bubble assemblage model employes a class D bubble growth expression and a simple class C model based on the work of Kobayashi (122). Bubble interaction and end effects are ignored and a class B model, distributed in the axial co-ordinate, is used to arrive at a conversion prediction.

(vii) The modified bubble assemblage model of Peters et. al. (48) follows a path parallel to that of the original bubble assemblage model. Different class D and C models are employed and the gas flow distribution in the class B model is somewhat more complex, but the approach is identical.

(viii) Weimer and Clough's (92) model of a fluidised bed gasifier employs two class D models: a bubble growth expression by Mori and Wen (62) and a jet penetration correlation by Basov (80). The class C model for the bubbling bed is that suggested by Kunii and Levenspiel (28), and the grid region class C model is based on the work of Behie and Kehoe (123). The overall mass balance model may be considered class B, since the MTC is crudely distributed in the axial direction. The MTC changes from a high (grid region) tot a low (bubbling bed) value in a discontinuous manner as discussed previously.

(ix) The scale-up procedure suggested by Krishna (124) is based on Darton's (41) bubble growth expression and Davidson's (17) bubble model. An analytical integration with respect to bed height is performed, and the bulk of the discussion revolves around the resulting lumped MTC. A limiting height for bubble growth h* is included in the model development, and is carried through as a required input. This quantity represents a level 2 data requirement.

(x) The scale-up procedure employed in the Shell Chlorine Study (117,118) involved, among other things, the extraction of a lumped MTC from RTD data on the basis of a simple class A model.

(xi) The reactor characterisation studies by Wippern et. al. (50) involved the extraction of a lumped MTC from RTD data, based on a number of alternative class A models.

(xii) The gas distributor study by Bauer et. al.(120) also involves the extraction, via a class A model, of an MTC from RTD data. This quantity is subsequently moulded to the form of an MTC per unit bubble-cloud interface on the basis of a class D bubble growth expression.

A highly popular experimental strategy is to perform an experiment with a reacting tracer under steady-state conditions, and to measure the conversion achieved. The analysis of such data is usually carried out by assuming a class A or B model and working backwards to calculate an MTC. Some of the studies in which this approach has been employed are:

(xiii) In the Shell Chlorine study (117), conversions were measured for ozone decomposition. A simple class A model was applied, and the resulting lumped MTC used for scale-up.

(xiv) Miyauchi et. al. (93) measured the conversion profiles of propylene in a system where propylene oxidation was in progress. A class B model was then applied in the form of a local Lewis-Gilliland-Glass plot (125), and an axially distributed MTC thus extracted.

Finally, it would seem appropriate to note that mechanistic bubble growth simulations such as those reported by Allahwala, Singh and Potter (126) may be regarded as class D models.

APPENDIX B

FORTRAN V LISTINGS OF THE SEVEN MODEL SOLUTIONS

```
PROC*RDLIB(1).MVDEX
      1             SUBROUTINE MVD(XB,DN,UO,UB,UD,ED,HF,E,NW,W,REM,CJM,NO)
      2       C
      3       C     MVD MODEL FREQUENCY RESPONSE
      4       C     ****************************
      5       C
      6             COMPLEX A(4),AL(3),R(3),WJ,CB,CE,H1,H2,COUT
      7             DIMENSION REM(30),CJM(30),W(30)
      8             DEL=(UO-UD)/(UB-UD)
      9             C1=UD/(UB*ED)
     10             C2=(1.-DEL)*ED*DN
     11             C3=DEL*XB
     12             EPS=1.0E-08
     13             ZZ=0.
     14             QQ=75.
     15       C
     16       C     MAIN FREQUENCY LOOP
     17       C
     18             DO 20 J=1,NW
     19             WJ=(HF/UB)*CMPLX(ZZ,W(J))
     20             A(1)=C3*XB/C2-(XB+WJ)*(C3/C2+WJ/DN)
     21             A(2)=-C1*(XB+WJ)/DN-C3/C2-WJ/DN
     22             A(3)=(XB+WJ)-C1/DN
     23             A(4)=1.
     24             CALL ROOTCP(A,3,EPS,100,R,JJ,$100)
     25             DO 35 K=1,3
     26             Q1=REAL(R(K))
     27             Q2=AIMAG(R(K))
     28             IF(Q1.GT.QQ) R(K)=CMPLX(QQ,Q2)
     29       35    CONTINUE
     30             AL(1)=1./R(1)*((CEXP(R(2))-CEXP(R(3)))/(R(1)+XB+WJ)
     31             AL(2)=1./R(2)*((CEXP(R(3))-CEXP(R(1)))/(R(2)+XB+WJ)
     32             AL(3)=1./R(3)*((CEXP(R(1))-CEXP(R(2)))/(R(3)+XB+WJ)
     33             CB=(AL(1)*CEXP(R(1)*E)+AL(2)*CEXP(R(2)*E)+AL(3)*CEXP(R(3)*E)
     34            #)/(AL(1)+AL(2)+AL(3))
     35             H1=XB*(AL(1)+AL(2)+AL(3))
     36             H2=0.
     37             DO 10 K=1,3
     38       10    H2=H2+AL(K)*(R(K)+XB+WJ)*CEXP(R(K)*E)
     39             CE=H2/H1
     40             IF(NO.EQ.1) GO TO 11
     41             COUT=(DEL*UB*CB+(1.-DEL)*UD*CE)/UO
     42             GO TO 12
     43       11    COUT=(DEL*CB+(1.-DEL)*ED*CE)/(DEL+(1.-DEL)*ED)
     44       12    CONTINUE
     45             REM(J)=REAL(COUT)
     46             CJM(J)=AIMAG(COUT)
     47             GO TO 21
     48       100   WRITE(6,1)
     49       1     FORMAT(1H0,'ROOTCP MAX ITERATIONS')
     50       21    CONTINUE
     51       20    CONTINUE
     52             RETURN
     53             END
```

```
PROC*RDLIB(1).CCBMEX
      1             SUBROUTINE CCBM(XBC,XCE,U0,UB,UE,ED,HF,E,ALPHA,NW,W,RE,CJ,N0)
      2       C
      3       C     COUNTERCURRENT BACKMIXING MODEL FREQUENCY RESPONSE
      4       C     ************************************************
      5       C
      6             COMPLEX A(4),R(3),AC(13),R1,R2,R3,S,P1,P2,P3
      7             COMPLEX C1,C2,C3,C4,C5,C6,CE0,CC0,CB,CC,CE,COUT
      8             DIMENSION W(30),RE(30),CJ(30)
      9             Z=0.
     10             EPS=1.0E-08
     11             DEL=(U0-ED*UE)/(UB*(1.+ALPHA*ED)-(1.+ALPHA)*ED*UE)
     12             AC(4)=XBC/(ALPHA*ED)
     13             AC(5)=XCE/(ALPHA*ED)
     14             AC(6)=(UB/UE)*(DEL*XCE/((1.-DEL-ALPHA*DEL)*ED))
     15             X1=(U0-DEL*UB)/(ALPHA*DEL*ED*UB)
     16             X2=(1.-DEL-ALPHA*DEL)*ED*UE/(ALPHA*DEL*ED*UB)
     17       C
     18       C     MAIN FREQUENCY LOOP
     19       C
     20             DO 10 J=1,NW
     21             S=(HF/UB)*CMPLX(Z,W(J))
     22             AC(1)=XBC+S
     23             AC(2)=(XBC+XCE)/(ALPHA*ED)+S
     24             AC(3)=AC(6)+(UB/UE)*S
     25             AC(7)=AC(1)+AC(2)+AC(3)
     26             AC(8)=AC(1)*AC(2)+AC(1)*AC(3)+AC(2)*AC(3)-AC(5)*AC(6)-AC(4)*XBC
     27             AC(9)=AC(1)*(AC(2)*AC(3)-AC(5)*AC(6))-AC(3)*AC(4)*XBC
     28             AC(10)=AC(2)+AC(3)+X1*XBC
     29             AC(11)=-X2*XBC
     30             AC(12)=AC(2)*AC(3)-AC(5)*AC(6)+AC(3)*XBC*X1
     31             AC(13)=AC(5)*XBC-AC(3)*XBC*X2
     32       C
     33       C
     34       C     LOAD THE POLY COEFFICIENTS INTO A AND CALL ROOTCP
     35       C
     36             A(1)=AC(9)
     37             A(2)=AC(8)
     38             A(3)=AC(7)
     39             A(4)=1.
     40             CALL ROOTCP(A,3,EPS,200,R,JJ,$100)
     41             KN=0
     42             KP=0
     43             DO 11 K=1,3
     44             IF(REAL(R(K)).LE..01) GO TO 12
     45             KP=KP+1
     46             IF(KP.EQ.1) R3=R(K)
     47             IF(KP.EQ.2) WRITE(6,2)
     48             GO TO 13
     49       12    KN=KN+1
     50             IF(KN.EQ.1) R1=R(K)
     51             IF(KN.EQ.2) R2=R(K)
     52             IF(KN.EQ.3) WRITE(6,2)
     53       2     FORMAT(1H0,'ROOTS VIOLATE BC ASSUMPTION IN CCBM')
     54       13    CONTINUE
     55       11    CONTINUE
     56       C
     57       C     COMPUTE CE0,CC0,CB,CC,CE AND COUT
     58       C
     59             CE0=-(R3**2+AC(10)*R3+AC(12))/(AC(11)*R3+AC(13))
```

```
60              P1=(AC(12)+AC(13)*CE0)/R3
61              CC0=X1-X2*CE0
62              P2=(AC(1)*AC(3)+(AC(1)*AC(5)*CE0+AC(3)*AC(4))/CC0)/R3
63              P3=-1.*(R3+AC(1)+AC(2)+AC(6)*CC0/CE0)
64              C1=(R1-P1)/(R1-R2)
65              C2=(R2-P1)/(R2-R1)
66              C3=(R1-P2)/(R1-R2)
67              C4=(R2-P2)/(R2-R1)
68              C5=(R1-P3)/(R1-R2)
69              C6=(R2-P3)/(R2-R1)
70              CB=C1*CEXP(R1*E)+C2*CEXP(R2*E)
71              CC=CC0*(C3*CEXP(R1*E)+C4*CEXP(R2*E))
72              CE=CE0*(C5*CEXP(R1*E)+C6*CEXP(R2*E))
73              IF(NO.EQ.1) GO TO 15
74              COUT=(CB+ALPHA*ED*CC)/(1.+ALPHA*ED)
75              GO TO 16
76      15      COUT=DEL*CB+DEL*ALPHA*ED*CC+(1.-DEL-ALPHA*DEL)*ED*CE
77              COUT=COUT/(DEL+ALPHA*DEL*ED+(1.-DEL-ALPHA*DEL)*ED)
78      16      CONTINUE
79              RE(J)=REAL(COUT)
80              CJ(J)=AIMAG(COUT)
81              GO TO 14
82      100     WRITE(6,1) W(J)
83      1       FORMAT(1H0,'ROOTCP FAILED AT W',F10.4)
84      14      CONTINUE
85      10      CONTINUE
86              RETURN
87              END
```

```
PROC*RDLIB(1).WFDEX
      1              SUBROUTINE WFD(XB,AL,UO,UB,ED,HF,E,NW,W,REM,CJM,NO)
      2        C
      3        C     WERTHER FILM DIFFUSION MODEL FREQUENCY RESPONSE
      4        C     ***********************************************
      5        C
      6              COMPLEX PHI,CBN,CBD,CEN,CED,COUT,S,CB,CE
      7              DIMENSION W(30),REM(30),CJM(30)
      8              DEL=UO/UB
      9              C1=(1.-DEL-DEL*AL)*ED
     10              DO 20 J=1,NW
     11              ZZ=0.
     12              S=(HF/UB)*CMPLX(ZZ,W(J))
     13              PHI=CSQRT(AL*ED*S/XB)
     14              CBN=C1*S*(S*CTANH(PHI)+XB*PHI)+
     15             *DEL*XB*PHI*(S+XB*PHI*CTANH(PHI))
     16              CBD=C1*S*CTANH(PHI)+DEL*XB*PHI
     17              CB=CEXP(-CBN*E/CBD)
     18              CEN=CB*(DEL*XB*PHI*(((CCOSH(PHI))**2-(CSINH(PHI))**2))
     19              CED=C1*S*CSINH(PHI)+DEL*XB*PHI*CCOSH(PHI)
     20              CE=CEN/CED
     21              IF(NO.EQ.1) GO TO 10
     22              COUT=CB
     23              GO TO 11
     24        10    COUT=(DEL*CB+(1.-DEL)*ED*CE)/(DEL+(1.-DEL)*ED)
     25        11    CONTINUE
     26              REM(J)=REAL(COUT)
     27              CJM(J)=AIMAG(COUT)
     28        20    CONTINUE
     29              RETURN
     30              END
```

```
PROC*RDLIB(1).BPD
      1              SUBROUTINE BPD(XB,ND,NB,U0,UB,UD,ED,HF,E,NW,W,RE,CJ,NO)
      2        C
      3        C     BUBBLE PHASE DISPERSION MODEL FREQUENCY RESPONSE
      4        C     ***********************************************
      5        C
      6              COMPLEX A(5),R(4),S,R1,R2,R3,R4,P1,P2
      7              COMPLEX C1,C2,C3,C4,CB0,CE0,CB,CE,COUT
      8              DIMENSION W(50),RE(50),CJ(50)
      9              REAL ND,NB
     10              Z=0.
     11              EPS=1.0E-08
     12              DEL=(U0-UD)/(UB-UD)
     13              XE=DEL*XB/((1.-DEL)*ED)
     14              UR=UD/(ED*UB)
     15        C
     16        C     MAIN FREQUENCY LOOP
     17        C
     18              DO 10 J=1,NW
     19              S=(HF/UB)*CMPLX(Z,W(J))
     20              A(1)=((XB+S)*(XE+S)-XB*XE)/(NB*ND)
     21              A(2)=((XE+S)+UR*(XB+S))/(NB*ND)
     22              A(3)=-(ND*(XB+S)+NB*(XE+S)-UR)/(NB*ND)
     23              A(4)=-(ND+UR*NB)/(NB*ND)
     24              A(5)=1.
     25              CALL ROOTCP(A,4,EPS,200,R,JJ,$100)
     26              KN=0
     27              KP=0
     28              DO 11 K=1,4
     29              IF(REAL(R(K)).LE.0.) GO TO 12
     30              KP=KP+1
     31              IF(KP.EQ.1) R3=R(K)
     32              IF(KP.EQ.2) R4=R(K)
     33              IF(KP.EQ.3) WRITE(6,2)
     34              GO TO 13
     35        12    KN=KN+1
     36              IF(KN.EQ.1) R1=R(K)
     37              IF(KN.EQ.2) R2=R(K)
     38              IF(KN.EQ.3) WRITE(6,2)
     39        2     FORMAT(1H0,'ROOTS VIOLATE BC ASSUMPTION IN BPD')
     40        13    CONTINUE
     41        11    CONTINUE
     42              CE0=XE/(ND*R3*R4*(NB*(R3+R4)-1))
     43              CB0=(XB+S+R3*R4*ND)/(NB*R3*R4*(ND*(R3+R4)-UR))
     44              P1=-(XE+S)/(NB*ND*R3*R4*CB0)
     45              P2=1./NB-(R3+R4)
     46              C1=(R1-P1)/(R1-R2)
     47              C2=(R2-P1)/(R2-R1)
     48              C3=(R1-P2)/(R1-R2)
     49              C4=(R2-P2)/(R2-R1)
     50              CB=CB0*(C1*CEXP(R1*E)+C2*CEXP(R2*E))
     51              CE=CE0*(C3*CEXP(R1*E)+C4*CEXP(R2*E))
     52              IF(NO.EQ.1) GO TO 15
     53              COUT=(DEL*UB*CB+(1.-DEL)*UD*CE)/U0
     54              GO TO 16
     55        15    COUT=(DEL*CB+(1.-DEL)*ED*CE)/(DEL+(1.-DEL)*ED)
     56        16    CONTINUE
     57              IF(UR.LT.0.) COUT=CB
     58              RE(J)=REAL(COUT)
     59              CJ(J)=AIMAG(COUT)
```

```
60              GO TO 14
61        100   WRITE(6,1) W(J)
62        1     FORMAT(1HO,'ROOTCP FAILED AT W ',F10.4)
63        14    CONTINUE
64        10    CONTINUE
65              RETURN
66              END
```

```
PROC*RDLIB(1).MBT
      1              SUBROUTINE MBT(XB,ND,UO,U,F,UD,ED,HF,E,NW,W,RE,CJ,NO)
      2        C
      3        C     TWO-PHASE MULTIPLE BUBBLE-TRACK MODEL FREQUENCY RESPONSE
      4        C     ********************************************************
      5        C
      6              COMPLEX AL(23),BT(7),GM(7),RH(7),A(8),R(7)
      7              COMPLEX S,AU(5),X(5),H1,H2,H3,H4,HS,CEO,CE,CB(5),COUT
      8              DIMENSION BU(5),U(5),F(5)
      9              DIMENSION W(30),RE(30),CJ(30)
     10              REAL ND
     11              Z=0.
     12              QQ=70.
     13              EPS=1.0E-08
     14              UB=0.
     15              DO 10 J=1,5
     16        10    UB=UB+U(J)*F(J)
     17              DEL=(UO-UD)/(UB-UD)
     18              XE=XB*DEL/((1.-DEL)*ED)
     19              UR=UD/(UB*ED)
     20              DO 11 J=1,5
     21        11    BU(J)=XB*UB/U(J)
     22        C
     23        C     MAIN FREQUENCY LOOP
     24        C
     25              DO 12 J=1,NW
     26              S=(HF/UB)*CMPLX(Z,W(J))
     27        C
     28        C     1. COMPUTE A'S AND ALPHA'S
     29        C
     30              DO 13 K=1,5
     31        13    AU(K)=(XB+S)*UB/U(K)
     32              AL(1)=AU(1)*AU(2)*AU(3)*AU(4)*AU(5)
     33              H1=AU(1)*AU(2)*AU(3)*AU(4)+AU(1)*AU(2)*AU(3)*AU(5)
     34              H2=AU(1)*AU(2)*AU(4)*AU(5)+AU(1)*AU(3)*AU(4)*AU(5)
     35              AL(2)=AU(2)*AU(3)*AU(4)*AU(5)+H1+H2
     36              H1=AU(1)*AU(2)*AU(3)+AU(1)*AU(2)*AU(4)+AU(1)*AU(2)*AU(5)
     37              H2=AU(1)*AU(3)*AU(4)+AU(1)*AU(3)*AU(5)+AU(1)*AU(4)*AU(5)
     38              H3=AU(2)*AU(3)*AU(4)+AU(2)*AU(3)*AU(5)+AU(3)*AU(4)*AU(5)
     39              AL(3)=AU(2)*AU(4)*AU(5)+H1+H2+H3
     40              H1=AU(1)*AU(2)+AU(1)*AU(3)+AU(1)*AU(4)+AU(1)*AU(5)
     41              H2=AU(2)*AU(3)+AU(2)*AU(4)+AU(2)*AU(5)+AU(3)*AU(4)
     42              AL(4)=AU(3)*AU(5)+AU(4)*AU(5)+H1+H2
     43              AL(5)=AU(1)+AU(2)+AU(3)+AU(4)+AU(5)
     44              DO 14 K=1,5
     45        14    X(K)=F(K)
     46              N=5
     47        30    CONTINUE
     48        C
     49        C     DOUBLE LOOP FOR ALPHA 6-10 & 11-15
     50        C
     51              AL(N+1)=X(1)+X(2)+X(3)+X(4)+X(5)
     52              H1=X(1)*(AU(2)+AU(3)+AU(4)+AU(5))+X(2)*(AU(1)+AU(3)+AU(4)+AU(5))
     53              H2=X(3)*(AU(1)+AU(2)+AU(4)+AU(5))+X(4)*(AU(1)+AU(2)+AU(3)+AU(5))
     54              AL(N+2)=X(5)*(AU(1)+AU(2)+AU(3)+AU(4))+H1+H2
     55              H1=X(1)*(AU(2)*AU(3)+AU(2)*AU(4)+AU(2)*AU(5)+AU(3)*AU(4)+
     56             *AU(3)*AU(5)+AU(4)*AU(5))
     57              H2=X(2)*(AU(1)*AU(3)+AU(1)*AU(4)+AU(1)*AU(5)+AU(3)*AU(4)+
     58             *AU(3)*AU(5)+AU(4)*AU(5))
     59              H3=X(3)*(AU(1)*AU(2)+AU(1)*AU(4)+AU(1)*AU(5)+AU(2)*AU(4)+
```

```
     *AU(2)*AU(5)+AU(4)*AU(5))
      H4=X(4)*(AU(1)*AU(2)+AU(1)*AU(3)+AU(1)*AU(5)+AU(2)*AU(3)+
     *AU(2)*AU(5)+AU(3)*AU(5))
      H5=X(5)*(AU(1)*AU(2)+AU(1)*AU(3)+AU(1)*AU(4)+AU(2)*AU(3)+
     *AU(2)*AU(4)+AU(3)*AU(4))
      AL(N+3)=H1+H2+H3+H4+H5
      H1=X(1)*(AU(2)*AU(3)*AU(4)+AU(2)*AU(3)*AU(5)+
     *AU(2)*AU(4)*AU(5)+AU(3)*AU(4)*AU(5))
      H2=X(2)*(AU(1)*AU(3)*AU(4)+AU(1)*AU(3)*AU(5)+
     *AU(1)*AU(4)*AU(5)+AU(3)*AU(4)*AU(5))
      H3=X(3)*(AU(1)*AU(2)*AU(4)+AU(1)*AU(2)*AU(5)+
     *AU(1)*AU(4)*AU(5)+AU(2)*AU(4)*AU(5))
      H4=X(4)*(AU(1)*AU(2)*AU(3)+AU(1)*AU(2)*AU(5)+
     *AU(1)*AU(3)*AU(5)+AU(2)*AU(3)*AU(5))
      H5=X(5)*(AU(1)*AU(2)*AU(3)+AU(1)*AU(2)*AU(4)+
     *AU(1)*AU(3)*AU(4)+AU(2)*AU(3)*AU(4))
      AL(N+4)=H1+H2+H3+H4+H5
      H1=X(1)*AU(2)*AU(3)*AU(4)*AU(5)+X(2)*AU(1)*AU(3)*AU(4)*AU(5)
      H2=X(3)*AU(1)*AU(2)*AU(4)*AU(5)+X(4)*AU(1)*AU(2)*AU(3)*AU(5)
      AL(N+5)=X(5)*AU(1)*AU(2)*AU(3)*AU(4)+H1+H2
      N=N+5
      DO 15 K=1,5
   15 X(K)=F(K)*BU(K)
      IF(N.EQ.10) GO TO 30
      AL(16)=-ND
      AL(17)=-AL(5)*ND+UR
      AL(18)=-AL(4)*ND+AL(5)*UR+(XE+S)
      AL(19)=-AL(3)*ND+AL(4)*UR+AL(5)*(XE+S)-AL(11)*XE
      AL(20)=-AL(2)*ND+AL(3)*UR+AL(4)*(XE+S)-AL(12)*XE
      AL(21)=-AL(1)*ND+AL(2)*UR+AL(3)*(XE+S)-AL(13)*XE
      AL(22)=AL(1)*UR+AL(2)*(XE+S)-AL(14)*XE
      AL(23)=AL(1)*(XE+S)-AL(15)*XE
C
C     LOAD THE POLYNOMIAL COEFFICIENTS INTO THE ARRAY A
C     AND CALL ROUTINE ROOTCP
C
      A(1)=AL(23)/AL(16)
      A(2)=AL(22)/AL(16)
      A(3)=AL(21)/AL(16)
      A(4)=AL(20)/AL(16)
      A(5)=AL(19)/AL(16)
      A(6)=AL(18)/AL(16)
      A(7)=AL(17)/AL(16)
      A(8)=1.
      AMAX=0.
      DO 22 K=1,8
      ACHECK=SQRT(REAL(A(K))**2+AIMAG(A(K))**2)
   22 IF(ACHECK.GT.AMAX) AMAX=ACHECK
      DO 23 K=1,8
   23 A(K)=A(K)/(AMAX*.1)
      CALL ROOTCP(A,7,EPS,500,R,JJ,$100)
      DO 24 KC=1,7
      Q1=REAL(R(KC))
      Q2=AIMAG(R(KC))
      IF(Q1.GT.QQ) R(KC)=CMPLX(QQ,Q2)
   24 CONTINUE
C
C     COMPUTE ARRAYS BETA, GAMMA AND RHO
C
      DO 16 K=1,7
```

```
120             BT(K)=R(K)**6+AL(5)*R(K)**5+AL(4)*R(K)**4+AL(3)*R(K)**3+
121            #AL(2)*R(K)**2+AL(1)*R(K)
122             GM(K)=(AL(6)*R(K)**4+AL(7)*R(K)**3+AL(8)*R(K)**2+
123            #AL(9)*R(K)+AL(10))*(XE/ND)
124             RH(K)=1.
125             DO 17 L=1,7
126             IF(L.EQ.K) GO TO 31
127             RH(K)=RH(K)*(R(K)-R(L))
128       31    CONTINUE
129       17    CONTINUE
130       16    CONTINUE
131       C
132       C      COMPUTE CEO AND CE
133       C
134             H1=0.
135             H2=0.
136             DO 18 K=1,7
137             H1=H1+GM(K)*R(K)*CEXP(R(K))/RH(K)
138             H2=H2+BT(K)*R(K)*CEXP(R(K))/RH(K)
139       18    CONTINUE
140             CEO=H1/H2.
141             CE=0.
142             DO 25 K=1,7
143       25    CE=CE+((CEO*BT(K)-GM(K))/RH(K))*CEXP(R(K)*E)
144       C
145       C     COMPUTE BUBBLE-TRACK CONCENTRATIONS
146       C
147             DO 19 K=1,5
148             H1=0.
149             DO 20 L=1,7
150             H1=H1+((CEO*BT(L)-GM(L))/(RH(L)*(AU(K)+R(L))))*
151            #((CEXP((AU(K)+R(L))*E)-1.)
152       20    CONTINUE
153       19    CB(K)=(1.+BU(K)*H1)*CEXP(-AU(K)*E)
154             COUT=0.
155             H1=0.
156             IF(NO.EQ.1) GO TO 26
157             DO 21 K=1,5
158             COUT=COUT+F(K)*U(K)*CB(K)
159       21    H1=H1+F(K)*U(K)
160             COUT=COUT/H1
161             GO TO 27
162       26    CONTINUE
163             DO 28 K=1,5
164       28    H1=H1+CB(K)*F(K)
165             COUT=(DEL*H1+(1.-DEL)*ED*CE)/(DEL+(1.-DEL)*ED)
166       27    CONTINUE
167             RE(J)=REAL(COUT)
168             CJ(J)=AIMAG(COUT)
169             GO TO 32
170       100   WRITE(6,1) W(J)
171       1     FORMAT(1HO,'ROOTCP FAILED AT W',F10.4)
172       32    CONTINUE
173       12    CONTINUE
174             RETURN
175             END
```

```
PROC*RDLIB(1).LMBP
      1              SUBROUTINE LMBP(KH,KL,DD,UOH,UOL,UBH,UBL,UD,ED,HF,HS,E,
      2             #NT,MT,DT,DTPR,CIN,COUT)
      3       C
      4       C      LATERALLY MIXED BUBBLE PHASE MODEL
      5       C      **********************************
      6       C
      7              DIMENSION CB(101,2),CE(101,2),V1(101),V2(101),A(101),B(101)
      8              DIMENSION C(101),D(101),CIN(501),COUT(501)
      9              REAL KH,KL
     10       C
     11       C      INITIALISATION
     12       C
     13              MAX=MT+1
     14              NSTOP=IFIX(FLOAT(NT)*DT/DTPR+.1)+1
     15              NPRINT=IFIX(DTPR/DT+.1)
     16              DZ=HF/FLOAT(MT)
     17              DELL=(UOL-UD)/(UBL-UD)
     18              DELH=(UOH-UD)/(UBH-UD)
     19              MSP=IFIX(FLOAT(MT)*HS/HF+.1)
     20              MTEST=IFIX(FLOAT(MT)*E+.1)
     21              DO 30 J=1,MAX
     22              CB(J,1)=0.
     23       30     CE(J,1)=0.
     24              COUT(1)=0.
     25              N=1
     26       C
     27       C      FUNCTION CONSTANTS
     28       C
     29              C1L=(UBL*DT)/(4.*DZ)
     30              C1H=(UBH*DT)/(4.*DZ)
     31              C2L=KL*DT/2.
     32              C2H=KH*DT/2.
     33              C3L=C1L*UD/(ED*UBL)
     34              C3H=C1H*UD/(ED*UBH)
     35              C4L=DT*DELL*KL/((1.-DELL)*ED*2.)
     36              C4H=DT*DELH*KH/((1.-DELH)*ED*2.)
     37              C5L=DD*DT/(2.*DZ**2)
     38              C5H=C5L
     39       C
     40       C      MAIN LOOP FOR TIME INCREMENTS
     41       C
     42              DO 10 I=2,NSTOP
     43              SLOPE=(CIN(I)-CIN(I-1))/(FLOAT(NPRINT))
     44              DO 9 IZ=1,NPRINT
     45       C
     46       C      1. BUBBLE PHASE TIME INCREMENT
     47       C
     48              DO 20 M=1,MAX
     49              IF(M.EQ.1) GO TO 21
     50              IF(M.EQ.MAX) GO TO 22
     51              IF(M.LT.MSP) GO TO 23
     52              IF(M.EQ.MSP) GO TO 19
     53              A(M)=-C1H
     54              B(M)=1.+C2H
     55              C(M)=C1H
     56              D(M)=C1H*CB(M-1,N)+(1.-C2H)*CB(M,N)-C1H*CB(M+1,N)+C2H*CE(M,N)*2.
     57              GO TO 24
     58       19     A(M)=0.
     59              B(M)=1.
```

```
      C(M)=0.
      D(M)=SLOPE*FLOAT(IZ)+CIN(I-1)
      GO TO 24
   21 A(M)=0.
      B(M)=1.
      C(M)=0.
      D(M)=0.
      GO TO 24
   22 A(M)=-2.*C1H
      B(M)=1.+C2H+C1H*2.
      C(M)=0.
      D(M)=2.*C1H*CB(M-1,N)+(1.-C2H-2.*C1H)*CB(M,N)+C2H*CE(M,N)*2.
      GO TO 24
   23 A(M)=-C1L
      B(M)=1.+C2L
      C(M)=C1L
      D(M)=C1L*CB(M-1,N)+(1.-C2L)*CB(M,N)-C1L*CB(M+1,N)+2.*C2L*CE(M,N)
   24 CONTINUE
   20 CONTINUE
      CALL TRIDAG(1,MAX,A,B,C,D,V1)
C
C     2. EMULSION PHASE TIME INCREMENT
C
      DO 25 M=1,MAX
      IF(M.EQ.1) GO TO 26
      IF(M.EQ.MAX) GO TO 27
      IF(M.LT.MSP) GO TO 28
      A(M)=-C3H-CSH
      B(M)=1.+2.*CSH+C4H
      C(M)=C3H-CSH
      D(M)=(C3H+CSH)*CE(M-1,N)+(1.-C4H-2.*CSH)*CE(M,N)+
     #(CSH-C3H)*CE(M+1,N)+C4H*(CB(M,N)+V1(M))
      GO TO 29
   26 A(M)=0.
      B(M)=1.+C4L+2.*CSL
      C(M)=-2.*CSL
      D(M)=2.*CSL*CE(M+1,N)+(1.-C4L-2.*CSL)*CE(M,N)+C4L*(CB(M,N)+V1(M))
      GO TO 29
   27 A(M)=-2.*CSH
      B(M)=1.+C4H+2.*CSH
      C(M)=0.
      D(M)=2.*CSH*CE(M-1,N)+(1.-C4H-2.*CSH)*CE(M,N)+C4H*(CB(M,N)+V1(M))

      GO TO 29
   28 A(M)=-C3L-CSL
      B(M)=1.+2.*CSL+C4L
      C(M)=C3L-CSL
      D(M)=(C3L+CSL)*CE(M-1,N)+(1.-2.*CSL-C4L)*CE(M,N)+
     #(CSL-C3L)*CE(M+1,N)+C4L*(CB(M,N)+V1(M))
   29 CONTINUE
   25 CONTINUE
      CALL TRIDAG(1,MAX,A,B,C,D,V2)
C
C     3. UPDATE FOR NEXT SMALL STEP
C
      II=(IFIX(FLOAT(IZ)/2.))*2
      IF(II.LT.IZ) N=1
      IF(II.EQ.IZ) N=2
      DO 11 K=1,MAX
```

```
118               C(C(K,N)=V1(K)
119         11    CE(K,N)=V2(K)
120         9     CONTINUE
121         C
122         C     4. UPDATE COUT
123         C
124               COUT(I)=DELH*V1(MTEST)+(1.-DELH)*ED*V2(MTEST)
125         10    CONTINUE
126               RETURN
127               END
```

```
PROC*RDLIB(1).LSBP
      1              SUBROUTINE LSBP(KH,KL,KL2,DD,UOH,UOL,UBH,UBL,UD,ED,HF,HS,E,
      2             #NT,MT,DT,DTPR,CIN,COUT)
      3       C
      4       C      LATERALLY SEGREGATED BUBBLE PHASE MODEL
      5       C      ***************************************
      6       C
      7              DIMENSION CB(101,2),CE(101,2),V1(101),V2(101),A(101),B(101)
      8              DIMENSION C(101),D(101),CIN(501),COUT(501)
      9              DIMENSION V3(101),CSP(101,2)
     10              REAL KH,KL,KL2
     11       C
     12       C      INITIALISATION
     13       C
     14              MAX=MT+1
     15              NSTOP=IFIX(FLOAT(NT)*DT/DTPR+.1)+1
     16              NPRINT=IFIX(DTPR/DT+.1)
     17              DZ=HF/FLOAT(MT)
     18              DELL=(UOL-UD)/(UBL-UD)
     19              DELH=(UOH-UOL-UD)/(UBH-UD)
     20              DEL=(UOH-UD)/(UBH-UD)
     21              F1=DELL/(DELL+DELH)
     22              F3=1.-F1
     23              MSP=IFIX(FLOAT(MT)*HS/HF+.1)
     24              MTEST=IFIX(FLOAT(MT)*E+.1)
     25              DO 30 J=1,MAX
     26              CB(J,1)=0.
     27              CSP(J,1)=0.
     28       30     CE(J,1)=0.
     29              COUT(1)=0.
     30              N=1
     31       C
     32       C      FUNCTION CONSTANTS
     33       C
     34              C1L=(UBL*DT)/(4.*DZ)
     35              C1H=(UBH*DT)/(4.*DZ)
     36              C2L=KL*DT/2.
     37              C2L2=KL2*DT/2.
     38              C2H=KH*DT/2.
     39              C3=C1H*UD/(ED*UBH)
     40              C4L=DT*DELL*KL2/((1.-DELL)*ED*2.)
     41              C4=DT*DEL*(F1*KL+F3*KH)/((1.-DEL)*ED*2.)
     42              CS=DD*DT/(2.*DZ**2)
     43              C4C=C4/(F1*KL+F3*KH)
     44       C
     45       C      MAIN LOOP FOR TIME INCREMENTS
     46       C
     47              DO 10 I=2,NSTOP
     48              SLOPE=(CIN(I)-CIN(I-1))/(FLOAT(NPRINT))
     49              DO 9 I7=1,NPRINT
     50       C
     51       C      1. BUBBLE PHASE TIME INCREMENT
     52       C
     53       C      1.1 GRID BUBBLES
     54       C
     55              DO 20 M=1,MAX
     56              IF(M.EQ.1) GO TO 21
     57              IF(M.EQ.MAX) GO TO 22
     58              IF(M.LT.MSP) GO TO 23
     59              A(M)=-C1L
```

```
      B(M)=1.+C2L
      C(M)=C1L
      D(M)=C1L*CB(M-1,N)+(1.-C2L)*CB(M,N)-C1L*CB(M+1,N)+C2L*CE(M,N)*2.
      GO TO 24
   21 A(M)=0.
      B(M)=1.
      C(M)=0.
      D(M)=0.
      GO TO 24
   22 A(M)=-2.*C1L
      B(M)=1.+C2L+C1L*2.
      C(M)=0.
      D(M)=2.*C1L*CB(M-1,N)+(1.-C2L-2.*C1L)*CB(M,N)+C2L*CE(M,N)*2.
      GO TO 24
   23 A(M)=-C1L
      B(M)=1.+C2L2
      C(M)=C1L
      D(M)=C1L*CB(M-1,N)+(1.-C2L2)*CB(M,N)-C1L*CB(M+1,N)+
     #2.*C2L2*CE(M,N)
   24 CONTINUE
   20 CONTINUE
      CALL TRIDAG(1,MAX,A,B,C,D,V1)
C
C     1.2 SPARGER BUBBLES
C
      DO 40 M=MSP,MAX
      IF(M.EQ.MSP) GO TO 41
      IF(M.EQ.MAX) GO TO 42
      A(M)=-C1H
      B(M)=1.+C2H
      C(M)=C1H
      D(M)=C1H*CSP(M-1,N)+(1.-C2H)*CSP(M,N)-
     #C1H*CSP(M+1,N)+2.*C2H*CE(M,N)
      GO TO 43
   41 A(M)=0.
      B(M)=1.
      C(M)=0.
      D(M)=SLOPE*FLOAT(IZ)+CIN(I-1)
      GO TO 43
   42 A(M)=-2.*C1H
      B(M)=1.+C2H+2.*C1H
      C(M)=0.
      D(M)=2.*C1H*CSP(M-1,N)+(1.-C2H-2.*C1H)*CSP(M,N)+
     #2.*C2H*CE(M,N)
   43 CONTINUE
   40 CONTINUE
      CALL TRIDAG(MSP,MAX,A,B,C,D,V3)
C
C     2. EMULSION PHASE TIME INCREMENT
C
      DO 25 M=1,MAX
      IF(M.EQ.1) GO TO 26
      IF(M.EQ.MAX) GO TO 27
      IF(M.LT.MSP) GO TO 28
      A(M)=-C3-C5
      B(M)=1.+2.*C5+C4
      C(M)=C3-C5
      D(M)=(C3+C5)*CE(M-1,N)+(1.-C4-2.*C5)*CE(M,N)+
     #(C5-C3)*CE(M+1,N)+C4L*(P1*KL*(CB(M,N)+V1(M))+P3*KH*(
     #CSP(M,N)+V3(M)))
```

```
      GO TO 29
   26 A(M)=0.
      B(M)=1.+C4L+2.*C5
      C(M)=-2.*C5
      D(M)=2.*C5*CE(M+1,N)+(1.-C4L-2.*C5)*CE(M,N)+C4L*(CB(M,N)+V1(M))
      GO TO 29
   27 A(M)=-2.*C5
      B(M)=1.+C4+2.*C5
      C(M)=0.
      D(M)=2.*C5*CE(M-1,N)+(1.-C4-2.*C5)*CE(M,N)+C4C*(F1*KL*(CB(M,N)+
     #V1(M))+F3*KH*(CSP(M,N)+V3(M)))
      GO TO 29
   28 A(M)=-C3-C5
      B(M)=1.+2.*C5+C4L
      C(M)=C3-C5
      D(M)=(C3+C5)*CE(M-1,N)+(1.-2.*C5-C4L)*CE(M,N)+
     #(C5-C3)*CE(M+1,N)+C4L*(CB(M,N)+V1(M))
   29 CONTINUE
   25 CONTINUE
      CALL TRIDAG(1,MAX,A,B,C,D,V2)
C
C     3. UPDATE FOR NEXT SMALL STEP
C
      II=(IFIX(FLOAT(IZ)/2.))*2
      IF(II.LT.IZ) N=1
      IF(II.EQ.IZ) N=2
      DO 11 K=1,MAX
      CB(K,N)=V1(K)
      CSP(K,N)=V3(K)
   11 CE(K,N)=V2(K)
    9 CONTINUE
C
C     4. UPDATE COUT
C
      COUT(IJ)=DEL*(F1*V1(MTEST)+F3*V3(MTEST))+
     #(1.-DEL)*ED*V2(MTEST)
   10 CONTINUE
      RETURN
      END
```

```
PROC*RDLIB(1).TRIDAG
      1       C
      2       C     SUBROUTINE FOR SOLVING A TRIDIAGONAL MATRIX SYSTEM OF
      3       C     EQUATIONS. NUMBERING OF EQUATIONS IS IF THROUGH L.
      4       C
      5             SUBROUTINE TRIDAG(IF,L,A,B,C,D,V)
      6             DIMENSION A(201),B(201),C(201),D(201),V(201)
      7             DIMENSION BETA(1001),GAMMA(1001)
      8       C
      9       C     COMPUTE ARRAYS GAMMA AND BETA
     10       C
     11             BETA(IF)=B(IF)
     12             GAMMA(IF)=D(IF)/BETA(IF)
     13             M=IF+1
     14             DO 10 J=M,L
     15             BETA(J)=B(J)-A(J)*C(J-1)/BETA(J-1)
     16             GAMMA(J)=(D(J)-A(J)*GAMMA(J-1))/BETA(J)
     17       10    CONTINUE
     18       C
     19       C     COMPUTE SOLUTION VECTOR V
     20       C
     21             V(L)=GAMMA(L)
     22             LAST=L-IF
     23             DO 11 J=1,LAST
     24             JJ=L-J
     25             V(JJ)=GAMMA(JJ)-C(JJ)*V(JJ+1)/BETA(JJ)
     26       11    CONTINUE
     27             DO 12 J=IF,L
     28             IF(V(J).LT.0.) V(J)=0.
     29       12    CONTINUE
     30             RETURN
     31             END
```

APPENDIX C

FOURIER TRANSFORM ROUTINE DEVELOPMENT AND TESTING

C1. DEVELOPMENT

For the conditions under which equation (4.5) is valid, the transfer function is related to the time-domain stimulus $C_{in}(t)$ and response $C_{out}(t)$ by:

$$G(jw) = \frac{\int_0^\infty e^{-jwt} C_{out}(t)dt}{\int_0^\infty e^{-jwt} C_{in}(t)dt} \qquad (C1)$$

or

$$G(jw) = \frac{\int_0^\infty C_{out}(t) \cos wt\, dt - j\int_0^\infty C_{out}(t) \sin wt\, dt}{\int_0^\infty C_{in}(t) \cos wt\, dt - j\int_0^\infty C_{in}(t) \sin wt\, dt} \qquad (C2)$$

The numerical evaluation of this expression is problematic. Himmelblau and Bischoff (127) discuss this, and Law and Bailey (128) suggest that accurate evaluation of the integrals is the key. The personal experience of the author has been that, in situations of this nature, a major source of error lies in the truncation of the time-domain data (i.e. the upper limit of the integrals) at some arbitrary time. The data is often truncated for practical reasons, and the selection of the truncation point is usually subjective. When process noise is present, information in the "tail" is lost and the choice of a truncation point may be particularly difficult.

The FT routine developed here inforporates the following features to minimise these effects:

(i) The numerical integration is performed by a double application of Simpson's Rule. The first integration is by exact fit second order polynomials on pairs of adjoining "strips", i.e. a conventional application of Simpson's Rule. The second is by third order exact fit polynomials to the three strips at either extreme, and second order poly= nomials to the intermediate pairs. The idea of the second application is to group strips which have not been paired in the first application. An average result is taken, and the overall effect is that of interpolating between overlapping second order exact fit polynomials.

(ii) Truncation is eliminated by fitting an exponential decay tail to the last 20% of the data by least squares, as shown in Figure C1. Analytical integrals based on this fitted decay tail are applied between t_f and infinity, the form being:

$$\int_{t_f}^{\infty} a_1 e^{-a_2 t} \sin(wt)\, dt = \frac{a_1 e^{-a_2 t_f}}{w^2 + a_2^2} \left[w \cos(wt_f) - a_2 \sin(wt_f)\right] \quad (C3)$$

$$\text{and} \int_{tf}^{\infty} a_1 e^{-a_2 t} \cos(wt)\, dt = \frac{-a_1 e^{-a_2 t_f}}{w^2 + a_2^2} \left[a_2 \cos(wt_f) + w \sin(wt_f)\right] \quad (C4)$$

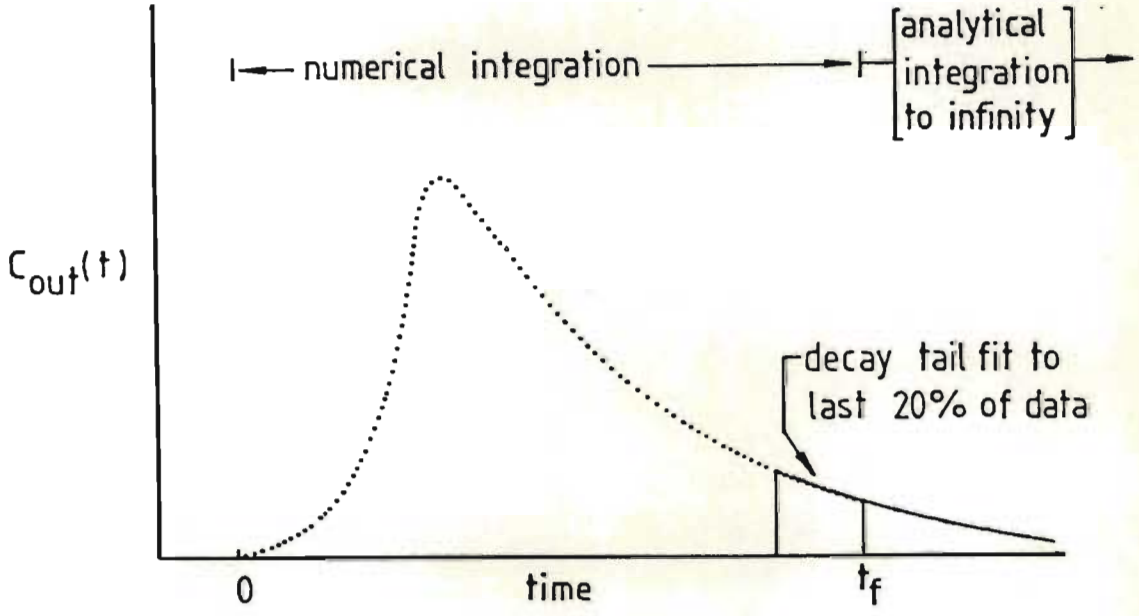

FIGURE C1 DECAY TAIL FIT AND INTEGRATION PROCEDURE

C2. TESTING

The Fourier Transform routine was tested against a simple tanks-in-series model. The theoretical time-domain impulse response for two perfectly mixed tanks with time constants τ_1 and τ_2 is:

$$E(t) = \frac{1}{\tau_2 - \tau_1} (\exp(-t/\tau_1) - \exp(-t/\tau_2)) \qquad (C5)$$

and the magnitude ratio of the corresponding frequency response:

$$|G(jw)| = \frac{1}{\sqrt{1+(w\tau_1)^2}\ \sqrt{1+(w\tau_2)^2}} \qquad (C6)$$

The discrete, truncated impulse response data given in Table C1 was supplied to the FT routine, and the ability of the latter to generate the frequency response given by equation (C6) tested. The time constants were fixed at 5 and 0.2 seconds.

The theoretical and numerical magnitude ratios are given in Figure C2. It is clear that the FT routine performs extremely well, even at frequencies well above those encountered in this study.

TIME (sec)	IMPULSE REPONSE
0	0
0.2	0.1061
0.4	0.1703
0.6	0.2070
0.8	0.2256
1.0	0.2325
1.2	0.2318
1.4	0.2265
1.6	0.2184
1.8	0.2086
2.0	0.1980
2.2	0.1872
2.4	0.1764
2.6	0.1659
2.8	0.1558
3.0	0.1462
3.2	0.1370
3.4	0.1283
3.6	0.1202
3.8	0.1125
4.0	0.1053

TABLE C1 FT ROUTINE TEST DATA

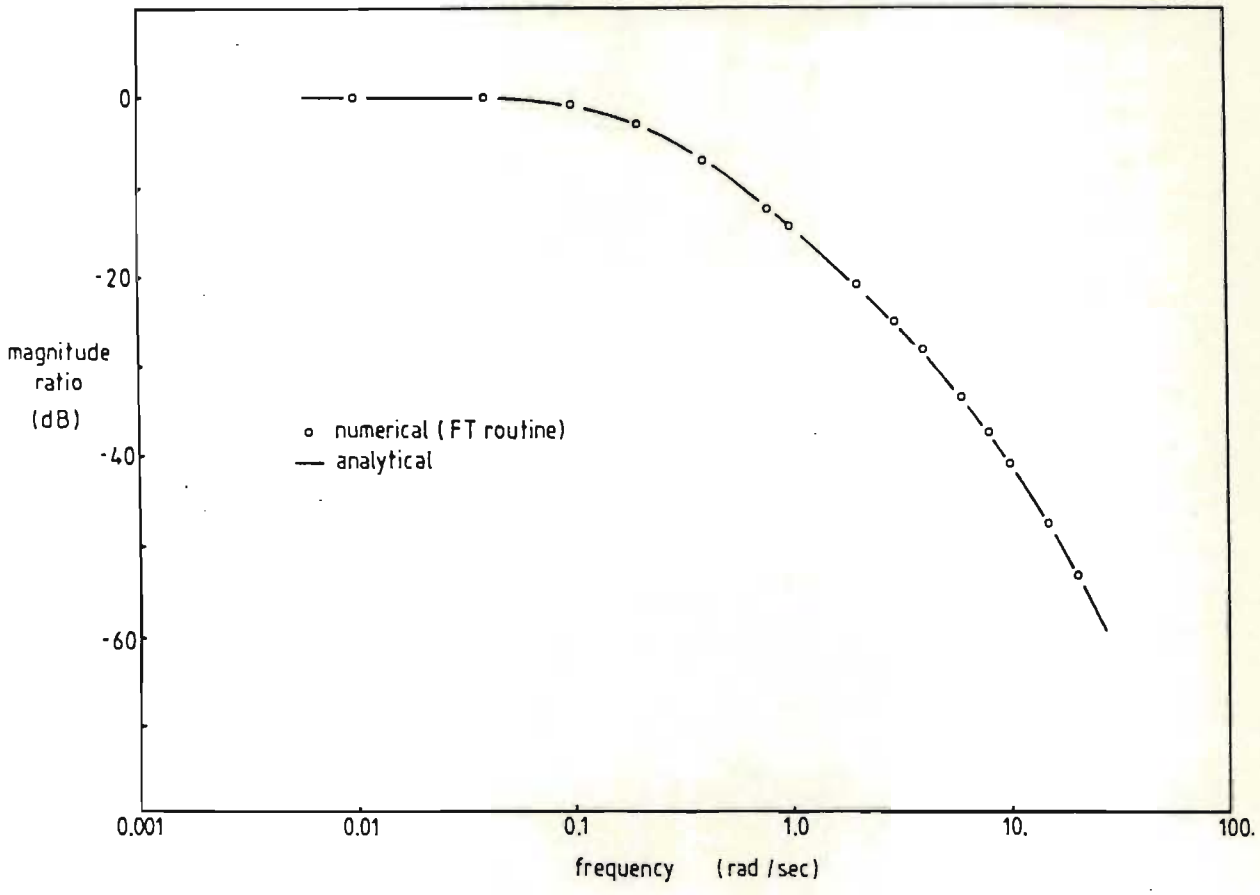

FIGURE C2 FOURIER TRANSFORM TEST RESULTS

C3. FORTRAN V LISTING OF THE FT ROUTINE

```
PROC*RDLIB(1).FT1
      1             SUBROUTINE FT1(X0,Y0,DX,DY,NX,NY,NZ,NDT,W,NW,RE,CJ)
      2       C
      3       C     FOURIER TRANSFORM ROUTINE
      4       C     *************************
      5       C
      6             DIMENSION X(1000),Y(1000),W(50),RE(50),CJ(50)
      7             DIMENSION A1(1000),A2(1000),A3(1000),A4(1000)
      8             DIMENSION X0(100),Y0(100),XH(20,2),YH(20,2)
      9       C
     10       C     DATA INTERPOLATION
     11       C
     12             THETA=.5
     13             DTX=DX/FLOAT(NDT)
     14             DTY=DY/FLOAT(NDT)
     15             X(1)=X0(1)
     16             Y(1)=Y0(1)
     17             NXM1=NX-1
     18             NYM1=NY-1
     19       C
     20       C     PROCESS INPUT SIGNAL
     21       C
     22             DO 19 JJ=1,NXM1
     23             K=1+NDT*(JJ-1)
     24             IF(JJ.EQ.1) GO TO 20
     25             IF(JJ.EQ.NXM1) GO TO 21
     26             DO 13 N=1,2
     27             T1=FLOAT(JJ-3+N)*DX
     28             T2=FLOAT(JJ-2+N)*DX
     29             T3=FLOAT(JJ-1+N)*DX
     30             X1=X0(JJ-2+N)
     31             X2=X0(JJ-1+N)
     32             X3=X0(JJ+N)
     33             CALL POLY(X1,X2,X3,T1,T2,T3,C1,C2,C3)
     34             DO 14 M=1,NDT
     35             T=FLOAT(JJ-1)*DX+FLOAT(M)*DTX
     36             XH(M,N)=C1+C2*T+C3*T**2
     37       14    IF(XH(M,N).LT.0.) XH(M,N)=0.
     38       13    CONTINUE
     39             DO 15 M=1,NDT
     40       15    X(M+K)=THETA*XH(M,1)+(1.-THETA)*XH(M,2)
     41             GO TO 22
     42       20    T1=0.
     43             T2=DX
     44             T3=2.*DX
     45             X1=X0(1)
     46             X2=X0(2)
     47             X3=X0(3)
     48             CALL POLY(X1,X2,X3,T1,T2,T3,C1,C2,C3)
     49             DO 16 M=1,NDT
     50             T=FLOAT(M)*DTX+FLOAT(JJ-1)*DX
     51             X(M+1)=C1+C2*T+C3*T**2
     52       16    IF(X(M+1).LT.0.) X(M+1)=0.
     53             GO TO 22
     54       21    DO 17 M=1,NDT
     55             T=FLOAT(M)*DTX+FLOAT(JJ-1)*DX
     56             X(M+K)=C1+C2*T+C3*T**2
     57       17    IF(X(M+K).LT.0.) X(M+K)=0.
     58       22    CONTINUE
     59       19    CONTINUE
```

```
      NXX=(NX-1)*NDT+1
      NN=(IFIX(FLOAT(NXX)/2.))*2
      IF(NN.EQ.NXX) NXX=NXX-1
C
C     PROCESS RESPONSE DATA
C
      DO 30 JJ=1,NYM1
      K=1+NDT*(JJ-1)
      IF(JJ.EQ.1) GO TO 31
      IF(JJ.EQ.NYM1) GO TO 32
      DO 33 N=1,2
      T1=FLOAT(JJ-3+N)*DY
      T2=FLOAT(JJ-2+N)*DY
      T3=FLOAT(JJ-1+N)*DY
      Y1=YO(JJ-2+N)
      Y2=YO(JJ-1+N)
      Y3=YO(JJ+N)
      CALL POLY(Y1,Y2,Y3,T1,T2,T3,C1,C2,C3)
      DO 34 M=1,NDT
      T=FLOAT(JJ-1)*DY+FLOAT(M)*DTY
      YH(M,N)=C1+C2*T+C3*T**2
34    IF(YH(M,N).LT.0.) YH(M,N)=0.
33    CONTINUE
      DO 35 M=1,NDT
35    Y(M+K)=THETA*YH(M,1)+(1.-THETA)*YH(M,2)
      GO TO 36
31    T1=0.
      T2=DY
      T3=2.*DY
      Y1=YO(1)
      Y2=YO(2)
      Y3=YO(3)
      CALL POLY(Y1,Y2,Y3,T1,T2,T3,C1,C2,C3)
      DO 37 M=1,NDT
      T=FLOAT(M)*DTY+FLOAT(JJ-1)*DY
      Y(M+1)=C1+C2*T+C3*T**2
37    IF(Y(M+1).LT.0.) Y(M+1)=0.
      GO TO 36
32    DO 38 M=1,NDT
      T=FLOAT(M)*DTY+FLOAT(JJ-1)*DY
      Y(M+K)=C1+C2*T+C3*T**2
38    IF(Y(M+K).LT.0.) Y(M+K)=0.
36    CONTINUE
30    CONTINUE
      NYY=(NY-1)*NDT+1
      NN=(IFIX(FLOAT(NYY)/2.))*2
      IF(NN.EQ.NYY) NYY=NYY-1
      NZZ=NZ*NDT
C
C     FIT DECAY TAIL TO Y(T)
C
      TMAX=DTY*FLOAT(NYY-1)
      TO=TMAX*.8
      CALL TAIL(Y,DTY,NYY,TO,TMAX,A,B,R)
      AO=A*EXP(-B*TO)
C
C     MAIN FREQUENCY LOOP
C
      DO 10 JW=1,NW
      WJ=W(JW)
```

```
      DO 11 J=1,NYY
      A1(J)=Y(J)*COS(WJ*FLOAT(J-1-NZZ)*DTY)
   11 A2(J)=Y(J)*SIN(WJ*FLOAT(J-1-NZZ)*DTY)
      DO 12 J=1,NXX
      A3(J)=X(J)*COS(WJ*FLOAT(J-1-NZZ)*DTX)
   12 A4(J)=X(J)*SIN(WJ*FLOAT(J-1-NZZ)*DTX)
      CALL SIMSON(A1,DTY,YR,NYY)
      CALL SIMSON(A2,DTY,YI,NYY)
      CALL SIMSON(A3,DTX,XR,NXX)
      CALL SIMSON(A4,DTX,XI,NXX)
C
C     CORRECT FOR DECAY TAIL
C
      YR=YR-A0*EXP(B*TMAX)*(B*COS(WJ*TMAX)+WJ*SIN(WJ*TMAX)
     #)/(WJ**2+B**2)
      YI=YI-A0*EXP(B*TMAX)*(B*SIN(WJ*TMAX)-WJ*COS(WJ*TMAX)
     #)/(WJ**2+B**2)
C
C     OUTPUT ARRAYS
C
      RE(JW)=(YR*XR+YI*XI)/(XR**2+XI**2)
      CJ(JW)=(YR*XI-YI*XR)/(XR**2+XI**2)
   10 CONTINUE
      RETURN
      END
```

```
PROC*RDLIB(1).SIMSON
     1              SUBROUTINE SIMSON(Y,DX,AREA,N)
     2              DIMENSION Y(2000)
     3        C
     4        C     THIS SUBROUTINE PERFORMS A NUMERICAL INTEGRATION
     5        C     OF THE TABULAR FUNCTION GIVEN IN THE ARRAY Y(N).
     6        C     SIMPSON'S RULE IS USED,SO THERE MUST BE AN ODD
     7        C     NUMBER OF DATA POINTS, EVENLY SPACED A DISTANCE
     8        C     DX APART.
     9        C
    10              I=(N-1)/2
    11              M=I-2
    12              IF(N.LT.11) GO TO 21
    13        C
    14        C     COMPUTE AREA USING 3/8 RULE FOR ENDS
    15        C
    16              SUM2=0.
    17              SUM4=0.
    18              DO 11 J=3,M
    19              SUM4=SUM4+Y(2*J+1)*4.
    20              SUM2=SUM2+Y(2*J)*2.
    21         11   CONTINUE
    22              PSUM=SUM2+SUM4+4.*Y(5)+Y(4)+Y(N-3)
    23              AIN=PSUM*DX/3.
    24              END1=Y(1)+3.*Y(2)+3.*Y(3)+Y(4)
    25              AEND1=END1*DX*3./8.
    26              END2=Y(N-3)+3.*Y(N-2)+3.*Y(N-1)+Y(N)
    27              AEND2=END2*DX*3./8.
    28              A2=AEND1+AEND2+AIN
    29        C
    30        C      COMPUTE AREA USING NORMAL SIMPSON
    31        C
    32        21    CONTINUE
    33              SUM2=0.
    34              SUM4=0.
    35              DO 10 J=1,I
    36              SUM4=SUM4+4.*Y(2*J)
    37              SUM2=SUM2+2.*Y(2*J-1)
    38         10   CONTINUE
    39              SUM=SUM2+SUM4+Y(N)-Y(1)
    40              A1=SUM*DX/3.
    41        C
    42        C      USE AVERAGE IF MORE THAN 10 DATA POINTS
    43        C
    44              IF(N.LT.11) AREA=A1
    45              IF(N.GE.11) AREA=(A1+A2)/2.
    46              RETURN
    47              END
```

```
PROC*RDLIB(1).TAIL
      1              SUBROUTINE TAIL(C,DX,N,T0,TMAX,A,B,R)
      2              DIMENSION C(500),F(500),X(500),Y(500)
      3        C
      4        C     THIS SUBROUTINE CALCULATES THE EXPONENTIAL
      5        C     DECAY CONSTANTS A AND B.
      6        C
      7        C     THE FORM IS: Y=A*EXP(B*(T-TREF))
      8        C
      9        C     R IS THE CORRELATION COEFFICIENT, UNITY FOR
     10        C     A PERFECT FIT (SIGN DEPENDENT ON SLOPE).
     11        C
     12              NO=IFIX((TMAX-T0)/DX+.2)+1
     13              T0=FLOAT(N-NO)*DX
     14              DO 20 J=1,NO
     15              F(J)=C(N-NO+J)
     16              IF(F(J).LE.0.) GO TO 22
     17              X(J)=FLOAT(J-1)*DX
     18        20    Y(J)=ALOG(F(J))
     19              SX=0.
     20              SY=0.
     21              SXX=0.
     22              SYY=0.
     23              SXY=0.
     24              DO 21 J=1,NO
     25              SXY=SXY+X(J)*Y(J)
     26              SXX=SXX+X(J)**2
     27              SYY=SYY+Y(J)**2
     28              SX=SX+X(J)
     29              SY=SY+Y(J)
     30        21    CONTINUE
     31              CXX=SXX-SX**2/FLOAT(NO)
     32              CYY=SYY-SY**2/FLOAT(NO)
     33              CXY=SXY-SX*SY/FLOAT(NO)
     34              B=CXY/CXX
     35              A=EXP(SY/FLOAT(NO)-B*SX/FLOAT(NO))
     36              R=CXY/SQRT(CXX*CYY)
     37              GO TO 23
     38        22    A=0.
     39              B=0.
     40              WRITE(6,24)
     41        24    FORMAT(1HO,'WARNING: ZEROS RETURNED FOR TAIL')
     42        23    CONTINUE
     43              RETURN
     44              END
```

```
PROC*RDLIB(1).POLY
      1              SUBROUTINE POLY(Y1,Y2,Y3,X1,X2,X3,A,B,C)
      2        C
      3        C     THIS SUBROUTINE COMPUTES THE COEFFICIENTS
      4        C     FOR A SECOND ORDER EXACT FIT POLYNOMIAL.
      5        C     THE FORM IS: Y=A+B*X+C*X**2
      6        C
      7              C=((Y1-Y2)/(X1-X2)-(Y2-Y3)/(X2-X3))/(X1-X3)
      8              B=(Y1-Y2)/(X1-X2)-C*(X1+X2)
      9              A=Y1-B*X1-C*X1**2
     10              RETURN
     11              END
```

APPENDIX D

LISTINGS OF THE SIMPLEX ROUTINE AND THE DRIVING PROGRAM

D1. FORTRAN V LISTING OF THE SIMPLEX ROUTINE

```
ROC*RDLIB(1).NELM
     1              SUBROUTINE NELM(X,F,EPS,P,FP,XS,H,IX,N,N1,NP)
     2        C
     3        C     ****************************************
     4        C     NELDER AND MEAD SIMPLEX SEQUENTIAL SEARCH
     5        C     ROUTINE
     6        C     ****************************************
     7        C
     8              DIMENSION X(1),P(1),FP(1),H(1),XS(1)
     9              ISH=1
    10              NN=N*(N+1)
    11              CALL CALF(N,X,F)
    12              FP(1)=F
    13              IF(IX)2, ,2
    14              DO 1 I=1,N
    15              K=I
    16              DO 1 J=1,N1
    17              P(K)=X(I)
    18              IF(I-J+1)1, ,1
    19              P(K)=X(I)+H(I)
    20        1     K=K+N
    21        2     K=1+N
    22              DO 3 I=2,N1
    23              DO 4 J=1,N
    24              X(J)=P(K)
    25        4     K=K+1
    26              CALL CALF(N,X,F)
    27        3     FP(I)=F
    28              IF(FP(1)-FP(2)) , ,5
    29              IH=2
    30              IL=1
    31              GO TO 6
    32        5     IH=1
    33              IL=2
    34        6     DO 7 I=3,N1
    35              IF(FP(I)-FP(IH)) , ,8
    36              IF(FP(I)-FP(IL)) ,7,7
    37              IL=I
    38              GO TO 7
    39        8     IH=I
    40        7     CONTINUE
    41              XN=N
    42        50    K1=NN
    43              DO 9 I=1,N
    44              K=I
    45              S=0.
    46              DO 10 J=1,N1
    47              IF(J-IH) ,10,
    48              S=S+P(K)
    49        10    K=K+N
    50              K1=K1+1
    51        9     P(K1)=S/XN
    52              K=NN+1
    53              DO 11 I=1,N
    54              X(I)=P(K)
    55        11    K=K+1
    56              CALL CALF(N,X,FO)
    57              S=0.
    58              DO 12 I=1,N1
    59        12    S=S+(FP(I)-FO)**2
```

```
      S=S/XN
      IF(S-EPS) 100,100,
      IF(IH-1) ,13,
      IS=1
      GO TO 14
13    IS=2
14    DO 15 I=1,N1
      IF(I-IH) ,15,
      IF(FP(I)-FP(IS))15,15,
      IS=I
15    CONTINUE
C
C     REFLECTION
C
      K=(IH-1)*N+1
      KO=NN+1
      DO 16 I=1,N
      X(I)=2.*P(KO)-P(K)
      K=K+1
16    KO=KO+1
      K=K-N
      CALL CALF(N,X,F)
      IF(F-FP(IL)) ,20,20
C
C     EXPANSION
C
      KO=NN+1
      DO 17 I=1,N
      XS(I)=2.*X(I)-P(KO)
17    KO=KO+1
      CALL CALF(N,XS,FS)
      IF(FS-FP(IL)) ,18,18
      DO 19 I=1,N
      P(K)=XS(I)
19    K=K+1
      FP(IH)=FS
      IL=IH
      IH=IS
      GO TO 30
18    IL=IH
      IH=IS
      FP(IL)=F
21    DO 22 I=1,N
      P(K)=X(I)
22    K=K+1
      GO TO 30
20    IF(F-FP(IS)) ,23,23
      FP(IH)=F
      IH=IS
      GO TO 21
23    IF(F-FP(IH)) ,25,25
      DO 24 I=1,N
      P(K)=X(I)
24    K=K+1
      FP(IH)=F
C
C     CONTRACTION
C
      K=K-N
25    KO=NN+1
```

```
120             DO 26 I=1,N
121             XS(I)=.5*(P(K)+P(K0))
122             K=K+1
123       26    K0=K0+1
124             K=K-N
125             CALL CALF(N,XS,FS)
126             IF(FS-FP(IH)) ,40,40
127             DO 27 I=1,N
128             P(K)=XS(I)
129       27    K=K+1
130             FP(IH)=FS
131             IF(FP(1)-FP(2)) , ,28
132             IH=2
133             GO TO 29
134       28    IH=1
135       29    DO 31 I=3,N1
136             IF(FP(I)-FP(IH))31,31,
137             IH=I
138       31    CONTINUE
139       30    GO TO 50
140       40    FP(1)=FP(IL)
141             KKK=MOD(ISH,10)
142             ISH=ISH+1
143             IF(IL-1) ,43,
144             K=(IL-1)*N
145             DO 41 I=1,N
146             K=K+1
147             X(I)=P(K)
148             P(K)=P(I)
149       41    P(I)=X(I)
150             IL=1
151       43    K=N
152             DO 42 I=2,N1
153             DO 42 J=1,N
154             K=K+1
155             P(K)=.5*(P(K)+P(J))
156             ISH=ISH+1
157       42    CONTINUE
158             GO TO 2
159       100   K=(IL-1)*N
160             DO 101 I=1,N
161             K=K+1
162             X(I)=P(K)
163       101   CONTINUE
164             F=FP(IL)
165             RETURN
166             END
```

D2. FORTRAN V LISTINGS OF THE MAIN PROGRAM AND THE OBJECTIVE FUNCTION ROUTINE

```
PROC*RDLIB(1).MAIN2
      1              DIMENSION T(3),P(15),FP(4),H(3),XS(3)
      2              DIMENSION W(30),REM(30),CJM(30),U(5),FU(5)
      3              REAL NB
      4        C
      5        C     ***********************************************
      6        C     MAIN PROGRAM FOR DETERMINING FFB MASS TRANSFER
      7        C     COEFFICIENTS BY SIMPLEX SEQUENTIAL SEARCH
      8        C     ***********************************************
      9        C
     10        C     INITIALISE SIMPLEX AND CALL OPTIMISATION
     11        C     ROUTINE
     12        C
     13              WRITE(6,23)
     14        23    FORMAT(1HO,'OPTIMISE? (1=YES)')
     15              READ(5,1) NOPT
     16              STOP=1.0E-08
     17              IX=0
     18              WRITE(6,70)
     19        70    FORMAT(1HO,'ENTER INITIAL STEP LENGTHS FOR P1&P2')
     20              READ(5,1) H(1),H(2)
     21              WRITE(6,10)
     22        10    FORMAT(1HO,'INITIAL VALUES FOR P1,P2?')
     23              READ(5,1) T(1),T(2)
     24        1     FORMAT()
     25              IF(NOPT.NE.1) GO TO 96
     26              CALL NELM(T,F,STOP,P,FP,XS,H,IX,2,3,8)
     27              WRITE(6,11) T(1),T(2),F
     28        11    FORMAT(1HO,'OPTIMISATION COMPLETE'//' PARAMETER VALUES:'/
     29             #'     P1 ',F10.4/'     P2 ',F10.4///5X,
     30             #'OBJECTIVE FUNCTION ',E10.4)
     31              WRITE(6,12)
     32        12    FORMAT(1HO,'MODEL RESPONSES? (1=YES)')
     33              READ(5,1) MY
     34              IF(MY.NE.1) GO TO 30
     35        C
     36        C     MODEL FREQUENCY RESPONSES
     37        C
     38        C     1. DATA INPUT
     39        C
     40        96    CONTINUE
     41              WRITE(6,13)
     42        13    FORMAT(1HO,'ENTER MODEL FIXED PARAMETERS')
     43              READ(5,1) U0,UB,UD,US,ED,HF,HT,ALPHA,NB
     44              E=HT/HF
     45              READ(5,1) (U(J),J=1,5)
     46              READ(5,1) (FU(J),J=1,5)
     47              READ(5,1) NW
     48              READ(5,1) (W(J),J=1,NW)
     49              WRITE(6,14)
     50        14    FORMAT(1HO,'MODEL CHOICE?')
     51              READ(5,1) MCH
     52        C
     53        C     3. USE ONE OF THE MODELS
     54        C
     55        C     3.1 MVD MODEL
     56        C
     57              ERROR=SQRT(F/FLOAT(NW))
     58              IF(MCH.EQ.2) GO TO 31
     59              IF(MCH.EQ.3) GO TO 32
```

```
      IF(MCH.EQ.4) GO TO 33
      IF(MCH.EQ.5) GO TO 34
      WRITE(6,15)
15    FORMAT(1H1,10X,'MAY-VAN DEEMTER MODEL TRANSFER FUNCTION'/
     #11X,39('*')/)
      WRITE(6,16) T(1),T(2),ERROR
16    FORMAT(1HO,5X,'XB=',F8.3/6X,'ND=',F8.3/
     #6X,'AVG ERROR ON NYQUIST PLOT',F10.5)
      CALL MVD(T(1),T(2),UO,UB,UD,ED,HF,E,NW,W,REM,CJM,1)
97    CONTINUE
      REZ=REM(1)
      DO 199 L=1,NW
      REM(L)=REM(L)/REZ
199   CJM(L)=CJM(L)/REZ
      WRITE(6,19)
19    FORMAT(1HO,10X,'FREQ',11X,'REAL',9X,'IMAGINARY',6X,'MAG RATIO',5X,
     #'PHASE ANGLE'/9X,72('*'))
      DO 63 J=1,NW
      RMAG=20.*ALOG10(SQRT(REM(J)**2+CJM(J)**2))
      ACORR=0.
      IF(REM(J).LT.0.) ACORR=180.
      ANG=ATAN(CJM(J)/REM(J))*57.3-ACORR
      WRITE(6,20) W(J),REM(J),CJM(J),RMAG,ANG
63    CONTINUE
20    FORMAT(1HO,5(5X,F10.4))
      GO TO 30
C
C     3.2 BPD MODEL
C
31    CONTINUE
      WRITE(6,81)
81    FORMAT(1H1,10X,'BUBBLE PHASE DISPERSION MODEL',
     #' TRANSFER FUNCTION'/11X,47('*')/)
      WRITE(6,82) T(1),T(2),NB,ERROR
82    FORMAT(1HO,5X,'XB=',F8.3/6X,'ND=',F8.3/6X,'NB=',F8.3/
     #6X,'AVG ERROR ON NYQUIST PLOT',F10.5)
      CALL BPD(T(1),T(2),NB,UO,UB,UD,ED,HF,E,NW,W,REM,CJM,1)
      GO TO 97
C
C     3.3 WFD MODEL
C
32    CONTINUE
      WRITE(6,83)
83    FORMAT(1H1,10X,'WERTHER FILM DIFFUSION MODEL',
     #' TRANSFER FUNCTION'/11X,46('*')/)
      WRITE(6,84) T(1),T(2),ERROR
84    FORMAT(1HO,5X,'XB=',F8.3/6X,'AL=',F8.3/
     #6X,'AVG ERROR ON NYQUIST PLOT',F10.5)
98    CALL WFD(T(1),T(2),UO,UB,ED,HF,E,NW,W,REM,CJM,1)
      GO TO 97
C
C     3.4 TWO-PHASE MBT MODEL
C
33    CONTINUE
      WRITE(6,85)
85    FORMAT(1H1,10X,'TWO-PHASE MBT MODEL FREQUENCY ',
     #'RESPONSE'/11X,38('*')/)
      WRITE(6,86) T(1),T(2),ERROR
86    FORMAT(1HO,5X,'XB=',F8.3/6X,'ND=',F8.3/6X,
     #'AVG ERROR ON NYQUIST PLOT',F10.5)
```

```
      CALL MBT(T(1),T(2),U0,U,FU,UD,ED,HF,E,NW,W,REM,CJM,1)
      GO TO 97
C
C     3.5 CC8M MODEL
C
34    CONTINUE
      WRITE(6,87)
87    FORMAT(1H1,10X,'COUNTERCURRENT BACKMIXING MODEL',
     #' TRANSFER FUNCTION'/11X,49('*')/)
      WRITE(6,88) T(1),T(2),ERROR
88    FORMAT(1H0,5X,'X8C=',F8.3/6X,'XCE=',F8.3/6X,
     #'AVG ERROR ON NYQUIST PLOT',F10.5)
      UE=UD/ED-US
      CALL CC8M(T(1),T(2),U0,U8,UE,ED,HF,E,ALPHA,NW,W,REM,CJM,1)
      GO TO 97
30    CONTINUE
      STOP
      END
```

```
PROC*RDLIB(1).CALF2
      1             SUBROUTINE CALF(N,P,OBJ)
      2       C
      3       C     ****************************************
      4       C     OBJECTIVE FUNCTION CALCULATION FOR SIMPLEX
      5       C     SEQUENTIAL SEARCH ROUTINE
      6       C     ****************************************
      7       C
      8             DIMENSION P(3),CIN(500),COUT(500),W(30),RE(30),CJ(30)
      9             DIMENSION CH(500),REM(30),CJM(30),RXX(200),RXY(200)
     10             DIMENSION U(5),FU(5)
     11             REAL NB
     12       C
     13       C     DATA INPUT: FIRST ITERATION ONLY
     14       C
     15             IF(NN.NE.0) GO TO 10
     16             NN=NN+1
     17             WRITE(6,30)
     18       30    FORMAT(1HO,'ENTER FIXED PARAMETERS')
     19             READ(5,1) UO,UB,UD,US,ED,H,HT,ALPHA,NB
     20             E=HT/H
     21             READ(5,1) (U(J),J=1,5)
     22             READ(5,1) (FU(J),J=1,5)
     23             READ(5,1) NW
     24             READ(5,1) (W(J),J=1,NW)
     25       1     FORMAT()
     26             WRITE(6,31)
     27       31    FORMAT(1HO,'ENTER ACTUAL RESPONSE DATA')
     28             READ(5,1) DX,DY,NX,NY,TS
     29             READ(5,1) (CIN(J),J=1,NX)
     30             READ(5,1) (COUT(J),J=1,NY)
     31             WRITE(6,32)
     32       32    FORMAT(1HO,'MODEL CHOICE?')
     33             READ(5,1) MCH
     34             WRITE(6,36)
     35       36    FORMAT(1HO,'PARAMETER FIXING: 1=P1 ; 2=P2')
     36             READ(5,1) MFIX
     37             P1=P(1)
     38             P2=P(2)
     39             NT=NY
     40             DT=DY
     41       C
     42       C     EXPERIMENTAL DATA MANIPULATION
     43       C
     44       C     1. SHIFT TIME AXIS
     45       C
     46             DO 40 J=1,NT
     47       40    CH(J)=COUT(J)
     48             MM=0
     49             DO 41 J=1,20
     50             XX=ABS(TS)-FLOAT(J)*DT
     51       41    IF(XX.GT.0.) MM=MM+1
     52             IF(TS.LT.0.) GO TO 50
     53       C
     54       C     POSITIVE SHIFT
     55       C
     56             TS=TS-FLOAT(MM)*DT
     57             NT=NT-MM
     58             DO 42 J=1,NT
     59       42    COUT(J)=CH(J+MM)
```

```
      NTM1=NT-1
      DO 43 J=1,NTM1
43    COUT(J)=COUT(J)+(COUT(J+1)-COUT(J))*TS/DT
      COUT(NT)=COUT(NT)+(COUT(NT)-CH(NT+MM-1))*TS/DT
      GO TO 51
C
C     NEGATIVE SHIFT
C
50    CONTINUE
      TS=TS+FLOAT(MM)*DT
      NT=NT+MM
      MMP1 =MM+1
      MMP2=MM+2
      DO 44 J=MMP1,NT
44    COUT(J)=CH(J-MM)
      DO 45 J=1,MM
45    COUT(J)=0.
      DO 46 J=MMP2,NT
46    COUT(J)=CH(J-MM)+(CH(J-MM)-CH(J-MM- 1))*TS/DT
      COUT(MMP1)=CH(1)+CH(1)*TS/DT
51    CONTINUE
C
C     2.COMPUTE FREQUENCY RESPONSE AND PRINT RESULTS
C
      NZ=1
      NDT=5
      WRITE(6,63)
63    FORMAT(1HO,'WINDOW LAG? (1=YES)')
      READ(5,1) WCH
      IF(WCH.NE.1) GO TO 64
      WRITE(6,66)
66    FORMAT(1HO,'ENTER NWIND')
      READ(5,1) NWIND
      JSTOP=NX-NWIND
      KSTOP=NWIND-1
      DO 67 J=NWIND,JSTOP
      RXX(J)=CIN(J)
      DO 68 K=1,KSTOP
68    RXX(J)=RXX(J)+(CIN(J+K)+CIN(J-K))*FLOAT(NWIND-K)/FLOAT(
     #NWIND)
67    RXX(J)=RXX(J)/FLOAT(NWIND)
      JSTOP=NY-NWIND
      DO 69 J=NWIND,JSTOP
      RXY(J)=COUT(J)
      DO 70 K=1,KSTOP
70    RXY(J)=RXY(J)+(COUT(J+K)+COUT(J-K))*FLOAT(NWIND-K)/
     #FLOAT(NWIND)
69    RXY(J)=RXY(J)/FLOAT(NWIND)
      DO 71 J=NWIND,JSTOP
71    COUT(J)=RXY(J)
      JSTOP=NX-NWIND
      DO 72 J=NWIND,JSTOP
72    CIN(J)=RXX(J)
64    CONTINUE
      CALL FT1(CIN,COUT,DX,DY,NX,NY,NZ,NDT,W,NW,RE,CJ)
      WRITE(6,33)
33    FORMAT(1H1,29X,'EXPERIMENTAL TRANSFER FUNCTION'/30X,
     #30('*')//)
      WRITE(6,34)
34    FORMAT(1HO,10X,'FREQ',11X,'REAL',9X,'IMAGINARY',6X,'MAG RATIO',
```

```
120           #5X,'PHASE ANGLE'/9X,72('*')]
121            REZ=RE(1)
122            DO 47 J=1,NW
123            RE(J)=RE(J)/REZ
124            CJ(J)=CJ(J)/REZ
125            RMAG=20.*ALOG10(SQRT(RE(J)**2+CJ(J)**2))
126            ACORR=0.
127            IF(RE(J).LT.0.) ACORR=180.
128            ANG=ATAN(CJ(J)/RE(J))*57.3-ACORR
129            WRITE(6,35) W(J),RE(J),CJ(J),RMAG,ANG
130       35   FORMAT(1H0,5(5X,F10.4))
131       47   CONTINUE
132       C
133       C    OPTIMISATION OUTPUT HEADING
134       C
135            WRITE(6,37)
136       37   FORMAT(1H1,15X,'OPTIMISATION'/16X,12('*')//)
137            WRITE(6,38)
138       38   FORMAT(1H0,5X,'P1',11X,'P2',11X,'OBJ'/4X,35('*'))
139       10   CONTINUE
140       C
141       C    MODEL FREQUENCY RESPONSE
142       C
143            IF(P(1).LT..0001) P(1)=.0001
144            IF(P(1).GT.100.) P(1)=100.
145            IF(MFIX.EQ.1) P(1)=P1
146            IF(MFIX.EQ.2) P(2)=P2
147            IF(MCH.EQ.2) GO TO 52
148            IF(MCH.EQ.3) GO TO 53
149            IF(MCH.EQ.4) GO TO 55
150            IF(MCH.EQ.5) GO TO 56
151       C
152       C    MVD MODEL
153       C
154            IF(P(2).LT..000001) P(2)=.000001
155            IF(P(2).GT.50.) P(2)=50.
156            CALL MVD(P(1),P(2),UO,UB,UD,ED,HT,E,NW,W,REM,CJM,1)
157            GO TO 54
158       C
159       C    BPD MODEL
160       C
161       52   CONTINUE
162            IF(P(2).LT..00001) P(2)=.00001
163            IF(P(2).GT.50.) P(2)=50.
164            CALL BPD(P(1),P(2),N8,UO,UB,UD,ED,HT,E,NW,W,REM,CJM,1)
165            GO TO 54
166       C
167       C    WFD MODEL
168       C
169       53   CONTINUE
170            IF(P(2).LT..0001) P(2)=.0001
171            IF(P(2).GT.50.) P(2)=50.
172            CALL WFD(P(1),P(2),UO,UB,ED,HT,E,NW,W,REM,CJM,1)
173            GO TO 54
174       C
175       C    TWO-PHASE MBT MODEL
176       C
177       55   CONTINUE
178            IF(P(2).LT..000001) P(2)=.000001
179            IF(P(2).GT.50.) P(2)=50.
```

```
180             CALL MBT(P(1),P(2),UO,U,FU,UD,ED,HT,E,NW,W,REM,CJM,1)
181             GO TO 54
182       C
183       C     CCBM MODEL
184       C
185       56    CONTINUE
186             IF(P(2).LT..001) P(2)=.001
187             IF(P(2).GT.100.) P(2)=100.
188             UE=UD/ED-US
189             CALL CCBM(P(1),P(2),UO,UB,UE,ED,HT,E,ALPHA,NW,W,REM,CJM,1)
190       54    CONTINUE
191       C
192       C     SET UP OBJECTIVE FUNCTION
193       C
194             REZ=REM(1)
195             DO 99 L=1,NW
196             REM(L)=REM(L)/REZ
197       99    CJM(L)=CJM(L)/REZ
198             OBJ=0.
199             DO 61 J=1,NW
200             OBJ=OBJ+(REM(J)-REM(J))**2+(CJM(J)-CJM(J))**2
201       61    CONTINUE
202             WRITE(6,1) P(1),P(2),OBJ
203             RETURN
204             END
```

APPENDIX E

AUTO AND CROSSCORRELATION CALCULATION DETAILS

Equations (5.6) and (5.7) may be re-written in a form more suitable for numerical evaluation as follows:

$$R_{Y_1Y_1}(i) = \frac{1}{n-i+1} \sum_{k=1}^{n-i+1} Y_1(k)\, Y_1(k+i-1) \qquad \text{(E1)}$$

and $$R_{Y_1Y_2}(i) = \frac{1}{n-i+1} \sum_{k=1}^{n-i+1} Y_1(k)\, Y_2(k+i-1) \qquad \text{(E2)}$$

It is understood that the time records are sampled at a constant frequency, and that one sampling period is associated with each increment in the counters i and k.

The calculation steps are:

(i) Normalise the data by letting

$$Y_1(k) = Y_1(k) - \frac{1}{n} \sum_{l=1}^{n} Y_1(l) \qquad \text{(E3)}$$

$$Y_2(k) = Y_2(k) - \frac{1}{n} \sum_{l=1}^{n} Y_2(l) \qquad \text{(E4)}$$

(ii) Compute the forward auto- and crosscorrelations by applying equations (E1) and (E2).

(iii) Compute the backward crosscorrelation (negative time lag) as follows:

$$R_{Y_1Y_2}(-i) = \frac{1}{n-i+1} \sum_{k=1}^{n-i+1} Y_1(k+i-1)\ Y_2(k) \qquad \text{(E5)}$$

BASIC LISTING OF THE CORRELATION FUNCTION PROGRAM

```
10  REM
20  REM    ********************************
30  REM    PRBS DATA MANIPULATION PROGRAM
40  REM    ********************************
50  REM
60  DIM X%(6000),Y%(6000)
70  INPUT "NMAX ? ";NM%
80  INPUT "NPOS ? ";NP%
90  INPUT "NNEG ? ";NN%
100 AI =  - 16256 + 1 * 16
110  REM ------- A/D DATA COLLECTION -------
120  PRINT "A/D DATA COLLECTION UNDER WAY"
130  FOR I = 1 TO NM%
140  POKE AI,6 * 16 + 1
150 X%(I) =  PEEK (AI + 1) * 256 +  PEEK (AI)
160  POKE AI,6 * 16 + 2
170 Y%(I) =  PEEK (AI + 1) * 256 +  PEEK (AI)
180  FOR J = 1 TO 103
190 K = J
200  NEXT J
220  PRINT I,X%(I),Y%(I)
230  NEXT I
240  PRINT "A/D DATA COLLECTION COMPLETE"
245  PR# 3
250  REM  ------- AUTO&CROSSCORRELATIONS -------
251  REM          1. POSITIVE TIME LAG
252 XA = 0
253 YA = 0
```

```
254  FOR J = 1 TO NM%
255 XA = XA + X%(J)
256 YA = YA + Y%(J)
257  NEXT J
258 XA = XA / NM%
259 YA = YA / NM%
260  FOR J = 1 TO NM%
261 X%(J) = X%(J) - XA
262 Y%(J) = Y%(J) - YA
263  NEXT J
265 XT = 0
270 YT = 0
275 XY = 0
280  FOR J = 1 TO NM%
290 XT = XT + X%(J) * X%(J)
300 YT = YT + Y%(J) * Y%(J)
310 XY = XY + X%(J) * Y%(J)
320  NEXT J
330 R1 = XT / NM%
340 R2 = YT / NM%
350 R3 = XY / NM%
360  FOR K = 0 TO NP%
370 NK = NM% - K
375 XT = 0
380 YT = 0
```

```
385 XY = 0
390  FOR L = 1 TO NK
400 XT = XT + X%(L) * X%(L + K)
410 YT = YT + Y%(L) * Y%(L + K)
420 XY = XY + X%(L) * Y%(L + K)
430  NEXT L
440 RX = XT / (NK * R1)
450 RY = YT / (NK * R2)
460 RQ = XY / (NK * R3)
470  PRINT K,RX,RY,RQ
480  NEXT K
490  REM        2. NEGATIVE TIME LAG
500  FOR K = 0 TO NN%
510 NK = NM% - K
520 XY = 0
530  FOR L = 1 TO NK
540 XY = XY + X%(L + K) * Y%(L)
550  NEXT L
560 RQ = XY / (NK * R3)
570 KN =  - 1 * K
580  PRINT KN,0,0,RQ
590  NEXT K
600  END
```

APPENDIX F

MODEL FITTING RESULTS FOR ALL RUNS

1. RUN ANALYSIS : MBT MODEL

1.1 0.05 m Tube

U_0 (m/s)	L_t (m)	X_b	N_d	$(K_{be})_b$ (sec^{-1})	D_d (m^2/s)	EI
0.17	0.40	1.94	0.14	3.45	0.032	1.00
0.19	0.40	1.60	0.30	2.71	0.077	1.00
0.24	0.40	1.29	0.35	2.41	0.094	1.00
0.30	0.40	1.20	0.38	2.31	0.13	1.00
0.14	0.97	2.50	.014	1.60	0.009	1.00
0.16	0.97	2.63	0.11	1.63	0.058	1.00
0.30	0.97	1.59	0.22	1.17	0.18	1.00
0.46	0.97	1.35	0.25	1.23	0.25	1.00
0.60	0.97	1.07	0.33	1.07	0.40	1.00
0.14	2.51	3.15	.0098	0.83	0.014	1.54
0.18	2.51	2.90	.010	0.86	0.015	1.75
0.26	2.51	2.04	.013	0.53	0.026	1.11
0.38	2.51	1.84	.012	0.50	0.032	1.07
0.57	2.51	1.15	.011	0.48	0.039	1.67
0.70	2.51	1.06	.0090	0.51	0.033	1.18
0.23	3.46	2.73	.016	0.61	0.045	1.00
0.38	3.46	2.08	.015	0.53	0.059	1.00
0.43	3.46	2.04	.023	0.58	0.081	1.00
0.59	3.46	1.50	.015	0.51	0.061	1.05

1.2 0.64 m Tube, 7 Coils

U_0 (m/s)	L_t (m)	X_b	N_d	$(K_{be})_b$ (sec^{-1})	D_d (m^2/s)	EI
0.13	0.49	0.95	5.1	1.45	1.8	1.00
0.19	"	0.64	6.4	1.11	2.7	1.00
0.22	"	0.68	0.46	1.28	0.25	1.03
0.27	"	0.52	0.06	1.12	0.04	1.00
0.32	"	0.60	5.0	1.35	3.5	1.00
0.15	0.95	1.22	0.97	1.00	0.90	1.00
0.25	"	0.84	0.75	0.84	0.94	1.06
0.28	"	0.81	1.8	0.92	2.6	1.03
0.38	"	0.65	1.3	0.80	2.3	1.26
0.44	"	0.56	1.2	0.61	2.6	1.00
0.17	1.95	1.58	0.28	0.87	0.55	1.00
0.20	"	1.33	0.37	0.76	0.80	1.00
0.26	"	1.07	0.55	0.67	1.7	1.00
0.34	"	0.80	5.2	0.62	16.9	1.00
0.39	"	0.75	0.51	0.62	1.8	1.00
0.53	"	0.46	1.3	0.40	5.4	1.00
0.16	3.05	1.85	0.32	0.83	1.3	1.00
0.23	"	1.34	1.55	0.63	7.9	1.00
0.30	"	1.16	0.20	0.57	1.2	1.00
0.37	"	0.88	0.73	0.44	4.9	1.00
0.42	"	0.72	1.03	0.43	7.4	1.00

1.3 0.64 m Tube, no Coils

U_0 (m/s)	L_t (m)	X_b	N_d	$(K_{be})_b$ (sec^{-1})	D_d (m^2/s)	EI
0.14	3.05	1.60	5.3	0.86	27.6	1.00
0.18	"	1.46	0.41	0.75	2.5	1.12
0.22	"	1.42	0.38	0.72	2.4	1.00
0.28	"	1.13	1.1	0.64	6.4	1.00
0.31	"	1.15	0.25	0.68	1.6	1.00

2. RUN ANALYSIS : MVD MODEL

2.1 0.05 m Tube

U_0 (m/s)	L_t (m)	X_b	N_d	EI
0.17	0.40	2.09	0.17	1.04
0.19	"	1.67	0.40	1.01
0.24	"	1.28	0.41	1.03
0.30	"	1.07	0.02	1.17
0.14	0.97	2.76	0.17	1.02
0.16	"	3.08	0.10	1.04
0.30	"	1.70	0.22	1.06
0.46	"	1.59	0.63	1.08
0.60	"	1.27	0.79	1.39
0.14	2.51	2.83	0	1.10
0.18	"	2.79	0	1.30
0.26	"	1.84	0	1.25
0.38	"	1.76	0	2.21
0.57	"	1.15	0	1.61
0.70	"	1.09	0	1.07
0.23	3.46	2.70	0	1.30
0.38	"	1.94	0	1.12
0.43	"	1.91	0	1.61
0.59	"	1.71	0	1.33

2.2 0.64 m Tube, 7 Coils

U_0 (m/s)	L_t (m)	X_b	N_d	EI
0.13	0.49	1.05	4.6	1.05
0.19	"	0.75	3.2	1.07
0.22	"	0.71	0.51	1.00
0.27	"	0.55	0.07	1.01
0.32	"	0.56	4.6	1.12
0.15	0.95	1.36	21	1.16
0.25	"	0.85	0.07	1.00
0.28	"	0.88	5.9	1.00
0.38	"	0.67	4.3	1.00
0.44	"	0.55	2.3	1.05
0.17	1.95	1.68	0.31	1.06
0.20	"	1.46	0.41	1.01
0.26	"	1.14	22	1.13
0.34	"	0.86	17	1.01
0.39	"	0.73	6.6	1.03
0.53	"	0.47	2.1	1.02
0.16	3.05	2.17	0.54	1.13
0.23	"	1.44	4.3	1.08
0.30	"	1.29	0.23	1.02
0.37	"	0.98	4.6	1.05
0.42	"	0.79	2.3	1.02

2.3 0.64 m Tube, no Coils

U_0 (m/s)	L_t (m)	X_b	N_d	EI
0.14	3.05	1.69	23	1.06
0.18	"	1.54	0.46	1.00
0.22	"	1.58	0.56	1.02
0.28	"	1.22	18	1.02
0.31	"	1.30	0.21	1.04

3. RUN ANALYSIS : BPD MODEL

3.1 0.05 m Tube

U_0 (m/s)	L_t (m)	X_b	N_d	EI
0.17	0.40	1.81	0.10	1.53
0.19	"	1.55	0.098	2.70
0.24	"	1.32	0.083	2.77
0.30	"	1.08	0.13	1.15
0.14	0.97	2.83	0.085	17.9
0.16	"	2.55	0.087	21.5
0.30	"	1.58	0.080	1.01
0.46	"	1.38	0.093	6.40
0.60	"	1.04	0.22	1.07
0.14	2.51	3.10	0	1.00
0.18	"	2.95	0	1.00
0.26	"	2.20	0.0010	1.00
0.38	"	1.88	0.0002	1.00
0.57	"	1.18	0	1.00
0.70	"	1.04	0	1.00
0.23	3.46	2.71	0	1.26
0.38	"	2.09	0	1.24
0.43	"	2.03	0	1.80
0.59	"	1.51	0	1.16

3.2 0.64 m Tube, 7 Coils

U_0 (m/s)	L_t (m)	X_b	N_d	EI
0.13	0.49	1.22	0.14	2.58
0.19	"	0.60	0	4.11
0.22	"	0.95	0.055	1.27
0.27	"	0.73	0.08	1.88
0.32	"	0.75	0	1.45
0.15	0.95	1.89	0.097	16.6
0.25	"	1.98	0.15	1.11
0.28	"	1.10	0.14	4.40
0.38	"	1.13	0.17	4.31
0.44	"	0.61	0.051	2.56
0.17	1.95	1.89	0.087	10.4
0.20	"	1.51	0.12	6.62
0.26	"	1.10	0.088	5.96
0.34	"	0.92	0.033	2.43
0.39	"	0.98	0.15	3.82
0.53	"	0.63	0.080	1.20
0.16	3.05	2.59	0	16.2
0.23	"	1.21	0	19.8
0.30	"	2.04	0.092	15.5
0.37	"	1.26	0.24	3.78
0.42	"	1.01	0.21	4.76

3.3 0.64 m Tube, no Coils

U_0 (m/s)	L_t (m)	X_b	N_d	EI
0.14	3.05	1.96	0	3.79
0.18	"	1.65	0	10.9
0.22	"	1.33	0.13	6.96
0.28	"	1.93	0.10	5.85
0.31	"	1.32	0	23.9

4. RUN ANALYSIS : CCBM MODEL

4.1 0.05 m Tube

U_0 (m/s)	L_t (m)	X_{bc}	X_{ce}	X_{be}	EI
0.17	0.40	2.54	2.90	1.36	1.60
0.19	"	2.45	2.39	1.21	2.98
0.24	"	2.04	2.33	1.09	3.18
0.30	"	1.01	>100	1.01	1.18
0.14	0.97	9.12	2.45	1.93	29.8
0.16	"	11.4	2.43	2.01	24.6
0.30	"	4.88	1.71	1.26	1.01
0.46	"	3.33	1.67	1.11	6.03
0.60	"	1.44	0.92	0.56	1.70
0.14	2.51	4.64	9.55	3.12	2.14
0.18	"	2.85	>100	2.85	1.30
0.26	"	2.39	4.22	1.53	2.43
0.38	"	1.91	>100	1.91	2.33
0.57	"	1.98	3.27	1.23	1.64
0.70	"	1.01	>100	1.01	1.81
0.23	3.46	54	3.93	3.93	1.07
0.38	"	5.16	3.83	2.20	1.12
0.43	"	3.63	5.61	2.21	1.50
0.59	"	3.50	3.28	1.69	1.00

Note: $X_{be} = (1/X_{bc} + 1/X_{ce})^{-1}$

4.2 0.64 m Tube, 7 Coils

U_0 (m/s)	L_t (m)	X_{bc}	X_{ce}	X_{be}	EI
0.13	0.49	1.19	>100	1.19	2.79
0.19	"	0.84	>100	0.84	2.94
0.22	"	1.96	4.42	1.36	1.89
0.27	"	1.10	16	1.03	7.11
0.32	"	1.86	2.54	1.07	1.64
0.15	0.95	1.86	>100	1.86	21.9
0.25	"	3.86	2.53	1.53	1.52
0.28	"	0.93	>100	0.93	4.29
0.38	"	0.77	>100	0.77	3.70
0.44	"	0.73	20	0.70	2.11
0.17	1.95	1.75	>100	1.75	12.3
0.20	"	1.36	>100	1.36	7.85
0.26	"	1.12	>100	1.12	6.31
0.34	"	0.78	>100	0.78	3.74
0.39	"	1.05	>100	1.05	2.33
0.53	"	0.72	5.03	0.63	1.19
0.16	3.05	2.11	>100	2.11	16.6
0.23	"	1.49	>100	1.49	17.2
0.30	"	1.53	>100	1.53	20.3
0.37	"	0.94	>100	0.94	4.02
0.42	"	0.81	>100	0.81	4.66

4.3 0.64 m Tube, no Coils

U_0 (m/s)	L_t (m)	X_{bc}	X_{ce}	X_{be}	EI
0.14	3.05	1.69	>100	1.69	2.92
0.18	"	4.56	6.60	2.70	6.05
0.22	"	2.03	13.4	1.76	5.03
0.28	"	1.31	>100	1.31	6.43
0.31	"	1.59	25	1.49	18.6

5. RUN ANALYSIS : WFD MODEL

5.1 0.05 m Unit

U_0 (m/s)	L_t (m)	X_b	α	EI
0.17	0.40	1.19	0	1.68
0.19	"	1.04	0	3.34
0.24	"	0.98	0	3.93
0.30	"	1.06	0	1.21
0.14	0.97	1.48	0.002	33.1
0.16	"	1.53	0	27.4
0.30	"	1.08	.005	1.26
0.46	"	0.98	0	7.02
0.60	"	0.55	0	1.60
0.14	2.51	2.96	0	1.22
0.18	"	2.90	0	1.38
0.26	"	1.92	0	1.31
0.38	"	1.72	0	2.30
0.57	"	1.17	0	1.70
0.70	"	1.16	0	1.68
0.23	3.46	2.72	0	1.25
0.38	"	1.95	0.004	1.09
0.43	"	2.07	0	1.58
0.59	"	1.55	0	1.15

5.2 0.64 m Unit, 7 Coils

U_0 (m/s)	L_t (m)	X_b	α	EI
0.13	0.49	0.70	0.012	3.00
0.19	"	0.58	0	3.79
0.22	"	0.82	0	2.02
0.27	"	0.37	1.62	6.41
0.32	"	0.60	0.52	1.85
0.15	0.95	1.07	0	21.0
0.25	"	0.93	0.054	2.21
0.28	"	0.72	0	5.50
0.38	"	0.62	0	3.53
0.44	"	0.58	0	3.32
0.17	1.95	1.15	0.061	11.7
0.20	"	0.89	0.033	8.46
0.26	"	0.84	0	6.47
0.34	"	0.62	0.0055	4.81
0.39	"	0.84	0	2.37
0.53	"	0.53	0	1.46
0.16	3.05	1.91	0	17.3
0.23	"	1.25	0.015	19.7
0.30	"	1.29	0	24.3
0.37	"	0.85	0	4.84
0.42	"	0.62	0	5.45

5.3 0.64 m Unit, no Coils

U_0 (m/s)	L_t (m)	X_b	α	EI
0.14	3.05	1.59	0	3.74
0.18	"	1.66	0	10.1
0.22	"	1.25	0	6.59
0.28	"	1.14	0	7.55
0.31	"	1.29	0	22.4

6. RUN ANALYSIS : LSBP MODEL

0.64 m Unit, 7 Coils, Sparger

U_0 (total) (m/s)	L_t (m)	K_s (sec^{-1})	D_d (m^2/sec)	X_s	EI
0.16	0.67	1.10	0.025	0.94	1.00
0.22	"	1.30	0	1.06	1.00
0.28	"	1.19	0	0.93	1.00
0.36	"	1.00	0	0.64	1.00
0.41	"	1.22	0	0.79	1.00
0.46	"	1.16	0	0.75	1.00
0.16	1.57	.78	0.089	1.41	1.00
0.19	"	.75	0.102	1.33	1.00
0.24	"	.69	0.097	1.06	1.00
0.27	"	0.72	0.030	1.12	1.00
0.31	"	0.79	0.120	1.14	1.00
0.38	"	0.67	0.011	0.94	1.00
0.43	"	0.63	0.009	0.85	1.00
0.12	2.67	0.70	0.205	1.92	1.00
0.17	"	0.68	0.914	1.45	1.00
0.24	"	0.66	0.011	1.28	1.00
0.26	"	0.59	0.032	1.13	1.00
0.30	"	0.64	0.054	1.20	1.00

7. RUN ANALYSIS : LMBP MODEL

0.64 m Unit, 7 Coils, Sparger

U_0 (total) (m/s)	L_t (m)	K_u (sec^{-1})	D_d (m^2/s)	EI
0.16	0.67	0.71	0.083	3.24
0.22	"	0.52	0.102	5.76
0.28	"	0.36	0.003	4.11
0.36	"	0.49	0	2.43
0.41	"	0.37	0	3.42
0.46	"	0.43	0	4.67
0.16	1.57	.62	0.024	1.08
0.19	"	0.50	0.042	1.43
0.24	"	0.55	0	1.91
0.27	"	0.43	0	66.7
0.31	"	0.48	0	4.21
0.38	"	0.30	0	10.3
0.43	"	0.26	0	2.59
0.12	2.67	0.51	0.039	1.47
0.17	"	0.34	0.126	1.05
0.24	"	0.30	0	1.59
0.26	"	0.37	0	3.22
0.30	"	0.34	0	1.20

LIST OF REFERENCES

1. A.M. SQUIRES, Paper presented at joint meeting of AIChE and Chem. Ind. and Eng. Soc. China, Peking (Sept. 1982).

2. C.E. JAHNIG, D.L. CAMPBELL and H.Z. MARTIN, Fluidization, ed. J.R. Grace and M. Matsen, Plenum Press, N.Y., (1980), p.3.

3. F.A. ZENZ and D.F. OTHMER, Fluidization and Fluid-Particle Systems, Reinhold, N.Y. (1960), p.36.

4. E.R. GILLILAND and E.A. MASON, Ind. Eng. Chem., 41 (1949), 1191.

5. E.R. GILLILAND and E.A. MASON, Ind. Eng. Chem., 44 (1952), 218.

6. P.V. DANKWERTS, J.W. JENKINS and G. PLACE, Chem. Eng. Sci., 3 (1954), 26.

7. A.R. HUNTLEY, W. GLASS and J.J. HEIGL, Ind. Eng. Chem., 53 (1961), 382.

8. R.D. TOOMEY and H.F. JOHNSTONE, Chem. Eng. Prog., 48 (1952), 220.

9. C.Y. SHEN and H.F. JOHNSTONE, AIChE J., 1 (1955), 349.

10. J.F. MATHIS and C.C. WATSON, AIChE J., 2 (1956), 518.

11. W.K. LEWIS, E.R. GILLILAND and W. GLASS, AIChE J., 5 (1959), 419.

12. W.G. MAY, Ind. Eng. Prog., 55, 12 (1959), 49

13. K.P. LANNEAU, Trans. I. Chem. E., 38 (1960), 125.

14. A. GOMEZPLATA and W.W. SHUSTER, AIChE J., 6 (1960) 454

15. J.J. VAN DEEMTER, Chem. Eng. Sci., 13 (1961), 143.

16. F.A. ZENZ, Pet. Ref., 36 (1957), 321.

17. J.F. DAVIDSON, Trans. Inst. Chem. Eng., 39 (1961), 230.

18. H. REUTER, Chem. Eng. Tech., 35, 98 (1963), 219.

19. M.R. JUDD, Ph.D. dissertation, University of Cape Town, 1965.

20. R. JACKSON, Trans. Inst. Chem. Eng., 41 (1963), 13.

21. J.D. MURRAY, J. Fluid Mech., 21 (1965), 465.

22. J.C. ORCUTT, J.F. DAVIDSON and R.L. PIGFORD, Chem. Eng. Prog. Symp. Ser., 38, 58 (1962),1.

23. R. HIGBIE, Trans. Am. Inst. Chem. Eng., 31 (1935), 365.

24. J.C. ORCUTT, Ph.D. dissertation, University of Delaware, 1960.

25. P.N. ROWE and K.S. SUTHERLAND, Trans. Inst. Chem. Eng., 42 (1964), T55.

26. P.N. ROWE and B.A. PARTRIDGE, Proc. Int. Symp. on Interaction between Fluids and Particles, Inst. Chem. Eng., 135 (June 1962).

27. P.N. ROWE and B.A. PARTRIDGE, Trans. Inst. Chem. Eng., 43 (1965), T157.

28. D. KUNII and O. LEVENSPIEL, Fluidization Engineering, John Wiley, New York (1969).

29. R. LATHAM, C. HAMILTON and O.E. POTTER, Brit. Chem. Eng., 13, (1967), 666.

30. G.K. STEVENS, R.J. SINCLAIR and O.E. POTTER, Pow. Tech., 1 (1967).

31. J. KUHNE and D. WIPPERN, Can. J. Chem. Eng., 58 (1980), 527.

32. T. MIYAUCHI, J. Chem. Eng. Japan, 7 (1974), 201.

33. T. MIYAUCHI, S. FURUSAKI, S. MOROOKA and Y. IKEDA, Adv. Chem. Eng., 11 (1981), 275.

34. H. KOBAYASHI, F. ARAI and T. CHIBA, Kagaku Kogaku, 29 (1965), 858.

35. J.R. GRACE, ACS Symp. Ser., 168 (1981), 3.

36. C. FRYER and O.E. POTTER, Ind. Eng. Chem. Fundam., 22, (1972), 338.

37. P.N. ROWE, Chem. Eng. Prog., 60, 3 (1964), 75.

38. J.R. GRACE, Chem. Eng. Sci., 26 (1971), 1955.

39. J.F. DAVIDSON and D. HARRISON, Fluidised Particles, Campbridge Univ. Press (1963).

40. T. MAMURO and I. MUCHI, Int. Chem. Eng., 5 (1965) 732.

41. R.J. BAYWATER, AIChE J. Symp. Ser., 74, 176 (1978), 126.

42. J.D. GABOR, Proc. Int. Symp. on Fluidisation, Netherlands Univ. Press, Amsterdam (1967), 230.

43. A.K. HAINES, R.P. KING and E.T. WOODBURN, AIChE J., 18, 3 (1972), 591.

44. J.A. VALENZUELA and L.R. GLICKSMAN, Pow. Tech., 38 (1984), 63.

45. O.E. POTTER, A.B. WHITEHEAD and H.V. NGUYEN, Chem. Eng. Aust., 6, 4 (1981), 42.

46. K. KATO and C.Y. WEN, Chem. Eng. Sci., 24 (1969), 135†.

47. S. MORI and C.Y. WEN, Fluidization Technology, ed. D.L. Keairns, Hemisphere, Washington, 1 (1976), 179.

48. M.H. PETERS, L. FAN and T.L. SWEENEY, Chem. Eng. Sci., 37, 4 (1982), 553.

49. D. WIPPERN, K. WITTMANN, J. KUHNE, H. HELMRICH and K. SCHUGERL, Chem. Eng. Commun., 10 (1981), 307.

50. J. LEHMANN and K. SCHUGERL, Chem. Eng. J., 15 (1978), 91.

51. M. YAMAZAKI, N. ITO and G. JIMBO, Kagaku Kogaku, 3 (1977), 272.

52. K. YOSHIDA, K. NAKAJIMA, N. HAMATANI and F. SHIMUZU, Fluidization, ed. J.F. Davidson and D.L. Keairns, Cambridge Univ. Press (1978), 13.

53. J. WERTHER, Int. J. Multiphase Flow, 3 (1977), 67.

54. P.N. ROWE and D.J. EVERETT, Trans. Inst. Chem. Eng., 43 (1965), 42.

55. D. GELDART, Pow. Tech., 6 (1972), 201.

56. J. WERTHER and O. MOLERUS, Int. J. Multiphase Flow, 1 (1973), 123.

57. T. TSUTSUI and T. MIYAUCHI, Int. J. Chem. Eng., 20, 3, (1980), 386.

58. P.N. ROWE, Chem. Eng. Sc., 31 (1976), 285.

59. J. WERTHER, Fluidization Technology, ed. D.L. Keairns, Hemisphere, Vol. 1 (1976), 215.

60. R.C. DARTON, A.D. LANAUZE, J.F. DAVIDSON and D. HARRISON, Trans. Inst. Chem. Eng., 55 (1977), 274.

61. H. KOBAYASHI, F. ARAI and T. CHIBA, Kagaku Kogaku, 4 (1966), 147.

62. S. MORI and C.Y. WEN, AIChE J., 21, 1 (1975), 109.

63. R.M. DAVIES and G.I. TAYLOR, Proc. Roy. Soc. Ser., A200 (1950), 375.

64. P.N. ROWE, Fluidization, ed. J.F. Davidson and D. Harrison, Academic Press, London (1971), Ch. 4.

65. J. WERTHER, Chem-Ing. Techn., 49 (1977), 193.

66. A.W. WEIMER and D.E. CLOUGH, AIChE J., 29, 3 (1983) 411.

67. D. HARRISON, J.F. DAVIDSON and J.W. DE KOCK, Trans. Inst. Chem. Eng., 39 (1961), 202.

68. A.M. SQUIRES, Chem. Eng. Prog. Symp. Ser., 58, 38 (1962), 57.

69. P.N. ROWE, Chem. Eng. Prog. Symp. Ser., 58, 38 (1962) 42.

70. P.S.B. STEWART and J.F. DAVIDSON, Pow. Tech., 1 (1967), 61.

71. D.J. NICKLIN, J.O. WILKES and J.F. DAVIDSON, Trans. Inst. Chem. Eng., 40 (1962), 61.

72. D.T. DUMITRESCU, Z. Angew. Math. Mech., 23 (1943) 139.

73. G. BIRKHOFF and D. CARTER, J. Rat. Mech. Anal., 6 (1957), 769.

74. S. HOVMAND and J.F. DAVIDSON, Fluidization, ed. J.F. Davidson and D. Harrison, Academic Press, London (1971), Ch.5.

75. S.P. SIT and J.R. GRACE, Chem. Eng. Sci., 33 (1978) 1115.

76. S.P. SIT and J.R. GRACE, Chem. Eng. Sci., 36 (1981), 317.

77. J. PEREIRA and P.H. CALDERBANK, Fluidization Technology, ed. D.L. Keairns, Hemisphere (1976), 115.

78. M.J. COOKE, W. HARRIS, J. HIGHLEY and D.F. WILLIAMS, Symp. on Fluidization I, Tripartite Chem. Eng. Conf., Montreal (Sept. 1968), Inst. Chem. Eng., 14.

79. S. HOVMAND, W. FREEDMAN and J.F. DAVIDSON, Trans. Inst. Chem. Eng., 49 (1971), 149.

80. V.A. BASOV, V.I. MARKEVKA, T. MELIK-AKHNAZAROV and D.I. OROCHKO, Int. Chem. Eng., 9 (1969), 263.

81. J.M.D. MERRY, AICh J., 21, 3 (1975), 507.

82. Y. YANG and D.L. KEAIRNS, Fluidization, ed. J.F. Davidson and D.L. Keairns, Cambridge University Press (1978), 208.

83. C.Y. WEN, M. HORIO, R. KRISHNAN, R. KHOSRVAI and P. RENGARAGJAN, Proc. 2nd Pacific Chem. Eng. Conf., Denver, Colorado, 2 (1977), 1182.

84. F.A. ZENZ, Trans. Inst. Chem. Eng. Symp. Ser., 30 (1968), 136.

85. T.M. KNOWLTON and I HIRSAN, Fluidization, ed. J.R. Grace and J.M. Matsen, Plenum Press, N.Y., (1980), 315.

86. W. YANG, IEC Fundamentals (in print).

87. P.N. ROWE, H.J. MacGILLIVRAY and D.J. CHEESMAN, Trans. Inst. Chem. Eng., 57 (1979), 94.

88. C.Y. WEN, N.R. DEOLE and L.H. CHEN, Pow. Tech., 31 (1982), 175.

89. L.A. BEHIE, Ph.D. dissertation, University of Western Ontario, London, Canada (1972).

90. A.F. ERRAZU, H.I. DE LASA and F. SARTI, Can. J. Chem. Eng., 57 (1979), 191.

91. H.I. DE LASA, A.F. ERRAZU, E. BARREIRO and S. SOLIOZ, Can. J. Chem. Eng., 59 (1981), 549.

92. A.W. WIEMER and D.E. CLOUGH, Chem. Eng. Sci., 38 (1981), 549.

93. T. MIYAUCHI, S. FURUSAKI and Y. YAMADA, Fluidization, ed. J.R. Grace and J.M. Matsen, Plenum Press, N.Y., (1980), 571.

94. O.E. POTTER, Catal. Rev. Sci. Eng., 17, 2 (1978), 155.

95. J.R. GRACE, AIChE Symp. Ser., 116, 67 (1971), 159.

96. P.N. ROWE, Proc. 2nd Int/5th Europ. Symp. on Chem. Reaction Eng., Elsevier, Amsterdam (1972), A0-1.

97. M. HORIO and C.Y. WEN, AIChE Symp. Ser., 73, 161 (1977), 9.

98. J. WERTHER, Chem. Eng. Sci., 35 (1980), 372.

99. D.M. HIMMELBLAU, Process Analysis by Statistical Methods, John Wiley, N.Y. (1970), ch. 12.

100. B. CARNAHAN, H.A. LUTHER and J.O. WILKES, Applied Numerical Methods, John Wiley, N.Y. (1969).

101. V.G. JENSON and G.V. JEFFREYS, Mathematical Methods in Chemical Engineering, Academic Press, London (1963).

102. J.M. BETTENCOURT, O.C. ZIEKIEWICZ and C. CANTIN, Int. J. Num. Methods in Eng., 17 (1981), 931.

103. J.A. NELDER and R. MEAD, Compt. J., 7 (1965), 308.

104. R.J. DRY, M.Sc. dissertation, University of Natal, 1982.

105. P.A.N. BRIGGS, P.H. HAMMOND, M.T.G. HUGHES and G.O. PLUMB, Proc. Inst. Mech. Eng., 79, 3H (1964), 53.

106. P.W. GALLIER, C.M. SLIEPCEVICH and T.H. PUCKETT, Chem. Eng. Prog. Symp. Ser., 57, 36 (1961), 59.

107. E.T. WOODBURN, R.P. KING and R.C. EVERSON, Can. J. Chem. Eng., 47 (1969), 301.

108. E.R. CORRAN and J.D. CUMMINS, "Binary Codes with Impulse Autocorrelation Functions for Dynamic Experiments", UKAEA, AEEW Report No. R210 (1962).

109. D. EVERETT, G.E.C. Journal, 33, 3 (1966), 115.

110. R.C. EVERSON, Ph.D. dissertation, University of Natal, 1967.

111. R.P. KING and E.T. WOODBURN, Research Report No. 327, NIM, Johannesburg (1968).

112. A.K. HAINES, Ph.D. disseration, University of Natal, 1970.

113. K. RIETEMA, Proc. Int. Symp. on Fluidization, Netherlands Univ. Press, Amsterdam (1967), 154.

114. A.R. ABRAHAMSEN and D. GELDART, Pow. Tech., 26 (1980), 47.

115. T. TSUTSUI and T. MIYAUCHI, Int. Chem. Eng., 20, 3 (1980) 386.

116. M.A. BERGOUGNOU, J. Bulk Pow. Solids Tech., 5, 3 (1981), 20.

117. W.P.M. VAN SWAAIJ and F.J. ZUIDERWEG, Proc. 2nd Int/5th Europ. Symp. on Chem. Reaction Eng., Elsevier, Amsterdam (1972), B9-25.

118. R.J. DE VRIES, W.P.M. VAN SWAAIJ, C. MANTOVANI and H. HEIJKOOP, ibid- B0-59.

119. R.J. BOTTON, Chem. Eng. Prog. Symp. Er., 66, 101 (1968), 8.

120. W. BAUER, J. WERTHER and G. EMIG, Ger. Chem. Eng., 4 (1981), 291.

121. J.R.F. GUEDES DE CARVAHLO and J.F. DAVIDSON, Chem. Eng. Sci., 37, 7 (1982), 1087.

122. H. KOBAYASHI, F. ARAI and T. SUNGAWA, Chem. Eng. Japan, 31 (1967), 239.

123. L.A. BEHIE and P. KEHOE, AIChE J., 19, 5 (1973), 1970.

124. R. KRISHNA, NATO Adv. Study Inst. Ser., Series E: Chem. Eng. Catal. Processes, 52, V2 (1981), 389.

125. T. MIYAUCHI and T. KIKUCHI, Preprint 42nd Ann. Meeting Soc. Chem. Eng. Japan, Hiroshima (1977), G305.

126. S.A. ALLAHWALA, B. SINGH and O.E. POTTER, Chem. Eng. Commun., 11 (1981), 255.

127. D.M. HIMMELBLAU and K.B. BISCHOFF, Process Analysis and Simulation, John Wiley, N.Y. (1968).

128. V.J. LAW and R.V. BAILEY, Chem. Eng. Sci., 18 (1963).